BIOELECTRONIC MEDICINES – NEW FRONTIERS IN AUTONOMIC NEUROMODULATION

EDITED BY: Arun Sridhar, Stephen Lewis, Philippe Blancou and Silvia V. Conde
PUBLISHED IN: Frontiers in Neuroscience

frontiers Research Topics

frontiers

ISSN 1664-8714
ISBN 978-2-88976-508-9
DOI 10.3389/978-2-88976-508-9

About Frontiers

Frontiers is more than just an open-access publisher of scholarly articles: it is a pioneering approach to the world of academia, radically improving the way scholarly research is managed. The grand vision of Frontiers is a world where all people have an equal opportunity to seek, share and generate knowledge. Frontiers provides immediate and permanent online open access to all its publications, but this alone is not enough to realize our grand goals.

Frontiers Journal Series

The Frontiers Journal Series is a multi-tier and interdisciplinary set of open-access, online journals, promising a paradigm shift from the current review, selection and dissemination processes in academic publishing. All Frontiers journals are driven by researchers for researchers; therefore, they constitute a service to the scholarly community. At the same time, the Frontiers Journal Series operates on a revolutionary invention, the tiered publishing system, initially addressing specific communities of scholars, and gradually climbing up to broader public understanding, thus serving the interests of the lay society, too.

Dedication to Quality

Each Frontiers article is a landmark of the highest quality, thanks to genuinely collaborative interactions between authors and review editors, who include some of the world's best academicians. Research must be certified by peers before entering a stream of knowledge that may eventually reach the public - and shape society; therefore, Frontiers only applies the most rigorous and unbiased reviews.
Frontiers revolutionizes research publishing by freely delivering the most outstanding research, evaluated with no bias from both the academic and social point of view. By applying the most advanced information technologies, Frontiers is catapulting scholarly publishing into a new generation.

What are Frontiers Research Topics?

Frontiers Research Topics are very popular trademarks of the Frontiers Journals Series: they are collections of at least ten articles, all centered on a particular subject. With their unique mix of varied contributions from Original Research to Review Articles, Frontiers Research Topics unify the most influential researchers, the latest key findings and historical advances in a hot research area! Find out more on how to host your own Frontiers Research Topic or contribute to one as an author by contacting the Frontiers Editorial Office: frontiersin.org/about/contact

BIOELECTRONIC MEDICINES – NEW FRONTIERS IN AUTONOMIC NEUROMODULATION

Topic Editors:
Arun Sridhar, Independent Researcher Milton Keynes, United Kingdom
Stephen Lewis, Case Western Reserve University, United States
Philippe Blancou, University of Nice Sophia Antipolis, France
Silvia V. Conde, New University of Lisbon, Portugal

Citation: Sridhar, A., Lewis, S., Blancou, P., Conde, S. V., eds. (2022). Bioelectronic Medicines – New Frontiers in Autonomic Neuromodulation.
Lausanne: Frontiers Media SA. doi: 10.3389/978-2-88976-508-9

Table of Contents

frontiers in Neuroscience

ORIGINAL RESEARCH
published: 11 March 2021
doi: 10.3389/fnins.2021.657361

High-Throughput Functional Characterization of Visceral Afferents by Optical Recordings From Thoracolumbar and Lumbosacral Dorsal Root Ganglia

Zichao Bian, Tiantian Guo, Shaowei Jiang, Longtu Chen, Jia Liu, Guoan Zheng and Bin Feng**

Department of Biomedical Engineering, University of Connecticut, Mansfield, CT, United States

OPEN ACCESS

Edited by:
Arun Sridhar, Independent Researcher, Milton Keynes, United Kingdom

Reviewed by:
Nick Spencer, Flinders University, Australia
Kenjiro Matsumoto, Kyoto Pharmaceutical University, Japan
Harumi Hotta, Tokyo Metropolitan Institute of Gerontology, Japan

***Correspondence:**
Guoan Zheng
guoan.zheng@uconn.edu
Bin Feng
fengb@uconn.edu

Specialty section:
This article was submitted to Autonomic Neuroscience, a section of the journal Frontiers in Neuroscience

Received: *22 January 2021*
Accepted: *22 February 2021*
Published: *11 March 2021*

Citation:
Bian Z, Guo T, Jiang S, Chen L, Liu J, Zheng G and Feng B (2021) High-Throughput Functional Characterization of Visceral Afferents by Optical Recordings From Thoracolumbar and Lumbosacral Dorsal Root Ganglia. Front. Neurosci. 15:657361. doi: 10.3389/fnins.2021.657361

Functional understanding of visceral afferents is important for developing the new treatment to visceral hypersensitivity and pain. The sparse distribution of visceral afferents in dorsal root ganglia (DRGs) has challenged conventional electrophysiological recordings. Alternatively, Ca^{2+} indicators like GCaMP6f allow functional characterization by optical recordings. Here we report a turnkey microscopy system that enables simultaneous Ca^{2+} imaging at two parallel focal planes from intact DRG. By using consumer-grade optical components, the microscopy system is cost-effective and can be made broadly available without loss of capacity. It records low-intensity fluorescent signals at a wide field of view (1.9 × 1.3 mm) to cover a whole mouse DRG, with a high pixel resolution of 0.7 micron/pixel, a fast frame rate of 50 frames/sec, and the capability of remote focusing without perturbing the sample. The wide scanning range (100 mm) of the motorized sample stage allows convenient recordings of multiple DRGs in thoracic, lumbar, and sacral vertebrae. As a demonstration, we characterized mechanical neural encoding of visceral afferents innervating distal colon and rectum (colorectum) in GCaMP6f mice driven by VGLUT2 promotor. A post-processing routine is developed for conducting unsupervised detection of visceral afferent responses from GCaMP6f recordings, which also compensates the motion artifacts caused by mechanical stimulation of the colorectum. The reported system offers a cost-effective solution for high-throughput recordings of visceral afferent activities from a large volume of DRG tissues. We anticipate a wide application of this microscopy system to expedite our functional understanding of visceral innervations.

Keywords: GCaMP, lumbar splanchnic, pelvic, visceral, dorsal root ganglia, visceral afferent, colorectal distension, optical recording

INTRODUCTION

Sensory information from the internal visceral organs is conveyed by visceral afferents, which transduce stimuli into trains of action potentials at the distal nerve endings embedded in visceral tissues (Spencer et al., 2014, 2016). Evoked action potentials are then transmitted to the spinal cord via long axons distal and central to their somata in the dorsal root ganglia (DRGs).

In pathophysiological conditions, visceral afferents can undergo functional changes to drive the persistence of disease conditions (Anand et al., 2007). For example, the sensitization of afferents innervating distal colon and rectum (colorectum) appears necessary for the prolonged visceral hypersensitivity and pain in irritable bowel syndrome (Feng et al., 2012a). A better functional understanding of visceral afferents in both health and diseases can potentially lead to the development of new treatment methods to reverse visceral hypersensitivity, the management of which is an unmet clinical need (Chen et al., 2017). Functional recordings from visceral afferents are challenged by the sparse nature of visceral innervations, i.e., visceral afferent somata being the minority in the DRG. For example, colorectal afferents make up less than 10% of the total afferent neurons in mouse L6 DRG, and the proportion is much smaller in adjacent DRGs (Guo et al., 2019).

The sparse distribution of visceral afferents in the DRG has prevented a wider application of conventional electrophysiological recordings to characterize visceral afferent functions. Only a handful of reports implemented intracellular DRG recordings by liquid-filled glass electrodes to characterize the neural encoding of afferents innervating the colon (Malin et al., 2011; Hibberd et al., 2016) and stomach (Bielefeldt et al., 2006). This is in contrast to a larger number of studies using similar approaches to record afferents innervating the skin (e.g., Woodbury and Koerber, 2007; Jankowski et al., 2010, 2012; Koerber et al., 2010; Molliver et al., 2011; Vrontou et al., 2013). Alternatively, recordings of visceral afferents were conducted by manually splitting afferent nerve trunk into microns thick filaments for single-fiber recordings (e.g., Feng and Gebhart, 2015) or using a miniature suction electrode to record from the nerve surface (e.g., Peiris et al., 2011). However, visceral organs are predominantly innervated by unmyelinated C-fibers and thinly myelinated Aδ-fibers (Sengupta and Gebhart, 1994; Danuser et al., 1997; Feng et al., 2012a; Herweijer et al., 2014; Schwartz et al., 2016), and their small axonal diameter has challenged single-fiber recordings using conventional electrodes or electrode arrays. In fact, there has been no convincing evidence in the literature demonstrating successful single-fiber recordings from unmyelinated C-type peripheral axons in mammalians by commercially available electrode arrays. Overall, electrophysiological approaches to characterize visceral afferent functions are technically challenging and can usually report no more than 100 neurons per study in the literature.

Alternatively, the fluorescent Ca^{2+} indicators like the Fura-2 and Fluo-4 have allowed the measurement of intracellular calcium concentrations, and corresponding algorithms have been developed to infer neural spike trains from intracellular calcium imaging data (Pachitariu et al., 2018). In addition, genetically encoded calcium indicators (GECI) can be selectively expressed in target neural populations to allow focused functional studies. Recently developed GECIs like GCaMP6f can rapidly alter their fluorescent responses within milliseconds to changes in intracellular calcium concentrations, which has made it possible to resolve individual spikes from GCaMP6f calcium responses when using fast scanning imaging methods like the confocal and two-photon microscopy (Podor et al., 2015). Recently, we and others have shown that conventional epi-fluorescence imaging is also capable to resolve individual spikes in CGaMP6f recordings (Emery et al., 2016; Kim et al., 2016; Smith-Edwards et al., 2016; Chisholm et al., 2018; Guo et al., 2019). This approach allows recording of neural activities from a whole mouse DRG (Guo et al., 2019), and thus is particularly suitable for studying visceral afferents whose somata are sparsely distributed in DRGs.

To enhance the recording efficiency from visceral afferents, we here report a cost-effective imaging system that allows optical GCaMP6f recordings of DRG neurons from a wide range of thoracic, lumbar, and sacral DRGs. By using two consumer-grade cameras with two photographic lenses, we simultaneously record GCaMP6f signals at two parallel focal planes with a 1.9-by-1.3-mm field of view, a ∼0.7 μm/pixel resolution, and a throughput of 50 frames per second for each camera. By tuning the ultrasonic motor ring within the photographic lenses, we can perform programmable control of axial focusing, providing a simple yet powerful tool for precise axial focus tracking without perturbing the sample (**Supplementary Materials 1, 2**). As an example, we implemented the optical recording system to characterize lumbar splanchnic and pelvic afferent innervations of the colorectum. We harvested thoracolumbar (T12 to L2) and lumbosacral (L5 to S1) DRGs innervating the colorectum via the lumbar splanchnic and pelvic nerves, respectively. We evoked colorectal afferent responses by delivering mechanical stimuli to the colorectum and implemented imaging stabilization algorithms to overcome the motion artifacts from mechanical disturbance. Furthermore, we have developed and optimized the post-processing algorithms to conduct unsupervised detection of visceral afferent responses from GCaMP6f recordings (**Supplementary Material 3**).

MATERIALS AND METHODS

All experiments were reviewed and approved by the University of Connecticut Institutional Animal Care and Use Committee (IACUC).

Optical Recording Setup

As shown in **Figures 1A,B**, the reported imaging system consists of the optical excitation and recording pathways. At the excitation path, we use a designated LED light source with the narrow frequency band (470 ± 13 nm) to excite GCaMP6f in DRG neurons. At the detection path, we use a high numerical aperture (NA) Nikon water dipping objective lens (16×, 0.8 NA) and two Canon photographic lenses (Canon EF 85 mm f/1.8 USM) for image acquisition. The system offers a wide field of view (1.9 by 1.3 mm) capable of capturing a whole mouse DRG. As shown in **Figure 1A**, the emitted fluorescence signals (506–545 nm) are evenly split into the two photographic lenses and captured by two image sensors (Sony IMX 183CLK, 2.4 μm pixel size). For both sensors, we perform 2 by 2 binning and acquire 8-bit gray-scale images at 50 frames per second. Each image resolution is 2,736 by 1,824 pixels with a 0.7 μm/pixel resolution at the focal plane in the DRG, sufficient to resolve the GCaMP6f signals in individual mouse DRG neurons of Φ10–40 μm as shown in **Figure 1C**.

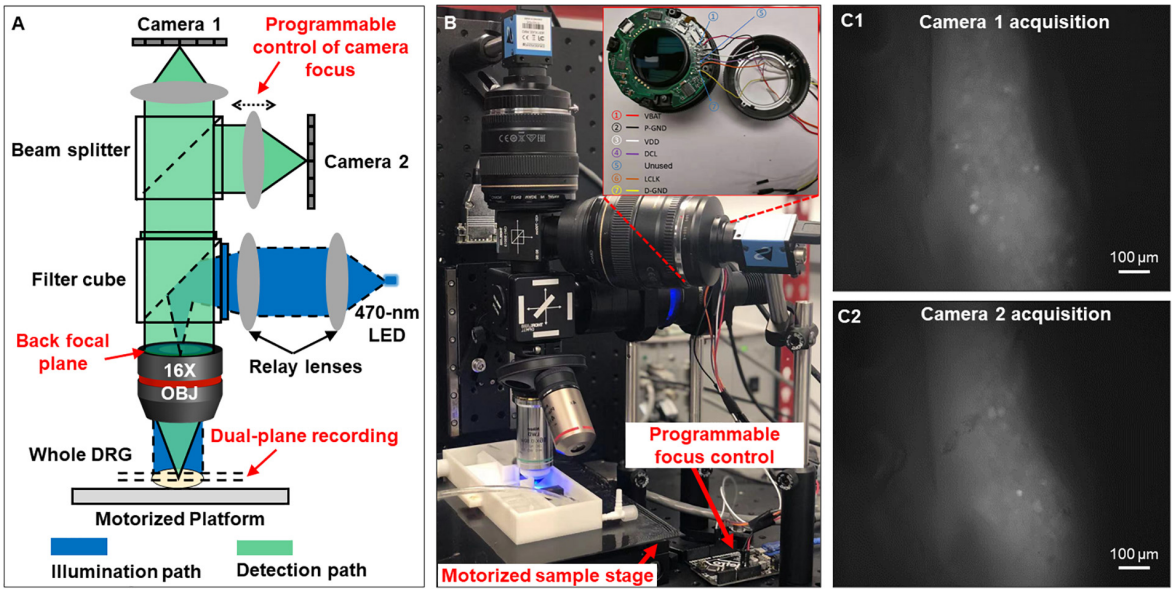

FIGURE 1 | Optical setup that simultaneously captures two focal planes of a whole DRG. **(A)** The schematic of the reported system. **(B)** The prototype setup. **(C)** Magnified view of the two focal planes recorded from an intact DRG.

One innovation of our microscopy system is that we can perform precise focus control using the two off-the-shelf Canon photographic lenses. For many electrophysiology experiments, axially moving the stage or the objective lens may perturb the samples, leading to image misalignment and movement artifacts. In our system, we perform remote focus control using the ultrasonic motor ring within the photographic lenses without perturbing the sample as shown in **Figure 1B**. The motors and control circuits inside the lens are connected to an Arduino Uno board (ATmega328P) via a 7-pin connector. By driving the motor ring to different positions, we can adjust the focal plane by up to 160 μm with a minimum axial step of 0.1 μm. Technical details for the remote focus control are reported in **Supplementary Material 2**.

The motorized sample stage (MS-2000 and LX-4000, Applied Scientific Instrument) in **Figure 1B** allows maximum sample movement of 100 mm in x and y directions and 50 mm in z direction. The motorized platform is controlled via an open-source software, micro-manager (Edelstein et al., 2014). The stage allows imaging of biological samples across a large field of view, for example, multiple lumbosacral and thoracolumbar DRGs inside mouse vertebrae. We have also developed customized programs with graphic-user-interfaces (GUI) to allow on-screen control of the image capturing. The source codes are included in **Supplementary Material 3**.

Transgenic Mice

The Ai95 mice (C57BL/6 background) carrying homozygous GCaMP6f gene (strain# 28865, The Jackson Laboratory, CT) and homozygous VGLUT2-Cre mice (strain# 28863, Jackson Laboratory, CT) were crossbred. The Ai95 mice carried the gene "CAG-GCaMP6f" in the Gt(ROSA)26Sor locus, which was preceded by a LoxP-flanked STOP cassette to prevent its expression. By crossing Ai95 mice with VGLUT2-Cre mice, the Cre-expressing cell population has the STOP cassette trimmed, resulting in expression of GCaMP6f in glutamatergic neurons expressing type 2 vesicular glutamate transporter (VGLUT2), which made up the vast majority of sensory neurons innervating the colorectum (Brumovsky et al., 2011). Offspring of both sexes aged 8–14 weeks with both heterozygous GCaMP6f and VGLUT2-Cre genes (i.e., VGLUT2/GCaMP6f) were used for optical recordings.

Ex vivo Functional Characterization of Colorectal Afferents

We implemented the above optical recording setup to characterize the afferent encoding functions by harvesting mouse colorectum, spinal nerves and ipsilateral T12 to S1 DRGs in continuity as shown in the schematic in **Figure 2A**. Mice 8–14 weeks of age were deeply anesthetized by intraperitoneal and intramuscular injection of a 0.4 mL cocktail of ketamine (120 mg/kg) and xylazine (10 mg/kg). Mice were then euthanized by perfusion from the left ventricle with modified ice-cold Krebs solution replacing sodium chloride with equal molar of sucrose (in mM: 236 Sucrose, 4.7 KCl, 25 $NaHCO_3$, 1.3 NaH_2PO_4, 1.2 $MgSO_4{\cdot}7H_2O$, 2.5 $CaCl_2$, 11.1 D-Glucose, 2 butyrate, 20 acetate) bubbled with carbogen (95% O_2, 5% CO_2), consistent with our prior *ex vivo* studies on colorectal afferents (Feng and Gebhart, 2011; Feng et al., 2016). A dorsal laminectomy was performed to expose the spinal cord and the thoracolumbar and lumbosacral DRG, i.e., from T12 to S1 DRG in **Figure 2B**. The colorectum with attached DRG and vertebrae was carefully dissected via blunt dissection, and transferred to a tissue chamber superfused with 32–34°C Krebs solution (in mM: 117.9 NaCl, 4.7 KCl,

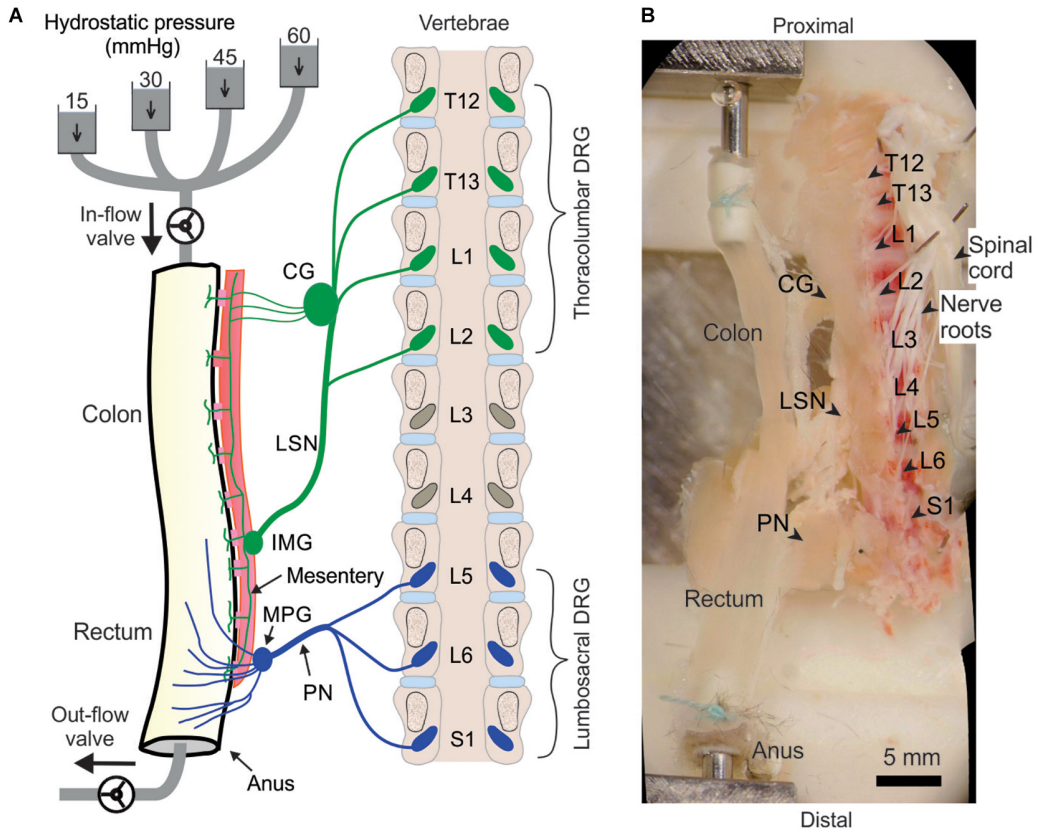

FIGURE 2 | Schematic **(A)** and photo **(B)** of the *ex vivo* preparation for functional recordings from afferents innervating distal colon and rectum (colorectum). The colorectum, spinal nerves, and T12—S1 DRGs were harvested from mice in continuity. The colorectum was cannulated and stimulated mechanically by graded pressure distension and mucosal shearing. The photo in **(B)** was from stitching multiple photos taken under a stereomicroscope. LSN, lumbar splanchnic nerve; PN, pelvic nerve; IMG, inferior mesenteric ganglion; MPG, major pelvic ganglion; CG, celiac ganglion.

25 $NaHCO_3$, 1.3 NaH_2PO_4, 1.2 $MgSO_4{\cdot}7H_2O$, 2.5 $CaCl_2$, 11.1 D-Glucose, 2 butyrate, 20 acetate) bubbled with carbogen (95% O_2, 5% CO_2). The dura mater covering thoracolumbar (T12 to S2) and lumbosacral (L5 to S1) DRG was carefully removed by blunt dissection using sharp forceps (#5SF Dumont forceps, Fine Science Tools).

Since most afferents innervating hollow visceral organs are mechanosensitive (Feng and Guo, 2020), we mechanically stimulate the colorectal endings by using a custom-built colorectal distension /perfusion device as illustrated in **Figure 2A**. The colorectum was cannulated and connected to a custom-built distending device with both in-let and out-let controlled by solenoid valves. Hydrostatic pressure columns of 15, 30, 45, and 60 mmHg filled with phosphate buffered saline (PBS) were used to deliver two distinct mechanical stimuli to colorectal afferents: colorectal distension and mucosal shearing. The control function of the solenoid valves was integrated into the same MATLAB program that captures the GCaMP6f images, allowing total program-controlled mechanical stimulation and optical recording of visceral afferents. The MATLAB program controls the solenoid valves via an Arduino microcontroller. To enable the research community to easily duplicate this distending device, we have reported in detail the hardware design, part information and the source code of the software in **Supplementary Materials 4**.

Optical Recording of Evoked Fluorescence GCaMP6f Signal

We capture the evoked GCaMP6f signal in each mouse DRG by high-resolution images (2,736 by 1,824 pixels after 2 by 2 binning), which provides a spatial resolution of 0.7 μm/pixel, sufficient to resolve individual DRG neurons. This system allows the recording of Ca^{2+} transients to resolve individual action potentials (APs) in a whole GCaMP6f-expressing DRG at two different focal planes simultaneously. The GCaMP6f signals were recorded at 50 frames per second, a sampling rate justified by the frequency spectrum of recorded Ca^{2+} transients. For a typical recording protocol of 40 s on one DRG, a total of 4,000 images are recorded, occupying 20 Gigabytes of hard drive space.

Automated Detection of GCaMP6f Signals From Recorded Image Stacks

We have developed an integrated routine to automatically extract GCaMP6f signals from recorded image stacks. The program first performs image alignment to account for the motion

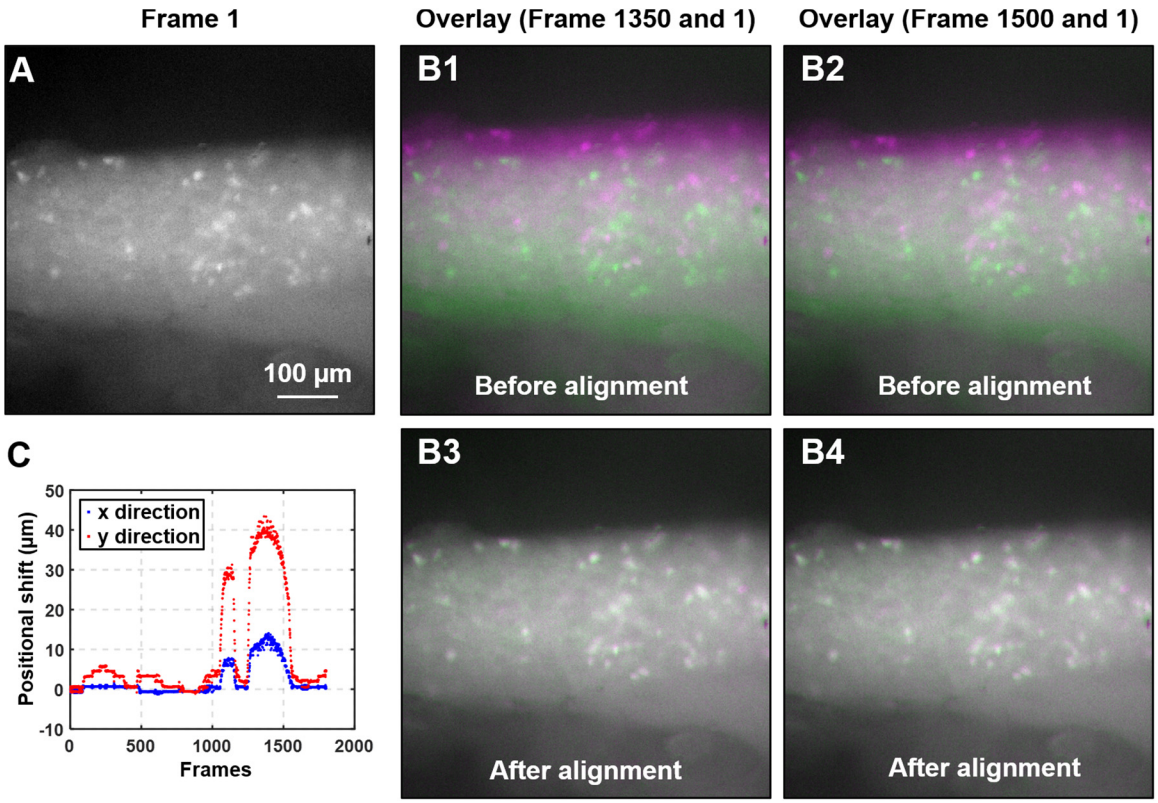

FIGURE 3 | Algorithm to mitigate the motion artifact during DRG recording. **(A)** The magnified view of the first frame of the captured image stack. **(B)** The overlays of two typical image frames (#1350 and 1500, in magenta color) with the first frame (in green). Significant motion artifacts were revealed with overlays in B1 and B2 before alignment, which was greatly reduced in B3 and B4 after alignment. **(C)** The translational shifts of all image frames recorded from a typical colorectal distension protocol.

artifacts during DRG recording, which is unavoidable when characterizing the mechanotransduction of visceral afferents by mechanically stimulating the attached colorectum. It will then automatically detect DRG neurons with positive GCaMP6f signals using a series of unsupervised signal processing algorithms as detailed below, i.e., marker-based watershed segmentation, band-pass filtering, and variance analysis.

Image Alignment

As illustrated in **Figures 3A,B1,B2**, there is usually translational movement of more than 30 μm in the recorded DRG images during mechanical colorectal distension or mucosal shearing. We employ a misalignment correction algorithm to correct this translational and slight rotational movement of DRG (Mattes et al., 2001). We use the first frame as the reference image and perform image registration for all other frames in the image stack by maximizing the mutual information (MI) of different images. MI is a measure of image matching, and it does not require the signal to be the same in the two images (i.e., the second image can be slightly distorted with respect to the first one). It is a measure of how well one can predict the signal in the second image from the signal intensity in the first image. MI has been widely used to match images captured under different imaging modalities (Li, 1990; Pluim et al., 2003). The mutual information MI between two images X and Y can be expressed as:

$$MI(X, Y) = H(X) H(Y) - H(X, Y) \quad (1)$$

where $H(X)$ and $H(Y)$ are the entropy of the two images, and $H(X, Y)$ is the joint entropy. A higher MI implies larger reduction in the uncertainty between the two distributions, which means the images are better aligned. In our implementation, we allow translational shift and image rotation in the registration process. We use a gradient descent algorithm to maximize the MI with subpixel accuracy (Van Der Bom et al., 2011). To ensure the convergence, we apply 50 iterations in the optimization process. **Figure 3A** shows the first frame of the captured image stack. **Figure 3B** shows the overlays between the unaligned/aligned images of two frames. We observed a significant positional drift without applying the MI alignment process as shown in **Figures 3B1,B2**, which were corrected by the alignment algorithm as shown in **Figures 3B3,B4**. Displayed in **Figure 3C** is the quantified positional shift in x and y directions for the recorded 2,000 images in one experiment, showing a maximum shift of over 40 μm. We did not plot the rotation angle as it is relatively insignificant compared to the translational shift. A representative image stack before and

TABLE 1 | Algorithm outline for automatic detection of GCaMP6f signals.

Algorithm outline

Input: Aligned time sequence images I_j ($j = 1, 2, \cdots, J$)
Output: GCaMP6f signals' profile S_m ($m = 1, 2, \cdots, M$) from activated DRG neurons

1 Calculate the variance map V of the image stack I_j ($j = 1, 2, \cdots, J$) along the time dimension
2 Initialize the global threshold H_G, the active neuron number P and neuron size rang R_{min}, R_{max}
3 **for** n = 1: N (different iterations) with condition if identified neurons p < estimation number P
4 Variance map V *Global threshold* $H_G \Rightarrow$ Binary image BW_{global}
Variance map V *Adaptive threshold* $H_A \Rightarrow$ Binary image $BW_{adaptive}$
5 $BW_{combined} = BW_{global} \cdot BW_{adpative}$, where '·' stands for point-wise multiplication
6 Morphological closing operation: $BW_{close} = (BW_{combined} \oplus SE) \ominus SE$ where structuring element $SE = [0, 1, 0; 1, 1, 1; 0, 1, 0]$
7 Morphological opening operation: $BW_{open} = (BW_{close} \ominus SE) \oplus SE$ where use the same structuring element SE as above
8 BW_{open} *Remove the small features* $\Rightarrow BW_{open\_updated}$
9 $BW_{open\_updated}$ *Clear the features at image border* $\Rightarrow BW_{updated}$
10 $BW_{updated}$ *Calculate the distance matrix* $\Rightarrow M_{distance}$
11 $M_{distance}$ *Watershed transform* $\Rightarrow L_{watershed}$
12 $L_{watershed}$ *Select neuron size between* R_{min} $R_{max} \Rightarrow L_{selected}$
13 Update the global threshold $H_{G\_updated} = H_G * \alpha$,where step size $\alpha = 0.75$
14 **end**

15 **for** m = 1:M (different neuron regions)
16 **for** j = 1: J (different captured images)
17 $S_{m\_j} = Mean\ (L_{select\_m} \cdot I_j)$ Calculate the average intensity profile of the neuron
18 **end**
19 **end**

after alignment is converted into two videos and reported in **Supplementary Video 1**.

Automatic Detection of GCaMP6f Signals

Table 1 summarizes the procedures of GCaMP6f signal detection. We first calculate the variance map V based on the aligned image stack I_j(j $= 1, 2, \cdots, J$), where I_j is the j^{th} captured image. We then initialize the global threshold H_G, the estimated number of active neurons P, and the size range of neuron R_{min} and R_{max}. In the iterative neuron identification process, the variance map V is converted into two binary images BW_{global} and $BW_{adaptive}$ using global threshold H_G and adaptive threshold H_A, respectively. The adaptive threshold H_A is chosen based on the local mean intensity in the neighborhood of each pixel. The pointwise product of the binary images BW_{global} and $BW_{adaptive}$ gives a binary image $BW_{combined}$, which represents the map where signals vary most at different time points. This binary map also suppresses the information outside the region of interest for better signal extraction. Next, we apply morphological closing and opening operations to $BW_{combined}$ as follows:

$$BW_{close} = (BW_{combined} \oplus SE) \ominus SE \quad (2)$$

$$BW_{open} = (BW_{close} \ominus SE) \oplus SE \quad (3)$$

where $\oplus$ denotes dilation, $\ominus$ denotes erosion, and we use a 3-by-3 structuring element SE of [0,1,0;1,1,1;0,1,0] in Eqs. (2, 3). These two morphological operations can clean up the background noise for better signal extraction. We further remove the small features that have fewer than 40 pixels in size from the binary result BW_{open} and clear the features at image borders. The updated binary result $BW_{updated}$ is then used to create the distance matrix $M_{distance}$ as follows:

$$M_{distance} = distance\ transform\ (BW_{updated}) \quad (4)$$

where the distance transform of a binary image is the distance from every pixel to the nearest nonzero-valued pixel of that image. The watershed transform of the distance matrix $M_{distance}$ then returns a label matrix $L_{watershed}$ that identifies the possible active neurons' locations (watershed regions). The predefined neuron size range R_{min} and R_{max} are used to select the expected neurons and update the label matrix as $L_{selected}$. At the end of this iterative process, the global threshold H_G is updated by a step size α. The custom-built graphic-user-interfaces (GUI) for automatic extraction of GCaMP6f is shown in **Figure 4A**. In **Figure 4B**, we plot the GCaMP6f signals of identified neurons for further analysis.

Afferent Identification and Classification

Mouse colorectal afferents were activated by two physiologically correlated stimuli at the colorectum: stepped luminal distension by hydrostatic fluid column of phosphate buffered saline (PBS, 15, 30, 45, and 60 mmHg of 5-s steps) and luminal shear flow of PBS (20–30 mL/min) (Guo et al., 2019). Based upon response profiles to graded distension and luminal shear, colorectal DRG neurons were functionally classified into four classes: low-threshold (LT) muscular, high-threshold (HT) muscular, mucosal, and muscular-mucosal classes. LT-muscular afferents responded to all four distension pressure levels whereas HT-muscular only responded to noxious distension pressure (30, 45, and 60 mmHg); colorectal intraluminal pressure beyond 20 mmHg was considered noxious to mice (Kamp et al., 2003; Feng et al., 2010). Mucosal afferents did not respond to distension but responded to luminal shear flow. Muscular-mucosal afferents responded to both luminal shear flow and colorectal distension at all four pressure levels.

Data Recording and Analysis

Extracted GCaMP6f signals in the form of pixel intensity (0–255) from individual DRG neurons were normalized by the pre-stimulus intensity. Peak GCaMP6f transients were determined when the signal increased by 3% within 200 mSec. The duration of the GCaMP6f transients were determined by the measuring temporal width of the signal at 25% of the peak intensity. Proportions of afferent classes were compared by Chi-square test using SigmaStat v4.0 (Systat software, Inc., San Jose, CA). $P < 0.05$ was considered significant.

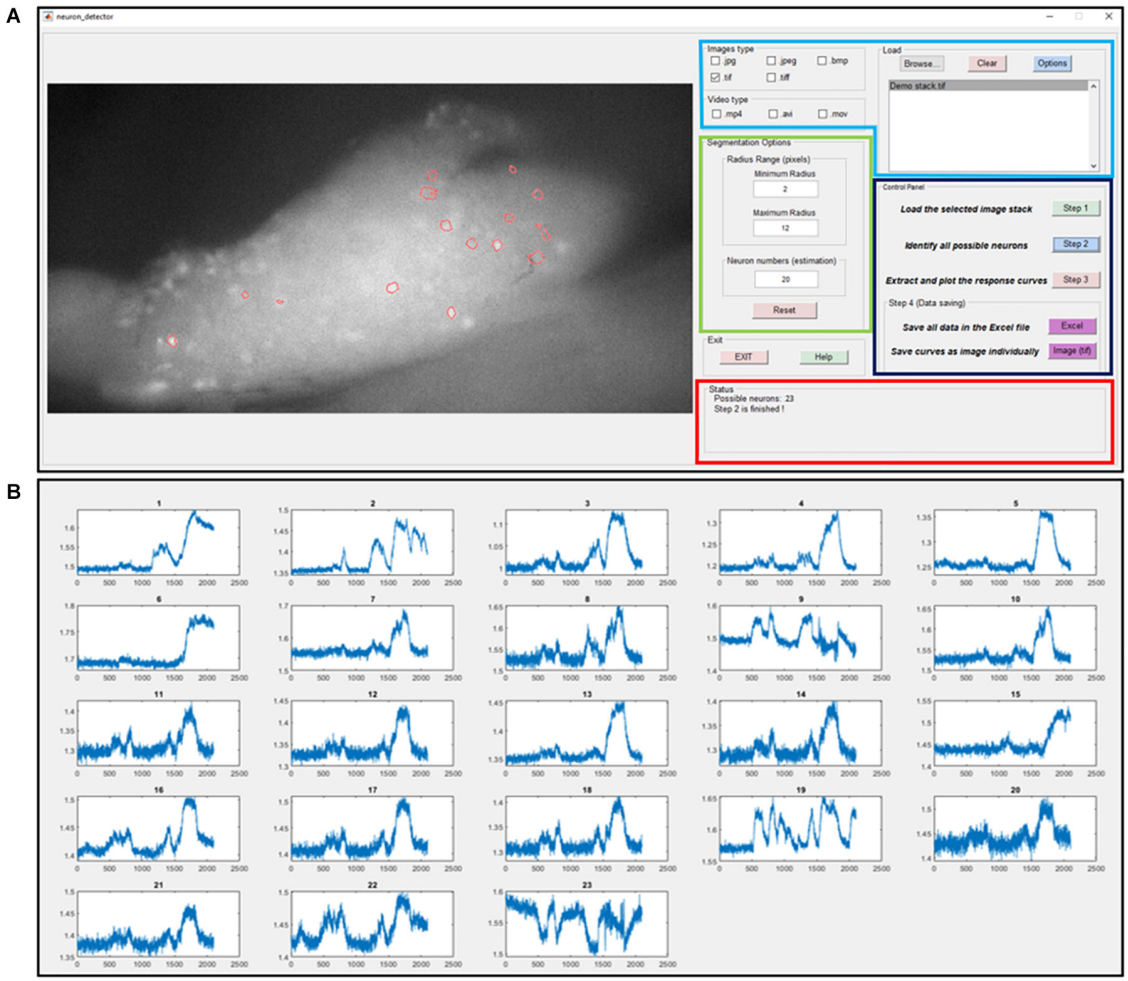

FIGURE 4 | The graphic-user-interface (GUI) of the custom-built software for automatic extraction of GCaMP6f responses from image stacks. **(A)** The GUI with five panels: The image process window (right), the input image format selection panel (right top with blue label), segmentation options (right middle with green label), control panel (right middle with black label) and status panel (right bottom with red label). **(B)** The extracted intensity profiles of evoked DRG neurons. Detailed descriptions are listed in **Supplementary Material 3**.

RESULTS

Using our custom-built imaging system, the evoked GCaMP6f transients in multiple DRGs were recorded at individual neural resolution. Displayed in **Figure 5** are evoked GCaMP6f transients ($\Delta F/F$, normalized fluorescent signals) in individual DRG neurons by electrical stimulation of attached dorsal roots. Recordings were conducted at 0.5, 2, and 4 Hz stimulation frequency (**Figure 5A**). The evoked GCaMP6f transients in **Figure 5B** showed a unanimous increase in baseline GCaMP6f intensity when stimulus frequency was beyond 0.5 Hz. The duration of the GCaMP6f transients was measured from 11 neurons at 0.5 Hz stimulation, showing an average duration of 1.31 ± 0.19 sec. Displayed in **Figure 5C** are the frequency domain of the GCaMP6f transients via fast Fourier transform, which shows that the majority of the signal frequency is between 0.3 and 5 Hz. The GCaMP6f signals were band-pass filtered (0.3–5 Hz) and displayed in **Figure 5D**. By analyzing the filtered signal, evoked single-spike GCaMP6f transients can be reliably detected in all recordings from 16 DRG neurons at 0.5 and 2 Hz stimulation, showing peak-to-peak $\Delta F/F$ above 3.5%. At 4-Hz stimulation, only 15% of the recordings (13 out of 87 DRG neurons in 4 mice) allow reliable detection of single-spike GCaMP6f transients (peak-to-peak $\Delta F/F$ above 3.5%) whereas the others do not.

In addition to electrical stimulation, mechanical colorectal distension and mucosal shearing were implemented to evoke GCaMP6f transients in individual colorectal DRG neurons (**Figures 6A,B**). The frequency domain of the GCaMP6f transients in **Figure 6C** indicates that the 0–5 Hz range covers most, if not all the signals of the GCaMP6f transients. Evoked afferent spikes by colorectal distension are generally high frequency (>2 Hz) to prevent reliable detection of single-spike GCaMP6f transients. In contrast, evoked afferent spikes by mucosal shearing are usually below 2 Hz and can be detected with single-spike resolution. The colorectal GCaMP6f signals

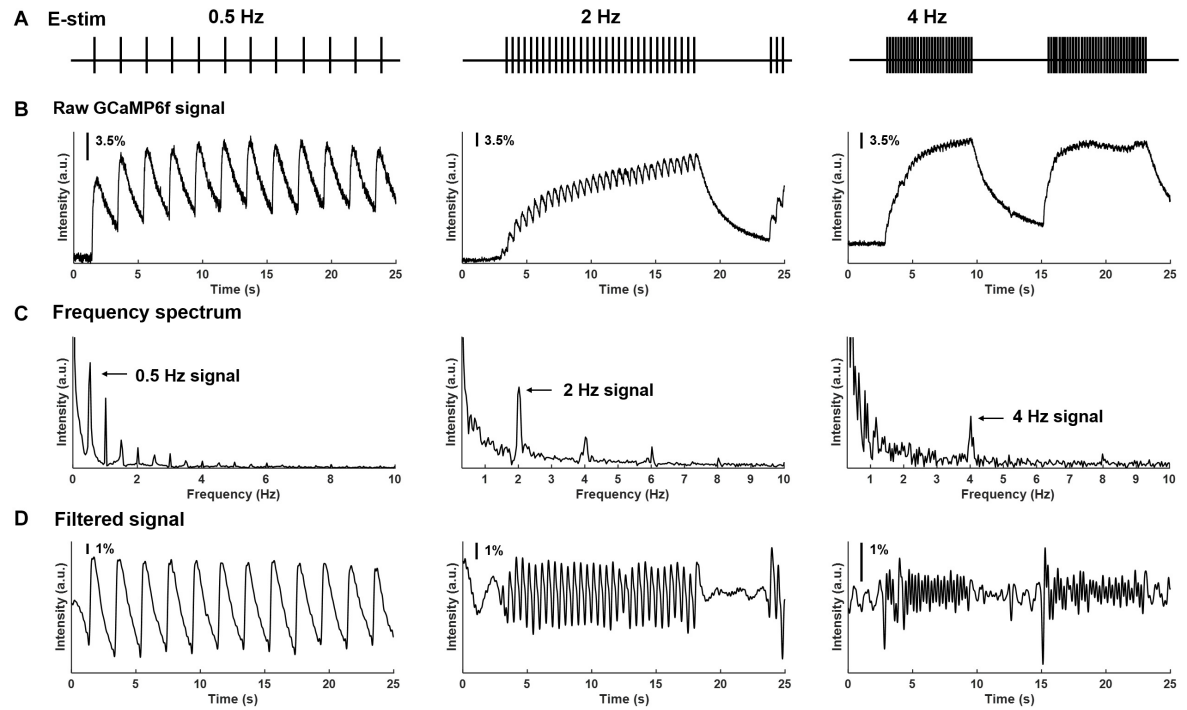

FIGURE 5 | Frequency spectrum analysis on GCaMP6f responses evoked by electrical stimulation of the attached dorsal root. **(A)** The implemented electrical stimulation at 0.5, 2, and 4 Hz, respectively. **(B)** Evoked GCaMP6f signals in individual DRG neurons. **(C)** The frequency domain of the GCaMP6f transients from fast Fourier transform. **(D)** Band-pass filtered GCaMP6f signals.

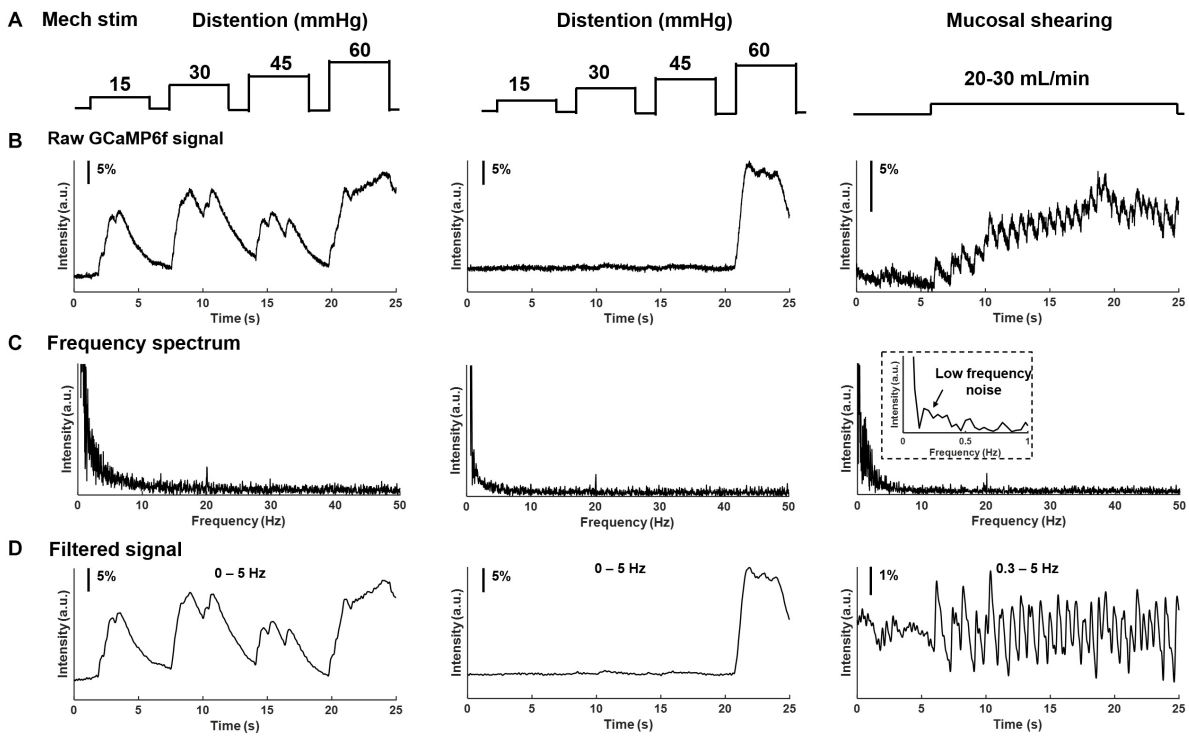

FIGURE 6 | Frequency spectrum analysis on GCaMP6f responses from colorectal afferents evoked by mechanical colorectal distension and mucosal shearing. **(A)** The implemented mechanical colorectal distension and luminal shear flow, respectively. **(B)** Evoked GCaMP6f signals in individual DRG neurons. **(C)** The frequency domain of the GCaMP6f transients from fast Fourier transform. **(D)** Band-pass filtered GCaMP6f signals.

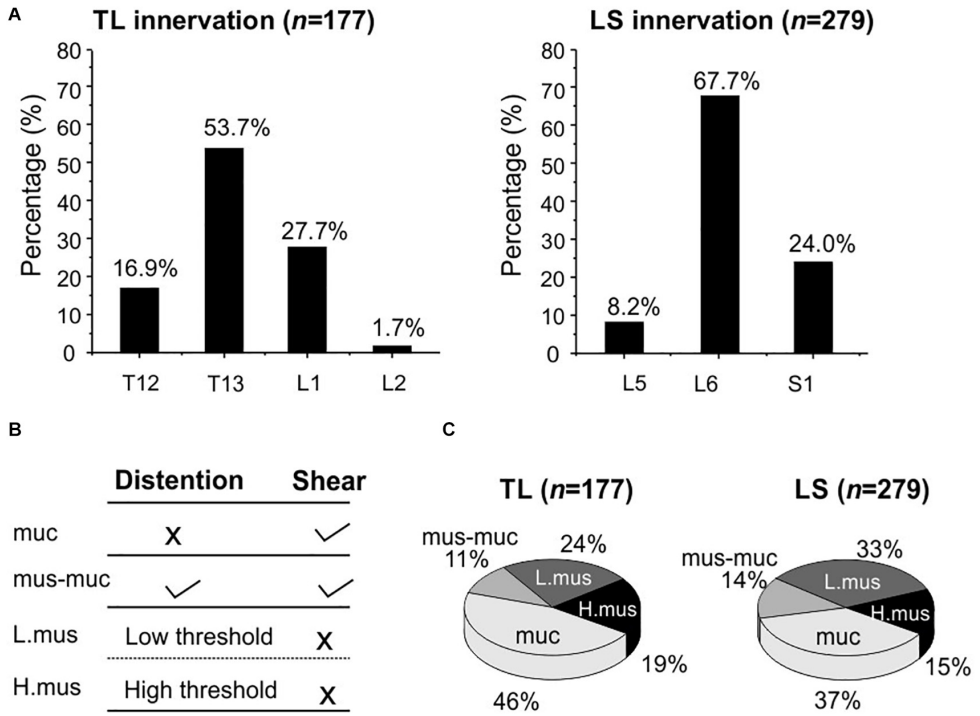

FIGURE 7 | Functional recording and characterization of afferents innervating mouse colorectum in both thoracolumbar (TL) and lumbosacral (LS) pathways. **(A)** The distribution of colorectal neurons in thoracolumbar (T12 to L2) and lumbosacral (L5 to S1) DRGs. **(B)** Functional classification of colorectal afferents based upon response profiles to colorectal distension (15, 30, 45, 60 mmHg) and mucosal shearing. **(C)** The distributions of four colorectal afferent classes within TL and LS innervations. muc, mucosal afferents; mus-mu, muscular-mucosal afferents; L.mus, low-threshold muscular afferents; H.mus, high-threshold muscular afferents.

were either low pass filtered (0–5 Hz for colorectal distension) or band-pass filtered (0.3–5 Hz for mucosal shearing) and displayed in **Figure 6D**.

Using our high-throughput imaging system, we recorded a total of 456 colorectal neurons from 12 male mice that respond to mechanical colorectal distension and/or mucosal shearing. Among the 456 colorectal afferents, the majority (61.2%) have somata in lumbosacral (LS) DRGs, i.e., from L5 to S1; the rest 38.8% have somata in thoracolumbar (TL) DRGs, i.e., from T12 to L2. The proportions of colorectal neurons in TL and LS DRGs are shown in **Figure 7A**, indicating concentrated presence of colorectal neurons in T13 and L6 DRGs of TL and LS innervation pathways, respectively. Colorectal afferent neurons were functionally classified into four groups based upon their response profiles to colorectal distension and/or mucosal shearing as shown in **Figure 7B**; refer to "Afferent identification and classification" in "Materials and Methods" section for details. The proportion of functionally distinct afferent groups in both TL and LS innervation pathways are displayed in **Figure 7C**. The proportions of colorectal afferent classes are not different between TL and LS pathways (Ch-square test, $p = 0.09$).

DISCUSSION

In this study, we reported a cost-effective high-throughput approach for functional characterization of afferents innervating visceral organs, which is generally challenging for the conventional electrophysiological recordings due to the sparse nature of visceral innervations. Functional characterization of neurons by optical recordings via GECI (Podor et al., 2015) is routinely conducted in the central nervous system (CNS) where stimulation modalities are usually either electrical or chemical. Peripheral sensory neurons encode additional stimulus modalities that are generally absent in the CNS, e.g., thermal and mechanical stimulations. Functional characterization of peripheral afferents requires applying stimuli to their nerve endings embedded in the end organs of innervation. Mechanical stimulation poses the greatest challenge for optical recordings compared to other stimuli (electrical, thermal, and chemical) due to the unavoidable motion artifacts of samples during mechanical disturbance. Even slight movement of tens of microns will lead to false optical recordings from neural somata, the diameters of which are usually in the same order.

Mechanical neural encoding is particularly crucial for visceral sensation and nociception (see Feng and Guo, 2020 for a recent review). The dominant perceptions from the viscera are discomfort and pain that are reliably evoked by mechanical distension of hollow visceral organs, but not by other pain-evoking stimuli to the skin like pinching, burning, inflammation, and cutting (Feng and Guo, 2020). Despite the importance of visceral mechanotransduction, there has been only one report in the literature characterizing mechanical visceral neural encoding by optical recordings (Guo et al., 2019), largely due to the

challenge of movement artifacts. Another major challenge for conducting optical neural recordings is the high cost of the optical setups, the most widely used of which are two-photon and confocal scanning fluorescent microscopes. This prohibits a wider application of optical recordings in studying visceral afferents. In the current study, we successfully addressed the above limitations in our custom-built optical setup by (1) applying a robust image alignment algorithm to account for the translational and rotational movement of neural samples, (2) using consumer-grade optical components and image sensors to assemble the whole setup from scratch within a limited budget, and (3) further reducing sample perturbation via remote focusing using the ultrasonic motor rings of the photographic lenses. The cost for parts of our optical recording system as listed in the **Supplementary Material 1** is likely less than 10% of the price for a typical fluorescence confocal microscope. We foresee a wider adoption of this approach by the research community, which will likely expedite the functional characterization of visceral afferents as well as neurons innervating non-visceral organs.

Compared with sensory innervations of the extremities, the DRGs are in closer proximity with visceral organs and thus more susceptible to mechanical stimuli to their nerve endings in the organ wall. In the current study, the recorded DRG images during mechanical colorectal distension of 60 mmHg can undergo translational movement of up to 50 microns and rotational movements of about 2 degrees. This has confounded the extraction of GCaMP6f signals from mouse colorectal DRG neurons which are generally 10–40 microns in diameter (Christianson et al., 2006a,b). To the best of our knowledge, this is the first report to document the application of an alignment algorithm to compensate image recordings of the DRG. Compared with the generic alignment algorithm based upon cross-correlation analysis (e.g., Guizar-Sicairos et al., 2008), we implemented an MI-based algorithm that does not require images to be identical (DRGs indeed showed different GCaMP6f intensity and pattern during mechanical stimulation protocols). After the alignment process, contours of individual DRG neurons generally fall within a margin around 2 microns wide, sufficiently small to avoid interfering with the ensuing extraction of GCaMP6f signals from individual somata.

We have further reduced the cost by assembling the optical recording setup using consumer-grade components, including the Canon photographic lenses and the SONY image sensors (IMX 183CLK). Compared with high-cost scientific CMOS cameras, the slightly lower sensitivity and quantum efficiency of the SONY sensor require about twice the exposure time as the scientific one to achieve comparable imaging quality. We conducted frequency spectrum analysis of recorded GCaMP6f transients and demonstrated that 0–5 Hz is the dominant frequency range of the evoked colorectal afferent activities, consistent with the maximum spike frequencies of about 5 Hz in mouse colorectal afferents from prior electrophysiological studies (Feng et al., 2010, 2012a). In addition, the relatively low cost of the SONY sensor allows us to adopt two cameras to simultaneously record at two parallel focal planes, i.e., recording from a volume of DRG tissue to double the efficiency. Instead of using a conventional microscope tube lens, we employ two Canon 85-mm photographic lenses in our platform. The photographic lens allows us to perform remote axial focus control with high spatial precision of 0.1 μm. By tuning the ultrasonic motor ring to different positions, the evoked GCaMP6f signals at the different planes of the DRG can be recorded without perturbing the samples. Also, using the commercial grade photographic lens for remote focus control significantly reduces the cost of our imaging system compared with high-cost piezo stages used in conventional microscopes.

We also implemented an unsupervised algorithm to allow automatic extraction of DRG neurons with positive GCaMP6f responses from recorded image stacks. The major advantage is that it can be used for various fluorescence imaging systems with different research purposes. By adjusting the estimated neuron size and number options in the GUI, users can modify the routine for their experiment systems. Both image format (like jpeg, tiff, and bmp) and video format data (like mp4, avi, and mov) can be processed using the reported GUI. We note that the recording and data processing are also not demanding in computing power, only requiring a personal computer with a modern CPU, 32 GB RAM and a solid-state drive. Compared with the usual manual process of marking neurons, our procedure allows expedited and unbiased processing of large amounts of image data in a robust and reliable fashion. We anticipate the adoption of this processing routine in the neuroscience research community for increasing the efficiency of extracting neural responses from larger datasets.

The calcium indicator GCaMP6f produces stronger fluorescent signals than GCaMP3 and 5 and has faster recovery kinetics than GCaMP6m, 6s, 7 (Ohkura et al., 2012; Chen et al., 2013; Muto et al., 2013), making it ideal for characterizing single-spike neural activities (Podor et al., 2015). We measured the temporal width of the GCaMP6f transients of individual action potential spikes in mouse DRG to be close to 1.3 sec, indicating complete recovery to baseline Ca^{2+} fluorescent levels when the spike frequency is below 0.5 Hz. We showed in the current study that spiking frequency below 2 Hz can be reliably determined in single-spike resolution from GCaMP6f transients in all DRG neurons, whereas frequency at 4 Hz can be determined in only 15% of the DRG neurons. This discrepancy in determining single spikes at 4 Hz stimulation likely reflects the different intracellular Ca^{2+} events in different DRG neurons. Consistent with the prior findings (Chisholm et al., 2018; Hartung and Gold, 2020), spike frequencies beyond 4 Hz will generally result in a large GCaMP6f transient, from which single spikes usually cannot be determined. A recent systematic study on mouse trigeminal ganglion neurons indicates that the magnitude and rate of those large GCaMP6f transients are not reliable measures of neural activity, nor can be used to assess changes in activities (Hartung and Gold, 2020). Thus, GCaMP6f will not allow a quantitative assessment of sensitized afferents with increased peak spike frequency, which is an indicator of peripheral sensitization in several mouse models of behavioral visceral hypersensitivity (Tanaka et al., 2011; Feng et al., 2012a,b; La et al., 2012). Hence in the current study, we used GCaMP6f responses to exclusively assess whether visceral neurons responded to certain mechanical

stimuli to the colorectum and used their response profiles to functionally separate them into different groups.

Our optical approach allows functional characterization of 456 afferents innervating the colorectum, reporting a large number of afferents than previous approaches using single-fiber electrophysiological recordings (Brierley et al., 2004; Feng and Gebhart, 2011). We used VGLUT2-Cre promoter to drive GCaMP6f expression because VGLUT2 is widely expressed in 97–98% of colorectal DRG neurons according to an immunohistological study (Brumovsky et al., 2011). To identify colorectal afferents in the thoracolumbar (TL) and lumbosacral (LS) pathways, single-fiber recordings were conducted on manually teased fine nerve filaments from the lumbar splanchnic (LSN) and pelvic nerves (PN), an approach that will not determine the relative innervation densities between the two pathways. In the current study, this non-biased optical recording approach allows us to determine that thoracolumbar pathway makes up a much smaller proportion of the total afferent innervation (39%) than the lumbosacral pathway (61%). Within the LS pathway, the proportion of mechanosensitive afferents is comparable to our previous report (Guo et al., 2019). Interestingly, mucosal afferents that encode luminal shearing make up a significant proportion in the TL pathway from current study, which contrasts with the limited number of mucosal afferents characterized by single-fiber recordings from the LSN (Brierley et al., 2004; Feng and Gebhart, 2011). We speculate that this is due to the slightly stronger mechanical stimuli of mucosal shearing induced by fluid flow in the tubular colorectum in the current study than the fine mechanical stroking by a 10 mg fine brush on flattened colorectum in previous studies (Brierley et al., 2004; Feng and Gebhart, 2011). In addition, the *ex vivo* preparation in the current study also includes small fibers that by-pass the celiac ganglion, an innervation pathway that was absent in previous studies when recordings were conducted exclusively from the LSN distal to the celiac ganglion. Further research is warranted to identify the exact innervation pathways that contribute to the neural encoding of colorectal mucosal shearing by thoracolumbar DRG, likely via nerve transection studies similar to a previous report (Kyloh et al., 2011).

CONCLUSION

In conclusion, we report a turnkey microscopy system that allows Ca^{2+} imaging of DRG neurons from a wide range of thoracic, lumbar, and sacral DRGs. By using two consumer-grade image sensors with two photographic lenses, we simultaneously record GCaMP6f signals at two parallel focal planes with a 1.9-by-1.3-mm field of view, a ∼0.7 μm/pixel resolution, and a throughput of 50 frames per second from each camera. By tuning the ultrasonic motor ring within the photographic lenses, we achieved programmable focus control in the axial direction, providing a simple yet powerful tool for precise axial focus tracking without perturbing the sample. The custom-built post-processing software implemented an image alignment algorithm based on mutual information to address motion artifacts and achieved automatic extraction of the GCaMP6f signals from DRG image stacks with high computing efficiency. As a demonstration, we functionally characterized 456 afferents innervating mouse colorectum in both thoracolumbar and lumbosacral pathways. The reported system offers a cost-effective solution for recording visceral afferent activities from a large volume of DRG tissues.

DATA AVAILABILITY STATEMENT

All datasets generated for this study are included in the article/**Supplementary Material**, further inquiries can be directed to the corresponding author/s.

ETHICS STATEMENT

The animal study was reviewed and approved by the University of Connecticut Institutional Animal Care and Use Committee (IACUC).

AUTHOR CONTRIBUTIONS

ZB, TG, and SJ prepared the display items. BF prepared the initial draft of the manuscript. BF and GZ supervised the project. All authors contributed to all aspects of manuscript preparation, revision, and editing.

FUNDING

This work was supported by the NINDS U01 NS113873 Grant awarded to BF and GZ and the NIDDK R01 DK120824 Grant awarded to BF.

SUPPLEMENTARY MATERIAL

The Supplementary Material for this article can be found online at: https://www.frontiersin.org/articles/10.3389/fnins.2021.657361/full#supplementary-material

REFERENCES

Anand, P., Aziz, Q., Willert, R., and Van, O. L. (2007). Peripheral and central mechanisms of visceral sensitization in man. *Neurogastroenterol. Motil.* 19, 29–46. doi: 10.1111/j.1365-2982.2006.00873.x

Bielefeldt, K., Zhong, F., Koerber, H. R., and Davis, B. M. (2006). Phenotypic characterization of gastric sensory neurons in mice. *Am. J. Physiol. Gastrointest. Liver Physiol.* 291, G987–G997. doi: 10.1152/ajpgi.00080.2006

Brierley, S. M., Jones, R. C. III, Gebhart, G. F., and Blackshaw, L. A. (2004). Splanchnic and pelvic mechanosensory afferents signal different qualities of colonic stimuli in mice. *Gastroenterology* 127, 166–178. doi: 10.1053/j.gastro.2004.04.008

Brumovsky, P. R., Robinson, D. R., La, J. H., Seroogy, K. B., Lundgren, K. H., Albers, K. M., et al. (2011). Expression of vesicular glutamate transporters type 1 and 2 in sensory and autonomic neurons innervating the mouse colorectum. *J. Comp. Neurol.* 519, 3346–3366. doi: 10.1002/cne.22730

Chen, L., Ilham, S. J., and Feng, B. (2017). Pharmacological approach for managing pain in irritable bowel syndrome: a review article. *Anesth. Pain Med.* 7:e42747. doi: 10.5812/aapm.42747

Chen, T.-W., Wardill, T. J., Sun, Y., Pulver, S. R., Renninger, S. L., Baohan, A., et al. (2013). Ultrasensitive fluorescent proteins for imaging neuronal activity. *Nature* 499, 295–300. doi: 10.1038/nature12354

Chisholm, K. I., Khovanov, N., Lopes, D. M., La Russa, F., and Mcmahon, S. B. (2018). Large scale in vivo recording of sensory neuron activity with GCaMP6. *eNeuro* 5, 1–14. doi: 10.1523/ENEURO.0417-17.2018

Christianson, J. A., Mcilwrath, S. L., Koerber, H. R., and Davis, B. M. (2006a). Transient receptor potential vanilloid 1-immunopositive neurons in the mouse are more prevalent within colon afferents compared to skin and muscle afferents. *Neuroscience* 140, 247–257. doi: 10.1016/j.neuroscience.2006.02.015

Christianson, J. A., Traub, R. J., and Davis, B. M. (2006b). Differences in spinal distribution and neurochemical phenotype of colonic afferents in mouse and rat. *J. Comp. Neurol.* 494, 246–259. doi: 10.1002/cne.20816

Danuser, H., Springer, J. P., Katofiasc, M. A., and Thor, K. B. (1997). Extrinsic innervation of the cat prostate gland: a combined tracing and immunohistochemical study. *J. Urol.* 157, 1018–1024. doi: 10.1097/00005392-199703000-00099

Edelstein, A. D., Tsuchida, M. A., Amodaj, N., Pinkard, H., Vale, R. D., and Stuurman, N. (2014). Advanced methods of microscope control using μManager software. *J. Biol. Methods* 1:e10. doi: 10.14440/jbm.2014.36

Emery, E. C., Luiz, A. P., Sikandar, S., Magnusdottir, R., Dong, X., and Wood, J. N. (2016). In vivo characterization of distinct modality-specific subsets of somatosensory neurons using GCaMP. *Sci. Adv.* 2:e1600990. doi: 10.1126/sciadv.1600990

Feng, B., Brumovsky, P. R., and Gebhart, G. F. (2010). Differential roles of stretch-sensitive pelvic nerve afferents innervating mouse distal colon and rectum. *Am. J. Physiol. Gastrointest. Liver Physiol.* 298, G402–G409. doi: 10.1152/ajpgi.00487.2009

Feng, B., and Gebhart, G. F. (2011). Characterization of silent afferents in the pelvic and splanchnic innervations of the mouse colorectum. *Am. J. Physiol. Gastrointest. Liver Physiol.* 300, G170–G180. doi: 10.1152/ajpgi.00406.2010

Feng, B., and Gebhart, G. F. (2015). In vitro functional characterization of mouse colorectal afferent endings. *J. Vis Exp.* 21:52310. doi: 10.3791/52310

Feng, B., and Guo, T. (2020). Visceral pain from colon and rectum: the mechanotransduction and biomechanics. *J. Neural Transm.* 127, 415–429. doi: 10.1007/s00702-019-02088-8

Feng, B., Joyce, S. C., and Gebhart, G. F. (2016). Optogenetic activation of mechanically insensitive afferents in mouse colorectum reveals chemosensitivity. *Am. J. Physiol. Gastrointest. Liver Physiol.* 310, G790–G798. doi: 10.1152/ajpgi.00430.2015

Feng, B., La, J.-H., Schwartz, E. S., Tanaka, T., Mcmurray, T. P., and Gebhart, G. F. (2012a). Long-term sensitization of mechanosensitive and -insensitive afferents in mice with persistent colorectal hypersensitivity. *Am. J. Physiol. Gastrointest. Liver Physiol.* 302, G676–G683. doi: 10.1152/ajpgi.00490.2011

Feng, B., La, J. H., Tanaka, T., Schwartz, E. S., Mcmurray, T. P., and Gebhart, G. F. (2012b). Altered colorectal afferent function associated with TNBS-induced visceral hypersensitivity in mice. *Am. J. Physiol. Gastrointest. Liver Physiol.* 303, G817–G824. doi: 10.1152/ajpgi.00257.2012

Guizar-Sicairos, M., Thurman, S. T., and Fienup, J. R. (2008). Efficient subpixel image registration algorithms. *Opt. Lett.* 33, 156–158. doi: 10.1364/OL.33.000156

Guo, T., Bian, Z., Trocki, K., Chen, L., Zheng, G., and Feng, B. (2019). Optical recording reveals topological distribution of functionally classified colorectal afferent neurons in intact lumbosacral DRG. *Physiol. Rep.* 7:e14097. doi: 10.14814/phy2.14097

Hartung, J. E., and Gold, M. S. (2020). GCaMP as an indirect measure of electrical activity in rat trigeminal ganglion neurons. *Cell Calcium* 89:102225. doi: 10.1016/j.ceca.2020.102225

Herweijer, G., Kyloh, M., Beckett, E. A. H., Dodds, K. N., and Spencer, N. J. (2014). Characterization of primary afferent spinal innervation of mouse uterus. *Front. Neurosci.* 8:202. doi: 10.3389/fnins.2014.00202

Hibberd, T. J., Kestell, G. R., Kyloh, M. A., Brookes, S. J., Wattchow, D. A., and Spencer, N. J. (2016). Identification of different functional types of spinal afferent neurons innervating the mouse large intestine using a novel CGRPalpha transgenic reporter mouse. *Am. J. Physiol. Gastrointest. Liver Physiol.* 310, G561–G573. doi: 10.1152/ajpgi.00462.2015

Jankowski, M. P., Rau, K. K., Soneji, D. J., Anderson, C. E., and Koerber, H. R. (2010). Enhanced artemin/GFRalpha3 levels regulate mechanically insensitive, heat-sensitive C-fiber recruitment after axotomy and regeneration. *J. Neurosci.* 30, 16272–16283. doi: 10.1523/JNEUROSCI.2195-10.2010

Jankowski, M. P., Rau, K. K., Soneji, D. J., Ekmann, K. M., Anderson, C. E., Molliver, D. C., et al. (2012). Purinergic receptor P2Y1 regulates polymodal C-fiber thermal thresholds and sensory neuron phenotypic switching during peripheral inflammation. *Pain* 153, 410–419. doi: 10.1016/j.pain.2011.10.042

Kamp, E. H., Jones, R. C. III, Tillman, S. R., and Gebhart, G. F. (2003). Quantitative assessment and characterization of visceral nociception and hyperalgesia in mice. *Am. J. Physiol. Gastrointest. Liver Physiol.* 284, G434–G444. doi: 10.1152/ajpgi.00324.2002

Kim, Y. S., Anderson, M., Park, K., Zheng, Q., Agarwal, A., Gong, C., et al. (2016). Coupled activation of primary sensory neurons contributes to chronic pain. *Neuron* 91, 1085–1096. doi: 10.1016/j.neuron.2016.07.044

Koerber, H. R., Mcilwrath, S. L., Lawson, J. J., Malin, S. A., Anderson, C. E., Jankowski, M. P., et al. (2010). Cutaneous C-polymodal fibers lacking TRPV1 are sensitized to heat following inflammation, but fail to drive heat hyperalgesia in the absence of TPV1 containing C-heat fibers. *Mol. Pain* 6:58. doi: 10.1186/1744-8069-6-58

Kyloh, M., Nicholas, S., Zagorodnyuk, V. P., Brookes, S. J., and Spencer, N. J. (2011). Identification of the visceral pain pathway activated by noxious colorectal distension in mice. *Front. Neurosci.* 5:16. doi: 10.3389/fnins.2011.00016

La, J. H., Feng, B., Schwartz, E. S., Brumovsky, P. R., and Gebhart, G. F. (2012). Luminal hypertonicity and acidity modulate colorectal afferents and induce persistent visceral hypersensitivity. *Am. J. Physiol. Gastrointest. Liver Physiol.* 303, G802–G809. doi: 10.1152/ajpgi.00259.2012

Li, W. (1990). Mutual information functions versus correlation functions. *J. Stat. Phys.* 60, 823–837. doi: 10.1007/BF01025996

Malin, S., Molliver, D., Christianson, J. A., Schwartz, E. S., Cornuet, P., Albers, K. M., et al. (2011). TRPV1 and TRPA1 function and modulation are target tissue dependent. *J. Neurosci.* 31, 10516–10528. doi: 10.1523/JNEUROSCI.2992-10.2011

Mattes, D., Haynor, D. R., Vesselle, H., Lewellyn, T. K., and Eubank, W. (2001). "Nonrigid multimodality image registration," in *Proceedings of the Medical imaging 2001: Image Processing*: *International Society for Optics and Photonics*, San Diego, CA, 1609–1620. doi: 10.1117/12.431046

Molliver, D. C., Rau, K. K., Mcilwrath, S. L., Jankowski, M. P., and Koerber, H. R. (2011). The ADP receptor P2Y1 is necessary for normal thermal sensitivity in cutaneous polymodal nociceptors. *Mol. Pain* 7:13. doi: 10.1186/1744-8069-7-13

Muto, A., Ohkura, M., Abe, G., Nakai, J., and Kawakami, K. (2013). Real-time visualization of neuronal activity during perception. *Curr. Biol.* 23, 307–311. doi: 10.1016/j.cub.2012.12.040

Ohkura, M., Sasaki, T., Sadakari, J., Gengyo-Ando, K., Kagawa-Nagamura, Y., Kobayashi, C., et al. (2012). Genetically encoded green fluorescent Ca 2+ indicators with improved detectability for neuronal Ca 2+ signals. *PLoS One* 7:e51286. doi: 10.1371/journal.pone.0051286

Pachitariu, M., Stringer, C., and Harris, K. D. (2018). Robustness of spike deconvolution for neuronal calcium imaging. *J. Neurosci.* 38, 7976–7985. doi: 10.1523/JNEUROSCI.3339-17.2018

Peiris, M., Bulmer, D. C., Baker, M. D., Boundouki, G., Sinha, S., Hobson, A., et al. (2011). Human visceral afferent recordings: preliminary report. *Gut* 60, 204–208. doi: 10.1136/gut.2010.221820

Pluim, J. P., Maintz, J. A., and Viergever, M. A. (2003). Mutual-information-based registration of medical images: a survey. *IEEE Trans. Med. Imaging* 22, 986–1004. doi: 10.1109/TMI.2003.815867

Podor, B., Hu, Y.-L., Ohkura, M., Nakai, J., Croll, R., and Fine, A. (2015). Comparison of genetically encoded calcium indicators for monitoring action potentials in mammalian brain by two-photon excitation fluorescence microscopy. *Neurophotonics* 2:021014. doi: 10.1117/1.NPh.2.2.021014

Schwartz, E. S., La, J. H., Young, E. E., Feng, B., Joyce, S., and Gebhart, G. F. (2016). Chronic prostatitis induces bladder hypersensitivity and sensitizes bladder afferents in the mouse. *J. Urol.* 196, 892–901. doi: 10.1016/j.juro.2016.03.077

Sengupta, J. N., and Gebhart, G. F. (1994). Characterization of mechanosensitive pelvic nerve afferent fibers innervating the colon of the rat. *J. Neurophysiol.* 71, 2046–2060. doi: 10.1152/jn.1994.71.6.2046

Smith-Edwards, K. M., Deberry, J. J., Saloman, J. L., Davis, B. M., and Woodbury, C. J. (2016). Profound alteration in cutaneous primary afferent activity produced by inflammatory mediators. *Elife* 5:e20527. doi: 10.7554/eLife.20527.012

Spencer, N. J., Kyloh, M., and Duffield, M. (2014). Identification of different types of spinal afferent nerve endings that encode noxious and innocuous stimuli in the large intestine using a novel anterograde tracing technique. *PLoS One* 9:e112466. doi: 10.1371/journal.pone.0112466

Spencer, N. J., Zagorodnyuk, V., Brookes, S. J., and Hibberd, T. (2016). Spinal afferent nerve endings in visceral organs: recent advances. *Am. J. Physiol. Gastrointest. Liver Physiol.* 311, G1056–G1063. doi: 10.1152/ajpgi.00319.2016

Tanaka, T., Shinoda, M., Feng, B., Albers, K. M., and Gebhart, G. F. (2011). Modulation of visceral hypersensitivity by glial cell line-derived neurotrophic factor family receptor α-3 in colorectal afferents. *Am. J. Physiol. Gastrointest. Liver Physiol.* 300, G418–G424. doi: 10.1152/ajpgi.00456.2010

Van Der Bom, I., Klein, S., Staring, M., Homan, R., Bartels, L. W., and Pluim, J. P. (2011). "Evaluation of optimization methods for intensity-based 2D-3D registration in x-ray guided interventions," in *Proceedings of the Medical Imaging 2011: Image Processing*: *International Society for Optics and Photonics 796223*, Lake Buena Vista, FL. doi: 10.1117/12.877655

Vrontou, S., Wong, A. M., Rau, K. K., Koerber, H. R., and Anderson, D. J. (2013). Genetic identification of C fibres that detect massage-like stroking of hairy skin in vivo. *Nature* 493, 669–673. doi: 10.1038/nature11810

Woodbury, C. J., and Koerber, H. R. (2007). Central and peripheral anatomy of slowly adapting type I low-threshold mechanoreceptors innervating trunk skin of neonatal mice. *J. Comp. Neurol.* 505, 547–561. doi: 10.1002/cne.21517

Conflict of Interest: The authors declare that the research was conducted in the absence of any commercial or financial relationships that could be construed as a potential conflict of interest.

frontiers in Neuroscience

MINI REVIEW
published: 13 April 2021
doi: 10.3389/fnins.2021.667036

Selective Vagus Nerve Stimulation as a Therapeutic Approach for the Treatment of ARDS: A Rationale for Neuro-Immunomodulation in COVID-19 Disease

Svetlana Mastitskaya, Nicole Thompson and David Holder*

Department of Medical Physics and Biomedical Engineering, University College London, London, United Kingdom

Acute respiratory distress syndrome (ARDS) is the most severe form of acute lung injury. It is induced by sepsis, aspiration, and pneumonia, including that caused by SARS coronavirus and human influenza viruses. The main pathophysiological mechanism of ARDS is a systemic inflammatory response. Vagus nerve stimulation (VNS) can limit cytokine production in the spleen and thereby dampen any systemic inflammation and inflammation-induced tissue damage in the lungs and other organs. However, the effects of increased parasympathetic outflow to the lungs when non-selective VNS is applied may result in bronchoconstriction, increased mucus secretion and enhance local pulmonary inflammatory activity; this may outweigh the beneficial systemic anti-inflammatory action of VNS. Organ/function-specific therapy can be achieved by imaging of localized fascicle activity within the vagus nerve and selective stimulation of identified organ-specific fascicles. This may be able to provide selective neuromodulation of different pathways within the vagus nerve and offer a novel means to improve outcome in ARDS. This has motivated this review in which we discuss the mechanisms of anti-inflammatory effects of VNS, progress in selective VNS techniques, and a possible application for ARDS.

Keywords: vagus nerve, neuromodulation, inflammation, cytokine storm, ARDS, COVID-19

OPEN ACCESS

Edited by:
Stephen Lewis,
Case Western Reserve University,
United States

Reviewed by:
Colin Reardon,
University of California, Davis,
United States
Rimenez Rodrigues de Souza,
The University of Texas at Dallas,
United States

****Correspondence:***
Svetlana Mastitskaya
s.mastitskaya@ucl.ac.uk

Specialty section:
This article was submitted to Autonomic Neuroscience, a section of the journal Frontiers in Neuroscience

Received: *11 February 2021*
Accepted: *23 March 2021*
Published: *13 April 2021*

Citation:
Mastitskaya S, Thompson N and Holder D (2021) Selective Vagus Nerve Stimulation as a Therapeutic Approach for the Treatment of ARDS: A Rationale for Neuro-Immunomodulation in COVID-19 Disease. Front. Neurosci. 15:667036. doi: 10.3389/fnins.2021.667036

INTRODUCTION

Acute respiratory distress syndrome (ARDS) is a fulminant condition which may result in a mortality rate of more than 40% (Diamond et al., 2020). It may be caused by direct lung injury due to bacterial or viral pneumonia, inhalation of smoke, toxic chemicals, or aspiration of gastric contents, or by indirect injury due to septic shock, acute pancreatitis, burn injury, or major trauma (Wong et al., 2019). Whether induced by pulmonary or extra-pulmonary insult, ARDS is caused by pulmonary injury which manifests as interstitial and alveolar edema, severe hypoxemia, endothelial injury, and an acute systemic inflammatory response which may rapidly progress to respiratory and multi-system failure (Matthay et al., 2019; Diamond et al., 2020). ARDS secondary to virally driven pneumonia is the predominant cause of mortality from SARS-CoV-2 infection (Mehta et al., 2020; Zhang et al., 2020).

Systemic Inflammatory Response in Severe COVID Patients

In COVID-19 disease, angiotensin-converting enzyme 2 (ACE2) on the surface of the cells serves as an entry point for SARS-CoV-2 virus (Hoffmann et al., 2020). It is richly expressed in lung epithelial cells, as well as in the heart, gastrointestinal tract (GIT) and kidneys (Samavati and Uhal, 2020). Elevated plasma levels of Angiotensin II (as a result of ACE2 internalization upon viral entry) in critically ill COVID-19 patients (Ni et al., 2020) may stimulate monocyte recruitment from the spleen. The monocytes migrate to the infected tissues within 24 h where they contribute to the initial inflammatory damage (Swirski et al., 2009) and promote neutrophilic activation and migration into the interstitial and alveolar spaces. If the innate immune system fails to clear the pathogen or repair the lungs from the insult, the overactivation of the systemic immune response results in release of the pro-inflammatory cytokines interleukin-1α (IL-1α), IL-6, IL-1β, tumor necrosis factor alpha (TNF-α), and interferon gamma (IFN-γ). This is commonly termed a "cytokine storm" (Mehta et al., 2020). Analysis of the lung immune microenvironment using bronchoalveolar lavage fluid from severe and moderate COVID-19 patients showed that highly inflammatory monocyte-derived splenic macrophages prevail in the excessive inflammatory response in the lungs from patients with ARDS (Liao et al., 2020). These macrophages of splenic origin are active producers of chemokines and cytokines which promote neutrophilic migration into alveolar space and hyperactivation. The activated neutrophils release proteases and reactive oxygen species which contribute to endo- and epithelial integrity disruption, the further increase of vascular permeability with protein-rich exudate floating in the alveoli, and formation of hyaline membranes (Matthay et al., 2019). Homeostatic mechanisms opposing the effects of systemic inflammation include endogenous glucocorticoid secretion and the release of anti-inflammatory cytokines such as IL-10 (Johnston and Webster, 2009); however, they may be insufficient to limit this fulminant inflammatory cascade.

Anti-inflammatory Therapy of Cytokine Storm and ARDS in COVID-Disease

Anti-inflammatory medications aiming at reducing the cytokine storm and systemic inflammation in COVID-19 patients include non-steroidal anti-inflammatory drugs, glucocorticoids, immunosuppressants, and antagonists of inflammatory cytokines (such as IL-6R antibodies, TNF inhibitors, IL-1R antagonists, etc.). Dexamethasone was shown to be effective in improving survival in critical and severe cases of COVID-19 infection—including those requiring mechanical ventilation due to ARDS (Horby et al., 2021). Until the COVID-19 pandemic, there was no conclusive evidence for the advantage of the steroids use for the prevention or treatment of ARDS associated with other causes, and it still needs to be established whether the benefits of prolonged low dose corticosteroids outweigh the short and long-term risks, including delayed recovery (Mokra et al., 2019). Another promising therapy using Tocilizumab, a monoclonal antibody against the receptor of pro-inflammatory cytokine IL-6, emerged as an alternative treatment for COVID-19 patients with a risk of acute systemic inflammatory response and in need of mechanical ventilation (Guaraldi et al., 2020). However, anti-inflammatory medications, such as corticosteroids, may delay the elimination of the virus and increase the risk of secondary infections in immunocompromised patients (Zhang et al., 2020). Drugs targeting a particular cytokine can only inhibit a specific inflammatory factor, and thus may not be effective enough in limiting the effects of other cytokines of significance. Therefore, choosing the correct time window for anti-inflammatory therapy and identifying the patients that are most likely to benefit from immunosuppression remains a critical issue. Patients with severe COVID-19 disease could be screened for hyperinflammation using laboratory trends (e.g., increased ferritin, decreased platelet counts, or erythrocyte sedimentation rate) to identify a subgroup of patients for whom immunosuppression could improve survival (Mehta et al., 2020). It is evident, however, that identification of such patients and initiation of an anti-inflammatory therapy is required well before their condition progresses to severe stages, as ARDS is an advanced manifestation of a cytokine storm, which by that point may already have caused irreversible damage.

VAGUS NERVE STIMULATION

The vagus nerve is the main component of the parasympathetic nervous system. It innervates the majority of visceral organs, including the pharynx, larynx, tracheobronchial tree and lungs, heart, esophagus, stomach, liver, gallbladder, pancreas, small intestine, and proximal colon (Thompson et al., 2019). Importantly, the vagus nerve plays an integral role in the connection between the nervous and immune systems (**Figure 1**; Borovikova et al., 2000; Kressel et al., 2020). Therefore, it is of particular interest in neuromodulation of inflammation. Vagus nerve stimulation (VNS) has indirect inhibitory effects on the cytokine production in the spleen even though there is no evidence for direct cholinergic (vagal) innervation of the spleen in humans (Verlinden et al., 2019). The existing methods of cervical VNS in human patients employ electrical stimulation of the entire nerve with circumferential wire loops. The applied electrical current activates the entire vagus and all its fibers, both afferent and efferent, which results in preferential activation of sensory (afferent) fibers because they have lower activation threshold. This can cause multiple unwanted side effects, such as nausea, cough, and headache, which may limit the VNS tolerability and efficiency (Howland, 2014).

An attractive possibility is to undertake selective stimulation of the cervical vagus nerve. Unfortunately, until recently, this was limited as the functional anatomy of fascicles in the vagus nerve was almost entirely unknown. In our group at University College London, we have developed a method to image localized fascicle compound action potential activity with Electrical Impedance Tomography (EIT) using a silicone rubber cuff with 14 circumferential electrodes (**Figure 2A**; Ravagli et al., 2019, 2020). Identified fascicles can then be selectively stimulated using two

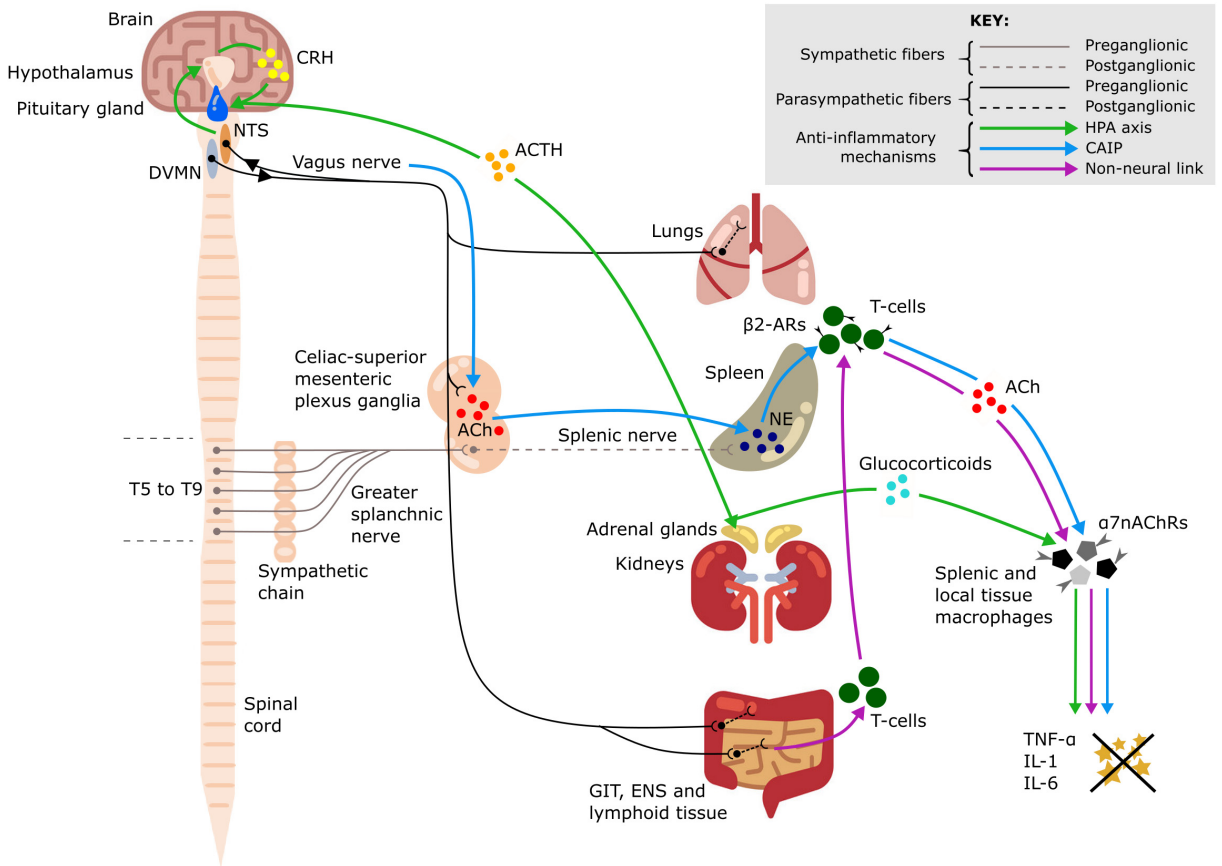

FIGURE 1 | Anti-inflammatory pathways of the vagus nerve. A schematic representation of the anti-inflammatory pathways of the vagus nerve including the hypothalamic-pituitary-adrenal (HPA) axis (green arrows), the cholinergic anti-inflammatory pathway (CAIP) (blue arrows) and the non-neural link between the vagus nerve and spleen (purple arrows). All three pathways result in attenuation of pro-inflammatory cytokine production, including tumor necrosis factor-α (TNF-α), interleukin-1 (IL-1), and interleukin-6 (IL-6). Dorsal motor nucleus of the vagus nerve (DVMN), nucleus of the solitary tract (NTS), gastrointestinal tract (GIT), enteric nervous system (ENS), thoracic vertebrae (T5–T9), acetylcholine (ACh), NE (norepinephrine), corticotropin-releasing hormone (CRH), adrenocorticotrophic hormone (ACTH), β2-adrenergic receptors (β2-ARs), and α7–nicotinic ACh receptors (α7nAChRs).

such electrode rings spaced 3 mm apart (**Figure 2B**; Aristovich et al., 2021). Our studies suggest the organotopic organization of the fascicles of the cervical vagus nerve in large mammals (sheep and pigs). Until now, three regions – namely cardiac, pulmonary and recurrent laryngeal—were localized within the cervical region of the vagus nerve and can be selectively modulated (**Figures 2B,C**). Work is in progress to achieve the same imaging and selective modulation of the other organs supplied by the vagus nerve. The findings are being independently validated by micro-computed tomography (microCT) tracing of fascicles from their end-organs (Thompson et al., 2020).

Systemic Anti-inflammatory Effects of VNS

Potent systemic anti-inflammatory effects of VNS suggest that VNS could be a promising alternative immunomodulatory treatment for patients with ARDS (Van Westerloo et al., 2006; Krzyzaniak et al., 2011; **Supplementary Table 1**). VNS was shown to attenuate the release of pro-inflammatory cytokines, modulate coagulation, prevent circulatory failure, and thus decrease organ dysfunction and improve survival in animal models of sepsis and endotoxemia (Borovikova et al., 2000; Van Westerloo et al., 2006). Clinical studies also demonstrated immunomodulatory effects of VNS—suppression of inflammation and improvement of clinical symptoms in rheumatoid arthritis (Koopman et al., 2016), intractable epilepsy (Majoie et al., 2011), atrial fibrillation (Stavrakis et al., 2015), and Crohn's Disease (Bonaz et al., 2016). These effects are mediated by the following mechanisms (**Figure 1**):

Hypothalamic-Pituitary-Adrenal Axis

Vagus nerve afferents express IL-1β receptors at the level of paraganglia and can therefore sense local and systemic inflammation (Bonaz et al., 2016). Activation of these afferents leads to glutamate release in the nucleus of the solitary tract (NTS). The NTS sends adrenergic projections to the paraventricular nucleus of the hypothalamus, which contains a population of corticotropin-releasing hormone (CRH) neurons (Hosoi et al., 2000). CRH then acts on the anterior pituitary gland

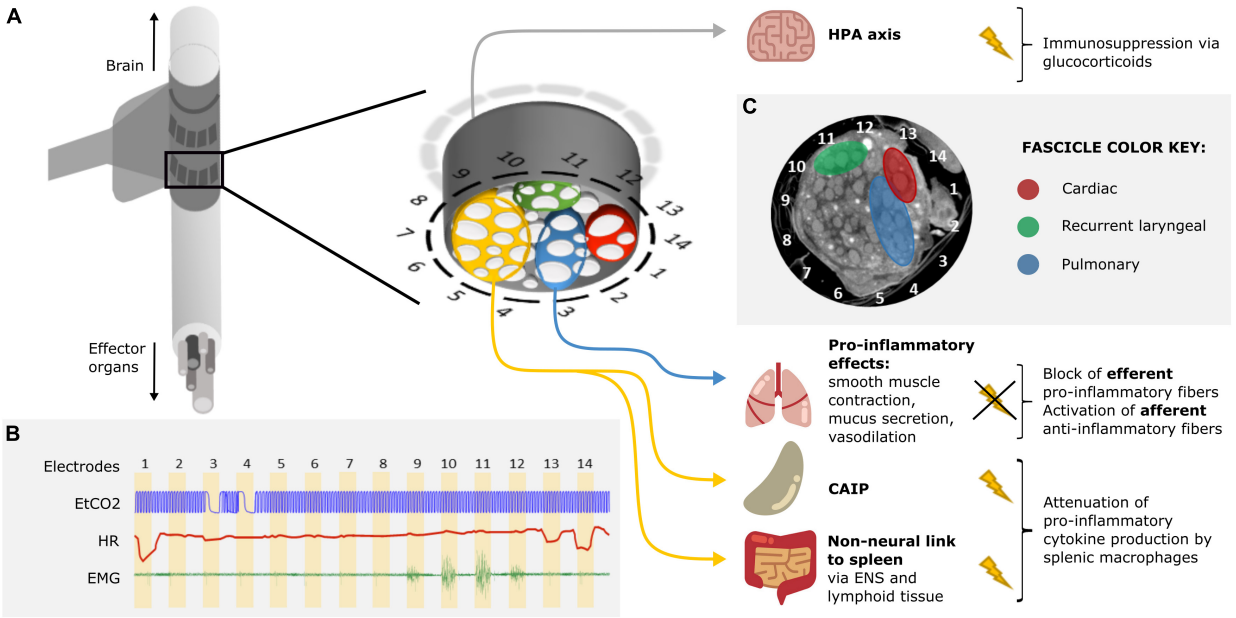

FIGURE 2 | Proposed approach for VNS in ARDS treatment. **(A)** A schematic of a silicone rubber cuff with 14 circumferential electrodes wrapped around the vagus nerve. Inset: a more detailed schematic of the cross-section of the vagus nerve surrounded by electrodes. The fascicles (white) of the nerve (gray) are grouped into four regions identified by selective stimulation and by subsequent micro-computed tomography (microCT): recurrent laryngeal (green), cardiac (red), pulmonary (blue), and the rest of the nerve with fascicles suspected to innervate the abdominal viscera (orange). Stimulation of the orange region of the nerve would result in the activation of the cholinergic anti-inflammatory pathway (CAIP) and the non-neural link between the vagus and the spleen, via the enteric nervous system (ENS) and lymphoid tissue of the gastrointestinal tract (GIT), via vagal efferents resulting in the attenuation of pro-inflammatory cytokine production. Stimulation of the vagal afferents would activate the hypothalamic-pituitary-adrenal (HPA) axis which would result in immunosuppression via glucocorticoids. Selective blocking of the pulmonary fascicles would prevent activation of pulmonary efferent fibers and the inflammation-potentiating effects of smooth muscle contraction, increased mucus secretion and vasodilation in the lungs. Overall, suppression of the immune reaction would be achieved. **(B)** Identification of organ-specific fascicles with a quick round of selective VNS. The pulmonary, cardiac, and recurrent laryngeal fascicles are localized by sequential stimulation of the radial sections of the nerve via electrode pairs 1–14 (stimulation for 30 s on each pair followed by 30 s recovery period) and reading out of physiological parameters: changes in respiration (end-tidal CO2, EtCO2), heart rate (HR), and contraction of the neck muscles (electromyography, EMG), accordingly. Pulmonary fascicles are located next to electrode pairs 3 and 4 (bradypnea); cardiac fascicles next to pairs 1, 13, and 14 (bradycardia); and recurrent laryngeal fascicles next to pairs 10 and 11 (maximal EMG signal). **(C)** A microCT cross-section of a vagus nerve at the cervical level with identified regions containing recurrent laryngeal (green), cardiac (red), and pulmonary (blue) fascicles (unpublished data, study on the left vagus nerve in pigs).

and stimulates the release of adrenocorticotropic hormone into systemic circulation (Hosoi et al., 2000) with an ultimate effect on the adrenal cortex and increased secretion of glucocorticoids which are very effective in suppressing the immune system (Fleshner et al., 1995; Bonaz et al., 2016).

Cholinergic Anti-inflammatory Pathway (CAIP)

This is a potent anti-inflammatory pathway in the spleen which is indirectly activated by stimulation of vagus nerve efferent fibers. The efferent innervation of the spleen comprises noradrenergic sympathetic fibers within the splenic nerve (Verlinden et al., 2019). Some vagal preganglionic neurons terminate in the celiac-superior mesenteric ganglia, where much of the postganglionic sympathetic nerve supply to the spleen is derived (Kressel et al., 2020). The axons of vagal preganglionic neurons form varicose-like structures surrounding individual splenic nerve cell bodies and thereby modulate the activity of the splenic nerve (Kressel et al., 2020). Acetylcholine (ACh) released from vagus nerve efferents in the celiac ganglion activates postsynaptic α7-nicotinic ACh receptors (α7nAChRs) of the splenic nerve (Vida et al., 2011). This results in the release of norepinephrine in the spleen where it acts on β2-adrenergic receptors of splenic $CD4^{+}$T-cells that also release ACh. T-cell derived ACh acts on α7nAChRs of splenic macrophages which leads to a decrease of pro-inflammatory cytokine production via inhibition of the transcription factor NF-kB p65 (Rosas-Ballina et al., 2008). The spleen is the major source of cytokine production in conditions of systemic inflammation such as sepsis; thus, the cholinergic anti-inflammatory pathway (CAIP) is a potent mechanism exploited by VNS for treatment of inflammatory diseases. Direct stimulation of the efferent vagus nerve inhibits the synthesis of pro-inflammatory cytokines in liver, spleen, and GIT, and also decreases their levels in systemic inflammatory responses to endotoxemia, ischemia, sepsis and other diseases (Rosas-Ballina et al., 2008; Dos Santos et al., 2011). It has been shown that the pro-inflammatory cytokine production is attenuated by VNS, but the release of IL-10, which has counter-inflammatory actions, is unaffected (Borovikova et al., 2000).

Non-neural Link From Vagus to Spleen

A critical review of the CAIP pathway is provided in the work by Martelli et al. (2014) who also suggest a non-neural

mechanism linking the activity of the vagus nerve to the decreased production of pro-inflammatory cytokines by splenic macrophages via activation of α7nAChRs receptors. The vagus nerve provides extensive innervation of secondary lymphoid tissue in the GIT and increased parasympathetic stimulation of these lymphoid depots mobilizes their ACh-synthesizing T-cells. The circulating T-cells are sequestered by the spleen, where they release ACh acting on α7nAChRs expressed by splenic macrophages (Martelli et al., 2014).

Inhibition of Tissue Macrophage Activity

A significant additional contribution to the anti-inflammatory effects of VNS is mediated by vagal efferent fibers which synapse on intrinsic neurons of the enteric nervous system in the GIT (Matteoli et al., 2014) and terminate in other visceral organs, including the liver (Borovikova et al., 2000) and lungs. Tissue macrophages contribute to the production of the pro-inflammatory cytokines released during a systemic inflammatory response; during an excessive response, this contributes to the cytokine storm and results in damage to multiple organs (Johnston and Webster, 2009). ACh released by vagal efferents acts on α7nAChRs of local tissue macrophages in the gut which leads to decreased production of the main pro-inflammatory cytokine, TNF-α (Matteoli et al., 2014). In the same way, the resident immune cells of the lungs—including alveolar macrophages, epithelial cells and activated infiltrating neutrophils—can be affected by ACh acting on their α7nAChRs to slow down the local inflammatory reaction and alleviate lung injury (Su et al., 2010).

Pulmonary Effects of VNS

Non-selective VNS will stimulate parasympathetic fibers to the lungs but this inadvertent activation may not be beneficial. It will activate pulmonary cholinergic efferents which have pro-inflammatory effects. Parasympathetic efferent stimulation leads to activation of muscarinic ACh (mACh) receptors on airway smooth muscle, glands, and vasculature which results in airway smooth muscle contraction, increased mucus secretion and vasodilation (Gosens et al., 2006). Whereas mucus secretion is an important mechanism of innate defense in airways, its excessive production and accumulation in alveoli during the inflammatory process impairs the blood-gas barrier, potentiates hypoxia and inflammatory injury (Fahy and Dickey, 2010). The predominant immune cells present in the air space are alveolar macrophages. ACh was found to stimulate these cells which resulted in the release of chemotactic activity for inflammatory cells, such as neutrophils, monocytes, and eosinophils (Sato et al., 1998). By blocking mACh receptors in mice, the production of cytokines contributing to inflammatory infiltrate and tissue damage in the lungs was inhibited (Gori et al., 2019).

On the other hand, stimulation of pulmonary afferent A-fibers (pulmonary stretch receptors) causes dyspnea and reflexly decreased parasympathetic tone, resulting in effects opposite to stimulation of pulmonary efferents—bronchodilation and decreased mucus secretion (Kubin et al., 2006). It is unclear if stimulation of the pulmonary vagal fascicles will preponderantly affect afferent or efferent fibers in the lungs. Selective VNS would be necessary to tease out whether pulmonary fibers should be stimulated or blocked to ameliorate the cytokine storm and improve outcome by modifying other parasympathetic controlled variables in ARDS.

VNS in Experimental Models of ARDS

In a rat model of venom-induced ARDS, vagal efferent stimulation was protective against Mesobuthus tamulus (MBT), but not against oleic acid (OA)-induced ARDS (Akella and Deshpande, 2015). The protective effect was explained by increased surfactant secretion and activation of the anti-inflammatory pathway. Interestingly, VNS was only effective in the MBT model—this model is characterized not only by pulmonary injury, but also by systemic cardiovascular alterations. Perhaps, the beneficial role of VNS, which was evident from prolonged survival of animals in this model, is attributed to cardiovascular effects of increased parasympathetic tone rather than its anti-inflammatory action on the lungs.

Beneficial effects of vagal efferent stimulation were reported in ventilator-induced ARDS (Brégeon et al., 2011; Dos Santos et al., 2011) and in peritonitis-induced lung injury (Boland et al., 2011), but not in other models of ARDS (sepsis and ventilation; Kox et al., 2012). In a rat model of endotoxemia-induced pulmonary inflammation potentiated by mechanical over-ventilation (Kox et al., 2012), no benefit of VNS was observed, which questions the clinical applicability of stimulation of the CAIP in systemically inflamed patients admitted to the ICU where mechanical ventilation is initiated. In this study, the vagus nerve was not transected; therefore, both afferent and efferent fibers were stimulated, and the stimulation was applied to the entirety of the nerve, with the potential detrimental effects of pulmonary efferent fiber stimulation outweighing the anti-inflammatory action of VNS. Additionally, the timing of VNS could be very critical—in this study, VNS was applied when septic shock was fully developed. It may be that the magnitude of the systemic reaction was already too high to be affected by VNS.

Proposed Approach for VNS in ARDS Treatment

It is evident that VNS assists in improving outcomes and mortality of immune dysregulation through its anti-inflammatory action (Dos Santos et al., 2011; Bonaz et al., 2016; Koopman et al., 2016; Liu et al., 2017). Existing techniques stimulate the entire nerve and often result in unwanted side effects or lack therapeutic effect due to insufficient intensity. We hypothesize that it may be possible to improve outcome in ARDS by selective VNS. This could permit employment of more optimal stimulation paradigms as they need not be limited by off-target side effects, and it may be that differential modulation of pulmonary vagal tone may yield additional benefits. Various techniques of selective VNS have been suggested, including anodal block (Tosato et al., 2007), depolarizing pre-pulses (Vuckovic et al., 2008), kilohertz electrical stimulation block (Patel et al., 2017), fiber-selective stimulation (McAllen et al., 2018) and spatially selective stimulation (Aristovich et al., 2021). Anodal block, depolarizing pre-pulses and fiber-specific stimulation allow for efficient mitigation of laryngeal side effects (Vuckovic et al., 2008) but not enough selectivity with regards

to target organs or effectors. Unlike fiber-specific stimulation, spatially selective VNS accounts for the organotopic arrangement of fibers within the cervical vagus nerve (**Figure 2**). It provides more precise targeting than fiber-specific VNS and has been demonstrated to mitigate side effects and successfully elicit organ-specific responses (Ordelman et al., 2013; Plachta et al., 2014; Aristovich et al., 2021).

Invasive vs Non-invasive VNS

Non-invasive VNS does not require surgical intervention, and thus improves the safety and tolerability of VNS. Currently, there are two types of non-invasive VNS—transcutaneous and auricular VNS. In transcutaneous VNS (tVNS), the stimulating electrodes are applied to the skin surface over the sternocleidomastoid muscle in the neck (Yap et al., 2020). Auricular VNS (aVNS) targets the sensory auricular branch of the vagus nerve in the ear. This method makes use of the auricular-vagal reflex which involves the auricular concha, vagus nerve, NTS and the dorsal motor nucleus of the vagus nerve (Yap et al., 2020). Both tVNS and aVNS have been shown to elicit similar therapeutic effects as VNS (Hein et al., 2013; Koopman et al., 2016; Subramanian et al., 2020; Yap et al., 2020).

However, both tVNS and aVNS do not allow for the modulation of the activity of the vagus nerve organ- or function-specifically—their disadvantage compared to invasive VNS. Invasive VNS uses a surgically implantable device wrapped around the cervical vagus nerve which allows for the suggested selective VNS with a specifically designed electrode cuff. Selective activation of certain fibers of the vagus nerve, such as certain desired pathways or functions (e.g., CAIP), but not others (e.g., pulmonary fibers), is unlikely to be feasible with tVNS or aVNS which only allow for indiscriminate stimulation of all fibers (Yuan and Silberstein, 2016).

Possible Risks and Challenges

Vagus nerve stimulation is known to have a number of off-target effects (voice alteration, cough, dyspnea, dysphagia, etc.) which are mostly stimulation-related (Howland, 2014). With the proposed use of selective stimulation, these adverse effects could be avoided. The risk of bronchoconstriction and increased mucus secretion associated with stimulation of pulmonary efferent fibers would need to be monitored and avoided as to not contribute to ARDS pathogenesis further. In addition, laryngeal and esophageal muscle contractions in intubated patients would need to be prevented (Zalvan et al., 2003), as it would be a risk for mechanical damage to the nerve and upper airway obstruction. Implanting a VNS device in critically ill patients in ICU can be challenging. Ideally, the decision on the VNS device implantation should be informed by early laboratory signs of systemic inflammation, and the patients who are likely to progress to ARDS would undergo the VNS device implantation prior to the full development of cytokine storm and ARDS.

CONCLUSION

The ability of VNS to contain immune activation at the crucial stages of a nascent response whilst not impairing the specific immunity against infectious agents is highly advantageous in treating ARDS and other immune dysregulation diseases. In contrast to immunosuppressive therapy, activation of the CAIP via abdominal efferents of the vagus nerve synapsing in the celiac-superior mesenteric ganglionic complex is desirable to attenuate the over-production of pro-inflammatory cytokines—the pathophysiological feature in ARDS. However, the effect of stimulation on the pulmonary fibers needs to be considered as it is likely that this will potentiate inflammation by activation of bronchoconstriction and mucus secretion, negating the beneficial anti-inflammatory effects of CAIP activation. Selective modulation of the vagus nerve could offer the greatest chance of improving ARDS outcomes by employing independent activation or block of the splenic and pulmonary immune pathways as needed.

AUTHOR CONTRIBUTIONS

SM and DH conceptualized and supervised the work. SM and NT wrote the manuscript. NT designed the figures. All authors contributed to the article and approved the submitted version.

FUNDING

This work was supported by the UK Medical Research Council (MRC grant No: MR/R01213X/1) and NIH SPARC (1OT2OD026545-01).

SUPPLEMENTARY MATERIAL

The Supplementary Material for this article can be found online at: https://www.frontiersin.org/articles/10.3389/fnins.2021.667036/full#supplementary-material

REFERENCES

Akella, A., and Deshpande, S. B. (2015). Vagal efferent stimulation protects against Mesobuthus tamulus venom-induced acute respiratory distress syndrome in rats. *Toxicon* 108, 189–201. doi: 10.1016/j.toxicon.2015.10.013

Aristovich, K., Donega, M., Fjordbakk, C., Tarotin, I., Chapman, C. A. R., Viscasillas, J., et al. (2021). Model-based geometrical optimisation and *in vivo* validation of a spatially selective multielectrode cuff array for vagus nerve neuromodulation. *J. Neurosci. Methods* 352:109079. doi: 10.1016/j.jneumeth.2021.109079

Boland, C., Collet, V., Laterre, E., Lecuivre, C., Wittebole, X., and Laterre, P.-F. (2011). Electrical vagus nerve stimulation and nicotine effects in peritonitis-induced acute lung injury in rats. *Inflammation* 34, 29–35. doi: 10.1007/s10753-010-9204-5

Bonaz, B., Sinniger, V., Hoffmann, D., Clarençon, D., Mathieu, N., Dantzer, C., et al. (2016). Chronic vagus nerve stimulation in Crohn's disease: a 6-month

follow-up pilot study. *Neurogastroenterol. Motil.* 28, 948–953. doi: 10.1111/nmo.12792

Borovikova, L. V., Ivanova, S., Zhang, M., Yang, H., Botchkina, G. I., Watkins, L. R., et al. (2000). Vagus nerve stimulation attenuates the systemic inflammatory response to endotoxin. *Nature* 405, 458–462. doi: 10.1038/35013070

Brégeon, F., Xeridat, F., Andreotti, N., Lepidi, H., Delpierre, S., Roch, A., et al. (2011). Activation of nicotinic cholinergic receptors prevents ventilator-induced lung injury in rats. *PLoS One* 6:e22386. doi: 10.1371/journal.pone.0022386

Diamond, M., Peniston Feliciano, H. L., Sanghavi, D., and Mahapatra, S. (2020). *Acute Respiratory Distress Syndrome (ARDS)*. (Treasure Island, FL: StatPearls Publishing LLC), 1–34.

Dos Santos, C. C., Shan, Y., Akram, A., Slutsky, A. S., and Haitsma, J. J. (2011). Neuroimmune regulation of ventilator-induced lung injury. *Am. J. Respir. Crit. Care Med.* 183, 471–482. doi: 10.1164/rccm.201002-0314OC

Fahy, J. V., and Dickey, B. F. (2010). Airway mucus function and dysfunction. *N. Engl. J. Med.* 363, 2233–2247. doi: 10.1056/NEJMra0910061

Fleshner, M., Goehler, L. E., Hermann, J., Relton, J. K., Maier, S. F., and Watkins, L. R. (1995). Interleukin-1β induced corticosterone elevation and hypothalamic NE depletion is vagally mediated. *Brain Res. Bull.* 37, 605–610. doi: 10.1016/0361-9230(95)00051-F

Gori, S., Alcain, J., Vanzulli, S., Moreno Ayala, M. A., Candolfi, M., Jancic, C., et al. (2019). Acetylcholine-treated murine dendritic cells promote inflammatory lung injury. *PLoS One* 14:e0212911. doi: 10.1371/journal.pone.0212911

Gosens, R., Zaagsma, J., Meurs, H., and Halayko, A. J. (2006). Muscarinic receptor signaling in the pathophysiology of asthma and COPD. *Respir. Res.* 7:73. doi: 10.1186/1465-9921-7-73

Guaraldi, G., Meschiari, M., Cozzi-Lepri, A., Milic, J., Tonelli, R., Menozzi, M., et al. (2020). Tocilizumab in patients with severe COVID-19: a retrospective cohort study. *Lancet Rheumatol.* 2, e474–e484. doi: 10.1016/S2665-9913(20)30173-9

Hein, E., Nowak, M., Kiess, O., Biermann, T., Bayerlein, K., Kornhuber, J., et al. (2013). Auricular transcutaneous electrical nerve stimulation in depressed patients: a randomized controlled pilot study. *J. Neural Transm.* 120, 821–827. doi: 10.1007/s00702-012-0908-6

Hoffmann, M., Kleine-Weber, H., Schroeder, S., Krüger, N., Herrler, T., Erichsen, S., et al. (2020). SARS-CoV-2 cell entry depends on ACE2 and TMPRSS2 and is blocked by a clinically proven protease inhibitor. *Cell* 181, 271–280.e8. doi: 10.1016/j.cell.2020.02.052

Horby, P., Lim, W. S., Emberson, J. R., Mafham, M., Bell, J. L., Linsell, L., et al. (2021). Dexamethasone in hospitalized patients with Covid-19 - preliminary report. *N. Engl. J. Med.* 384, 693–704. doi: 10.1056/NEJMoa2021436

Hosoi, T., Okuma, Y., and Nomura, Y. (2000). Electrical stimulation of afferent vagus nerve induces IL-1β expression in the brain and activates HPA axis. *Am. J. Physiol. Regul. Integr. Comp. Physiol.* 279, R141–R147. doi: 10.1152/ajpregu.2000.279.1.R141

Howland, R. H. (2014). Vagus nerve stimulation. *Curr. Behav. Neurosci. Rep.* 1, 64–73. doi: 10.1007/s40473-014-0010-5

Johnston, G. R., and Webster, N. R. (2009). Cytokines and the immunomodulatory function of the vagus nerve. *Br. J. Anaesth.* 102, 453–462. doi: 10.1093/bja/aep037

Koopman, F. A., Chavan, S. S., Miljko, S., Grazio, S., Sokolovic, S., Schuurman, P. R., et al. (2016). Vagus nerve stimulation inhibits cytokine production and attenuates disease severity in rheumatoid arthritis. *Proc. Natl. Acad. Sci. U.S.A.* 113, 8284–8289. doi: 10.1073/pnas.1605635113

Kox, M., Vaneker, M., Van Der Hoeven, J. G., Scheffer, G.-J., Hoedemaekers, C. W., and Pickkers, P. (2012). Effects of Vagus nerve stimulation and vagotomy on systemic and pulmonary inflammation in a two-hit model in rats. *PLoS One* 7:e34431. doi: 10.1371/journal.pone.0034431

Kressel, A. M., Tsaava, T., Levine, Y. A., Chang, E. H., Addorisio, M. E., Chang, Q., et al. (2020). Identification of a brainstem locus that inhibits tumor necrosis factor. *Proc. Natl. Acad. Sci. U.S.A.* 117, 29803–29810. doi: 10.1073/pnas.2008213117

Krzyzaniak, M. J., Peterson, C. Y., Cheadle, G., Loomis, W., Wolf, P., Kennedy, V., et al. (2011). Efferent vagal nerve stimulation attenuates acute lung injury following burn: the importance of the gut-lung axis. *Surgery* 150, 379–389. doi: 10.1016/j.surg.2011.06.008

Kubin, L., Alheid, G. F., Zuperku, E. J., and Mccrimmon, D. R. (2006). Central pathways of pulmonary and lower airway vagal afferents. *J. Appl. Physiol.* 101, 618–627. doi: 10.1152/japplphysiol.00252.2006

Liao, M., Liu, Y., Yuan, J., Wen, Y., Xu, G., Zhao, J., et al. (2020). Single-cell landscape of bronchoalveolar immune cells in patients with COVID-19. *Nat. Med.* 26, 842–844. doi: 10.1038/s41591-020-0901-9

Liu, Y., Tao, T., Li, W., and Bo, Y. (2017). Regulating autonomic nervous system homeostasis improves pulmonary function in rabbits with acute lung injury. *BMC Pulm. Med.* 17:98. doi: 10.1186/s12890-017-0436-0

Majoie, H. J. M., Rijkers, K., Berfelo, M. W., Hulsman, J. A. R. J., Myint, A., Schwarz, M., et al. (2011). Vagus nerve stimulation in refractory epilepsy: effects on pro- and anti-inflammatory cytokines in peripheral blood. *Neuroimmunomodulation* 18, 52–56. doi: 10.1159/000315530

Martelli, D., Mckinley, M. J., and Mcallen, R. M. (2014). The cholinergic anti-inflammatory pathway: a critical review. *Auton. Neurosci. Basic Clin.* 182, 65–69. doi: 10.1016/j.autneu.2013.12.007

Matteoli, G., Gomez-Pinilla, P. J., Nemethova, A., Di Giovangiulio, M., Cailotto, C., Van Bree, S. H., et al. (2014). A distinct vagal anti-inflammatory pathway modulates intestinal muscularis resident macrophages independent of the spleen. *Gut* 63, 938–948. doi: 10.1136/gutjnl-2013-304676

Matthay, M. A., Zemans, R. L., Zimmerman, G. A., Arabi, Y. M., Beitler, J. R., Mercat, A., et al. (2019). Acute respiratory distress syndrome. *Nat. Rev. Dis. Prim.* 5:18. doi: 10.1038/s41572-019-0069-0

McAllen, R. M., Shafton, A. D., Bratton, B. O., Trevaks, D., and Furness, J. B. (2018). Calibration of thresholds for functional engagement of vagal A, B and C fiber groups *in vivo*. *Bioelectron. Med.* 1, 21–27. doi: 10.2217/bem-2017-0001

Mehta, P., Mcauley, D. F., Brown, M., Sanchez, E., Tattersall, R. S., and Manson, J. J. (2020). COVID-19: consider cytokine storm syndromes and immunosuppression. *Lancet* 395, 1033–1034. doi: 10.1016/S0140-6736(20)30628-0

Mokra, D., Mikolka, P., Kosutova, P., and Mokry, J. (2019). Corticosteroids in acute lung injury: the dilemma continues. *Int. J. Mol. Sci.* 20:4765. doi: 10.3390/ijms20194765

Ni, W., Yang, X., Yang, D., Bao, J., Li, R., Xiao, Y., et al. (2020). Role of angiotensin-converting enzyme 2 (ACE2) in COVID-19. *Crit. Care* 24:422. doi: 10.1186/s13054-020-03120-0

Ordelman, S. C., Kornet, L., Cornelussen, R., Buschman, H. P., and Veltink, P. H. (2013). Selectivity for specific cardiovascular effects of vagal nerve stimulation with a multi-contact electrode cuff. *IEEE Trans. Neural Syst. Rehabil. Eng.* 21, 32–36. doi: 10.1109/tnsre.2012.2214058

Patel, Y. A., Saxena, T., Bellamkonda, R. V., and Butera, R. J. (2017). Kilohertz frequency nerve block enhances anti-inflammatory effects of vagus nerve stimulation. *Sci. Rep.* 7:39810. doi: 10.1038/srep39810

Plachta, D. T. T., Gierthmuehlen, M., Cota, O., Espinosa, N., Boeser, F., Herrera, T. C., et al. (2014). Blood pressure control with selective vagal nerve stimulation and minimal side effects. *J. Neural Eng.* 11:036011. doi: 10.1088/1741-2560/11/3/036011

Ravagli, E., Mastitskaya, S., Thompson, N., Aristovich, K., and Holder, D. (2019). Optimization of the electrode drive pattern for imaging fascicular compound action potentials in peripheral nerve with fast neural electrical impedance tomography (EIT). *Physiol. Meas.* 40:115007. doi: 10.1088/1361-6579/ab54eb

Ravagli, E., Mastitskaya, S., Thompson, N., Iacoviello, F., Shearing, P. R., Perkins, J., et al. (2020). Imaging fascicular organization of rat sciatic nerves with fast neural electrical impedance tomography. *Nat. Commun.* 11:6241. doi: 10.1038/s41467-020-20127-x

Rosas-Ballina, M., Ochani, M., Parrish, W. R., Ochani, K., Harris, Y. T., Huston, J. M., et al. (2008). Splenic nerve is required for cholinergic antiinflammatory pathway control of TNF in endotoxemia. *Proc. Natl. Acad. Sci. U.S.A.* 105, 11008–11013. doi: 10.1073/pnas.0803237105

Samavati, L., and Uhal, B. D. (2020). ACE2, Much More Than Just a Receptor for SARS-COV-2. *Front. Cell. Infect. Microbiol.* 10:317. doi: 10.3389/fcimb.2020.00317

Sato, E., Koyama, S., Okubo, Y., Kubo, K., and Sekiguchi, M. (1998). Acetylcholine stimulates alveolar macrophages to release inflammatory cell chemotactic activity. *Am. J. Physiol.* 274, L970–L979.

Stavrakis, S., Humphrey, M. B., Scherlag, B. J., Hu, Y., Jackman, W. M., Nakagawa, H., et al. (2015). Low-level transcutaneous electrical vagus nerve stimulation

suppresses atrial fibrillation. *J. Am. Coll. Cardiol.* 65, 867–875. doi: 10.1016/j.jacc.2014.12.026

Su, X., Matthay, M. A., and Malik, A. B. (2010). Requisite role of the cholinergic alpha7 nicotinic acetylcholine receptor pathway in suppressing Gram-negative sepsis-induced acute lung inflammatory injury. *J. Immunol.* 184, 401–410. doi: 10.4049/jimmunol.0901808

Subramanian, M., Edwards, L., Melton, A., Branen, L., Herron, A., Sivasubramanian, M. K., et al. (2020). Non-invasive vagus nerve stimulation attenuates proinflammatory cytokines and augments antioxidant levels in the brainstem and forebrain regions of Dahl salt sensitive rats. *Sci. Rep.* 10:17576. doi: 10.1038/s41598-020-74257-9

Swirski, F. K., Nahrendorf, M., Etzrodt, M., Wildgruber, M., Cortez-Retamozo, V., Panizzi, P., et al. (2009). Identification of splenic reservoir monocytes and their deployment to inflammatory sites. *Science* 325, 612–616. doi: 10.1126/science.1175202

Thompson, N., Mastitskaya, S., and Holder, D. (2019). Avoiding off-target effects in electrical stimulation of the cervical vagus nerve: neuroanatomical tracing techniques to study fascicular anatomy of the vagus nerve. *J. Neurosci. Methods* 325:108325. doi: 10.1016/j.jneumeth.2019.108325

Thompson, N., Ravagli, E., Mastitskaya, S., Iacoviello, F., Aristovich, K., Perkins, J., et al. (2020). MicroCT optimisation for imaging fascicular anatomy in peripheral nerves. *J. Neurosci. Methods* 338:108652. doi: 10.1016/j.jneumeth.2020.108652

Tosato, M., Yoshida, K., Toft, E., and Struijk, J. J. (2007). Quasi-trapezoidal pulses to selectively block the activation of intrinsic laryngeal muscles during vagal nerve stimulation. *J. Neural Eng.* 4, 205–212. doi: 10.1088/1741-2560/4/3/005

Van Westerloo, D. J., Giebelen, I. A. J., Meijers, J. C. M., Daalhuisen, J., De Vos, A. F., Levi, M., et al. (2006). Vagus nerve stimulation inhibits activation of coagulation and fibrinolysis during endotoxemia in rats. *J. Thromb. Haemost.* 4, 1997–2002. doi: 10.1111/j.1538-7836.2006.02112.x

Verlinden, T. J. M., Van Dijk, P., Hikspoors, J., Herrler, A., Lamers, W. H., and Köhler, S. E. (2019). Innervation of the human spleen: a complete hilum-embedding approach. *Brain Behav. Immun.* 77, 92–100. doi: 10.1016/j.bbi.2018.12.009

Vida, G., Peña, G., Deitch, E. A., and Ulloa, L. (2011). α7-cholinergic receptor mediates vagal induction of splenic norepinephrine. *J. Immunol.* 186, 4340–4346. doi: 10.4049/jimmunol.1003722

Vuckovic, A., Tosato, M., and Struijk, J. J. (2008). A comparative study of three techniques for diameter selective fiber activation in the vagal nerve: anodal block, depolarizing prepulses and slowly rising pulses. *J. Neural Eng.* 5, 275–286. doi: 10.1088/1741-2560/5/3/002

Wong, J. J. M., Leong, J. Y., Lee, J. H., Albani, S., and Yeo, J. G. (2019). Insights into the immuno-pathogenesis of acute respiratory distress syndrome. *Ann. Transl. Med.* 7, 504–504. doi: 10.21037/atm.2019.09.28

Yap, J. Y. Y., Keatch, C., Lambert, E., Woods, W., Stoddart, P. R., and Kameneva, T. (2020). Critical review of transcutaneous vagus nerve stimulation: challenges for translation to clinical practice. *Front. Neurosci.* 14:284. doi: 10.3389/fnins.2020.00284

Yuan, H., and Silberstein, S. D. (2016). Vagus nerve and vagus nerve stimulation, a comprehensive review: Part III. *Headache* 56, 479–490. doi: 10.1111/head.12649

Zalvan, C., Sulica, L., Wolf, S., Cohen, J., Gonzalez-Yanes, O., and Blitzer, A. (2003). Laryngopharyngeal dysfunction from the implant vagal nerve stimulator. *Laryngoscope* 113, 221–225. doi: 10.1097/00005537-200302000-00005

Zhang, W., Zhao, Y., Zhang, F., Wang, Q., Li, T., Liu, Z., et al. (2020). The use of anti-inflammatory drugs in the treatment of people with severe coronavirus disease 2019 (COVID-19): the Perspectives of clinical immunologists from China. *Clin. Immunol.* 214:108393. doi: 10.1016/j.clim.2020.108393

Conflict of Interest: The authors declare that the research was conducted in the absence of any commercial or financial relationships that could be construed as a potential conflict of interest.

frontiers in Neuroscience

SYSTEMATIC REVIEW
published: 30 April 2021
doi: 10.3389/fnins.2021.664740

Auricular Vagus Neuromodulation—A Systematic Review on Quality of Evidence and Clinical Effects

Nishant Verma[1,2], *Jonah D. Mudge*[1,2], *Maïsha Kasole*[1,2], *Rex C. Chen*[1,2], *Stephan L. Blanz*[1,2], *James K. Trevathan*[1,2], *Eric G. Lovett*[3], *Justin C. Williams*[1,2,4] *and Kip A. Ludwig*[1,2,4]*

[1] Department of Biomedical Engineering, University of Wisconsin – Madison, Madison, WI, United States, [2] Wisconsin Institute for Translational Neuroengineering (WITNe) – Madison, Madison, WI, United States, [3] LivaNova PLC, Minneapolis, MN, United States, [4] Department of Neurosurgery, University of Wisconsin – Madison, Madison, WI, United States

OPEN ACCESS

Edited by:
Arun Sridhar, Independent Researcher, Milton Keynes, United Kingdom

Reviewed by:
Stavros Zanos, Feinstein Institute for Medical Research, United States
Wouter De Jonge, Academic Medical Center, Netherlands
Matteo Donega, Consultant, Village-Neuf, France

***Correspondence:**
Kip A. Ludwig
kip.ludwig@wisc.edu

Specialty section:
This article was submitted to Autonomic Neuroscience, a section of the journal Frontiers in Neuroscience

Received: *05 February 2021*
Accepted: *25 March 2021*
Published: *30 April 2021*

Citation:
Verma N, Mudge JD, Kasole M, Chen RC, Blanz SL, Trevathan JK, Lovett EG, Williams JC and Ludwig KA (2021) Auricular Vagus Neuromodulation—A Systematic Review on Quality of Evidence and Clinical Effects. Front. Neurosci. 15:664740. doi: 10.3389/fnins.2021.664740

Background: The auricular branch of the vagus nerve runs superficially, which makes it a favorable target for non-invasive stimulation techniques to modulate vagal activity. For this reason, there have been many early-stage clinical trials on a diverse range of conditions. These trials often report conflicting results for the same indication.

Methods: Using the Cochrane Risk of Bias tool we conducted a systematic review of auricular vagus nerve stimulation (aVNS) randomized controlled trials (RCTs) to identify the factors that led to these conflicting results. The majority of aVNS studies were assessed as having "some" or "high" risk of bias, which makes it difficult to interpret their results in a broader context.

Results: There is evidence of a modest decrease in heart rate during higher stimulation dosages, sometimes at above the level of sensory discomfort. Findings on heart rate variability conflict between studies and are hindered by trial design, including inappropriate washout periods, and multiple methods used to quantify heart rate variability. There is early-stage evidence to suggest aVNS may reduce circulating levels and endotoxin-induced levels of inflammatory markers. Studies on epilepsy reached primary endpoints similar to previous RCTs testing implantable vagus nerve stimulation therapy. Preliminary evidence shows that aVNS ameliorated pathological pain but not evoked pain.

Discussion: Based on results of the Cochrane analysis we list common improvements for the reporting of results, which can be implemented immediately to improve the quality of evidence. In the long term, existing data from aVNS studies and salient lessons from drug development highlight the need for direct measures of local neural target engagement. Direct measures of neural activity around the electrode will provide data for the optimization of electrode design, placement, and stimulation waveform parameters to improve on-target engagement and minimize off-target activation. Furthermore, direct measures of target engagement, along with consistent evaluation of blinding success,

must be used to improve the design of controls—a major source of concern identified in the Cochrane analysis. The need for direct measures of neural target engagement and consistent evaluation of blinding success is applicable to the development of other paresthesia-inducing neuromodulation therapies and their control designs.

Keywords: auricular stimulation, systematic review, vagus nerve stimulation or VNS, auricular vagus nerve stimulation, transcutaneous vagus nerve stimulation, microneurography, target engagement, blinding (masking)

INTRODUCTION

Electrical stimulation of the nervous system, commonly known as neuromodulation, manipulates nervous system activity for therapeutic benefits. The wandering path of the vagus nerve, the tenth cranial nerve, and its communication with several visceral organs and brain structures makes it an attractive target to address many diseases. Vagus nerve stimulation (VNS) to treat epilepsy has been approved by the United States Food and Drug Administration (FDA) since 1997 (Wellmark, 2018). An implantable pulse generator (IPG) is implanted below the clavicle and delivers controlled doses of electrical stimulation through electrodes wrapped around the cervical vagus. Due to the safety vs. efficacy profile of the therapy, implantable VNS is currently a last line therapy after patients have been shown refractory to at least two appropriately dosed anti-epileptic drugs (American Association of Neurological Surgeons, 2021). Implantable VNS for epilepsy is purported to work through vagal afferents terminating in the nucleus of the solitary tract (NTS). NTS in turn has direct or indirect projections to the nuclei providing noradrenergic, endorphinergic, and serotonergic fibers to different parts of the brain (Kaniusas et al., 2019).

In a similar fashion, the auricular branch of the vagus also projects to the NTS, carrying somatosensory signals from the ear (Kaniusas et al., 2019). The superficial path of the nerve (Bermejo et al., 2017) in the ear means a low amplitude electrical stimulation applied at the surface of the skin can, in theory, generate electric field gradients at the depth of the nerve sufficient to alter its activity. Auricular vagus nerve stimulation (aVNS) delivered percutaneously or transcutaneously offers a method to modulate neural activity on the vagus nerve with the potential for a more favorable safety profile. **Figure 1** shows innervation of the auricle by four major nerve branches, overlapping regions of innervation in the auricle, and several electrode designs to deliver electrical stimulation at the ear.

Given aVNS can be implemented with minimally invasive approaches and has the potential to modulate vagal activity, there have been many early-stage clinical trials investigating a diverse range of potential therapeutic indications, including heart failure, epilepsy, depression, pre-diabetes, Parkinson's, and rheumatoid arthritis. Several companies are already developing aVNS devices, such as Parasym (London, UK), Cerbomed (Erlangen, Germany), Spark Biomedical (Dallas, Texas, USA), SzeleSTIM (Vienna, Austria), Ducest Medical (Ducest, Mattersburg, Germany), Innovative Health Solutions (Versailles, IN, USA), and Hwato (Suzhou, Jiangsu Province, China). Despite the large number of aVNS clinical studies, clinical evidence to support a specific therapeutic outcome is often mixed, with conflicting trial results for the same physiological outcome measure (Burger et al., 2020; Keute et al., 2021).

According to the Oxford Center for Evidence Based Medicine's (CEBM) Levels of Clinical Evidence Scale, the highest level of clinical evidence is a systematic review of multiple high-quality double-blinded, randomized, and controlled clinical trials (RCTs) with narrow confidence intervals, each homogeneously supporting the efficacy and safety of a therapy for a specific clinical outcome (Centre for Evidence-Based Medicine, 2009). However, reaching this level of evidence is costly and time-consuming. Years of precursor clinical studies with fewer number of subjects are needed to identify the most efficacious embodiment of the therapy that can be safely delivered. Data from these precursor studies are required to design more definitive clinical studies. The field of aVNS, being relatively new clinically, is understandably still in these early phases of clinical development.

We performed a systematic review of aVNS RCTs with two primary goals: (1) to provide an accessible framework for the aVNS community to review current studies for specific outcome measures as a resource to inform future study design and (2) to perform a qualitative assessment of the current level of clinical evidence to support aVNS efficacy for the most common outcome measures reported. To this end, the Cochrane Risk of Bias Tool (Sterne et al., 2019)—a framework previously used to identify risk of bias in RCT studies of epidural spinal cord stimulation (Duarte et al., 2020b) and dorsal root ganglion stimulation (Deer et al., 2020) to treat pain—was first used to assess the quality of evidence in individual aVNS RCTs. These data were aggregated to broadly assess the current level of clinical evidence, according to the Oxford CEBM scale, to support aVNS efficacy across the common physiological outcomes. Our efforts were not intended to provide a precise assessment of the current level of clinical evidence but to identify the most common gaps in clinical study design and reporting. These gaps were analyzed to identify systematic next steps that should be addressed before aVNS can move to a higher level of evidence for any specific clinical outcome.

METHODS

Search Method

Our literature search was designed to identify reports of clinical RCTs testing aVNS as an intervention. Two databases were searched systematically: PubMed and Scopus (includes MEDLINE and Embase databases). Additionally, two search strategies were used. The first strategy combined search terms

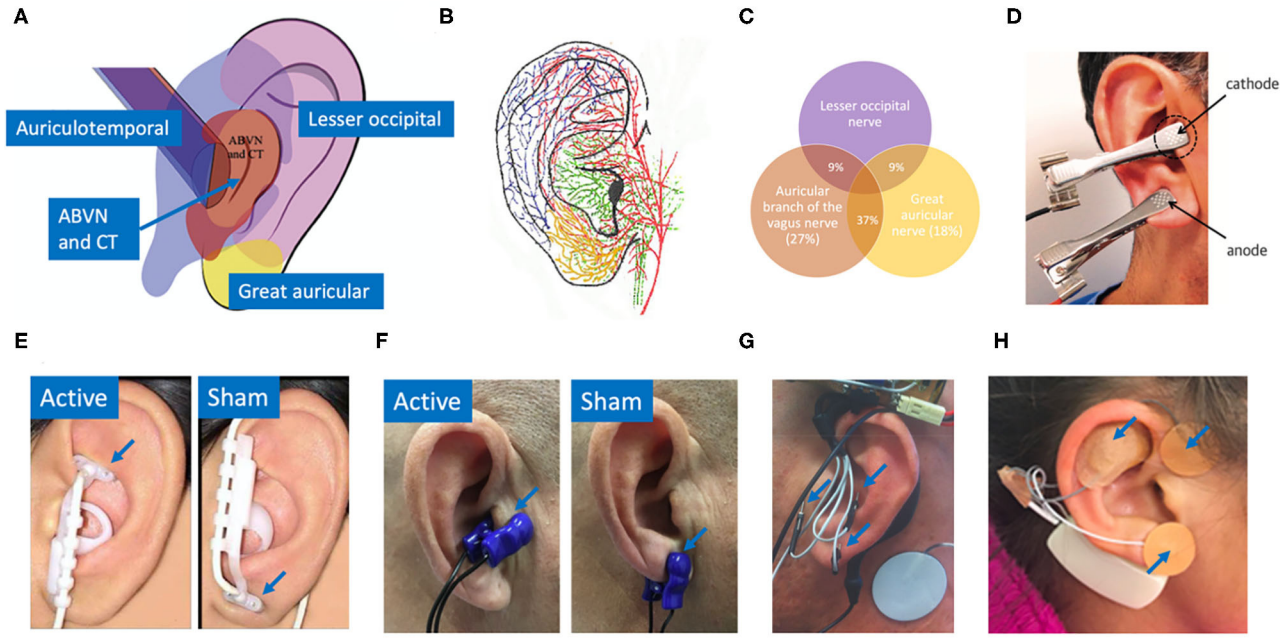

FIGURE 1 | (A) Innervation of the auricle by five nerves (Watanabe et al., 2016): auricular branch of the vagus nerve (ABVN), chorda tympani (CT) from the facial nerve, auriculotemporal nerve originating from the mandibular branch of the trigeminal nerve, great auricular nerve, and lesser occipital nerve. **(B)** Artist impression of auricular innervation (He et al., 2012). Refer to Peuker and Filler (2002) dissection study mapping the innervation of the human auricle performed in 7 cadavers for original photographs. Note, microdissection cannot trace the finest of nerve branches. **(C)** Overlapping regions of innervation reported between the auricular branch of the vagus nerve (ABVN), great auricular nerve (GAN), and lesser occipital nerve (Peuker and Filler, 2002). Here the ABVN and GAN overlap for 37% of the area on the medial dorsal middle third of the ear—setting the precedent for large overlaps in regions innervated by different nerves. Commonly used electrodes: **(D)** Clips transcutaneously targeting the tragus and earlobe simultaneously in the intervention group (Stavrakis et al., 2015). **(E)** NEMOS electrodes by Cerbomed (Erlangen, Germany) transcutaneously targeting cymba concha in the intervention group and ear lobe in the sham group (Frangos et al., 2015). **(F)** Parasym (London, UK) transcutaneously targeting tragus in the intervention group and ear lobe in the sham group (Stavrakis et al., 2020). **(G)** Percutaneously targeting intrinsic auricular muscles zones in the intervention group (Cakmak et al., 2017). **(H)** Innovative Health Solutions (Versailles, IN, USA) percutaneously targeting several cranial nerves in the auricular and periauricular region in the intervention group (Kovacic et al., 2017).

related to aVNS and RCT. The second search strategy focused on search terms related to commercial aVNS devices and their manufacturers. Complete search strings for both strategies are available in **Supplementary Material 1**. The search was last updated in July 2020. In addition, citations of all selected studies were searched to identify additional studies that met the inclusion criteria. The citations of relevant reviews (Murray et al., 2016; Yap et al., 2020) were also searched. Duplicate records were removed, and the remaining records were screened at a title and abstract level to check if a clinical RCT on auricular stimulation was reported.

As our primary goal was to assess the effects of auricular stimulation, studies using any stimulation modality from any field, including acupuncture and electroacupuncture were initially included as long as the intervention was at the auricle. When it became evident that a meta-analysis would not be possible due to incomplete reporting of information, we decided to exclude traditional Chinese medicine (TCM) studies, which typically used acupuncture, electroacupuncture, or acupuncture beads. Studies were considered TCM studies if acupoints were used to justify location of stimulation or if they were published in a TCM journal. This is captured in **Figure 2** adapted from PRISMA (Moher et al., 2009). All studies excluded at the end of the search after full-text review are listed in **Supplementary Material 2**.

Inclusion and Exclusion Criteria

In papers where more than one clinical trial was reported, each trial that was randomized and controlled was included in the systematic review; non-RCT portions of included publications were not analyzed. Only publications 1991 and after were included, with the cutoff marking the first time autonomic activity biomarkers were reportedly measured during auricular stimulation (Johnson et al., 1991).

Included studies had to report measurements of direct clinical significance. This exclusion partially relied on whether the study claimed direct clinical implications of their findings. Additionally, studies were excluded if the measurements did not have a well-established link to clinically significant outcomes. For instance, pupil size, functional magnetic resonance imaging (fMRI), electroencephalography (EEG), and somatosensory evoked potentials (SSEPs) are secondary physiological measures of target engagement (Burger et al., 2020). Although they may be useful to study the mechanisms of aVNS, they do not have well-established links to clinically significant outcomes. In comparison, heart rate variability (HRV), a measure of

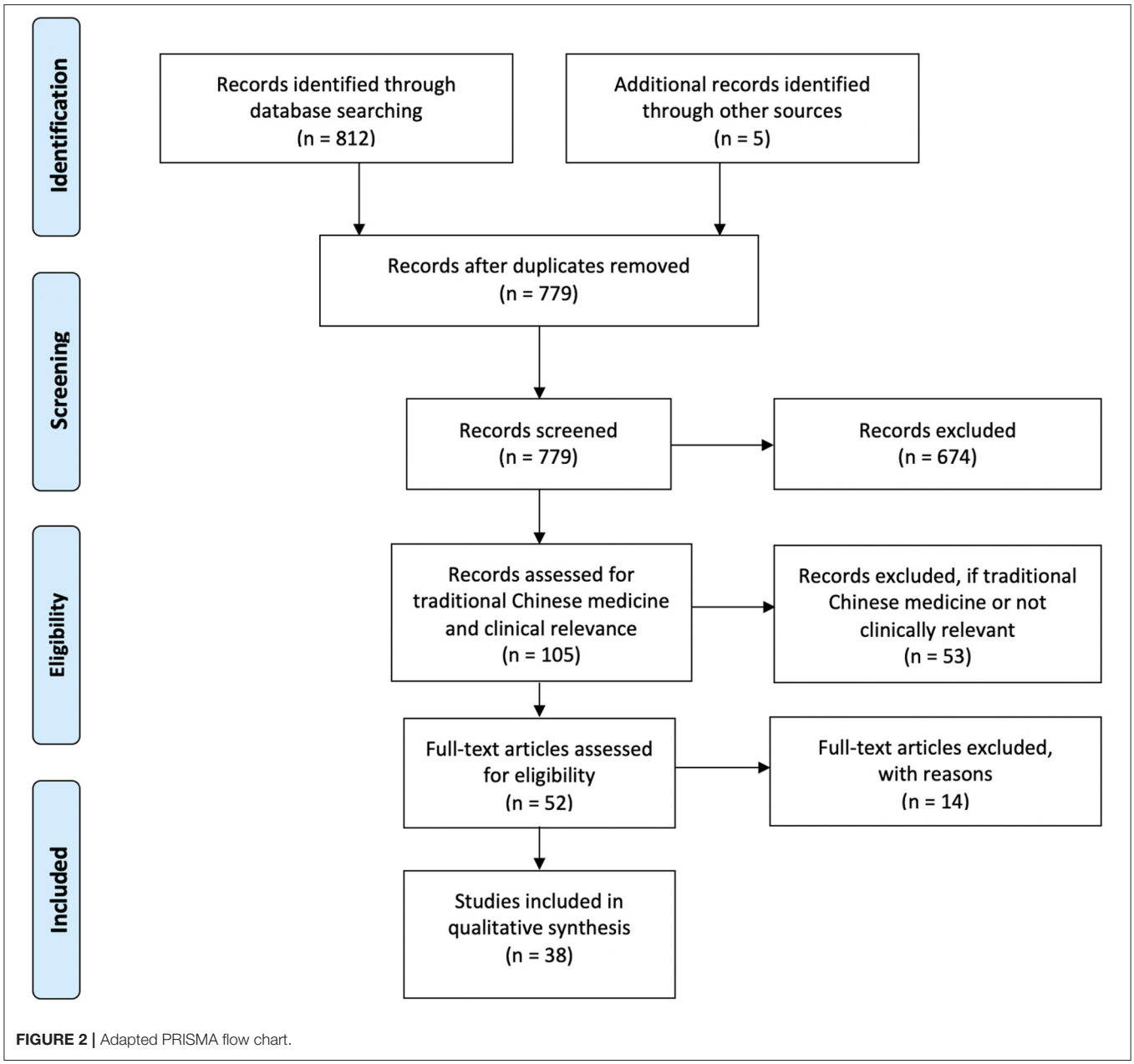

FIGURE 2 | Adapted PRISMA flow chart.

sympathovagal tone, is considered a measurement of direct clinical significance as sympathovagal imbalance is related to several disease states (Bootsma et al., 2003). Similarly, studies focused on cognitive neuroscience topics, such as behavior, learning, fear extinction, or executive functions were excluded. In contrast, psychological studies addressing addiction, depression, pain, and stress were included in the final qualitative review as they have had direct clinical significance.

Cochrane Risk of Bias 2.0 Tool to Assess Quality of Evidence

We used the Cochrane risk of bias 2.0 tool (RoB), an established tool to assess bias in clinical RCTs (Sterne et al., 2019), which has been cited over 40,000 times in Google Scholar, to evaluate the quality of evidence in each study. The RoB tool assesses bias in five subsections intended to capture the most common sources of possible bias in clinical studies. It is important to note a rating of "some" or "high" risk of bias does not mean that researchers conducting the study were themselves biased, or that the results they found are inaccurate. Deviations from ideal practice frequently occur due to a variety of potentially uncontrollable reasons. These deviations from the ideal just increase the chance that any stated result is a "false negative" or a "false positive" beyond the stated statistical convention used in the study.

For each study, the tool provides a suggested algorithm to rate bias through a series of guiding questions across the following five sections. Each section ends with a bias assignment of

"low," "some concerns," or "high." Template rubrics provided by Cochrane with the answers to these guiding questions have been included for every study evaluated in **Supplementary Material 9**. At several instances, the suggested algorithm was overridden by the reviewer with justification annotated on the individual rubric found in **Supplementary Material 9**. Below is an explanation of how each subsection was evaluated with respect to aVNS, see (Higgins et al., 2019) for more information on the recommended implementation of the Cochrane assessment tool.

Bias Arising From the Randomization Process

Randomization is important in a clinical study to ensure that differences in the outcome measure between the treatment and control groups were related to the intervention as opposed to an unintended difference between the two groups at baseline. To obtain a rating of "low" risk of bias, the study had to (1) randomize the allocation sequence, (2) conceal the randomized sequence from investigators and subjects till the point of assignment, and (3) test for baseline differences even after randomization. The latter is essential as even in a truly randomized design, it is conceivable that randomization yields an unequal distribution of a nuisance variable across the two groups. This is more likely to occur in studies with a smaller number of participants (Kang et al., 2008), which is the sample size found in many aVNS studies. Even in studies with a crossover design—meaning participants may receive a treatment and then, after an appropriate wash-out period, receive a sham therapy—it is important to test for baseline differences and that an equal number of subjects be presented with sham or therapy first (Nair, 2019).

Bias Due to Deviations From Intended Interventions

During the implementation of a clinical trial it is foreseeable for several subjects who were randomized to a given group to not receive the intended intervention or for blinding to be compromised. Compromised blinding is especially pertinent in neuromodulation studies, including aVNS studies, where there may be a difference in paresthesia or electrode location between the intervention and control group (Robbins and Lipton, 2017). Marked visual or perceptual differences between intervention groups can clue investigators and subjects to become aware of the treatment or control arm assignments, thereby violating the principle of blinding and deviating from the intended intervention. In order to receive a "low" risk of bias score, the study must have minimized and accounted for deviations from intended intervention due to unblinding, lack of adherence, or other failures in implementation of the intervention.

Bias Due to Missing Outcome Data

In conducting a clinical trial, being unable to record all intended outcome measures on all subjects is common. This can happen for a variety of reasons, including participant withdrawal from the study, difficulties in making a measurement on a given day, or records being lost or unavailable for other reasons (Higgins et al., 2019). In assessing how missing data may lead to bias it is important to consider the reasons for missing outcome data as well as the proportions of missing data. In general, if data was available for all, or nearly all participants, this measure was given "low" risk of bias. If there was notable missing data that was disproportionate between the treatment and control group, or the root cause for missing data suggested there may be a systemic issue, this measure was rated "some concerns" or "high" risk of bias depending on severity.

Bias in Measurement of the Outcome

How an outcome was measured can introduce several potential biases into subsequent analyses. Studies in which the assessor was blinded, the outcome measure was deemed appropriate, and the measurement of the outcome was performed consistently between intervention and control groups were generally considered "low" risk of bias. If the outcome assessor was not blinded but the outcome measure was justified as unlikely to be influenced by knowledge of intervention the study was also generally considered "low" risk of bias.

Bias in Selection of the Reported Result

An important aspect in reporting of clinical trial results is to differentiate if the data is exploratory or confirmatory (Hewitt et al., 2017). Exploratory research is used to generate hypotheses and models for testing and often includes analyses that are done at least in part retrospectively and are therefore not conclusive. Exploratory research is intended to minimize false negatives but is more prone to false positives. Confirmatory research is intended to rigorously test the hypothesis and is designed to minimize false positives. An important aspect of confirmatory research is pre-registration of the clinical trial before execution, including outlining the hypothesis to be studied, the data to be collected, and the analysis methods to be used. This is necessary to ensure that the investigators did not (1) collect data at multiple timepoints but report only some of the data, (2) use several analysis methods on the raw data in search for statistical significance, or (3) evaluate multiple endpoints without appropriate correction for multiple comparisons. Each of these common analysis errors violates the framework by which certain statistical methods are intended to be conducted—introducing an additional chance of yielding a false positive result. Studies that pre-registered their primary outcomes and used the measurements and analyses outlined in pre-registration generally scored "low" risk of bias in this category.

Information Extraction

Each paper was read in its entirety and a summary table was completed capturing study motivation, study design, study results, and critical review. Study motivation outlined the study hypothesis and hypothesized therapeutic mechanism of action if mentioned in the paper. We also noted whether implantable VNS had achieved the hypothesized effect in humans. Study design encapsulated subject enrollment information (diseased or healthy, the power of the study, and the inclusion and exclusion criteria), type of control and blinding, group design (crossover or parallel), stimulation parameters, randomization, baseline comparison, and washout periods. Lastly, study results included primary and secondary endpoints, adverse effects,

excluded and missing data, and statistical analysis details (pre-registered, handling of missing and incomplete data, multiple group comparison, etc.). Study results also analyzed if the effect was due to a few responders or improvements across the broad group, worsening of any subjects, control group effect size, and clinical relevance and significance of findings. Where sufficient information was reported, standardized effect size was calculated using Hedges' g (Turner and Bernard, 2006).

Each publication had a primary reviewer, and an additional secondary reviewer went through all papers. Any concerns raised by either reviewer were discussed as a group. If crucial basic information (e.g., which ear was stimulated, electrode used, etc.) was not reported (NR), an attempt was made to reach out to the author and if unsuccessful, to infer the information from similar studies by the group. Inferred or requested information is annotated as such. This effort helped highlight incomplete reporting of work while maximizing available information for the review to conduct an informed analysis.

A sortable table summarizing the design and result features of every reviewed study has been included as an excel file in **Supplementary Material 3** to allow viewing based on specific features of interest. Design and result features have been reduced to common keywords in this spreadsheet to facilitate sorting; however, this means specific details of outcome measures have been reduced to general categories in some cases.

RESULTS

A total of 38 articles were reviewed totaling 41 RCTs—two each in the publications by Hein et al. (2013), Cakmak et al. (2017), and Badran et al. (2018). In an initial review of the RCTs, it was apparent that a wide variety of electrode designs, stimulation parameters, study methodologies, and clinical indications were tested. As a framework by which to organize this multifaceted problem in the results below, we first discuss the electrode designs and stimulation parameters used across aVNS studies with the goal of identifying the most common aVNS implementation strategies and rationale for selection. Next, we discuss the study design features across all studies, again with the goal of identifying the most common practices. We then provide an assessment of all studies, regardless of clinical indication, using the Cochrane risk of bias (RoB) tool. Finally, we discuss the commonly measured outcomes based on treatment indication to identify which findings were most consistent across studies—couching the synthesis in results from the RoB analysis.

aVNS Electrode Designs, Configurations, and Stimulation Parameters Across Studies

Upon initial review, it was immediately evident that implementation of both active and sham varied greatly across studies. **Table 1** details the electrode design, configuration (monopolar or bipolar), target location, and stimulation parameters for the active and control arms of the study.

Table 1 is organized by indication type, then primary endpoints, then RoB score. Data is organized in the following columns:

Primary Endpoints

The main result of clinical interest. Studies are grouped by endpoints measured within their respective indications. For example, within the cardiac diseases indication the studies investigating inflammatory cytokine levels are located adjacent to each other.

Active Waveform and Location

Frequency, pulse width (PW), on/off cycle duration (duty cycle), and stimulation location.

Active Amplitude and Electrode Type

Current amplitude, titration method used to reach that amplitude, and electrode type and stimulator model when available. Titration methods are denoted as sub-sensory, first sensory, strong sensory (not painful), painful, or set at a particular amplitude. These terms reflect the cues that investigators used (Badran et al., 2019) to determine the stimulation amplitude for each subject:

Sub-sensory Titration

Stimulation was kept just below the threshold of paresthesia sensation.

First Sensory Titration

Subject is barely able to feel a cutaneous sensation.

Strong Sensory Titration

Subject feels a strong, but not painful or uncomfortable sensation from the stimulation.

Pain Titration

Stimulation amplitude is increased until the subject feels a painful or uncomfortable sensation.

Set Stimulation

Fixed amplitude across all subjects—resulting in different levels of sensation due to the individual's unique anatomy and perception.

Control

Control group stimulation amplitude, control design (sham or placebo), and stimulation location. Following Duarte et al. (2020b), we defined sham as when the control group experience from the subject perspective is identical to the active group experience—including paresthesia and device operating behavior. Conversely, placebo control is defined when the control group subjects do not experience the same paresthesia, device operation, or clinician interaction as the active group subjects.

Table 1 details the electrode design, configuration (monopolar or bipolar), target location, and stimulation parameters for the active and control arms of the study and shows that implementation of both active and sham varied greatly across studies. **Figure 3** shows a box plot presenting the distribution of pulse widths, stimulation current amplitudes, and frequencies

TABLE 1 | Electrode design, configuration, target location, and stimulation parameters (sorted by indication type, primary endpoints, and color coded RoB score).

Author (y) indication*	Primary endpoints	Active waveform** and location	Active amplitude and electrode type***	Control
		Cardiac		
Andreas et al. (2019) Postoperative atrial fibrillation	Postoperative atrial fibrillation assessed on ECG	1 Hz, PW NR, 40 min on 20 min off Side NR Triangular fossa	Sub-sensory (1 mA), Ducest Neurostimulator V	Sham: same location, low level stimulation (mA NR)
Stavrakis et al. (2015) Atrial fibrillation	Atrial fibrillation cycle length and duration, TNF-a, CRP	20 Hz, 1 ms PW, on/off cycle NR Right tragus	50% of heart sinus rate slowing current threshold (mA NR), Grass S88 stimulator clip electrodes	Placebo: no current, same location
Stavrakis et al. (2020) Atrial Fibrillation	Atrial fibrillation burden assessed on ECG	20 Hz, 200 μs PW, on/off cycle NR Right tragus	Strong sensory (1 mA below mild pain threshold, mean 16.8 mA), Parasym clip electrodes	Sham: diff amplitude (mean 19.9 mA), diff location (right earlobe)
Badran et al. (2018) Heart rate	ΔHR during stimulation	9 waveforms (1, 10, 25 Hz) × (100, 200, 500 μs PW), on/off cycle NR Left tragus	2x sensory threshold (at 100 μs PW: 9.28 ± 2.56 mA, at 200 μs PW: 5.32 ± 1.60 mA, at 500 μs PW: 3 ± 0.93 mA), custom clip electrodes	Sham: At 100 μs PW: 6.57 ± 1.83 mA. At 200 μs PW: 3.64 ± 1.26 mA. At 500 μs PW: 1.97 ± 0.71 mA. diff location (earlobe)
Afanasiev et al. (2015) Coronary Insufficiency and LV dysfunction	Heart rate and 6 min walk distance	Frequency NR, PW NR, on/off cycle NR Side NR concha	Titration method NR (mean 0.05–0.15 mA), electrode NR	Placebo: same location (concha)
Tobaldini et al. (2019) Orthostatic stress	ΔHR, LF/HF, systolic arterial BP variance, RR interval pattern, respiratory rate	25 Hz, 200 ms PW (reported 200 ms in methods and 200 us in discussion), on/off cycle NR, phase NR Left cymba concha	First sensory (1–6 mA), NEMOS ball contact electrodes	Placebo: No stimulation, same location.
Fisher et al. (2018) Hypertension	Percentage decrease in median systolic blood pressure (SBP)	25 Hz, 15 ms PW, 1 s duration (gated to exhalation), biphasic Left cymba concha and beneath antihelix	Strong sensory (mA NR), stimulator NR, surface electrodes	Placebo: no current, same location
Stowell et al. (2019) Hypertension	Arterial blood pressure	2, 10, 25, or 100 Hz. 300 μs PW, 1 s on/off Left cymba concha	Strong sensory (mA NR) Urostim device, custom-built ergonomic electrodes	Placebo: no current, same location
Zamotrinsky et al. (2001) coronary artery disease	HR, BP, LV diastolic function, LV filling	3 Hz, 1,500 μs PW, on/off cycle NR Bilateral cavum concha	Titration method NR (0.2–1.25 mA), acupuncture needles	No intervention
Antonino et al. (2017) Baroreflex sensitivity	cBRS from systolic blood pressure and RR interval HRV (LF/HF)	30 Hz, 200 μs PW, on/off cycle NR Bilateral tragus	Sensory threshold (10–50 mA device range), ear clip electrodes	1 Placebo 1 Sham: same waveform (mA NR), diff location (bilateral earlobe)
Bretherton et al. (2019) HRV and baroreflex sensitivity	cBRS and HRV	30 Hz, 200 μs PW, on/off cycle NR Side NR inner & outer tragus	Sensory threshold (2–4 mA), custom TENS electrodes	Placebo: same location (inner and outer tragus)
Clancy et al. (2014) HRV and sympathetic activity	HRV (LF/HF)	30 Hz, 200 μs PW, continuous, Side NR inner and outer tragus	Sensory threshold (10–50 mA device range), V-TENS Plus with modified surface electrodes	Placebo: no current, same location
De Couck et al. (2017) HRV	ECG with HRV	25 Hz, 250 μs PW, on/off cycle NR Bilateral cymba concha	Strong sensory (mean ~0.7 mA), NEMOS ball contact electrodes	Placebo: no current, same location
Borges et al. (2019) Cardiac vagal activity	HRV	25 Hz, PW of 200–300 μs, 30 s on/off Left cymba concha	Set stimulation (1 mA) and strong sensory stimulation (2.5 ± 0.93 mA), NEMOS ball contact electrodes	Sham: same set stimulation, different strong sensory stimulation (2.76 ± 1.01 mA), diff location (earlobe)
Tran et al. (2019) LV Strain and autonomic tone	LV global longitudinal strain	20 Hz, 200 μs PW, on/off cycle NR Right tragus	Strong sensory (1 mA below pain threshold, mean 22.6 mA active), Parasym earclip electrodes	Sham: diff current (mean 21.8 mA), diff location (right earlobe)
Yu et al. (2017) Myocardial ischemia-reperfusion Injury	Ventricular premature beat incidence	20 Hz, 1 ms PW, 5 s on/off Right tragus	50% of heart sinus rate slowing threshold, clip electrodes (S20 stimulator, Jinjiang, Chengdu City, China)	Placebo: no current, same location (right tragus)
		Epilepsy		
Bauer et al. (2016) Epilepsy	Reduction in seizure frequency (per 28 days)	25 Hz, 250 μs PW, on/off cycle NR Left concha	Sensory threshold (0.50 ± 0.47 mA), NEMOS ball contact electrode	Sham: diff waveform 1 Hz and 1.02 ± 0.83 mA, same location (left concha)

(Continued)

TABLE 1 | Continued

Author (y) indication*	Primary endpoints	Active waveform** and location	Active amplitude and electrode type***	Control
Aihua et al. (2014) Epilepsy	Reduction in seizure frequency (per month)	20 Hz, 200 ms PW, on/off cycle NR Bilateral concha and external ear canal	Pain threshold (mA NR), electrode NR	Sham: same waveform (mA NR), diff location (bilateral earlobe)
Rong et al. (2014) Epilepsy	Seizure frequency (per 4 weeks)	20–30 Hz, ≤ 1 ms PW Ear side NR cymba concha and cavum concha	Set stim (1 mA), electrode with 3 carbon-impregnated silicone tips (Suzhou Medical Appliance Co. Ltd.)	Sham: same waveform, diff location; contacts at scapha and antihelical fold
		Pain		
Straube et al. (2015) Chronic migraine	Decrease in headache per 28 days	25 Hz, 250 μs PW, 30 s on/off Left concha	Strong sensory (mA NR), NEMOS ball contact electrodes	Sham: 1 Hz frequency, same location
Janner et al. (2018) Pain	Perceived pain intensity and temporal summation of pain	100 Hz, 200 μs PW, 0.01 s on/0.49 s off Bilateral cymba concha	Strong sensory (mA NR), custom earplug electrodes wrapped in NaCl-soaked wool	Sham: same waveform, diff location (earlobe). Placebo: same location, no current
Kovacic et al. (2017) GI pain	Change in max abdominal pain intensity and composite of Pain-Frequency-Severity-Duration scale	Alternating 1 Hz and 10 Hz every 2 s, 1 ms PW, 2 hrs on/off Side NR Earlobe, triangular fossa, ventral periauricular tragus	Sub-sensory (mA NR), 2 mm titanium percutaneous electrodes (monopolar)	Sham: no current (sub sensory like active), same location
Kutlu et al. (2020) Fibromyalgia	Visual analog sale, beck depression scale, beck anxiety scale, fibromyalgia impact questionnaire, short form-36 for life quality	10 Hz, <500 μs PW, biphasic asymmetrical Bilateral tragus and concha	First sensory (mA NR), custom designed surface electrodes	Only exercise (active group is exercise and aVNS)
Busch et al. (2013) Pain	Thermal, mechanical, and pressure pain thresholds	25 Hz, 250 μs PW, on/off cycle NR Left concha	First sensory (1.6 ± 1.5 mA), STV02 (Cerbomed) electrodes	Placebo: no current, same location
Juel et al. (2017) Pain and GI motility	ECG and PPG, mechanical pain threshold, cold pressor test, and drink test (ultrasound imaging)	30 Hz, 250 μs PW, continuous Left concha	Pain/uncomfortable (intensity increased to counteract habituation, device rated between 0.1 and 10 mA), NEMOS ball contact electrodes	Sham: same waveform, diff location (left earlobe)
Frokjaer et al. (2016) Gastroduodenal motility and pain threshold	ECG and PPG, mechanical pain threshold, cold pressor test, and drink test (ultrasound imaging)	30 Hz, 250 μs PW, continuous Left concha	Strong sensory (1.07 mA), NEMOS ball contact electrode	Sham: diff amplitude (mean 1.57 mA), diff location (left earlobe)
Napadow et al. (2012) Pain	Mechanical deep-tissue pain intensity rating, and temporal pain summation	30 Hz, 450 μs PW, 0.5 s on/off, gated to exhalation phase of respiration Left cymba concha and antihelix/cavum concha slope	Strong sensory (mA NR), modified press-tack electrodes (0.20 × 1.5 mm)	Sham: same waveform, diff location (left earlobe)
Johnson et al. (1991) Pain threshold and autonomic function	Electrical pain threshold and autonomic function	100 Hz pulses every 2.4 Hz, 10 ms PW, 10 ms on/off, Right concha	Strong sensory (mA NR), carbon rubber electrodes	Sham: same waveform, diff location (antitragus)
Laqua et al. (2014) Pain	Electrical pain threshold	Alternating between 2 and 10 Hz, 200 μs PW, on/off cycle NR Bilateral concha (anode) and mastoid (cathode)	Strong sensory (mA NR), silver EEG electrode at anode and PECG electrode at cathode	Placebo: subsensory stim, same location
		Psychological		
Hein et al. (2013) Depression	Hamilton depression rating scale, Beck's depression inventory	1.5 Hz, PW NR, on/off cycle NR Bilateral concha	Sub-sensory (0–600 μA device range in study 1 and 130 μA in study 2), TENS-2000 (study 1) and TENS-1000 (study 2) Auri-Stim Medical, Inc. with corresponding electrodes (4 contacts)	Placebo: no current, same location
Hasan et al. (2015) Schizophrenia	Positive and negative schizophrenia symptom scale	25 Hz, 30 s on/180 s off, 250 μs PW, phase NR Left outer ear canal	Strong sensory (mA NR), CM02 (Cerbomed) titan electrodes	Placebo: no current, same location

(Continued)

TABLE 1 | Continued

Author (y) indication*	Primary endpoints	Active waveform** and location	Active amplitude and electrode type***	Control
Burger et al. (2019) Negative thought occurrence	Number of negative thought intrusions	25 Hz, 250 μs PW, 30 s on/off Left cymba concha	Set (0.5 mA), NEMOS ball contact electrodes	Sham: same waveform, diff location (left earlobe)
		Others		
Addorisio et al. (2019) Rheumatoid arthritis	Endotoxin-induced IL-6, IL-1β, and TNF	∼160 Hz vibrations, Right cymba concha	NA (vibratory device)	Sham: same waveform diff location (right gastrocnemius)
Salama et al. (2020) Acute inflammatory response after lung lobectomy	CRP, IL6, IL10, IL-1B, IL-18, TNF-a	1 Hz, 200 μs PW, 40 min on 20 min off Side NR Triangular Fossa	First sensory (230 nA), ∼2 mm needles	No intervention
Huang et al. (2014) Impaired glucose tolerance	2-h plasma glucose levels	20 Hz, ≤ 1 ms PW, phase NR Side NR concha	Set (1 mA, intensity adjusted based on tolerance of subjects), electrodes similar to Rong et al. (2014)	Sham: same waveform, diff location (superior scapha)
Cakmak et al. (2017) Parkinson's	Motor examination (part III of the unified Parkinson's disease rating scale)	130 Hz, 100 μs PW, continuous, biphasic Ipsilateral ear to dominant motor symptoms in tragicus, antitragicus, and helicis minor muscles	Strong sensory (100–130 μA), percutaneous electrodes	Placebo: no current, 2 percutaneous electrodes in upper helix
Maharjan et al. (2018) Olfactory function	Odor threshold test and supra-threshold test	80 or 10 Hz, 180 μs PW, on/off cycle NR Left internal (concha) and external ear	Pain threshold (0.1–10 mA), electrode NR	Sham: same waveform, diff location (left earlobe)
Tutar et al. (2020) Tinnitus	Tinnitus handicap inventory and depression anxiety stress scales	200 Hz, 1 ms PW, on/off cycle NR Unilateral and bilateral cymba concha	First sensory (10–30 mA), silver electrodes (Provile TENS stimulator) (monopolar)	Placebo: same location

Risk of Bias score indicated by box color: red for "high," orange for "some concerns," and green for "low" risk of bias.
Monophasic if phase not otherwise specified.
Bipolar if electrode polarity not otherwise specified. Configuration considered monopolar only if the return electrode is distant enough not to activate the target region.
BP, Blood pressure; CRP, c-reactive protein; diff, different; ECG, electrocardiogram; GI, gastrointestinal; HR, heart rate; HRV, heart rate variability; IL, interleukin; LV, left ventricular; LF/HF, low frequency/high frequency (LF/HF); NR, not reported; PPG, photoplethysmogram; PW, pulse width; Cbrs, spontaneous cardiac baroreflex sensitivity; TENS, transcutaneous electrical nerve stimulation; TNF-a, tumor necrosis factor alpha. A full list of abbreviations is found in ***Supplementary Material 3****.*

used across studies. In the active arm, the interquartile range (IQR) of stimulation current amplitudes was 0.2–5 mA, pulse width was 200–500 μs, and frequency of stimulation was 10–26 Hz. It is notable that the commonly used aVNS waveform parameters are similar to the parameters typically used for stimulation of the cervical vagus at a pulse width of 250 μs and frequency of 20 Hz (LivaNova, 2017), which uses surgically implanted epineural cuff electrodes. Outside of the IQR, the spread of the parameters is wide.

The large variation in waveform parameters is indicative of the exploratory nature of aVNS studies and underscores the difficulties in comparisons across studies where similar indications use widely different parameters. The variations in pulse width and stimulation frequency are due to the range of values chosen by investigators. The variations in stimulation amplitude are more nuanced and discussed next.

While the large variation in pulse width and frequency parameters can be explained as choices made by investigators, the sources of the large variation in stimulation current amplitude is not as trivial. It is important to consider differences in electrode design, material, area, and stimulation polarity when comparing stimulation current amplitudes across studies. This is because electrode geometry and contact area have the potential to impact target engagement of underlying nerves (Poulsen et al., 2020). Furthermore, nerve activation is a function of current density at the stimulating electrode (Rattay, 1999), and it is not possible to accurately estimate current density without knowing electrode geometry. Another source of variability arises from the fact that different studies used different titration methods to determine stimulation current amplitude. In the studies reviewed, current amplitude was often calibrated to different levels of paresthesia perception. The level of paresthesia subjects feel is related to current density, which is once again related to stimulation current through electrode geometry.

In order to determine an optimal stimulation paradigm, target engagement must be thoroughly quantified with respect to the aforementioned variables. Direct measures of target engagement of the nerve branches exiting the auricle will further our understanding of optimal stimulation parameters (see section Long Term Solutions—Target Engagement on directly measuring local neural target engagement).

aVNS Trial Designs Across Studies

The way in which studies were designed also varied greatly. Of the 41 RCTs reviewed, 20 used a crossover design while 21 opted for a parallel design. In terms of control group design, 19 studies used

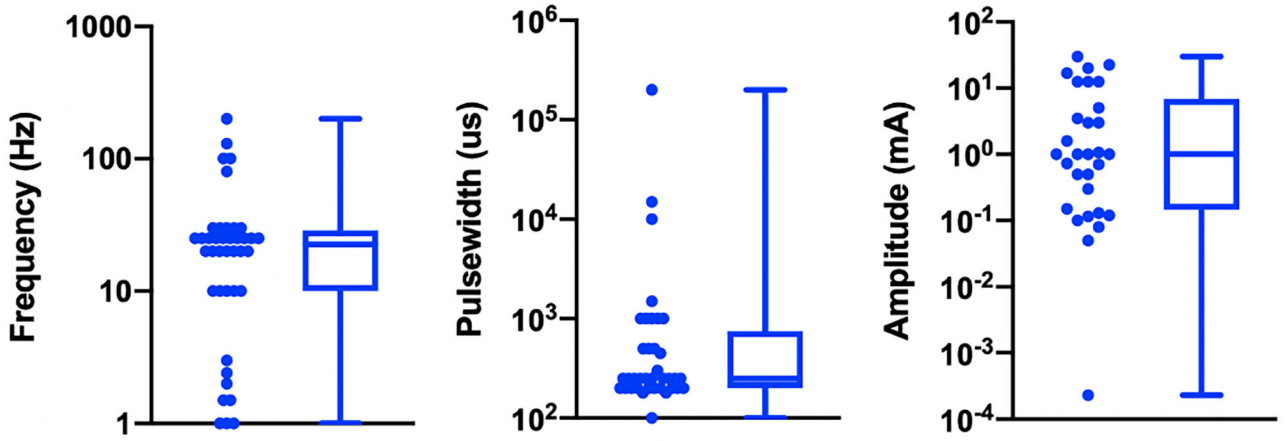

FIGURE 3 | Visualization of stimulation waveform parameters in 41 reviewed aVNS RCTs. Illustrated here are the interquartile ranges, maximums, minimums, and medians of the stimulation waveform parameters, including extreme cases. Median stimulation amplitude is 1.0 mA, pulse width is 250 us, and frequency is 22.5 Hz. Studies that report ranges for parameters are included as a single value representing the average of the boundaries of that range.

a sham, 17 a placebo, 2 used both sham and placebo, and 3 had no intervention as control. Studies also varied in duration: 12 were chronic and 29 were acute. The differences between these study design methods are important to emphasize and explored in section Long Term Solutions—Improvement in Control Design and Blinding.

Table 2 summarizes study designs and is organized by indication type, then primary endpoints, then RoB score. Data is organized in the following columns:

Primary Endpoints

The main result of clinical interest. Studies are grouped by endpoints measured within their respective indications. For example, within the cardiac diseases indication the studies investigating inflammatory cytokine levels are located adjacent to each other.

Subjects Analyzed

Sample size and whether subjects were healthy or diseased.

Control

Following Duarte et al. (2020b), we defined sham as when the control group experience from the subject perspective is identical to the active group experience—including paresthesia and device operating behavior. Conversely, placebo control is defined when the control group subjects do not experience the same paresthesia, device operation, or clinician interaction as the active group subjects.

Design

Study type (parallel or crossover), study time scale (acute or chronic), and intervention duration. Studies were classified as parallel if they randomized participants to intervention arms and each subject was assigned to only one intervention arm. Studies were classified as crossover if each subject group received every treatment but in a different order from the other subject groups (Nair, 2019). In some instances, the initial experimental group remained on the same intervention for the course of the study, while the control group was switched to the experimental intervention. These studies were classified as parallel, since not every subject received both interventions. Studies were classified as acute or chronic based on their duration being shorter or longer than 30 days, respectively.

Risk of Bias Tool to Assess Quality of Evidence

The Cochrane 2.0 Risk of Bias (RoB) assessment subscores for each study are summarized in **Table 3**. Explanations for each RoB subscore assignment [L = low (green), S = some concerns (orange), and H = high (red)] can be found generally explained in section Cochrane Risk of Bias 2.0 Tool to Assess Quality of Evidence and specifically explained for each study reviewed in **Supplementary Material 9**. The RoB tool provides a suggested algorithm to determine overall score based on the subscores of all sections. In several instances, the suggested algorithm was overridden by the reviewer with justification annotated on the individual rubric found in **Supplementary Material 9**.

Only two studies (Bauer et al., 2016; Maharjan et al., 2018) were assigned an overall "low" risk of bias. This is unsurprising, as the risk of bias assessment is rigorous and aVNS studies are in the less rigorous exploratory stages of investigation. Subsection and overall score percentages are illustrated in **Figure 4**.

The subsection "randomization process" was one of the best-scoring sections, in part because we assumed randomization was concealed from study investigators and subjects, even if the methodology to do so was not explicit. The studies that scored poorly in this section did not check for baseline imbalances between randomized groups or had baseline imbalances suggesting possible issues with the randomization method.

Notably, the "deviations from intended interventions" subsection tended to have the highest risk of bias. This

TABLE 2 | Study designs (sorted by indication type, primary endpoints, and color coded RoB score).

Author (y) indication*	Primary endpoints	Subjects analyzed, disease	Control	Design
Cardiac				
Andreas et al. (2019) Postoperative atrial fibrillation	Postoperative atrial fibrillation assessed on ECG	40, patients undergoing cardiac surgery	Sham	Parallel, acute (1 h)
Stavrakis et al. (2015) Atrial fibrillation	Atrial fibrillation cycle length and duration, TNF-a, CRP	40, paroxysmal atrial fibrillation ablation patients	Placebo	Parallel, acute (1 h)
Stavrakis et al. (2020) Atrial Fibrillation	Atrial fibrillation burden assessed on ECG	53, paroxysmal atrial fibrillation patients	Sham	Parallel, chronic (6 months)
Badran et al. (2018) Heart rate	ΔHR during stimulation.	35, healthy	Sham	Crossover, acute (duration NR)
Manasiev et al. (2015) Coronary insufficiency and LV dysfunction	Heart rate and 6 mins walk distance.	70, coronary insufficiency/LV dysfunction patients	Placebo	Parallel, acute (~1 h)
Tobaldini et al. (2013) Orthostatic stress	ΔHR, LF/HF, systolic arterial BP variance, RR interval pattern, respiratory rate	13, healthy	Placebo	Crossover, acute (~30 min)
Fisher et al. (2018) Hypertension	Percentage decrease in median systolic blood pressure (SBP)	10, hypertensive	Placebo	Crossover, acute (duration NR)
Stowell et al. (2019) Hypertension	Arterial blood pressure	12, diagnosed with primary hypertension	Placebo	Crossover, acute (5 days)
Zamotrinsky et al. (2001) Coronary artery disease	HR, BP, LV diastolic function, LV filling	18, stable angina pectoris class IV	No intervention	Parallel, acute (~10 days)
Antonino et al. (2017) Baroreflex sensitivity	cBRS from systolic blood pressure and RR interval HRV (LF/HF)	13, healthy	Both placebo and sham	Crossover, acute (duration NR)
Bretherton et al. (2019) HRV and baroreflex sensitivity	cBRS and HRV	14, healthy	Placebo	Crossover, acute (1 week)
Clancy et al. (2014) HRV and sympathetic activity	HRV (LF/HF)	48, healthy	Placebo	Parallel, acute (~15 min)
De Couck et al. (2017) HRV	ECG with HRV	30, healthy	Placebo	Crossover, acute (duration NR)
Borges et al. (2013) Cardiac vagal activity	HRV	60, healthy	Sham	Crossover, acute (duration NR)
Tran et al. (2019) LV strain and autonomic tone	LV global longitudinal strain	24, diagnosed with diastolic dysfunction by echocardiogram	Sham	Crossover, acute (duration NR)
Yu et al. (2017) Myocardial ischemia-reperfusion injury	Ventricular premature beat incidence	95, myocardial ischemia-reperfusion injury patients	Placebo	Parallel, acute (~2.5 h)
Epilepsy				
Bauer et al. (2016) Epilepsy	Reduction in seizure frequency (per 28 days)	58, epileptic	Sham	Parallel, chronic (20 weeks)
Aihua et al. (2014) Epilepsy	Reduction in seizure frequency (per month)	47, epileptic	Sham	Parallel, chronic (12 months)
Rong et al. (2014) Epilepsy	Seizure frequency (per 4 weeks)	144, epileptic	Sham	Parallel, chronic (24 weeks)
Pain				
Straube et al. (2015) Chronic migraine	Decrease in headache (per 28 days)	46, chronic migraine patients	Sham	Parallel, chronic (12 weeks)
Janner et al. (2018) Pain	Perceived pain intensity and temporal summation of pain	49, healthy	Both placebo and sham	Crossover, acute (8 days)
Kovacic et al. (2017) GI pain	Change in max abdominal pain intensity and composite of pain-frequency-severity-duration scale	104, children with GI pain	Sham	Parallel chronic (4 weeks)
Kutlu et al. (2020) Fibromyalgia	Visual analog sale, beck depression scale, beck anxiety scale, fibromyalgia impact questionnaire, short form-36 for life quality	52, fibromyalgia patients	No intervention	Parallel, chronic (4 weeks)
Busch et al. (2013) Pain	Thermal, mechanical, and pressure pain thresholds	48, healthy	Placebo	Crossover, acute (2 days)

(Continued)

TABLE 2 | Continued

Author (y) indication*	Primary endpoints	Subjects analyzed, disease	Control	Design
Juel et al. (2017) Pain and GI motility	ECG and PPG, mechanical pain threshold, cold pressor test, and drink test (ultrasound imaging)	20, chronic pancreatitis patients	Sham	Crossover, acute (7 days)
Frokjaer et al. (2016) Gastroduodenal motility and pain threshold	ECG and PPG, mechanical pain threshold, cold pressor test, and drink test (ultrasound imaging)	18, healthy	Sham	Crossover, acute (~6 days)
Napadow et al. (2012) Pain	Mechanical deep-tissue pain intensity rating, and temporal pain summation	15, chronic pelvic pain due to endometriosis patients	Sham	Crossover, acute (~1 week)
Johnson et al. (1991) Pain threshold and autonomic function	Electrical pain threshold and autonomic function	24, healthy	Sham	Parallel, acute (~15 min)
Laqua et al. (2014) Pain	Electrical pain threshold	21, healthy	Placebo	Crossover, acute (~1 week)
Psychological				
Hein et al. (2013) Depression	Hamilton Depression Rating Scale, Beck's Depression Inventory	37, majorly depressed	Placebo	Parallel, chronic (~2 weeks)
Hasan et al. (2015) Schizophrenia	Positive and negative schizophrenia symptom scale	17, schizophrenic	Placebo	Parallel, chronic (26 weeks)
Burger et al. (2019) Negative thought occurrence	Number of negative thought intrusions	97, high worriers	Sham	Parallel, acute (~20 min)
Others				
Addorisio et al. (2019) Rheumatoid arthritis	Endotoxin-induced interleukin (IL)-6, IL-1β, and TNF	19, healthy	Sham	Crossover, acute (duration NR)
Salama et al. (2020) Acute inflammatory response after lung lobectomy	CRP, IL6, IL10, IL-1B, IL-18, TNF-a	100, lobectomy via thoracotomy in patients with non-small cell lung cancer	No intervention	Parallel, acute (5 days)
Huang et al. (2014) Impaired glucose tolerance	2-hr plasma glucose levels	102, impaired glucose tolerance patients	Sham	Parallel, chronic (12 weeks)
Cakmak et al. (2017) Parkinson's	Motor symptoms	24, Parkinson's Hoehn and Yahr stage 2–3	Placebo	Crossover, acute (duration NR)
Maharjan et al. (2018) Olfactory function	Odor threshold test and supra-threshold test	18, healthy	Sham	Crossover, acute (7 days)
Tutar et al. (2020) Tinnitus	Tinnitus handicap inventory and depression anxiety stress scales	60, 20 per group, each with constant tinnitus >3-month duration	Placebo	Parallel, chronic (~1 month)

**Risk of Bias score indicated by box color: red for "high," orange for "some concerns," and green for "low" risk of bias.*
BP, Blood pressure; CRP, c-reactive protein; ECG, electrocardiogram; GI, gastrointestinal; HR, heart rate; HRV, heart rate variability; IL, interleukin; LV, left ventricular; LF/HF, low frequency/high frequency; NR, not reported; PPG, photoplethysmogram; cBRS, spontaneous cardiac baroreflex sensitivity; TNF-a, tumor necrosis factor alpha. A full list of abbreviations is found in ***Supplementary Material 3****.*

was mainly due to issues with potential subject unblinding as a result of easily perceptible differences between active and control groups. For example, in a crossover design, the subject experiences both the paresthesia-inducing active intervention and the non-paresthesia-inducing placebo control. The difference in paresthesia may unblind the subject to the identity of the active vs. control interventions.

The subsection "missing outcome data" was generally scored as "low" risk of bias across studies. Studies scoring "high" or "some concerns" had unreported outcome data with a non-trivial difference in the proportion of missing data between interventions.

The "measurement of the outcome" subsection also generally scored a "low" risk of bias across studies. In order to score "some concerns" or worse, outcome assessor blinding to subject intervention had to be compromised. For a "high" RoB score in this section, studies measured endpoints that could be influenced by investigator unblinding, such as investigator-assessed disease evaluation questionnaires. Empirical measurements such as heart rate and blood pressure were less susceptible to this kind of bias and hence scored better.

The subsection with the highest risk for bias ("high" or "some concerns" scores) was "selection of the reported results." This was primarily due to a lack of pre-registration in most studies. Suggestions to improve study reporting are listed in section Short Term Solutions—Guide to Reporting.

Summary of Outcome Measures Across Indications

The RoB analysis revealed potential for bias in the outcomes of the studies reviewed. Here, the studies are grouped by outcome measures—cardiac, inflammatory, epilepsy, and pain.

TABLE 3 | RoB overall and section scores (sorted by overall score).

Author (y)	Randomization process	Deviations from intended interventions	Missing outcome data	Measurement of the outcome	Selection of the reported result	Overall risk of bias
Bauer et al. (2016)	L	L	L	L	L	L
Maharjan et al. (2018)	L	L	L	L	L	L
Addorisio et al. (2019)	L	S	L	L	S	S
Aihua et al. (2014)	S	H	L	S	S	S
Andreas et al. (2019)	L	S	L	L	L	S
Antonino et al. (2017)	L	L	S	L	S	S
Badran et al. (2018)	L	L	L	L	S	S
Bretherton et al. (2019)	L	L	L	L	S	S
Burger et al. (2019)	L	L	L	L	S	S
Busch et al. (2013)	L	S	L	L	S	S
Cakmak et al. (2017)	L	H	L	L	L	S
Clancy et al. (2014)	L	S	L	L	S	S
De Couck et al. (2017)	L	L	L	L	S	S
Hein et al. (2013)	L	L	L	S	S	S
Huang et al. (2014)	S	L	L	L	S	S
Janner et al. (2018)	L	L	L	L	S	S
Juel et al. (2017)	L	S	L	L	S	S
Kovacic et al. (2017)	L	S	L	L	L	S
Rong et al. (2014)	L	S	L	L	S	S
Stavrakis et al. (2015)	L	S	L	L	S	S
Stavrakis et al. (2020)	L	L	L	L	S	S
Tran et al. (2019)	L	S	L	L	S	S
Tutar et al. (2020)	L	S	L	S	S	S
Afanasiev et al. (2016)	H	S	H	L	S	H
Borges et al. (2019)	L	S	L	L	S	H
Fisher et al. (2018)	S	H	H	S	H	H
Frøkjaer et al. (2016)	S	S	L	L	S	H
Hasan et al. (2015)	L	H	L	L	S	H
Johnson et al. (1991)	S	H	L	S	S	H
Kutlu et al. (2020)	S	H	L	L	L	H
Laqua et al. (2014)	L	S	L	L	H	H
Napadow et al. (2012)	S	H	S	L	H	H
Salama et al. (2020)	L	H	L	S	S	H
Stowell et al. (2019)	L	S	L	L	S	H
Straube et al. (2015)	L	H	L	L	L	H
Tobaldini et al. (2019)	S	H	L	L	S	H
Yu et al. (2017)	L	H	L	L	S	H
Zamotrinsky et al. (2001)	L	S	L	S	S	H

L, low risk of bias (green); S, some concerns (yellow), and H, high risk of bias (red).
The Cochrane tools' suggested algorithms to determine subsection and overall scores did not always take into account certain caveats in study design. In such instances, the suggested algorithm is overridden, and a justification is provided in the study specific RoB rubric in ***Supplementary Material 9****.*

The outcome measures of the studies—regardless of indication—are qualitatively synthesized and couched in the findings of the RoB assessment. Findings from the RoB assessment are used to point out instances where trial design or reporting may have influenced interpretation of the trial outcomes. For reviews comprehensively synthesizing pre-clinical and both non-randomized and randomized clinical studies by indication, without emphasis on RoB, see Yap et al. (2020) and Jiang et al. (2020).

Cardiac Related Effects of aVNS

The most common cardiac effects assessed were changes to heart rate (HR) and sympathovagal balance. To measure sympathovagal balance, heart rate variability (HRV) was used.

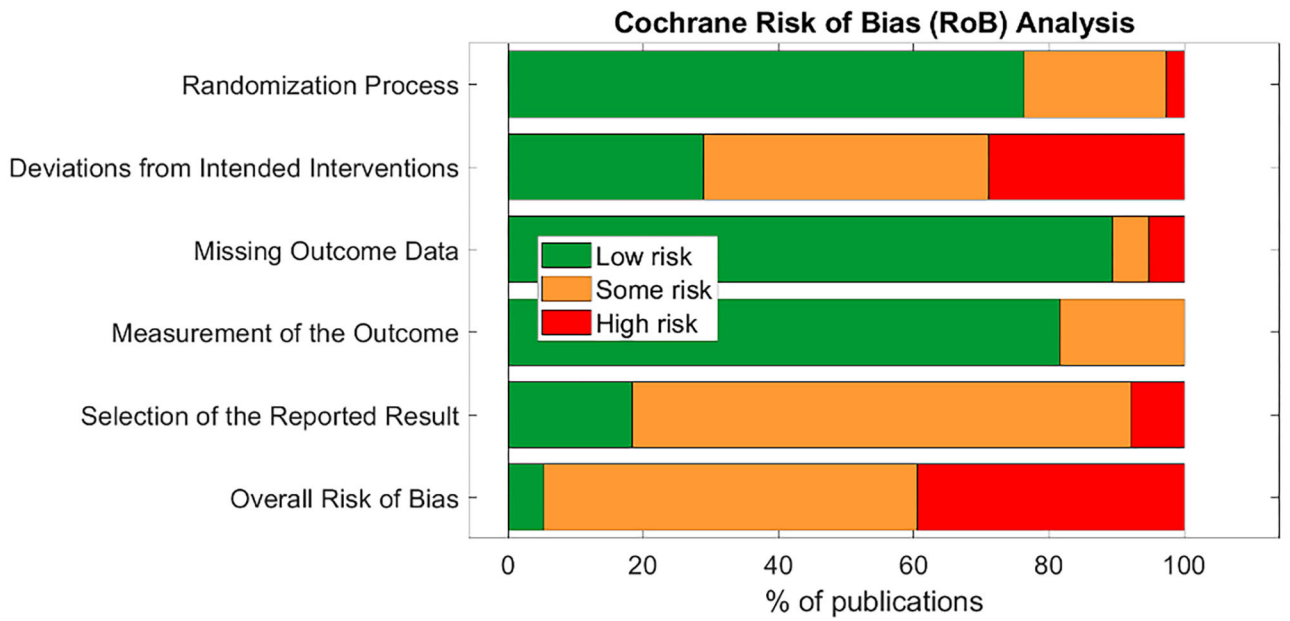

FIGURE 4 | Summary of Cochrane Risk of Bias overall and section scores for 38 publications reviewed.

Fifteen studies with cardiac, pain, or other indications reported HR or HRV measures and are summarized in **Table 4**. Results conflicted across studies for heart rate changes and sympathovagal balance but suggest aVNS may have an effect on both. However, there are concerns that these results may be attributed to trial design and inconsistent measurement methods.

Studies that reported a change in HR measured a modest mean drop of 2–3 beats per minute (BPM) in the active group. However, almost half of the 11 trials reporting HR effects reported no significant difference in effect between or within control and active stimulation. Stavrakis et al. (2015) and Yu et al. (2017) attained a consistent decrease in HR in every subject by increasing the stimulation amplitude until a decrease in HR was measured. They reported a mean stimulation threshold to elicit a HR decrease that was above the mean threshold for discomfort. In addition, Frøkjaer et al. (2016) and Juel et al. (2017) reported a significant decrease in HR during sham at the earlobe but not during active stimulation at the conchae and tragus. This observation suggests that decrease in HR may not be vagally mediated but perhaps mediated by trigeminal or cervical nerve branch afferents (see **Figure 1A**) or sympathetic efferents (Cakmak, 2019). See Cakmak (2019) for a comprehensive discussion on possible auricular stimulation pathways and mechanisms. Taken together, there is evidence for the effects of auricular stimulation on decreasing HR at high stimulation amplitudes, but it is uncertain if this decrease is mediated by the auricular branch of the vagus.

HRV, used as a measure of sympathovagal balance, was quantified inconsistently across studies and may not be an accurate indicator of whole body sympathovagal balance. Shown at the bottom of **Table 4** are multiple ways to analyze electrocardiogram (ECG) data for HRV. Different ways to quantify HRV enables multiple comparisons—which were often not appropriately corrected for—in search of statistical significance. HRV was calculated differently across studies making it difficult to uniformly draw conclusions across the aggregate of studies. Furthermore, HRV is not a measure of whole body sympathovagal tone, but of cardiac vagal activity—it relies on the physiological variance in HR with breathing. More variance in HR during breathing indicates more vagal control and a corresponding shift in cardiac sympathovagal balance to parasympathetic (Goldberger, 1999). Contradictory results on the parasympathetic effects of aVNS indicates that either the effects of aVNS on HRV are inconsistent, or that HRV is an unreliable measure of cardiac sympathovagal balance (Bootsma et al., 2003; Billman, 2013; Hayano and Yuda, 2019; Marmerstein et al., 2021), or both. Overall, the effects of aVNS on sympathovagal balance conflict between studies. Similarly, Wolf et al. (2021), in a meta-analysis pre-print, concluded that there was "no support for the hypothesis that HRV is a robust biomarker for acute [aVNS]."

Given that cardiac effects are closely related to a subject's comfort and stress levels, it is important to consider trial design influences such as subject familiarization. For example, a clinical trial visit could increase stress levels and blood pressure of the subjects (Wright et al., 2015) and mask any potential therapeutic effects of aVNS on blood pressure. Another example of subject familiarization is related to HRV. Borges et al. (2019) tried to accommodate for subject familiarization by delivering a 5 min "familiarization" stimulation at the cymba concha before the experimental intervention. Unfortunately, baseline HRV measurements were taken immediately after these

TABLE 4 | Summary of cardiac (heart rate and heart rate variability) studies.

Author (y) indication*	HR results	HRV results	Active stimulation level**	Active waveform	Subjects analyzed, disease
Antonino et al. (2017) Baroreflex sensitivity	Active: 2–3 BPM decrease Sham: not significant	Active: LF/HF parasympathetic Sham at earlobe: LF/HF parasympathetic Placebo: LF/HF sympathetic	First sensory	30 Hz, 200 μs PW	13, healthy
Badran et al. (2018) Heart rate	Active: ∼2.40 BPM decrease Sham: not significant	NA	2x sensory threshold	10 Hz, 500 μs PW	35, healthy
Bretherton et al. (2019) HRV and baroreflex sensitivity	NA	Active: LF/HF parasympathetic Placebo: not significant	Sensory threshold	30 Hz, 200 μs PW	14, healthy
Burger et al. (2019) Negative thought occurrence	NA	Active: not significant (RMSSD) Sham: not significant	Strong sensory	25 Hz, 250 μs PW	97, high worriers
Clancy et al. (2014) HRV and sympathetic activity	Active: HR decreased (data not reported) Placebo: not significant	Active: LF/HF parasympathetic Placebo: not significant	First sensory	30 Hz, 200 μs PW	48, healthy
De Couck et al. (2017) HRV	NA	Active: SDNN parasympathetic; no significant changes in LF/HF, LF, HF, RMSSD Placebo: SDNN parasympathetic; no significant changes in LF/HF, LF, HF, RMSSD	Strong sensory	25 Hz, 250 μs PW	30, healthy
Janner et al. (2018) Pain	No significant effects of aVNS on HR (data not reported)	NA	Strong sensory	100 Hz, 200 μs PW	49, healthy
Juel et al. (2017) Pain and GI motility	Active: not significant Sham: ∼2.8 BPM decrease, at earlobe	Active: RMSSD parasympathetic relative to sham, sympathetic relative to baseline Sham at earlobe: RMSSD sympathetic	Pain	30 Hz, 250 μs PW	20, chronic pancreatitis patients
Tran et al. (2019) LV strain and autonomic tone	No significant effects of aVNS on HR (data not reported)	Active: SDNN no change, RMSSD parasympathetic, pNN50 sympathetic, LF/HF parasympathetic Sham at earlobe: SDNN parasympathetic, RMSSD parasympathetic, pNN50 no change, LF/HF sympathetic	Strong sensory	20 Hz, 200 μs PW	24, diagnosed with diastolic dysfunction by ECG
Yu et al. (2017) Myocardial ischemia-reperfusion injury	HR decrease in every subject (values not reported)	NA	Sinus rate slowing threshold	20 Hz, 1 ms PW	95, myocardial ischemia-reperfusion injury patients
Borges et al. (2019) Cardiac vagal activity	NA	Active: RMSSD sympathetic between resting and second half stim Sham: not significant	Strong sensory	25 Hz, PW of 200– 300 μs	60, healthy
Frokjaer et al. (2016) Gastroduodenal motility and pain threshold	Active: not significant Sham: ∼2.2 BPM decrease, at earlobe	Active: RMSSD parasympathetic at 20 min and sympathetic at 25 min Sham at earlobe: RMSSD sympathetic at 20 min and parasympathetic at 25 min	Strong sensory	30 Hz, 250 μs PW	18, healthy
Johnson et al. (1991) Pain threshold and autonomic function	No significant effects of aVNS on HR (data not reported)	NA	Strong sensory	100 Hz pulses every 2.4 Hz, 10 ms PW	24, healthy
Laqua et al. (2014) Pain	No significant effects of aVNS on HR (data not reported)	NA	Strong sensory	Alternating between 2 and 10 Hz, 200 μs PW	21, healthy
Napadow et al. (2012) Pain	No significant effects of aVNS on HR (data not reported)	NA	Strong sensory	30 Hz, 450 μs PW	15, chronic pelvic pain patients

(Continued)

TABLE 4 | Continued

Author (y) indication*	HR results	HRV results	Active stimulation level**	Active waveform	Subjects analyzed, disease
HRV Measurements					
LF/HF	Ratio of low frequency over high frequency cardiac activity (frequency-domain measurement)				
RMSSD	Root mean square of successive differences between heartbeats (time-domain measurement)				
pNN50	The proportion of NN50 divided by the total number of NN (RR) intervals. NN50 is the number of times successive heartbeat intervals exceed 50ms (time-domain measurement)				
SDNN	Standard deviation of the NN (RR) intervals (time-domain measurement)				

*Risk of Bias score indicated by box color: red for "high," orange for "some concerns," and green for "low" risk of bias.
Refer to text above **Table 1 for definitions of all active stimulation levels (First sensory titration: Subject is barely able to feel a cutaneous sensation. Strong sensory titration: Subject feels a strong, but not painful or uncomfortable sensation from the stimulation. Pain titration: Stimulation amplitude is increased until the subject feels a painful or uncomfortable sensation). BP, Blood pressure; BPM, beats per minute; ECG, electrocardiogram; GI, gastrointestinal; HR, heart rate; HRV, heart rate variability; LV, left ventricular; NR, not reported; PPG, photoplethysmogram; PW, pulse width; cBRS, spontaneous cardiac baroreflex sensitivity. A full list of abbreviations is found in **Supplementary Material 3**.

"familiarization" stimulation sessions and could be affected by the stimulation delivered. Hence, there is no true baseline measurement—before any stimulation is applied—of HRV and casts doubt on the findings of the study, which claimed no significant effects of aVNS on HRV. In summary, conflicting results on the cardiac effects of aVNS could be attributed to trial design and measurement methods.

Inflammatory Related Effects of aVNS

Seven studies with cardiac or anti-inflammatory indications measured cytokine levels and are summarized in **Table 5**. Cytokine levels were either measured directly in drawn blood (circulating) or after an *in vitro* endotoxin-induced challenge on drawn blood. In the four studies that measured circulating cytokine levels, results are somewhat conflicting. Stavrakis et al. (2020) reported a significant decrease in tumor necrosis factor alpha (TNF-α) and no significant changes in IL-6, IL-1β, IL-10, and IL-17, consistent with subjects with moderate atrial fibrillation burden and not suffering from any inflammatory condition. TNF-α is one of the most abundant mediators in inflamed tissue and is present in the acute inflammatory response (Parameswaran and Patial, 2010). In subjects being treated for myocardial infarction, Yu et al. (2017) reported that the active group was significantly lower than the control group for all measured cytokine levels [TNF-α, IL-6, IL-1β, and high-mobility group-box 1 protein (HMGB1)]. Unlike Stavrakis et al. (2020) and Yu et al. (2017), Salama et al. (2020) reported no statistically significant change in TNF-α, along with lower levels of c-reactive protein (CRP) and IL-6, compared to control. CRP is also an acute phase protein whose release from the liver is stimulated by increased levels of IL-6 (Del Giudice and Gangestad, 2018). Lastly, Afanasiev et al. (2016) measured HSP60 and HSP70, which are heat shock proteins and responsible for preventing damage to proteins in response to stressors such as high temperature (Morimoto, 1993). Both HSP60 and HSP70 increased significantly in Afanasiev et al. (2016), indicating a potential anti-inflammatory effect.

The limited applicability of *in vitro* endotoxin-induced assays was discussed in Stoddard et al. (2010), Yang et al. (2011), and Thurm and Halsey (2005). Additionally, Broekman et al. (2015) provided an example where an *in vitro* assay was unsuccessful in identifying disease severity in patients with a quiescent autoimmune disorder. Nonetheless, we summarize the findings on anti-inflammatory effects of aVNS on *in vitro* endotoxin-induced assays. In Stavrakis et al. (2015), acute stimulation was delivered intraoperatively to subjects undergoing ablation treatment for atrial fibrillation. After 1 h of stimulation, there was a significant decrease in TNF-α and CRP levels in femoral vein draws. In Addorisio et al. (2019), vibrotactile stimulation was applied for only 2 min and showed a statistically significant decrease in endotoxin-induced cytokine levels of TNF-α, IL-6, and IL-1βin blood drawn 1 h after stimulation.

Overall, these studies provide evidence that aVNS may reduce circulating levels and endotoxin-induced levels of inflammatory markers and suggest a potential anti-inflammatory effect of aVNS. The clinical relevance of endotoxin-induced measures needs to be further explored and the implications of lowered circulating cytokine levels on disease burden needs to be further investigated in RCTs.

Epilepsy Related Effects of aVNS

The three studies that investigated the antiepileptic effects of aVNS were all chronic studies and are summarized in **Table 6**. All used stimulation frequencies between 20 and 30 Hz similar to implantable VNS (LivaNova, 2017). However, other stimulation parameters varied widely. All studies reported a 20–40% decrease in seizure frequency from baseline and showed significance from baseline after a few weeks to months of daily prescribed stimulation.

Based on these three chronic studies, there is some evidence to support the anti-epileptic effects of aVNS. The primary outcomes of these non-invasive interventions are comparable to that of implantable VNS in studies of similar duration and sample size (Ben-Menachem et al., 1994; Handforth et al., 1998). However, due to concerns over unblinding and weaker evidence in between group analysis compared to within group analysis, it is possible that the effects may be attributed to placebo. The concern that this effect is placebo is exacerbated by the fact that the

TABLE 5 | Summary of inflammatory studies.

Author (y) indication*	aVNS group cytokine level results (compared to control)	Measurement method	Subjects analyzed, disease
Addorisio et al. (2019) Rheumatoid arthritis	TNF-α decrease ($p < 0.05$)	Endotoxin-induced	19, healthy
	IL-6 decrease ($p < 0.001$)		
	IL-1β decrease ($p < 0.01$)		
Andreas et al. (2019) Postoperative atrial fibrillation	IL-6 not significant	Endotoxin-induced	40, patients undergoing cardiac surgery
	CRP not significant		
Stavrakis et al. (2015) Atrial fibrillation	TNF-α decrease ($p < 0.05$)	Endotoxin-induced	40, paroxysmal atrial fibrillation ablation patients
	IL-6 not significant		
	IL-10 not significant		
	CRP decrease ($p < 0.05$)		
Stavrakis et al. (2020) Atrial fibrillation	TNF-α decrease ($p = 0.0093$)	Circulating	53, paroxysmal atrial fibrillation patients
	IL-6 not significant		
	IL-1β not significant		
	IL-17 not significant		
Yu et al. (2017) Myocardial ischemia-reperfusion injury	TNF-α lower increase than control ($p < 0.05$)	Circulating	95, myocardial ischemia-reperfusion injury patients
	IL-6 lower increase than control ($p < 0.05$)		
	IL-1β lower increase than control ($p < 0.05$)		
	HMGB1 lower increase than control ($p < 0.05$)		
Manasiev et al. (2016) Coronary insufficiency and LV dysfunction	Active group 1a HSP60 increase ($p < 0.05$); HSP70 increase ($p < 0.05$)	Circulating	70, coronary insufficiency/LV dysfunction patients
	Active group 2 HSP60 not significant; HSP70 increase ($p < 0.05$)		
Salama et al. (2020) Acute inflammatory response after lung lobectomy	TNF-α not significant	Circulating	100, lobectomy via thoracotomy in patients with non-small cell lung cancer
	IL-6 lower increase than control ($p = 0.02$)		
	IL-10 not significant		
	IL-1β not significant		
	IL-18 not significant		
	CRP lower increase than control ($p = 0.01$)		

**Risk of Bias score indicated by box color: red for "high," orange for "some concerns," and green for "low" risk of bias.*
CRP, C-reactive protein; IL, interleukin; LV, left ventricular; TNF-a, tumor necrosis factor alpha. A full list of abbreviations is found in ***Supplementary Material 3****.*

studies used widely varying stimulation parameters yet achieved similar results.

Pain Related Effects of aVNS

Ten studies investigated the effects of aVNS on the amelioration of pain and are summarized in **Table 7**. Five studies investigated the effects of aVNS on evoked pain threshold levels in healthy subjects but used varying pain-assessment methods. One study investigated the effects of aVNS on evoked pain threshold levels in chronic pancreatitis patients (Juel et al., 2017). The other four studies examined the effects of aVNS on self-reported pain scores in patients already suffering from pain due to endometriosis (Napadow et al., 2012), chronic migraine (Straube et al., 2015), fibromyalgia (Kutlu et al., 2020), and gastrointestinal (GI) disorders (Kovacic et al., 2017).

Across studies, the observed effects of aVNS for pain are highly varied. In studies that investigated evoked pain thresholds, results showed negligible changes in pain threshold levels due to aVNS therapy. For chronic migraines, Straube et al. (2015) reported a therapeutic effect in both the 1 and 25 Hz stimulation groups. Unexpectedly, the 1 Hz stimulation, originally designated as sham in the trial design, resulted in a reduction of headaches—comparable to medications used in migraine prevention—while the 25 Hz treatment had a smaller effect on the reduction of headaches (−7.0 episodes with 1 Hz vs. −3.3 episodes with 25 Hz over 28 days). Studies to isolate stimulation parameters that are therapeutic for pain are needed given that the 1 Hz stimulation, generally considered a sham due to its low frequency, was more effective than the 25 Hz intervention group. For gastrointestinal-related pain and chronic pelvic pain, pain was also significantly ameliorated by aVNS therapy. Overall,

TABLE 6 | Summary of epilepsy studies.

Author (y) indication*	Results	Active waveform	Study duration	Subjects analyzed, disease
Auricular VNS				
Bauer et al. (2016) Epilepsy	**Between group (not significant):** 2.9% ± 94.4 increase in 1 Hz sham group seizure frequency per 28 days and 23.4% ± 47.2 decrease in 25 Hz active group ($p = 0.146$)	25 Hz, 250 μs PW	20 weeks	58, epileptic
Aihua et al. (2014) Epilepsy	**Between group (S)**: not significant until 12 months; active median seizure frequency per month 4.0 (IQR 2.8–8.3) vs. sham median 8.0 (IQR 4.5–12.0) ($p < 0.001$)	20 Hz, 200 ms PW	12 months	47, epileptic
	Within group (S): Active seizure frequency per month reduced by 40% over 12 months; active baseline 6.0 (IQR I4.8–25.0) to 5.5 (IQR 3.0–12.0) at 6 months ($p < 0.001$) and 4.0 (IQR 2.8–8.3) at 12 months ($p < 0.001$)			
Rong et al. (2014) Epilepsy	**Between group (S)**: After 8 weeks, seizure frequency per 4 weeks decreased from 84.6 ± 145.5 to 48.6 ± 118.8 in active and 66.43 ± 85.5 to 58.8 ± 88 in sham ($p < 0.05$)	20–30 Hz, ≤1 ms PW	24 weeks	144, epileptic
Cervical implanted VNS				
Author (y)	**Results**			**Study Duration**
Ben-Menachem et al. (1994)	30.9% active seizure frequency decrease per 12 weeks, 11.3% sham decrease ($p = 0.036$ between, $p < 0.001$ active within, $p = 0.072$ sham within)			14 weeks
Handforth et al. (1998)	28% active seizure frequency decrease over 3 months, 15% sham decrease ($p = 0.04$ between, p <0.0001 active within, $p < 0.0001$ sham within)			3 months

**Risk of Bias score indicated by box color: red for "high," orange for "some concerns," and green for "low" risk of bias.*
IQR, Interquartile range; PW, pulse wdith. A full list of abbreviations is found in ***Supplementary Material 3****.*

these studies provide evidence that aVNS may be therapeutic for some pain conditions, but more studies are needed to further explore the effectiveness for specific medical conditions and rule out significant contributions from placebo effects.

Other Effects of aVNS

Other potential effects of aVNS investigated clinically included severity of motor symptoms in Parkinson's disease, depression, schizophrenia, obesity, impaired glucose tolerance, gastroduodenal motility, and tinnitus. Most of these effects were only investigated in a single RCT and there is not sufficient evidence to synthesize and evaluate across trials. The results of these individual studies are summarized in **Supplementary Material 3**. More studies are needed to further explore the effects of aVNS for these indications.

DISCUSSION

This is the first systematic review applying the Cochrane Risk of Bias (RoB) framework to auricular vagus nerve stimulation (aVNS) clinical trials. Our systematic review of 38 publications, totaling 41 RCTs, shows high heterogeneity in trial design and outcomes—even for the same indication. In the extreme, outcomes for heart rate effects of aVNS ranged from a consistent decrease in every subject in two studies to no heart rate effects in other studies. Findings on heart rate variability (HRV) conflict between studies and were hindered by trial designs including inappropriate washout periods and multiple methods used to quantify HRV. Early-stage evidence suggests aVNS reduces circulating levels and endotoxin-induced levels of inflammatory markers. Studies on epilepsy reached primary endpoints similar to previous RCTs on implantable VNS, albeit with concerns over quality of blinding. Clinical studies that tested aVNS for pain showed preliminary evidence of ameliorating pathological pain but not induced pain. Across the board, there are concerns on the extent of the contributions by placebo effects—especially since novel medical devices, such as aVNS devices, which also produce abnormal sensations (i.e., paresthesia), have a known larger placebo effect (Doherty and Dieppe, 2009).

The highest level of clinical evidence is multiple homogenous high quality RCTs as outlined in the Oxford CEBM Levels of Clinical Evidence Scale. The outcomes of these trials must consistently support the efficacy and safety of the therapy for a specific clinical indication. In the reviewed trials, several root causes—design of control, unblinding, and inconsistent reporting of results—raise the level of concern for bias in the outcomes. The current quality of evidence for aVNS RCTs supporting a particular clinical indication may generally be placed at grade 2, for "low quality" RCT, on the Oxford CEBM scale (Centre for Evidence-Based Medicine, 2009). An RCT is considered "low quality" for reasons including imprecise estimates, variability in results, indirect evidence, and presence of publication bias. For aVNS to reach the highest quality of clinical evidence for a particular indication, multiple RCTs must homogeneously support the safety and efficacy of the therapy for that indication.

In the following sections, we discuss gaps and improvements informed by our systematic review to aid the development of aVNS therapies. In the short term, we suggest improvements in the reporting of clinical trial results to allow meta-analysis of

TABLE 7 | Summary of pain studies.

Author (y) indication*	Results (compared to control)	Duration of study	Subjects analyzed, disease
Busch et al. (2013) Pain	**Not significant: fourteen** parameters were measured on both ipsilateral and contralateral. The pilot study did not correct for multiple comparisons. Mechanical and tonic heat pain parameters were marked for statistical significance and planned to be investigated further.	2 sessions (48 hrs apart)	48, healthy
Janner et al. (2018) Pain	**Not significant:** perceived pain intensity and temporal summation of pain not significant between active, placebo, and sham.	4 sessions (48 h apart)	49, healthy
Juel et al. (2017) Pain and GI motility	**Not significant:** no significance in evoked pain threshold between active and sham.	2 sessions (1 week apart)	20, chronic pancreatitis patients
Kovacic et al. (2017) GI pain	**Significant:** sham had significantly higher intensity pain at end of 3 weeks (median 7.0, IQR 5.0–9.0) compared to active (5.0, 4.0–7.0; $p = 0.003$). The composite score of the Pain-Frequency-Severity-Duration (PFSD) was significantly lower in the active group (8.4, IQR 3.2–16·2) than those in the sham group (15.2, 4.4–36.8) $p = 0.003$.	4 weeks	104, children with GI pain
Frokjaer et al. (2016) Gastroduodenal motility and pain threshold	**Not significant:** compared to sham, evoked pain threshold on bone increased ($p = 0.001$). Muscle evoked pain thresholds were significantly different at baseline ($p = 0.013$).	2 sessions (~6 days apart)	18, healthy
Johnson et al. (1991) Pain threshold and autonomic function	**Not significant:** no significance in evoked pain threshold or autonomic measures between any of the 3 active groups and control.	1 session	24, healthy
Kutlu et al. (2020) Fibromyalgia	**Not significant:** little improvement in pain visual analog scale ($p = 0.084$), physical role difficulty ($p = 0.496$), or emotional role difficulty ($p = 0.194$) between control (exercise) and active group (aVNS and exercise).	4 weeks	52, fibromyalgia patients
Laqua et al. (2014) Pain	**Not significant:** no significant evoked pain threshold difference between aVNS and placebo.	2 sessions (1 week apart)	21, healthy
Napadow et al. (2012) Pain	**Significant:** reduction in deep pain intensity rating ($p = 0.049$). Reduction in temporal summation ($p = 0.04$).	2 sessions (1 week apart)	15, chronic Pelvic Pain due to endometriosis patients
Straube et al. (2015) Chronic migraine	**Significant:** headache occurrence −7.0 per 28 days in 1 Hz group (36.4% reduction) and −3.3 in 25 Hz group (17.4% reduction) ($p = 0.035$).	12 weeks	46, chronic migraine patients

**Risk of Bias score indicated by box color: red for "high," orange for "some concerns," and green for "low" risk of bias.*
GI, Gastrointestinal; IQR, interquartile range. A full list of abbreviations is found in ***Supplementary Material 3****.*

results across aVNS studies. In the long term, we highlight the need for direct measures of target engagement as biomarkers to study therapeutic effects and therapy limiting side effects, and better translate learnings from animal models to humans. Also in the long term, we discuss the needs and associated challenges in careful design of controls and maintenance of blinding.

Short Term Solutions—Guide to Reporting

Several steps can be implemented immediately to increase the quality and consistency of reporting in aVNS studies, enabling comparison of results across studies.

Across the studies, the greatest risk of bias came from the Cochrane section "selection of reported results." A comprehensive guide to clinical trial reporting is found published by the CONSORT group along with detailed elaborations (Moher et al., 2010). See Kovacic et al. (2017) for an aVNS study that followed the CONSORT reporting recommendations. Pre-registration of trials, use of appropriate statistical analysis, justifying clinical relevance of outcome measures, and contextualizing clinical significance of results are discussed here. These ideas are summarized in **Table 8**. If followed across aVNS studies, these suggestions would reduce the risk of bias identified in the RoB section reporting of results and enable the synthesis of knowledge by making reporting more comparable across studies (Farmer et al., 2020).

Pre-registration

Pre-registration of planned enrollment, interventions, outcome measures and time points, and statistical plan to reach primary and secondary endpoints reduces risk of bias in the reporting of results. When the trial is reported, commentary should be made on adherence and deviations from the pre-registration with appropriate justifications. Exploratory analysis of the data may still be performed but needs to be denoted. Exploratory analysis can be used to suggest design of future investigations. The amount of exploratory analysis should be limited, and all non-significant exploratory analysis performed before reaching the significant results should also be reported. Of the 41 aVNS RCTs reviewed, 13 RCTs pre-registered, but only 5 had sufficient information to be considered a complete pre-registration. Pre-registration reduces risk of bias in reporting of results by preventing analysis of only select measures (section 5.1 of RoB rubric) and multiple analysis of data (section 5.2 of RoB rubric).

Appropriate Statistical Analysis

Data may be analyzed in many ways to claim the effect of an intervention. For example, studies may report a between group analysis comparing the change in the active arm to the change in the control arm or a within group analysis comparing the active arm after treatment to baseline. The more

TABLE 8 | Checklist for trial reporting.

	Item
✓	Pre-register
✓	Use appropriate statistical analysis
✓	Justify choice of between versus within group analysis
✓	Perform baseline comparison (even in crossover studies)
✓	Perform statistical test for carryover effects
✓	Report individual results
✓	Justify clinical relevance of outcome measures
✓	Discuss clinical significance of results
✓	Compare outcome to existing therapy
✓	Consider subject population when generalizing findings

appropriate method for a controlled study is a between group comparison of the active arm vs. the control arm. Several studies claimed statistically significant findings based just on the within group analysis even if the between group analysis was non-significant. An example illustrating this difference is found in **Supplementary Material 6**. Pre-registration of the planned statistical analysis will discourage unjustified multiple analysis of the data.

In crossover design studies, there was a major gap in the reporting of baseline comparison between randomized groups. Even in a crossover design where each subject receives all interventions, it is crucial to compare baseline differences between groups as one would do for a parallel study. This is especially pertinent in pilot studies with small sample sizes, where a baseline imbalance between groups is more likely to occur and affect the trial outcome (Kang et al., 2008). Additionally, if the order of intervention becomes pertinent, due to an incomplete washout period or compromised blinding, then it is essential that the baseline randomization between groups is balanced to enable further analysis.

Another concerning gap in crossover design studies was in the lack of reporting the statistical test for carryover effects. The test detects if the order of intervention received had an effect on the outcome (Shen and Lu, 2006). The test for carryover effects shows significance when there are incomplete washout effects, baseline imbalances, or compromise in blinding. It is perhaps the single most important gauge of the quality of a crossover design and should always be performed and reported—only 4 of 20 crossover design studies reported the carryover effects test. A baseline comparison between groups will ensure that baseline differences do not contribute to significance in the test for crossover effects—allowing effects from incomplete washout periods and compromised blinding to be isolated.

Reporting of individual results is a simple and effective way to convey the average and variance in outcomes, the fraction of responders, and worsening of symptoms (if any) in the non-responders. In Stavrakis et al. (2020) there is worsening of symptoms in the non-responders (53% of the active group) at the 3-month evaluation, which is also the only time point at which atrial fibrillation burden is measured concurrently during stimulation. This clinically relevant finding was evident during review because individual results were presented. Individual results were only presented in 10 of 41 aVNS studies reviewed. Reporting of individual results should be considered where allowed by clinical trial protocol.

Justify Clinical Relevance of Outcome Measures

The outcome measure itself may not be established as clinically relevant. For example, *in vitro* endotoxin-induced cytokine measurements were used to proxy *in vivo* immune response in several aVNS studies including Addorisio et al. (2019). While endotoxin-induced cytokine levels produce a stronger signal, they may not be clinically relevant in the case of an auto-immune disease such as Rheumatoid Arthritis tested in Addorisio et al. (2019).

The clinical accuracy of the measurement tool must also be considered. For example, aVNS studies often used photoplethysmography (PPG) based methods at the finger to measure blood pressure. Given the change in blood pressure signal during aVNS is already small, it is unnecessary to lose statistical power by using less accurate PPG based methods (Elgendi et al., 2019) to measure blood pressure. Clancy et al. (2014) used both a finger-based PPG, Finometer®, and a traditional arm sphygmomanometer to measure blood pressure and concluded that the increase in blood pressure measured using the Finometer® may be due to an artifact of the PPG measurement method. Discussion on clinical relevance of the outcome measure provides justification for the selection of reported results.

Contextualize Clinical Significance of Results

An outcome that is statistically significant does not necessarily indicate clinical significance. Contextualizing the trial results allows the reader to better understand the clinical significance of the findings. This may be done by comparing the study outcome to the outcome of the standard of care or another therapy. For example, Cakmak et al. (2017), in an aVNS trial for Parkinson's disease, showed a 5.3 points improvement on the UPDRS part 3 for motor symptoms (Goetz et al., 2008). Their result could be contextualized with the 18.4 points improvement in DBS (Kahn et al., 2019).

Clinical significance of results should be discussed in relevance to the subject population—particularly with consideration to disease severity and heterogeneity. For example, Juel et al. (2017) repeated a study in the diseased population after Frøkjaer et al. (2016) first reported a similar trial in healthy subjects. While the study in healthy subjects concluded significant findings, the subsequent study in diseased subjects did not. They cited pathological neural circuitry as a possible reason. Whether the difference was due to pathophysiology or differences in trial design and analysis is uncertain. Regardless, inclusion and exclusion criteria often restrict the subjects enrolled in terms of disease severity and heterogeneity and consideration should be given to the study subject population when discussing clinical significance of the findings.

Lessons From Drug World

As the translation of drugs into clinical use is more established than neuromodulation therapies, it is instructive to review the translation of drugs for pitfalls in moving toward FDA market approved therapies. Less than 12% of drugs that received an FDA Investigational New Drug approval to begin human studies (the current stage of development of many aVNS based therapies) reached market approval (Paul et al., 2010; DiMasi et al., 2016). Gupta et al. (2011) identified several factors that hindered the successful translation of drug therapies from early-stage results to market approval, which are also relevant to aVNS therapies.

1. Lack of pharmacodynamic measures in early-stage clinical trials to confirm drug activity (Gallo, 2010). This is similar to the lack of evidence that aVNS is activating desired fiber types in the auricular branch of the vagus and not activating other fiber types including those within the great auricular, lesser occipital, facial, and trigeminal nerves which innervate the auricular and periauricular region.
2. Lack of validated biomarkers for on- and off-target engagement—impacting our ability to assess and confirm therapeutic activity vs. side effects (Institute of Medicine, 2014). Again, similar to the lack of biomarkers in aVNS trials to confirm on- and off-target nerve activation.
3. Lack of predictability of animal models for humans (Johnson et al., 2001). Relevant in aVNS to translatability of electrode configuration, dosing, and stimulation parameters given changes in size, neuroanatomy, and neurophysiology from animal models to humans. A concern confirmed by other neuromodulation therapies (De Ferrari et al., 2017).

A method to directly measure local neural target engagement will provide an immediate biomarker of on- and off-target activity and forestall some of the hurdles encountered in drug therapy development. A minimally invasive method to measure target engagement percutaneously could be deployed across preclinical models and early clinical studies (Ottaviani et al., 2020). Doing so would increase the translatability of findings by providing data to titrate electrode design, placement, and stimulation waveform parameters to optimize for on-target engagement.

Long Term Solutions—Target Engagement

On- and off-target nerve activation is especially relevant in the case of the auricle that is innervated by several nerves with uncertainty on the specific areas of innervation in literature and across subjects. Data from direct measures of on- and off-target engagement could be used (1) to titrate the therapy by adjusting electrode design, placement, and stimulation waveform parameters to optimize on-target engagement, (2) to scale pre-clinical animal doses to humans by preserving the fiber types activated, and (3) to help investigate fundamental mechanisms of action by isolating local neural pathways.

aVNS is commonly delivered at the cymba concha with the assumption that the cymba concha is innervated only by the auricular vagus. This is based on two pieces of evidence. Firstly, Peuker and Filler (2002) showed the cymba concha is innervated only by the auricular vagus in 7 of 7 cadavers. Notwithstanding, there may be variation in innervation or spread of the electric field, which could activate the neighboring auriculotemporal branch of the trigeminal nerve and even the great auricular nerve. Variations in peripheral nerve innervation has been well-studied for other regions of the body, such as the hand (Bas and Kleinert, 1999; Guru et al., 2015). The reliance on the Peuker and Filler study is concerning due to its small sample size. Given the importance of the claims in Peuker and Filler, a further dissection study with a larger sample size is called for to investigate whether the results hold over a larger population of ethnically diverse individuals. Secondly, functional magnetic resonance imaging (fMRI) evidence is also used to suggest vagal innervation of the conchae (Frangos et al., 2015). However, fMRI is a surrogate measure of target engagement and is especially problematic when imaging deep in the brainstem, as described below.

Target engagement is commonly established using secondary surrogates such as fMRI, somatosensory evoked potentials (SSEPs), and cardiac measures. Secondary surrogates of target engagement are often contaminated with physical and biological noise, leading to potential confounds. For example, Botvinik-Nezer et al. (2020) and Becq et al. (2020) showed that results of fMRI studies were highly dependent on data processing techniques applied. In addition, pathways starting from the trigeminal nerve in the auricle also connect to NTS (Chiluwal et al., 2017), and activate the same region in the brain when in fact the auricular vagus might not be recruited during stimulation. fMRI of the brainstem is further complicated (Napadow et al., 2019) as distance from the measurement coils increases, the effective resolution decreases (Gruber et al., 2018). Still further, novelty, such as being stimulated in the ear or being in an MRI scanner, activates the locus coeruleus (LC) (Wagatsuma et al., 2018), which has connections with NTS. Thereby confounding potential aVNS effects on NTS with LC induced activity due to novelty effects. Lastly, fMRI has non-standard results between subjects requiring individual calibration and making subject to subject comparisons challenging. Additionally, SSEP recordings are sometimes contaminated and misinterpreted due to EMG leakage (Usami et al., 2013). The common measures of target engagement are secondary surrogates and prone to confounds—creating a need for direct measures of local target engagement at the nerve trunks innervating the auricle.

Given the lack of direct measures of local target engagement, aVNS studies rely largely on stimulation parameters that are similar to those used for implantable VNS. The assumption that these stimulation parameters will result in similar target engagement and therapeutic effects may not hold due to the differences in target fiber type, fiber orientation, and electrode design and contact area—all of which affect neural recruitment. Cardiac effects of implantable VNS are thought to be mediated by activation of parasympathetic efferent B fibers innervating the heart (Sabbah et al., 2011) or aortic baroreceptor afferents depending on the stimulation parameters used. Studies of the baroreceptors at the aorta and carotid sinus bulb identified fiber types consistent with Aδ and C fibers (Seagard et al., 1990; Reynolds et al., 2006). Strikingly, consensus workshops have suggested that aVNS is mediated by activation of Aβ

fibers (Kaniusas et al., 2019). There is also no evidence of baroreceptors identified in the ear. These difference between the auricular and cervical vagus suggests a direct porting of stimulation parameters developed for implantable VNS would be insufficient to invoke cardiac responses, unless another yet unidentified mechanism for cardiac responses mediated through NTS is responsible, which can be targeted by Aβ fiber input that then indirectly modulates sympathetic or parasympathetic input to the heart. Unlike stimulation of the cervical vagus nerve trunk, where the electrode contacts are oriented parallel to the target axons, electrode contacts for aVNS do not have consistent orientation with respect to the target axons, which exist as a web of axons in the auricle. Orientation of fibers relative to the stimulation electrode have a large effect on fiber recruitment (Grill, 1999) and could potentially lead to preferential activation of nerve pathways oriented in a particular direction to the stimulation contacts, as well as inconsistent activation of specific fiber types across the auricle. Additionally, target fibers in the auricle transition to unmyelinated fibers as they approach sensory receptor cells (Provitera et al., 2007). For these reasons, while cathodic leading stimulation might have lower recruitment thresholds in implantable VNS, the principle may not hold for aVNS (Anderson et al., 2019). In aVNS, target fiber type, electrode design, electrode size, transcutaneous placement, and orientation of the target fiber relative to the electrode are different both compared to implantable VNS and across aVNS studies. Therefore, it is unsurprising that stimulation parameters ported from implantable VNS may not replicate the physiological effects or recruitment of fiber types that have been observed during implantable VNS.

In relation to electrode design, injected charge density, as opposed to current or voltage, is the most relevant metric of neural activation. This is because stimulation evoked action potentials occur in regions of the neural cell membrane where there is an elevated charge density (McNeal, 1976; Rattay, 1999). For effective comparison across studies using different electrodes, it is imperative to report on the electrode area, especially on the area as it makes contact with tissue, along with stimulation current.

The above discussion stresses a general lack of confidence in ascertaining which of several nerve trunks innervating the auricle are being activated during aVNS that may be generating the on- or off-target effects. Cakmak et al. (2017) further proposed that the therapeutic effects they reported for motor symptoms of Parkinson's diseases came from direct recruitment of the intrinsic auricular muscles instead of the auricular vagus nerve. The fundamentals of neural stimulation do not support directly porting stimulation parameters from implantable VNS. Therefore, it is important to understand which fiber types on the auricular vagus are being activated, if at all. This knowledge requires direct measures of local target engagement from the nerves innervating the auricle.

To further the development of aVNS, it will be essential to understand local target engagement of the nerve trunks innervating the ear. Ultrasound guided (Ritchie et al., 2016) percutaneous microelectrode recordings (Ottaviani et al., 2020) from the major nerve trunks innervating the ear, similar to the technique to measure muscle sympathetic nerve activity (MSNA), provides a way to directly measure local neural recruitment. Real-time data on neural target engagement would enable optimization of stimulation parameters, electrode, and control designs (Chang et al., 2020). These data would also improve translation of stimulation dosages from animal models to humans. Tsaava et al. (2020) showed that the anti-inflammatory effects of implantable VNS are stimulation dose dependent and could lead to the worsening of inflammation at certain dosages. Since target engagement in humans is currently unknown, there is no consistent means of determining dosage accurately—raising potential safety concerns. This minimally invasive method to record neural target engagement is already used clinically and could be rapidly translated to the clinic for use in titrating neuromodulation therapies.

Understanding primary target engagement at the ear will also further our understanding of aVNS mechanisms. For example, large animal recordings of evoked compound action potentials from the major nerve trunks innervating the ear may help in understanding the relationship between on- and off-target nerve engagement and corresponding physiological effects. Simultaneous recordings at the cervical vagus may allow differentiation of direct efferent vagal effects vs. NTS mediated effects, which would appear with a longer latency due to synaptic delay and longer conduction path length. Measuring neural target engagement at the auricle provides a first step to systematically studying aVNS mechanisms and optimizing clinical effects.

Long Term Solutions—Improvement in Control Design and Blinding

The design of an indistinguishable yet non-therapeutic control is central to maintaining the blinding in a clinical trial. Stemming from limited understanding of local target engagement and mechanism of action of aVNS, it is difficult to implement an active control (i.e., sham) that has similar perception to the therapeutic group but will not unknowingly engage a therapeutic pathway. This uncertainty in the therapeutic inertness of the control violates some of the basic premises for a RCT and makes it difficult to evaluate aVNS RCTs on the Oxford Scale for clinical evidence. Systematic effort must be made to design controls, which are key to maintaining blinding in aVNS RCTs.

Common control designs used in aVNS studies are summarized in **Figure 5**. A placebo is defined when the electrode placement and device are similar to the active intervention, but no stimulation is delivered. A waveform sham is defined when a different—non-therapeutic—waveform is delivered at the same location as active intervention. In a location sham, the same waveform as active intervention is delivered at a different location on the auricle and should not engage a therapeutic nerve. Lastly, no intervention or a pharmacological control may be used. Location sham was the most common control used in 16 of 41 RCTs reviewed. These different control designs are evaluated at length in **Supplementary Material 4** along with

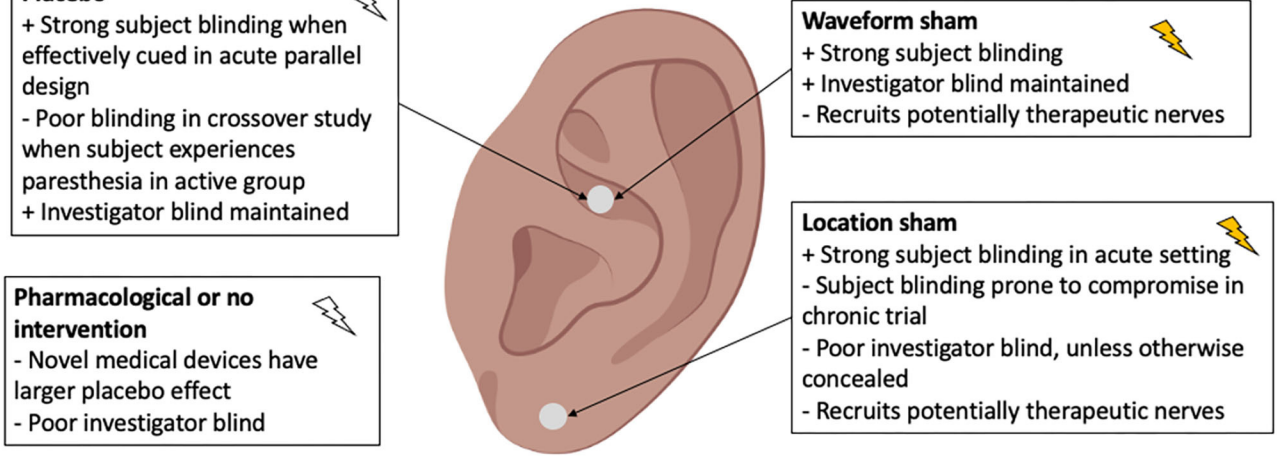

FIGURE 5 | Types of controls used in aVNS clinical trials. The ideal control is indistinguishable from active intervention, to both subject and investigator, yet therapeutically inert.

recommendations on appropriate control types depending on trial design.

Inappropriate implementation of the control group resulted in compromised blinding in many studies. Subject unblinding occurred when subjects were able to feel a paresthesia in the active intervention but not in the control. For example, in cross-over trials, where subjects undergo both the active and control intervention, *post-hoc* assessment of blinding becomes critical given the perception of sensation being unequal could easily break the blind. Investigator unblinding occurred when investigators were able to see differences in electrode placement or device operation. Unblinding due to inappropriate control design is the main contributor leading to risk of bias in the Cochrane section "deviation from intended intervention." The design of appropriate controls is difficult for trials testing non-pharmacological interventions—especially for paresthesia-inducing neuromodulation trials (Robbins and Lipton, 2017; Translating neuromodulation, 2019)—but is essential to establish a double blind.

To aid in the maintenance of the double blind, appropriate design of controls and consistent evaluation of blinding are required. Measurement of target engagement via microneurography of the major nerve trunks innervating the ear (Ottaviani et al., 2020) will enable understanding of neural recruitment occurring during active and sham stimulation and guide appropriate design of controls. Appropriate design of controls for non-invasive neuromodulation studies are discussed at length in **Supplementary Material 4**. In addition, *post-hoc* evaluation of blinding in subjects and investigators will gather knowledge on the blind quality setup by respective control designs. Methods to assess the quality of blinding in non-invasive neuromodulation studies are discussed in **Supplementary Material 5**. Three-armed trials (no treatment, placebo/sham, and treatment) will also generate data on extent of the placebo effect and quality of blinding (Howick et al., 2013). Over time, the consistent use of control designs and evaluation of blinding will grow our understanding of the concealability and therapeutic inertness of various control methods.

Applicability of Findings to Similar Neuromodulation Therapies

The discussion on lack of direct measures of target engagement and unknowns surrounding implementation of perceptually similar yet therapeutically inert controls to maintain the double blind are applicable to other neuromodulation therapies—especially paresthesia inducing therapies such as implantable VNS and spinal cord stimulation (SCS).

Study of local target engagement in neuromodulation therapies such as implantable VNS and SCS will inform stimulation parameters, possible mechanisms of action, and electrode design and placement to maximize on-target nerve recruitment and minimize therapy limiting off-target effects such as muscle contractions (Yoo et al., 2013; Nicolai et al., 2020). To investigate the central mechanisms of action we first have to establish local target engagement to determine which on- and off-target nerves are recruited during stimulation and which fiber types are recruited at therapeutically relevant levels of stimulation. Measurement of local target engagement in preclinical and early clinical studies provides a bottom-up approach to systematically develop and deploy neuromodulation therapies.

A systematic review and meta-analysis of SCS RCTs for pain showed that the quality of control used had an impact on the effect size of the outcome, (Duarte et al., 2020b). They concluded that thorough consideration of control design and consequent subject and investigator blinding is essential to improve the quality of evidence on SCS therapy for pain (Duarte et al., 2020a). A systematic review of dorsal root ganglion (DRG) stimulation for pain also showed serious concern for bias across all studies reviewed due to compromised subject and investigator blinding (Deer et al., 2020). The suggestions

laid forth on measuring local target engagement and consistent *post-hoc* evaluation of blinding in subjects and investigators will expand our knowledge of effective control design for paresthesia inducing neuromodulation therapies such as aVNS, SCS, and implantable VNS.

Limitations of This Review

This review is based on experience in other neuromodulation clinical trials and pre-clinical studies, existing frameworks for analysis such as the Cochrane Risk of Bias and Oxford clinical scale, and literature review motivated by an interest in conducting future aVNS clinical trials. However, at the writing of this article, none of the authors have conducted an aVNS clinical trial. Secondly, this is a systematic review but not a meta-analysis. Due to insufficient reporting in trials, a meta-analysis could not be conducted. The analysis was more qualitative with the intention of summarizing the quality of evidence in the field and making recommendations to improve clinical translatability. Thirdly, this review was not pre-registered, blinded, or formally randomized. Additionally, while the RoB tool provides a consistent method to evaluate trials where the shortcoming is stated explicitly, the ability to identify confounds is often reliant on the critical reading of the reviewer. This made it possible for a secondary reviewer to find additional risk of bias in several instances, which were initially missed by the primary reviewer but included upon identification and consensus. Lastly, numerous instances of missing information in trial reporting were identified and attempts were made to reach out to the authors for that information. These attempts were not always successful. Overall, the points made in the review are robust and withstand the limitations.

CONCLUSION

Based on our review of 38 publications, which reported on 41 aVNS clinical RCTs, aVNS shows physiological effects but has not yet shown strong clinically significant effects consistently supported by multiple studies. This review: (1) Identifies concerns in the design of trials, particularly control and blinding, and incomplete reporting of information using the Cochrane Risk of Bias analysis. (2) Finds aVNS studies are presently exploratory in nature, which is appropriate given the early stage of research of the aVNS field. (3) Qualitatively synthesizes study outcomes by clinical indications. (4) Proposes guidelines for the reporting of aVNS clinical trials, which can be implemented immediately to improve the quality of evidence. (5) Proposes progress in the field has been limited by lack of direct measures of neural target engagement at the site of stimulation. Measures of target engagement will inform therapy optimization, translation, and mechanistic understanding. (6) Proposes consistent *post-hoc* evaluation of subject and investigator blinding and direct measures of local neural target engagement to improve the design of controls for maintenance of blinding.

As a field, neuromodulation has not yet attained social normality or gained widespread adoption as a first-line therapy (Pagnin et al., 2004; Payne and Prudic, 2009; Li et al., 2020). To that end, our responsibility as pioneers is to move the field forward and build its credibility by thoroughly reporting on appropriately designed clinical trials. Given the conflicting data across aVNS studies, it is critical to implement high standards for rigor and quality of evidence to better assess the state of aVNS for a given indication.

DATA AVAILABILITY STATEMENT

The original contributions generated for the study are included in the article/**Supplementary Material**, further inquiries can be directed to the corresponding author/s.

AUTHOR CONTRIBUTIONS

NV, JT, EL, JW, and KL contributed to conception and design of the study. NV, JM, MK, and RC conducted the systematic search. NV, JM, MK, and RC reviewed the included articles. NV wrote the first draft of the manuscript. JM, MK, SB, and KL wrote sections of the manuscript. All authors contributed to manuscript revision, read, and approved the submitted version.

FUNDING

The work presented here was funded by the Defense Advanced Research Projects Agency Biological Technologies Office (BTO) program title Targeted Neuroplasticity Training (TNT) under the auspices of Doug Weber and Tristan McClure-Begley through the Space and Naval Warfare Systems Command Pacific with cooperative agreement no. N66001-17-2-4010. The views, opinions, and/or findings expressed are those of the author and should not be interpreted as representing the official views or policies of the Department of Defense or the U.S. Government.

ACKNOWLEDGMENTS

Eric H. Chang for notes on endotoxin-induced cytokine assays. Carly Frieders, Arkaprabha Banerjee, Maria LaLuzerne, Megan Settell, Robbin Miranda, Rick Chappell, Carolyn Huff, and Harrell Huff for reviewing drafts of this publication. Members of the Wisconsin Institute for Translational Neuroengineering (WITNe) for feedback during group meetings.

SUPPLEMENTARY MATERIAL

The Supplementary Material for this article can be found online at: https://www.frontiersin.org/articles/10.3389/fnins.2021.664740/full#supplementary-material

REFERENCES

Translating Neuromodulation (2019). *Translating Neuromodulation. Nat. Biotechnol.* 37, 967–967. doi: 10.1038/s41587-019-0263-3

Addorisio, M. E., Imperato, G. H., de Vos, A. F., Forti, S., Goldstein, R. S., Pavlov, V. A., et al. (2019). Investigational treatment of rheumatoid arthritis with a vibrotactile device applied to the external ear. *Bioelectron. Med.* 5:4. doi: 10.1186/s42234-019-0020-4

Afanasiev, S. A., Pavliukova, E. N., Kuzmichkina, M. A., Rebrova, T., Anfinogenova, Y., Likhomanov, K. S., et al. (2016). Nonpharmacological correction of hypersympatheticotonia in patients with chronic coronary insufficiency and severe left ventricular dysfunction: nonpharmacological correction of hypersympatheticotonia. *Ann. Noninvasive Electrocardiol.* 21, 548–556. doi: 10.1111/anec.12349

Aihua, L., Lu, S., Liping, L., Xiuru, W., Hua, L., and Yuping, W. (2014). A controlled trial of transcutaneous vagus nerve stimulation for the treatment of pharmacoresistant epilepsy. *Epilepsy Behav.* 39, 105–110. doi: 10.1016/j.yebeh.2014.08.005

American Association of Neurological Surgeons (2021). *Vagus Nerve Stimulation*. Available online at: https://www.aans.org/Patients/Neurosurgical-Conditions-and-Treatments/Vagus-Nerve-Stimulation (accessed January 12, 2021).

Anderson, D. N., Duffley, G., Vorwerk, J., Dorval, A. D., and Butson, C. R. (2019). Anodic stimulation misunderstood: preferential activation of fiber orientations with anodic waveforms in deep brain stimulation. *J. Neural. Eng.* 16:016026. doi: 10.1088/1741-2552/aae590

Andreas, M., Arzl, P., Mitterbauer, A., Ballarini, N. M., Kainz, F.-M., Kocher, A., et al. (2019). Electrical stimulation of the greater auricular nerve to reduce postoperative atrial fibrillation. *Circ. Arrhythm. Electrophysiol.* 12:e007711. doi: 10.1161/CIRCEP.119.008067

Antonino, D., Teixeira, A. L., Maia-Lopes, P. M., Souza, M. C., Sabino-Carvalho, J. L., Murray, A. R., et al. (2017). Non-invasive vagus nerve stimulation acutely improves spontaneous cardiac baroreflex sensitivity in healthy young men: a randomized placebo-controlled trial. *Brain Stimul.* 10, 875–881. doi: 10.1016/j.brs.2017.05.006

Badran, B. W., Mithoefer, O. J., Summer, C. E., LaBate, N. T., Glusman, C. E., Badran, A. W., et al. (2018). Short trains of transcutaneous auricular vagus nerve stimulation (taVNS) have parameter-specific effects on heart rate. *Brain Stimul.* 11, 699–708. doi: 10.1016/j.brs.2018.04.004

Badran, B. W., Yu, A. B., Adair, D., Mappin, G., DeVries, W. H., Jenkins, D. D., et al. (2019). Laboratory administration of Transcutaneous Auricular Vagus Nerve Stimulation (taVNS): technique, targeting, and considerations. *J. Vis. Exp.* 143:e58984. doi: 10.3791/58984

Bas, H., and Kleinert, J. M. (1999). Anatomic variations in sensory innervation of the hand and digits. *J. Hand Surg. Am.* 24, 1171–1184. doi: 10.1053/jhsu.1999.1171

Bauer, S., Baier, H., Baumgartner, C., Bohlmann, K., Fauser, S., Graf, W., et al. (2016). Transcutaneous Vagus Nerve Stimulation (tVNS) for treatment of drug-resistant epilepsy: a randomized, double-blind clinical trial (cMPsE02). *Brain Stimul.* 9, 356–363. doi: 10.1016/j.brs.2015.11.003

Becq, G. J.-P. C., Barbier, E. L., and Achard, S. (2020). Brain networks of rats under anesthesia using resting-state fMRI: comparison with dead rats, random noise and generative models of networks. *J. Neural Eng.* 17:045012. doi: 10.1088/1741-2552/ab9fec

Ben-Menachem, E., Manon-Espaillat, R., Ristanovic, R., Wilder, B. J., Stefan, H., Mirza, W., et al. (1994). Vagus nerve stimulation for treatment of partial seizures: 1. a controlled study of effect on seizures. *Epilepsia* 35, 616–626. doi: 10.1111/j.1528-1157.1994.tb02482.x

Bermejo, P., López, M., Larraya, I., Chamorro, J., Cobo, J. L., Ordóñez, S., et al. (2017). Innervation of the human cavum conchae and auditory canal: anatomical basis for transcutaneous auricular nerve stimulation. *Biomed. Res. Int.* 2017, 1–10. doi: 10.1155/2017/7830919

Billman, G. E. (2013). The LF/HF ratio does not accurately measure cardiac sympatho-vagal balance. *Front. Physio.* 4:26. doi: 10.3389/fphys.2013.00026

Bootsma, M., Swenne, C. A., Janssen, M. J. A., Cats, V. M., and Schalij, M. J. (2003). Heart rate variability and sympathovagal balance: pharmacological validation. *Neth. Heart J.* 11, 250–259.

Borges, U., Laborde, S., and Raab, M. (2019). Influence of transcutaneous vagus nerve stimulation on cardiac vagal activity: not different from sham stimulation and no effect of stimulation intensity. *PLoS ONE* 14:e0223848. doi: 10.1371/journal.pone.0223848

Botvinik-Nezer, R., Holzmeister, F., Camerer, C. F., Dreber, A., Huber, J., Johannesson, M., et al. (2020). Variability in the analysis of a single neuroimaging dataset by many teams. *Nature* 582, 84–88. doi: 10.1038/s41586-020-2314-9

Bretherton, B., Atkinson, L., Murray, A., Clancy, J., Deuchars, S., and Deuchars, J. (2019). Effects of transcutaneous vagus nerve stimulation in individuals aged 55 years or above: potential benefits of daily stimulation. *Aging* 11, 4836–4857. doi: 10.18632/aging.102074

Broekman, M. M. T. J., Roelofs, H. M. J., Hoentjen, F., Wiegertjes, R., Stoel, N., Joosten, L. A., et al. (2015). LPS-stimulated whole blood cytokine production is not related to disease behavior in patients with quiescent Crohn's disease. *PLoS ONE* 10:e0133932. doi: 10.1371/journal.pone.0133932

Burger, A. M., D'Agostini, M., Verkuil, B., and Van Diest, I. (2020). Moving beyond belief: a narrative review of potential biomarkers for transcutaneous vagus nerve stimulation. *Psychophysiology* 57:e13571. doi: 10.1111/psyp.13571

Burger, A. M., Van der Does, W., Thayer, J. F., Brosschot, J. F., and Verkuil, B. (2019). Transcutaneous vagus nerve stimulation reduces spontaneous but not induced negative thought intrusions in high worriers. *Biol. Psychol.* 142, 80–89. doi: 10.1016/j.biopsycho.2019.01.014

Busch, V., Zeman, F., Heckel, A., Menne, F., Ellrich, J., and Eichhammer, P. (2013). The effect of transcutaneous vagus nerve stimulation on pain perception – an experimental study. *Brain Stimul.* 6, 202–209. doi: 10.1016/j.brs.2012.04.006

Cakmak, Y. O. (2019). Concerning auricular vagal nerve stimulation: occult neural networks. *Front. Hum. Neurosci.* 13:421. doi: 10.3389/fnhum.2019.00421

Cakmak, Y. O., Apaydin, H., Kiziltan, G., Gündüz, A., Ozsoy, B., Olcer, S., et al. (2017). Rapid alleviation of Parkinson's disease symptoms via electrostimulation of intrinsic auricular muscle zones. *Front. Hum. Neurosci.* 11:338. doi: 10.3389/fnhum.2017.00338

Centre for Evidence-Based Medicine (2009). *Oxford Centre for Evidence-Based Medicine: Levels of Evidence (March 2009)*. Available online at: https://www.cebm.ox.ac.uk/resources/levels-of-evidence/oxford-centre-for-evidence-based-medicine-levels-of-evidence-march-2009 (accessed November 26, 2020).

Chang, Y.-C., Cracchiolo, M., Ahmed, U., Mughrabi, I., Gabalski, A., Daytz, A., et al. (2020). Quantitative estimation of nerve fiber engagement by vagus nerve stimulation using physiological markers. *Brain Stimul.* 13, 1617–1630. doi: 10.1016/j.brs.2020.09.002

Chiluwal, A., Narayan, R. K., Chaung, W., Mehan, N., Wang, P., Bouton, C. E., et al. (2017). Neuroprotective effects of trigeminal nerve stimulation in severe traumatic brain injury. *Sci. Rep.* 7:6792. doi: 10.1038/s41598-017-07219-3

Clancy, J. A., Mary, D. A., Witte, K. K., Greenwood, J. P., Deuchars, S. A., and Deuchars, J. (2014). Non-invasive vagus nerve stimulation in healthy humans reduces sympathetic nerve activity. *Brain Stimul.* 7, 871–877. doi: 10.1016/j.brs.2014.07.031

De Couck, M., Cserjesi, R., Caers, R., Zijlstra, W. P., Widjaja, D., Wolf, N., et al. (2017). Effects of short and prolonged transcutaneous vagus nerve stimulation on heart rate variability in healthy subjects. *Autonomic Neurosci.* 203, 88–96. doi: 10.1016/j.autneu.2016.11.003

De Ferrari, G. M., Stolen, C., Tuinenburg, A. E., Wright, D. J., Brugada, J., Butter, C., et al. (2017). Long-term vagal stimulation for heart failure: eighteen month results from the NEural Cardiac TherApy foR Heart Failure (NECTAR-HF) trial. *Int. J. Cardiol.* 244, 229–234. doi: 10.1016/j.ijcard.2017.06.036

Deer, T. R., Hunter, C. W., Mehta, P., Sayed, D., Grider, J. S., Lamer, T. J., et al. (2020). A systematic literature review of dorsal root ganglion neurostimulation for the treatment of pain. *Pain Med.* 21, 1581–1589. doi: 10.1093/pm/pnaa005

Del Giudice, M., and Gangestad, S. W. (2018). Rethinking IL-6 and CRP: Why they are more than inflammatory biomarkers, and why it matters. *Brain Behav. Immun.* 70, 61–75. doi: 10.1016/j.bbi.2018.02.013

DiMasi, J. A., Grabowski, H. G., and Hansen, R. W. (2016). Innovation in the pharmaceutical industry: new estimates of R&D costs. *J. Health Econ.* 47, 20–33. doi: 10.1016/j.jhealeco.2016.01.012

Doherty, M., and Dieppe, P. (2009). The "placebo" response in osteoarthritis and its implications for clinical practice. *Osteoarthritis Cartilage* 17, 1255–1262. doi: 10.1016/j.joca.2009.03.023

Duarte, R. V., McNicol, E., Colloca, L., Taylor, R. S., North, R. B., and Eldabe, S. (2020a). Randomized placebo-/sham-controlled trials of spinal cord stimulation: a systematic review and methodological appraisal. *Neuromodulation* 23, 10–18. doi: 10.1111/ner.13018

Duarte, R. V., Nevitt, S., McNicol, E., Taylor, R. S., Buchser, E., North, R. B., et al. (2020b). Systematic review and meta-analysis of placebo/sham controlled randomised trials of spinal cord stimulation for neuropathic pain: *Pain* 161, 24–35. doi: 10.1097/j.pain.0000000000001689

Elgendi, M., Fletcher, R., Liang, Y., Howard, N., Lovell, N. H., Abbott, D., et al. (2019). The use of photoplethysmography for assessing hypertension. *npj Digit. Med*. 2:60. doi: 10.1038/s41746-019-0136-7

Farmer, D. F., Strzelczyk, A., Finisguerra, A., Gourine, A. V., Gharabaghi, A., Hasan, A., et al. (2020). International consensus based review and recommendations for minimum reporting standards in research on transcutaneous vagus nerve stimulation (Version 2020). *Front. Hum. Neurosci.* 14:568051. doi: 10.3389/fnhum.2020.568051

Fisher, H., Stowell, J., Garcia, R., Sclocco, R., Goldstein, J., Napadow, V., et al. (2018). "Acute effects of respiratory-gated auricular vagal afferent nerve stimulation in the modulation of blood pressure in hypertensive patients," in *2018 Computing in Cardiology Conference (CinC)* (Maastricht), 1–4. doi: 10.22489/CinC.2018.346

Frangos, E., Ellrich, J., and Komisaruk, B. R. (2015). Non-invasive access to the vagus nerve central projections via electrical stimulation of the external ear: fMRI evidence in humans. *Brain Stimul.* 8, 624–636. doi: 10.1016/j.brs.2014.11.018

Frøkjaer, J. B., Bergmann, S., Brock, C., Madzak, A., Farmer, A. D., Ellrich, J., et al. (2016). Modulation of vagal tone enhances gastroduodenal motility and reduces somatic pain sensitivity. *Neurogastroenterol. Motil.* 28, 592–598. doi: 10.1111/nmo.12760

Gallo, J. M. (2010). Pharmacokinetic/ pharmacodynamic-driven drug development: pharmacokinetic/pharmacodynamic-driven drug development. *Mt. Sinai J. Med.* 77, 381–388. doi: 10.1002/msj.20193

Goetz, C. G., Tilley, B. C., Shaftman, S. R., Stebbins, G. T., Fahn, S., Martinez-Martin, P., et al. (2008). Movement disorder society-sponsored revision of the unified Parkinson's disease rating scale (MDS-UPDRS): scale presentation and clinimetric testing results: MDS-UPDRS: clinimetric assessment. *Mov. Disord.* 23, 2129–2170. doi: 10.1002/mds.22340

Goldberger, J. J. (1999). Sympathovagal balance: how should we measure it? *Am. J. Physiol. Heart Circulat. Physiol.* 276, H1273–H1280. doi: 10.1152/ajpheart.1999.276.4.H1273

Grill, W. M. (1999). Modeling the effects of electric fields on nerve fibers: influence of tissue electrical properties. *IEEE Trans. Biomed. Eng.* 46, 918–928. doi: 10.1109/10.775401

Gruber, B., Froeling, M., Leiner, T., and Klomp, D. W. J. (2018). RF coils: a practical guide for nonphysicists: RF Coils. *J. Magn. Reson. Imaging* 48, 590–604. doi: 10.1002/jmri.26187

Gupta, U., Bhatia, S., Garg, A., Sharma, A., and Choudhary, V. (2011). Phase 0 clinical trials in oncology new drug development. *Perspect. Clin. Res.* 2:13. doi: 10.4103/2229-3485.76285

Guru, A., Kumar, N., Ravindra Shanthakumar, S., Patil, J., Nayak Badagabettu, S., Aithal Padur, A., et al. (2015). Anatomical study of the ulnar nerve variations at high humeral level and their possible clinical and diagnostic implications. *Anat. Res. Int.* 2015, 1–4. doi: 10.1155/2015/378063

Handforth, A., DeGiorgio, C. M., Schachter, S. C., Uthman, B. M., Naritoku, D. K., Tecoma, E. S., et al. (1998). Vagus nerve stimulation therapy for partial-onset seizures: a randomized active-control trial. *Neurology* 51, 48–55. doi: 10.1212/WNL.51.1.48

Hasan, A., Wolff-Menzler, C., Pfeiffer, S., Falkai, P., Weidinger, E., Jobst, A., et al. (2015). Transcutaneous noninvasive vagus nerve stimulation (tVNS) in the treatment of schizophrenia: a bicentric randomized controlled pilot study. *Eur. Arch. Psychiatry Clin. Neurosci.* 265, 589–600. doi: 10.1007/s00406-015-0618-9

Hayano, J., and Yuda, E. (2019). Pitfalls of assessment of autonomic function by heart rate variability. *J. Physiol. Anthropol.* 38:3. doi: 10.1186/s40101-019-0193-2

He, W., Wang, X., Shi, H., Shang, H., Li, L., Jing, X., et al. (2012). Auricular acupuncture and vagal regulation. *Evid. Based Complement. Alternat. Med.* 2012:786839. doi: 10.1155/2012/786839

Hein, E., Nowak, M., Kiess, O., Biermann, T., Bayerlein, K., Kornhuber, J., et al. (2013). Auricular transcutaneous electrical nerve stimulation in depressed patients: a randomized controlled pilot study. *J. Neural. Transm.* 120, 821–827. doi: 10.1007/s00702-012-0908-6

Hewitt, J. A., Brown, L. L., Murphy, S. J., Grieder, F., and Silberberg, S. D. (2017). Accelerating biomedical discoveries through rigor and transparency. *ILAR J.* 58, 115–128. doi: 10.1093/ilar/ilx011

Higgins, P. J., Savović, J., Page, J. M., Elbers, G. R., Sterne, A. J., (2019). *Cochrane Training Chapter 8: Assessing Risk of Bias in a Randomized Trial*. Available online at: https://training.cochrane.org/handbook/current/chapter-08 (accessed November 26, 2020).

Howick, J., Friedemann, C., Tsakok, M., Watson, R., Tsakok, T., Thomas, J., et al. (2013). Are treatments more effective than placebos? A systematic review and meta-analysis. *PLoS ONE* 8:e62599. doi: 10.1371/journal.pone.0062599

Huang, F., Dong, J., Kong, J., Wang, H., Meng, H., Spaeth, R. B., et al. (2014). Effect of transcutaneous auricular vagus nerve stimulation on impaired glucose tolerance: a pilot randomized study. *BMC Complement. Altern. Med.* 14:203. doi: 10.1186/1472-6882-14-203

Institute of Medicine. (2014). *Improving and Accelerating Therapeutic Development for Nervous System Disorders: Workshop Summary*. Washington, DC: The National Academies Press.

Janner, H., Klausenitz, C., Gürtler, N., Hahnenkamp, K., and Usichenko, T. I. (2018). Effects of electrical transcutaneous vagus nerve stimulation on the perceived intensity of repetitive painful heat stimuli: a blinded placebo- and sham-controlled randomized crossover investigation. *Anesthesia Analgesia* 126, 2085–2092. doi: 10.1213/ANE.0000000000002820

Jiang, Y., Po, S. S., Amil, F., and Dasari, T. W. (2020). Non-invasive low-level tragus stimulation in cardiovascular diseases. *Arrhythm. Electrophysiol. Rev.* 9, 40–46. doi: 10.15420/aer.2020.01

Johnson, J. I., Decker, S., Zaharevitz, D., Rubinstein, L. V., Venditti, J. M., Schepartz, S., et al. (2001). Relationships between drug activity in NCI preclinical *in vitro* and *in vivo* models and early clinical trials. *Br. J. Cancer* 84, 1424–1431. doi: 10.1054/bjoc.2001.1796

Johnson, M. I., Hajela, V. K., Ashton, C. H., and Thompson, J. W. (1991). The effects of auricular transcutaneous electrical nerve stimulation (TENS) on experimental pain threshold and autonomic function in healthy subjects: *Pain* 46, 337–342. doi: 10.1016/0304-3959(91)90116-F

Juel, J., Brock, C., Olesen, S., Madzak, A., Farmer, A., Aziz, Q., et al. (2017). Acute physiological and electrical accentuation of vagal tone has no effect on pain or gastrointestinal motility in chronic pancreatitis. *JPR Volume* 10, 1347–1355. doi: 10.2147/JPR.S133438

Kahn, L., Mathkour, M., Lee, S. X., Gouveia, E. E., Hanna, J. A., Garces, J., et al. (2019). Long-term outcomes of deep brain stimulation in severe Parkinson's disease utilizing UPDRS III and modified Hoehn and Yahr as a severity scale. *Clin. Neurol. Neurosurg.* 179, 67–73. doi: 10.1016/j.clineuro.2019.02.018

Kang, M., Ragan, B. G., and Park, J.-H. (2008). Issues in outcomes research: an overview of randomization techniques for clinical trials. *J. Athl. Train.* 43, 215–221. doi: 10.4085/1062-6050-43.2.215

Kaniusas, E., Kampusch, S., Tittgemeyer, M., Panetsos, F., Gines, R. F., Papa, M., et al. (2019). Current directions in the auricular vagus nerve stimulation I – a physiological perspective. *Front. Neurosci.* 13:854. doi: 10.3389/fnins.2019.00854

Keute, M., Machetanz, K., Berelidze, L., Guggenberger, R., and Gharabaghi, A. (2021). Neuro-cardiac coupling predicts transcutaneous auricular Vagus Nerve Stimulation effects. *Brain Stimul.* 14, 209–216. doi: 10.1016/j.brs.2021.01.001

Kovacic, K., Hainsworth, K., Sood, M., Chelimsky, G., Unteutsch, R., Nugent, M., et al. (2017). Neurostimulation for abdominal pain-related functional gastrointestinal disorders in adolescents: a randomised, double-blind, sham-controlled trial. *Lancet Gastroenterol. Hepatol.* 2, 727–737. doi: 10.1016/S2468-1253(17)30253-4

Kutlu, N., Özden, A. V., Alptekin, H. K., and Alptekin, J. Ö. (2020). The impact of auricular vagus nerve stimulation on pain and life quality in patients with fibromyalgia syndrome. *Biomed Res. Int.* 2020, 1–10. doi: 10.1155/2020/8656218

Laqua, R., Leutzow, B., Wendt, M., and Usichenko, T. (2014). Transcutaneous vagal nerve stimulation may elicit anti- and pro-nociceptive effects under

experimentally-induced pain — a crossover placebo-controlled investigation. *Autonomic Neurosci.* 185, 120–122. doi: 10.1016/j.autneu.2014.07.008

Li, M., Yao, X., Sun, L., Zhao, L., Xu, W., Zhao, H., et al. (2020). Effects of electroconvulsive therapy on depression and its potential mechanism. *Front. Psychol.* 11:80. doi: 10.3389/fpsyg.2020.00080

LivaNova (2017). *VNS Therapy Dosing Guideline SenTiva*. Available online at: https://vnstherapy.com/healthcare-professionals/sites/vnstherapy.com.healthcare-professionals/files/SenTiva_Dosing_Guide_2019-DIGITAL.PDF (accessed November 26, 2020).

Maharjan, A., Wang, E., Peng, M., and Cakmak, Y. O. (2018). Improvement of olfactory function with high frequency non-invasive auricular electrostimulation in healthy humans. *Front. Neurosci.* 12:225. doi: 10.3389/fnins.2018.00225

Marmerstein, J. T., McCallum, G. A., and Durand, D. M. (2021). Direct measurement of vagal tone in rats does not show correlation to HRV. *Sci. Rep.* 11:1210. doi: 10.1038/s41598-020-79808-8

McNeal, D. R. (1976). Analysis of a model for excitation of myelinated nerve. *IEEE Trans. Biomed. Eng.* BME-23, 329–337. doi: 10.1109/TBME.1976.324593

Moher, D., Hopewell, S., Schulz, K. F., Montori, V., Gotzsche, P. C., Devereaux, P. J., et al. (2010). CONSORT 2010 Explanation and Elaboration: updated guidelines for reporting parallel group randomised trials. *BMJ* 340, c869–c869. doi: 10.1136/bmj.c869

Moher, D., Liberati, A., Tetzlaff, J., Altman, D. G., and The PRISMA Group (2009). Preferred reporting items for systematic reviews and meta-analyses: the prisma statement. *PLoS Med.* 6:e1000097. doi: 10.1371/journal.pmed.1000097

Morimoto, R. (1993). Cells in stress: transcriptional activation of heat shock genes. *Science* 259, 1409–1410. doi: 10.1126/science.8451637

Murray, A. R., Atkinson, L., Mahadi, M. K., Deuchars, S. A., and Deuchars, J. (2016). The strange case of the ear and the heart: The auricular vagus nerve and its influence on cardiac control. *Autonomic Neurosci.* 199, 48–53. doi: 10.1016/j.autneu.2016.06.004

Nair, B. (2019). Clinical trial designs. *Indian Dermatol. Online J.* 10, 193–201. doi: 10.4103/idoj.IDOJ_475_18

Napadow, V., Edwards, R. R., Cahalan, C. M., Mensing, G., Greenbaum, S., Valovska, A., et al. (2012). Evoked pain analgesia in chronic pelvic pain patients using respiratory-gated auricular vagal afferent nerve stimulation. *Pain Med.* 13, 777–789. doi: 10.1111/j.1526-4637.2012.01385.x

Napadow, V., Sclocco, R., and Henderson, L. A. (2019). Brainstem neuroimaging of nociception and pain circuitries: *PAIN Rep.* 4:*E*745. doi: 10.1097/PR9.0000000000000745

Nicolai, E. N., Settell, M. L., Knudsen, B. E., McConico, A. L., Gosink, B. A., Trevathan, J. K., et al. (2020). Sources of off-target effects of vagus nerve stimulation using the helical clinical lead in domestic pigs. *J. Neural. Eng.* 17:046017. doi: 10.1088/1741-2552/ab9db8

Ottaviani, M. M., Wright, L., Dawood, T., and Macefield, V. G. (2020). *In vivo* recordings from the human vagus nerve using ultrasound-guided microneurography. *J. Physiol.* 598, 3569–3576. doi: 10.1113/JP280077

Pagnin, D., de Queiroz, V., Pini, S., and Cassano, G. B. (2004). Efficacy of ECT in depression: a meta-analytic review. *J. ECT* 20:8. doi: 10.1097/00124509-200403000-00004

Parameswaran, N., and Patial, S. (2010). Tumor necrosis factor-α signaling in macrophages. *Crit. Rev. Eukar. Gene Expr.* 20, 87–103. doi: 10.1615/CritRevEukarGeneExpr.v20.i2.10

Paul, S. M., Mytelka, D. S., Dunwiddie, C. T., Persinger, C. C., Munos, B. H., Lindborg, S. R., et al. (2010). How to improve R&D productivity: the pharmaceutical industry's grand challenge. *Nat. Rev. Drug Discov.* 9, 203–214. doi: 10.1038/nrd3078

Payne, N. A., and Prudic, J. (2009). Electroconvulsive therapy: Part I. a perspective on the evolution and current practice of ECT. *J. Psychiatr. Pract.* 15, 346–368. doi: 10.1097/01.pra.0000361277.65468.ef

Peuker, E. T., and Filler, T. J. (2002). The nerve supply of the human auricle. *Clin. Anat.* 15, 35–37. doi: 10.1002/ca.1089

Poulsen, A. H., Tigerholm, J., Meijs, S., Andersen, O. K., and Mørch, C. D. (2020). Comparison of existing electrode designs for preferential activation of cutaneous nociceptors. *J. Neural. Eng.* 17:036026. doi: 10.1088/1741-2552/ab85b1

Provitera, V., Nolano, M., Pagano, A., Caporaso, G., Stancanelli, A., and Santoro, L. (2007). Myelinated nerve endings in human skin. *Muscle Nerve.* 35, 767–775. doi: 10.1002/mus.20771

Rattay, F. (1999). The basic mechanism for the electrical stimulation of the nervous system. *Neuroscience* 89, 335–346. doi: 10.1016/S0306-4522(98)00330-3

Reynolds, P. J., Fan, W., and Andresen, M. C. (2006). Capsaicin- resistant arterial baroreceptors. *J. Negat. Results Biomed.* 5:6. doi: 10.1186/1477-5751-5-6

Ritchie, M. K., Wilson, C. A., Grose, B. W., Ranganathan, P., Howell, S. M., and Ellison, M. B. (2016). Ultrasound-guided greater auricular nerve block as sole anesthetic for ear surgery. *Clin. Pract.* 6:856. doi: 10.4081/cp.2016.856

Robbins, M. S., and Lipton, R. B. (2017). Transcutaneous and percutaneous neurostimulation for headache disorders. *Headache* 57, 4–13. doi: 10.1111/head.12829

Rong, P., Liu, A., Zhang, J., Wang, Y., He, W., Yang, A., et al. (2014). Transcutaneous vagus nerve stimulation for refractory epilepsy: a randomized controlled trial. *Clin. Sci.* doi: 10.1042/CS20130518. [Epub ahead of print].

Sabbah, H. N., Ilsar, I., Zaretsky, A., Rastogi, S., Wang, M., and Gupta, R. C. (2011). Vagus nerve stimulation in experimental heart failure. *Heart Fail. Rev.* 16, 171–178. doi: 10.1007/s10741-010-9209-z

Salama, M., Akan, A., and Mueller, M. R. (2020). Transcutaneous stimulation of auricular branch of the vagus nerve attenuates the acute inflammatory response after lung lobectomy. *World J. Surg.* 44, 3167–3174. doi: 10.1007/s00268-020-05543-w

Seagard, J. L., van Brederode, J. F., Dean, C., Hopp, F. A., Gallenberg, L. A., and Kampine, J. P. (1990). Firing characteristics of single-fiber carotid sinus baroreceptors. *Circ. Res.* 66, 1499–1509. doi: 10.1161/01.RES.66.6.1499

Shen, D., and Lu, Z. (2006). *Estimate Carryover Effect in Clinical Trial Crossover Designs*, 7. Available online at: https://www.lexjansen.com/pharmasug/2006/Posters/PO16.pdf

Stavrakis, S., Humphrey, M. B., Scherlag, B. J., Hu, Y., Jackman, W. M., Nakagawa, H., et al. (2015). Low-level transcutaneous electrical vagus nerve stimulation suppresses atrial fibrillation. *J. Am. Coll. Cardiol.* 65, 867–875. doi: 10.1016/j.jacc.2014.12.026

Stavrakis, S., Stoner, J. A., Humphrey, M. B., Morris, L., Filiberti, A., Reynolds, J. C., et al. (2020). TREAT AF (Transcutaneous Electrical Vagus Nerve Stimulation to Suppress Atrial Fibrillation). *JACC Clin. Electrophysiol.* 6, 282–291. doi: 10.1016/j.jacep.2019.11.008

Sterne, J. A. C., Savović, J., Page, M. J., Elbers, R. G., Blencowe, N. S., Boutron, I., et al. (2019). RoB 2: a revised tool for assessing risk of bias in randomised trials. *BMJ* 366:l4898. doi: 10.1136/bmj.l4898

Stoddard, M. B., Pinto, V., Keiser, P. B., and Zollinger, W. (2010). Evaluation of a whole-blood cytokine release assay for use in measuring endotoxin activity of Group B neisseria meningitidis vaccines made from Lipid A acylation mutants. *CVI* 17, 98–107. doi: 10.1128/CVI.00342-09

Stowell, J., Garcia, R., Staley, R., Sclocco, R., Fisher, H., Napadow, V., et al. (2019). "Dose-optimization of Respiratory-Gated Auricular Vagal Afferent Nerve Stimulation (RAVANS) for blood pressure modulation in hypertensive patients," in *2019 Computing in Cardiology (CinC)* (Singapore), 1–4. doi: 10.22489/CinC.2019.098

Straube, A., Ellrich, J., Eren, O., Blum, B., and Ruscheweyh, R. (2015). Treatment of chronic migraine with transcutaneous stimulation of the auricular branch of the vagal nerve (auricular t-VNS): a randomized, monocentric clinical trial. *J. Headache Pain* 16:63. doi: 10.1186/s10194-015-0543-3

Thurm, C. W., and Halsey, J. F. (2005). "Measurement of cytokine production using whole blood," in *Current Protocols in Immunology*, eds. J. E. Coligan, B. E. Bierer, D. H. Margulies, E. M. Shevach, and W. *Strober* (Hoboken, NJ: John Wiley & Sons, Inc.), *im*0718bs66.

Tobaldini, E., Toschi-Dias, E., Appratto de Souza, L., Rabello Casali, K., Vicenzi, M., Sandrone, G., et al. (2019). Cardiac and peripheral autonomic responses to orthostatic stress during transcutaneous vagus nerve stimulation in healthy subjects. *JCM* 8:496. doi: 10.3390/jcm8040496

Tran, N., Asad, Z., Elkholey, K., Scherlag, B. J., Po, S. S., and Stavrakis, S. (2019). Autonomic neuromodulation acutely ameliorates left ventricular strain in humans. *J. Cardiovasc. Trans. Res.* 12, 221–230. doi: 10.1007/s12265-018-9853-6

Tsaava, T., Datta-Chaudhuri, T., Addorisio, M. E., Masi, E. B., Silverman, H. A., Newman, J. E., et al. (2020). Specific vagus nerve stimulation parameters alter serum cytokine levels in the absence of inflammation. *Bioelectron Med.* 6:8. doi: 10.1186/s42234-020-00042-8

Turner, H. M. III, and Bernard, R. M. (2006). Calculating and synthesizing effect sizes. *CICSD* 33, 42–55. doi: 10.1044/cicsd_33_S_42

Tutar, B., Atar, S., Berkiten, G., Üstün, O., Kumral, T. L., and Uyar, Y. (2020). The effect of transcutaneous electrical nerve stimulation (TENS) on chronic subjective tinnitus. *Am. J. Otolaryngol.* 41:102326. doi: 10.1016/j.amjoto.2019.102326

Usami, K., Kawai, K., Sonoo, M., and Saito, N. (2013). Scalp-recorded evoked potentials as a marker for afferent nerve impulse in clinical vagus nerve stimulation. *Brain Stimul.* 6, 615–623. doi: 10.1016/j.brs.2012.09.007

Wagatsuma, A., Okuyama, T., Sun, C., Smith, L. M., Abe, K., and Tonegawa, S. (2018). Locus coeruleus input to hippocampal CA3 drives single-trial learning of a novel context. *Proc. Natl. Acad. Sci. U.S.A.* 115, E310–E316. doi: 10.1073/pnas.1714082115

Watanabe, K., Tubbs, R. S., Satoh, S., Zomorodi, A. R., Liedtke, W., Labidi, M., et al. (2016). Isolated deep ear canal pain: possible role of auricular branch of vagus nerve—case illustrations with cadaveric correlation. *World Neurosurg.* 96, 293–301. doi: 10.1016/j.wneu.2016.08.102

Wellmark (2018). *Vagus Nerve Stimulation (VNS) and Vagal Blocking Therapy*. Available online at: https://www.wellmark.com/Provider/MedpoliciesAndAuthorizations/MedicalPolicies/policies/Vagus_Nerve_Stimulation.aspx?fbclid=IwAR0Bq8iogosvLVR7p3xBW7J5fIziGxbyQk-2MnRRKADoQcJ0qJFotbOk_dM (accessed November 26, 2020).

Wolf, V., Kühnel, A., Teckentrup, V., Koenig, J., and Kroemer, N. B. (2021). Does non-invasive vagus nerve stimulation affect heart rate variability? A living and interactive Bayesian meta-analysis. *bioRxiv [preprint]*. doi: 10.1101/2021.01.18.426704

Wright, B. J., O'Brien, S., Hazi, A., and Kent, S. (2015). Increased systolic blood pressure reactivity to acute stress is related with better self-reported health. *Sci. Rep.* 4:6882. doi: 10.1038/srep06882

Yang, B., Pham, T., Goldbach-Mansky, R., and Gadina, M. (2011). Accurate and simple measurement of the pro-inflammatory cytokine IL-1β using a whole blood stimulation assay. *J. Vis. Exp.* 49:e2662. doi: 10.3791/2662

Yap, J. Y. Y., Keatch, C., Lambert, E., Woods, W., Stoddart, P. R., and Kameneva, T. (2020). Critical review of transcutaneous vagus nerve stimulation: challenges for translation to clinical practice. *Front. Neurosci.* 14:284. doi: 10.3389/fnins.2020.00284

Yoo, P. B., Lubock, N. B., Hincapie, J. G., Ruble, S. B., Hamann, J. J., and Grill, W. M. (2013). High-resolution measurement of electrically-evoked vagus nerve activity in the anesthetized dog. *J. Neural Eng.* 10:026003. doi: 10.1088/1741-2560/10/2/026003

Yu, L., Huang, B., Po, S. S., Tan, T., Wang, M., Zhou, L., et al. (2017). Low-level tragus stimulation for the treatment of ischemia and reperfusion injury in patients with ST-Segment elevation myocardial infarction. *JACC Cardiovasc. Intervent.* 10, 1511–1520. doi: 10.1016/j.jcin.2017.04.036

Zamotrinsky, A. V., Kondratiev, B., and de Jong, J. W. (2001). Vagal neurostimulation in patients with coronary artery disease. *Autonomic Neurosci.* 88, 109–116. doi: 10.1016/S1566-0702(01)00227-2

Conflict of Interest: EL is an employee of LivaNova PLC. JW and KL are scientific board members and have stock interests in NeuroOne Medical Inc., a company developing next generation epilepsy monitoring devices. JW also has an equity interest in NeuroNexus technology Inc., a company that supplies electrophysiology equipment and multichannel probes to the neuroscience research community. KL is also a paid member of the scientific advisory board of Cala Health, Blackfynn, Abbott and Battelle. KL also is a paid consultant for Galvani and Boston Scientific. KL is a consultant to and co-founder of Neuronoff Inc. None of these associations are directly relevant to the work presented in this manuscript.

The remaining authors declare that the research was conducted in the absence of any commercial or financial relationships that could be construed as a potential conflict of interest.

frontiers in Neuroscience

REVIEW
published: 24 May 2021
doi: 10.3389/fnins.2021.685872

Selective Neuromodulation of the Vagus Nerve

Adam Fitchett, Svetlana Mastitskaya and Kirill Aristovich**

Department of Medical Physics and Biomedical Engineering, University College London, London, United Kingdom

Vagus nerve stimulation (VNS) is an effective technique for the treatment of refractory epilepsy and shows potential for the treatment of a range of other serious conditions. However, until now stimulation has generally been supramaximal and non-selective, resulting in a range of side effects. Selective VNS (sVNS) aims to mitigate this by targeting specific fiber types within the nerve to produce functionally specific effects. In recent years, several key paradigms of sVNS have been developed—spatially selective, fiber-selective, anodal block, neural titration, and kilohertz electrical stimulation block—as well as various stimulation pulse parameters and electrode array geometries. sVNS can significantly reduce the severity of side effects, and in some cases increase efficacy of the treatment. While most studies have focused on fiber-selective sVNS, spatially selective sVNS has demonstrated comparable mitigation of side-effects. It has the potential to achieve greater specificity and provide crucial information about vagal nerve physiology. Anodal block achieves strong side-effect mitigation too, but is much less specific than fiber- and spatially selective paradigms. The major hurdle to achieving better selectivity of VNS is a limited knowledge of functional anatomical organization of vagus nerve. It is also crucial to optimize electrode array geometry and pulse shape, as well as expand the applications of sVNS beyond the current focus on cardiovascular disease.

Keywords: vagus nerve, fascicular anatomy, electrical stimulation, neuromodulation, fiber-specificity, spatial specificity

OPEN ACCESS

Edited by:
Stephen Lewis,
Case Western Reserve University,
United States

Reviewed by:
Kip Ludwig,
University of Wisconsin-Madison,
United States
Martin Gerbert Frasch,
University of Washington,
United States

****Correspondence:***
Svetlana Mastitskaya
s.mastitskaya@ucl.ac.uk
Kirill Aristovich
k.aristovich@ucl.ac.uk

Specialty section:
This article was submitted to Autonomic Neuroscience, a section of the journal Frontiers in Neuroscience

Received: *25 March 2021*
Accepted: *27 April 2021*
Published: *24 May 2021*

Citation:
Fitchett A, Mastitskaya S and Aristovich K (2021) Selective Neuromodulation of the Vagus Nerve. Front. Neurosci. 15:685872. doi: 10.3389/fnins.2021.685872

INTRODUCTION

The vagus nerve (VN) is one of the most promising targets for neuromodulation. The discovery in the 1980s that VN stimulation (VNS) can stop seizures in dogs lead to VNS for epilepsy treatment, with the first VN stimulators approved by the United States Federal Drug Administration in 1997 (Krahl, 2012). By 2018, over 100,000 patients had been implanted with VNS devices (Purser et al., 2018). Since the 1990s, evidence of a role for the VN in regulating diverse physiological functions has sparked interest in VNS beyond epilepsy treatment; VNS has been investigated for addressing treatment-resistant depression, cardiovascular disease, sepsis, chronic pain, obesity, diabetes, lung injury, stroke, traumatic brain injury and arthritis (Johnson and Wilson, 2018). This interest has driven the continuous development of better VNS devices and stimulation techniques.

A major motivation to optimize the implementation of VNS has been the prevalence of side effects (Noller et al., 2019), including bradycardia, bradypnea, apnea, indigestion, throat and tonsil pain, cough, hoarseness, nausea and vomiting, headache, diaphragmatic flutter and paresthesia (Ben-Menachem, 2001, 2002). These side effects result primarily from the common practice of

stimulating the whole VN, as opposed to selectively stimulating only the parts responsible for modulating a given function (Plachta et al., 2014; Aristovich et al., 2021).

This review presents a brief overview of major clinical applications of VNS with regard to known anatomy and physiological functions of the VN, followed by in-depth discussion of major paradigms for selective VNS (sVNS) and the advantages of each paradigm. It is a focused review which attempts to cover the recent studies on sVNS. It provides an assessment of the future clinical applicability of sVNS and discusses what recent attempts to achieve selective activation of nerve fibers have revealed about VN physiology.

Anatomy and Functions of the Vagus Nerve

The VN (whose name means "wandering") is the longest nerve in the autonomic nervous system, projecting from the brain to a number of organs in the thorax and abdomen including the heart, lungs, larynx, pharynx, stomach, spleen, pancreas, liver, intestines, and ovaries (**Figure 1A**; Thompson et al., 2019). There are two VNs (left and right), but convention is to refer to the VN in the singular, even though there are some functional differences between the two VNs; most importantly, the right VN innervates the sinoatrial node of the heart whereas the left VN innervates the atrioventricular node. Despite extensive research over the last century, the functional fascicular anatomy of this complex nerve remains poorly understood (Thompson et al., 2020).

The VN contains both efferent and afferent fibers. The afferent fibers make up the vast majority (up to 90%) and relay interoceptive information from various organs to the brain and spinal cord; the remainder are parasympathetic efferents that allow the VN to influence the activity of innervated organs (Thompson et al., 2019). The VN also projects to areas within the brain and central nervous system (CNS), including the nucleus tractus solitarius (NTS), locus coeruleus (LC), thalamus, hippocampus, amygdala and other regions (**Figure 1B**; Thompson et al., 2019). Parasympathetic efferents originate in the dorsal motor nucleus and nucleus ambiguous. Sensory afferents within the cervical VN have their cell bodies in the nodose ganglia and extend their central projections to the NTS (Thompson et al., 2019).

Like all large peripheral nerves, the VN contains a mixture of different types of nerve fibers, which are organized into bundles (fascicles). The fibers vary in diameter and conduction velocity, with Aα fibers the largest and fastest (diameter 13–20 μm, conduction velocity 80–120 ms^{-1}), C fibers the smallest and slowest (0.2–1.5 μm, 0.5–2 ms^{-1}), and Aβ, Aγ, Aδ, and B fibers intermediate (Whitwam, 1976; Kandel et al., 2020). In humans, the VN at the cervical level typically contains between 5–8 fascicles, but individual variations have been documented at 1–21 per side) (Hammer et al., 2018). It is not definitely known whether each fascicle contains only one type of fiber (afferent or efferent) or both, or whether the fascicles are somatotopically arranged (i.e., arranged according to end-effect organ). Although, there is evidence for the latter and against the former (Settell et al., 2020).

To avoid off-target effects and improve overall efficacy of VNS, it is necessary to selectively stimulate fibers with known anatomical projection within the trunk of the VN (Thompson et al., 2019). On one hand, organ-specific branching of the VN, somatotopic organization of the cell bodies of vagal neurons in the brainstem nuclei, and clear evidence that VNS can elicit functionally specific physiological effects (Aristovich et al., 2021) have strengthened the belief that VN fibers are grouped somatotopically. On the other hand, evidence in the pig suggests a "bimodal" organization, in which motor and sensory fibers form two spatially distinct groups (Settell et al., 2020). It is possible that fibers are organized both bimodally and somatotopically. It is also important to bear in mind that anatomical variation of the VN exists between species, and so data from experimental animals do not necessarily translate to humans (Thompson et al., 2019). For example, there is evidence for somatotopic organization of the pseudounipolar cell bodies of sensory afferents in nodose ganglia. However, more recent research has suggested that this organization may only be present in pigs but not in humans (Settell et al., 2021). Large differences also exist in the diameter of the VN between species; this should be considered when evaluating the translational potential of VNS techniques demonstrated in small animals (such as rodents).

Side Effects of Non-selective VNS

During nerve stimulation, fibers are activated in order of size from the largest (A fibers) to the smallest (C fibers). The majority of side effects of nsVNS that limit its therapeutic efficacy (throat and tonsil pain, hoarseness) are associated with the activation of large A fibers innervating the mucosa and muscles of larynx and pharynx (Gold et al., 2016). Cough, another common side effect of VNS, is a reflex response to activation of rapidly adapting pulmonary stretch receptors (Aδ myelinated fibers in pulmonary epithelium) (Kubin et al., 2006).

Acute apnea and bradypnea result from the Hering-Breuer inflation reflex caused by stimulation of pulmonary A-fiber afferents innervating the slowly adaptive pulmonary stretch receptors present in the smooth muscles of the airways (Kubin et al., 2006). Cardioinhibitory action of VNS is attributed to stimulation of efferent myelinated B fibers (Qing et al., 2018). Bradycardia may also result from activation of the sinoatrial node when stimulating the right VN. For this reason, VNS is generally applied on the left side (Krahl, 2012). It is evident that electrical stimulation applied to the cervical VN preferentially activates large motor and sensory fibers (Aα and Aβ fibers) because they have a lower activation threshold than smaller efferent fibers (Ardell et al., 2017), therefore, simply altering parameters such as frequency and amplitude is not sufficient to alleviate these side effects, and may lead to a reduction in efficacy (Handforth et al., 1998; Ardell et al., 2017; Aristovich et al., 2021). Aα motor efferents projecting to the larynx also have low activation threshold. It is interesting to note that many papers do not specify the parameters used for VNS (Kwan et al., 2016). Systematic reporting of parameters in studies where VNS is used would greatly assist in optimizing those parameters for the reduction of side effects.

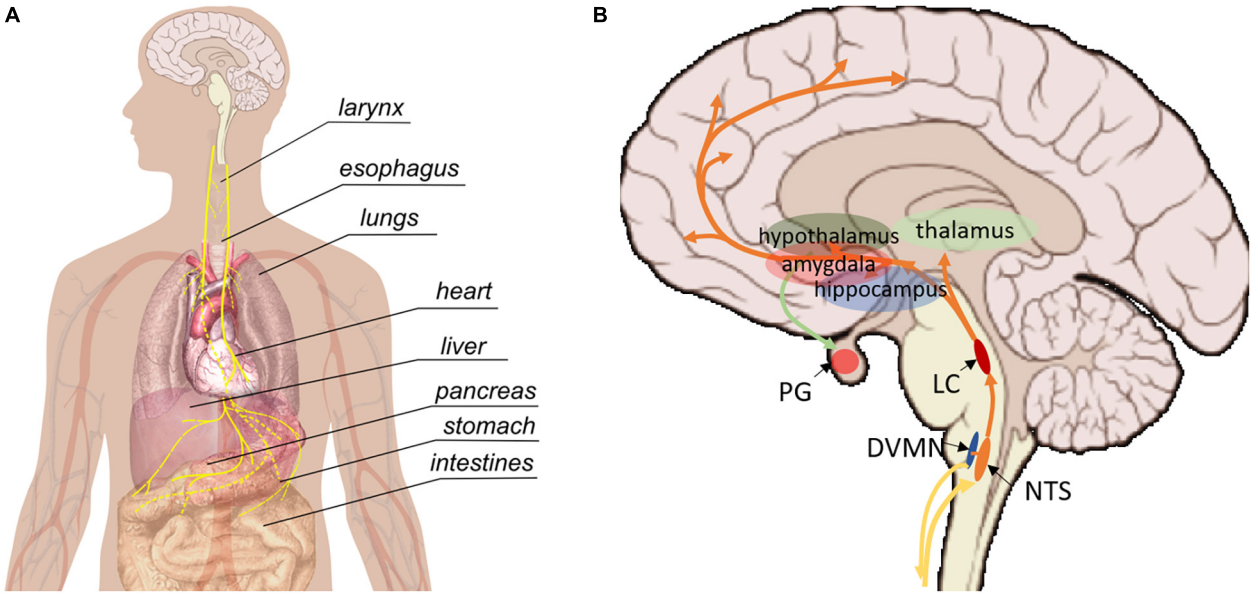

FIGURE 1 | Pathways involved in vagus nerve stimulation. **(A)** Peripherally, the vagus nerve provides afferent and efferent innervation of the majority of visceral organs. **(B)** Central regions that are impacted by vagus nerve stimulation. NTS, nucleus tractus solitarii; DVMN, dorsal motor nucleus of the VN; LC, locus coeruleus, PG, pituitary gland.

Unintentional activation of low-threshold motor nerve fibers during nsVNS could also be attributed to sub-optimal insulation of the electrode array. The current may leak out of the insulation, spreading to and activating any nearby fibers with a sufficiently low activation threshold (Nicolai et al., 2020). It is important to note that the risk of the current leak would be magnified by the use of more complex circuits, which is the case in sVNS where multiple current sources are usually required. This should be taken into account when designing the devices for sVNS.

APPLICATIONS OF VNS

Stimulation of the whole left cervical VN is an FDA-approved treatment for focal epilepsy and treatment-resistant depression (Krahl and Clark, 2012; Lv et al., 2019). Other clinical applications that have been explored for VNS include generalized seizures, cardiovascular disease, inflammation, obesity, chronic pain, respiratory disease, traumatic brain injury, stroke, post-traumatic stress disorder (Johnson and Wilson, 2018). Of these, cardiovascular applications have proven of greatest interest in the development of sVNS, due to the need to selectively target smaller diameter vagal fibers innervating the heart.

Heart Failure

Autonomic nervous system dysfunction, due to excessive sympatho-excitation and withdrawal of parasympathetic (vagal) tone, is a key mechanism of heart failure (Binkley et al., 1991; Floras and Ponikowski, 2015). VNS increased survival, slowed down the progression of myocardial remodeling, and improved ventricular function in numerous experimental models of heart failure (Li et al., 2004; Agarwal et al., 2016) as well as in some clinical studies (De Ferrari et al., 2010; Premchand et al., 2014). Moderate electrical stimulation (up to 2 mA) applied to the cervical VN preferentially activates afferent sensory fibers, which have a lower activation threshold than efferent fibers. This leads to a reflex low-level sympatho-excitation and increased heart rate (HR) (Ardell et al., 2017). Aggressive stimulation (>2.5 mA) could recruit efferent fibers responsible for vagally mediated lowering of the HR, but this would cause significant side effects, including dysphonia, neck pain, and cough (Zannad et al., 2014).

Ischemia-Reperfusion Injury

Myocardial ischemia-reperfusion injury (IR injury) refers to myocardial damage caused by blood supply returning to myocardial tissue following ischemia. It is frequently triggered by clinical therapies such as thrombolytic therapy or percutaneous transluminal coronary intervention (PCI). Preclinical studies in rats have shown that – following IR injury – VNS decreases infarct size, inflammation and incidence of ischemia-induced arrhythmias, oxidative stress, and apoptosis in cardiomyocytes (Mioni et al., 2005; Calvillo et al., 2011). These effects are predominantly mediated by efferent vagal fibers (Mastitskaya et al., 2012; Nuntaphum et al., 2018). There are no clinical data on cervical VNS in acute myocardial injuries.

Arrhythmia

VNS has successfully been used to manage both atrial and ventricular arrhythmias in preclinical and clinical studies (Li and Yang, 2009). VNS administered at a voltage below the bradycardia threshold significantly increases the effective refractory period, which suppresses atrial fibrillation (Li and Yang, 2009). It would be interesting to explore the comparative efficacy of potential

sVNS techniques to manage arrhythmia without the risk of unintentional bradycardia.

Focal Epilepsy

Epilepsy is a chronic neurological disorder characterized by episodes of aberrant synchronous neural activity, also known as seizures. Seizures can result in loss of consciousness, loss of motor coordination and other neurological symptoms (Scheffer et al., 2017). Epilepsy is generally treated with anti-epileptic drugs, but up to 30% of cases do not respond to medication (Moshé et al., 2015). For these refractory epilepsy patients, surgical resection of the epileptogenic zone may be necessary. However, this cannot be carried out in 50% of patients and is ineffective in 30% of the remaining ones (Neligan et al., 2012). VNS of the left cervical VN has emerged as a safe and reliable means of treating such patients. It is believed that solely afferent fibers are involved in the mechanisms of VNS therapeutic effects for epilepsy, because epilepsy is primarily a disorder of the brain. Accordingly, an optimal seizure-suppressive sVNS would avoid activation of efferent fibers projecting to the heart, lungs and other organs in the torso. If the internal anatomy of the VN is functionally organized, it would also be desirable to locate and selectively activate the fascicles responsible for seizure-suppression (Thompson et al., 2019). It is not known which VN fascicles, if any, project to implicated brain regions, but evidence for spatial organization in respect to cardiac and pulmonary projections may help to discover this by a process of elimination (Aristovich et al., 2021).

Treatment-Resistant Depression

Major depressive disorder (MDD), also known as clinical depression, is a psychological disorder in which an individual experiences consistent and persistent low mood for at least 2 weeks (Otte et al., 2016). Around 30% of MDD patients have treatment-resistant depression, usually defined as MDD that does not respond to two distinct courses of anti-depressant medication. VNS was approved for treatment-resistant depression in 2005, with over 4,000 patients currently undergoing this treatment (Otte et al., 2016).

Inflammation

The VN serves as an important communication link between the immune system and brain. VNS has proven successful in treating disorders involving local and systemic inflammatory response due to its anti-inflammatory effects (Rosas-Ballina et al., 2011; Vida et al., 2011). VNS achieves these effects via activation of two major pathways: the cholinergic anti-inflammatory pathway (CAIP) and hypothalamic-pituitary-adrenal (HPA) axis (Hoffmann et al., 2012). CAIP involves release of acetylcholine (ACh) from VN efferents in the celiac mesenteric ganglia, which acts on post-synaptic α-7-nicotinic ACh receptors of the splenic nerve leading to the release of noradrenaline in the spleen, which dampens pro-inflammatory cytokine production by macrophages (Rosas-Ballina et al., 2011; Vida et al., 2011). Activation of HPA axis is attributable to vagal afferent fibers projecting to the nucleus of the solitary tract (NTS) in the brainstem. Stimulation of vagal afferents activates the adrenergic projections from NTS to the hypothalamus, release of corticotropin-releasing hormone and production of adrenocorticotropic hormone by the pituitary gland with an ultimate effect on the adrenal cortex and increased secretion of glucocorticoids (Hoffmann et al., 2012).

Asthma and Chronic Obstructive Pulmonary Disease

Asthma and chronic obstructive pulmonary disease (COPD) are respiratory illnesses involving potentially life-threatening airway obstruction. This can be caused by enhanced parasympathetic activity, which results in airway smooth muscle contraction, increased mucus secretion and vasodilation in pulmonary vessels. This activity is also the dominant component of oedema in lung inflammation. High voltage VNS resulting in stimulation of vagal efferents in the lungs is ill-advised, as it could lead to bronchospasm as a side effect. However, low voltage VNS has been shown to preferentially activate vagal afferents and cause bronchodilation due to systemic increase of catecholamines via activation of the HPA axis (Hoffmann et al., 2012).

SELECTIVE VNS

Paradigms of VNS

A number of research groups have demonstrated that it is possible to achieve functionally specific effects from sVNS by selectively targeting and modulating organ function in various animal models and human patients (Pečlin et al., 2009; Plachta et al., 2014; Aristovich et al., 2021). sVNS results in similar or improved therapeutic effects compared to nsVNS, whereas side effects are reduced (Plachta et al., 2014). Hence, optimization of sVNS has become an important endeavor in nerve stimulation research.

Several major sVNS paradigms have been developed: fiber-selective stimulation, spatially selective stimulation, anodal block, kilohertz electrical stimulation (KES) block and neural titration. Across these paradigms, the development of sVNS techniques has typically focused on optimizing the shape of the stimulation pulse, the geometry of the electrode array and the stimulation protocol. In the following section, we provide an overview of the methods, effects and recent advances of the major sVNS paradigms.

Existing sVNS Techniques

The most basic approach to sVNS is to identify which branch of the nerve projects to the organ(s) of interest, and then stimulate that branch. This method has been used since at least 1992, when Furukawa and Okada (1992) demonstrated responses in the gallbladder of a dog from stimulation of the whole gastric branch (Furukawa and Okada, 1992). However, this method is incompatible with established surgical procedures. These are optimized for implantation of cuff arrays around the cervical VN with minimal complications (Ben-Menachem, 2002). Thus, it is more desirable to achieve sVNS through optimized stimulation of the cervical VN.

One potential approach for achieving selectivity at the cervical level is to surgically tease apart the VN and apply stimulation solely to particular fascicles. This could be done with a microchannel array (Lancashire et al., 2016). However, the functional anatomy of the VN is not characterized well enough. It would also be highly invasive, risking severe irreversible nerve damage. For these reasons, microchannel arrays are not widely used in humans, and less invasive sVNS procedures are desired.

Besides transcutaneous stimulation – which is unlikely to produce selective effects due to current spreading as it passes through the skin and connective tissue – the least invasive practice uses a cuff array that wraps around the nerve (Chapman et al., 2018). With such arrays, two main paradigms for sVNS have been demonstrated:

(1) fiber-selective stimulation: exploits the different activation thresholds of VN fibers to separately activate selected fiber type.
(2) spatially selective stimulation: application of electrical stimulus to specific area of the nerve cross-section to only activate selected fascicles.

Both approaches have recently been demonstrated (Plachta et al., 2014; Dali et al., 2018), with the fiber-selective approach proving more popular (see **Table 1**). However, evidence for spatial organization in the VN, combined with difficulties in avoiding the activation of larger fibers, has motivated the search for a spatially selective paradigm (Plachta et al., 2014). One should also bear in mind that it is not possible to completely separate these two paradigms, since protocols that aim at fiber-selectivity usually involve some degree of spatial-selectivity and vice versa (Vuckovic et al., 2008).

With a cuff array, it is also possible to implement blocking of nerve impulse propagation (both selectively and non-selectively). Kilohertz electrical stimulation block (KES block) is a type of blocking that is designed to ensure impulses only travel in one direction along the VN; this ensures a certain degree of functional selectivity, akin to that achieved by vagotomy (Patel and Butera, 2018). KES can also be used as a technique to achieve fiber-selective stimulation (Vuckovic et al., 2008), as can the more common form of nerve blocking, anodal block. Anodal block occurs when the anode (positive terminal) of a pair of electrodes causes hyperpolarization in the section of the nerve below it (**Figure 2B**; Vuckovic et al., 2008); hyperpolarizing axons (bringing them to a negative potential) closes voltage-gated sodium channels in the plasma membrane, preventing an action potential from being generated. The mechanisms of KES are still being investigated, although it is believed that KES inactivates sodium channels through excessive depolarization of the nerve (Kilgore and Bhadra, 2004). These forms of the block are often imperfect; realistically, they are more likely to achieve a partial block than a full directional selectivity.

Neural titration, introduced by Ardell and colleagues (Ardell et al., 2015, 2017), relies on the establishment of a dynamic equilibrium (neural fulcrum) that cancels out side effects (in their case focusing on bradycardia). Fibers that elicit bradycardia (vagal efferents) and fibers that elicit tachycardia (afferents) were activated at the same time, and stimulation amplitude was adjusted until the effects of the two fiber-types were perfectly balanced (Ardell et al., 2017).

Fiber-Selective VNS

Most of the recent research in sVNS has focused on applications for cardiovascular disease (see **Table 1**). Whereas VNS for epilepsy and MDD primarily requires activation of larger fibers (A and B types), cardiac neuromodulation primarily requires activation of smaller fibers (B and C types) (Dali et al., 2018). Since the threshold for activation of smaller fibers is at a higher current amplitude (Bawa et al., 2014), cardiovascular VNS would be expected to engender more severe side effects than VNS for epilepsy and MDD. Thus, several research groups have focused on developing fiber-selective VNS for cardiovascular applications.

Tosato et al. (2007) explored the selective control of HR in a porcine model, using anodal block to prevent the activation of larger fibers (**Figures 2B**, **3A**). They were able to successfully lower HR while reducing laryngeal side effects by up to 77% (Tosato et al., 2007). They compared three different methods for achieving selective activation of cardiac vagal fibers: depolarizing pre-pulses, slowly rising pulses and anodal block (Vuckovic et al., 2008). A depolarizing pre-pulse (**Figure 2C**) is a small stimulus, which arrives just before the main stimulatory pulse with an amplitude just below the excitation threshold of the largest fibers; this pre-pulse raises the excitation threshold of those fibers through sodium channel inactivation (although it may also lead to anodal break excitation when it ends) (Vuckovic et al., 2008). Slowly rising pulses (**Figure 2D**) have an initial curved ramp, which reverses recruitment order by inactivating sodium channels and exploiting variations in the spatial distribution of membrane potential between fiber types (Hennings et al., 2005). Anodal block completely prevented activation of Aβ fibers in two out of five pigs, and reduced Aβ activity by 60–90% in the other three (Vuckovic et al., 2008). The large diameter of the VN in pigs necessitated high-amplitude current (up to 10 mA) to implement the block. This may have led to excitation of fibers at the edge of the nerve, hence preventing full block (Vuckovic et al., 2008). Depolarizing pre-pulses achieved up to a 90% reduction in Aβ activity; slowly rising pulses achieved up to 60%. This was determined by observing the reduction in size of the Aβ component of the compound action potential via electroneurogram. The authors endorse depolarizing pre-pulses as their preferred method, being the only one of the three approaches that was effective with safe levels of charge-injection (Vuckovic et al., 2008). It should be noted that whether a pulse can be achieved with safe charge injection depends to some extent on electrode geometry, and it may also vary between species.

Ahmed et al. (2020) have demonstrated that anodal block is capable of eliciting a significant degree of directional selectivity in the rat VN, although efficacy was inconsistent. Swapping the orientation of the cathode and anode was associated with preferential activation of efferent or afferent fibers, as shown by differential effects on breathing or HR, respectively. In 3 out of 17 rats, however, the opposite effect of electrode polarity was observed; the authors attribute this to anatomical differences

TABLE 1 | Major recent papers on sVNS in chronological order.

Publication	sVNS Method(s)	Outcomes	Pulse parameters	Electrode geometry
Tosato et al., 2007. Quasi-trapezoidal pulses to selectively block the activation of intrinsic laryngeal muscles during vagal nerve stimulation," *J. Neur. Eng*. 4. 3. 205–12.	Anodal block for fiber-selective control of HR in pig.	Success lowering HR laryngeal side effects reduced by 77%.	Quasi-trapezoidal pulse. Flat phase 0.6 ms and exponentially decaying phase 2.4 ms; maximal response at 5–15 mA with QT pulses, 0.5–20 Hz, **Figure 2F**.	3.4 mm inner diameter cuffs with 1 mm wide platinum rings, 4 mm spacing in between rings **Figure 3B**.
Vuckovic et al., 2008. A comparative study of three techniques for diameter selective fiber activation in the vagal nerve: anodal block, depolarizing prepulses and slowly rising pulses. *J. Neur. Eng.* 5. 3. 275–86.	Compare anodal block, depolarizing pre-pulses, slowly rising pulses; selectively activate smaller fibers in pig.	60–100% reduction in Aβ fiber activity with anodal block. Up to 90% reduction with depolarizing pre-pulses. Up to 60% with slowly rising pulses.	Anodal block: quasi-trapezoidal pulse with 0.4–1 ms flat period and up to 1 ms exponentially decaying phase. 4–12 mA. Max 30 Hz, **Figure 2B**. Depolarizing pre-pulse: 0.2–0.8 ms low amplitude pulse (highest excitation threshold determined experimentally) followed by 0.2–0.6 ms higher amplitude pulse (2–6 mA). Max 105 Hz, **Figure 2C**. Slowly rising pulses: 1–5 ms exponentially or hyperbolically rising curve followed by 0–0.1 ms flat period. 2–6 mA. Max 28 Hz, **Figure 2D**.	Split cylinder cuff electrodes. Tripole with 3 mm separation between contacts used for stim.
Rozman and Peclin, 2008. Selective stimulation of autonomic nerves and recording of electroneurograms in a canine model. *Artificial Organs.* 32. 8. 592–6.	Fiber-selective stim with electrodes in varying positions around nerve circumference control HR and RR in dog.	Successful selective modulation of HR and RR.	Current, biphasic, charge balanced quasi-trapezoidal pulse as in Peclin and Rozman (2009), see above, **Figure 2F**.	39 rectangular electrodes arranged in a matrix of 9 parallel groups, with the stim section 11 groups of 3 electrodes in the middle of the matrix, and two blocking sections with 11 electrodes each positioned bilaterally to the stim section, **Figure 3F**.
Peclin and Rozman, 2009. A model of selective left VNS and recording in a man. *IFMBE*. 1628–31.	Fiber-selective stim to control HR in humans.	Successful reduction of HR preferential activation of B fibers over A fibers.	Current, biphasic, charged-balanced quasi-trapezoidal pulse; cathodic with approx 1 mA square leading edge, 0.3 ms plateau and exponentially decaying phase of 0.3 ms; anodic rectangular pulse of low magnitude **Figure 2F**.	39 rectangular electrodes with thirteen circumferential groups of 3 electrodes. 0.6 × 1 mm. Inner diameter of cuff 2.5 mm, length 20 mm. [Details given in Rozman et al. (1993)] **Figure 3F**.
Ordelman et al., 2013. Selectivity for Specific cardiovascular effects of Vagal nerve Stimulation with a multi-contact electrode cuff. *IEEE Trans. Neural Syst. Rehab. Eng*. 21. 1.	Spatially selective stim with a muti-contact cuff in pig.	Increased efficacy in cardiac modulation compared to nsVNS (greater number of cardiac parameters significantly altered by stim).	Biphasic pulses. Second pulse has exponential shape, 1st phase pulse width 0.3 ms, 1–10 mA, 10–50 Hz. Burst stim maintained up to 60 s, **Figures 2A,B**.	One config has rings, 15 mm long with 3 circular electrodes, interelectrode distance 4 mm. Surface area of each 2 mm^2. Spacing of electrodes at 90-degree intervals, **Figure 3B**.
Plachta et al., 2013. BaroLoop: using a multichannel cuff electrode and selective stimulation to reduce blood pressure. *Conf. Proc. IEEE Eng. Med. Biol. Soc.* 755–8.	Demonstration of system for BP control via spatially selective stim. Data from rats.	Successful control of BP with "almost no side effects."	Biphasic rectangular pulses, adjusted for charge balance. Tripole which shows baroreceptive activity located; center electrode of this tripole is cathode against two large ring electrodes. 200 pulses per stim 30–50 Hz, 0.3–1 mA, inter-stimulus interval 10 s **Figure 2A**.	24 electrodes, arranged in 8 tripoles around the cuff perimeter with 45 degree spacing. Cuff length 12 mm, diameter 0.8 mm. Distance between cross-sectional electrodes 2 mm **Figure 3D**.

(Continued)

TABLE 1 | Continued

Publication	sVNS Method(s)	Outcomes	Pulse parameters	Electrode geometry
Plachta et al., 2014. Blood pressure control with selective vagal nerve stimulation and minimal side effects. *J. Neur. Eng.*. 11. 036011.	Spatially selective tripolar stim in rats control BP without altering HR.	Significant reduction in BP with no bradypnea and less than 25% reduction in HR.	Current controlled, charge balanced, rectangular pulses 200 pulses per stim. Interval at least 10 s between stim 30–50 Hz, 0.3–1 mA, pulse width 0.1–0.5 ms, **Figure 2A**.	Same as in Plachta et al., 2013 (see above).
Pečlin and Rozman, 2014. Alternative paradigm of selective VN stimulation tested on an isolated porcine VN. *The Scientific World Journal*. 310283.	Fiber-selective stim. Experiments in pigs. Demonstration of "quasi-trapezoidal" pulse shape.	Limited fiber-selective VNS was achieved, with increased A fiber activation and decreased B fiber activation.	Current, biphasic, charged-balanced quasi-trapezoidal pulse; cathodic with approx 1 mA square leading edge, 0.3 ms plateau and exponentially decaying phase of 0.3 ms; anodic rectangular pulse of low magnitude **Figure 2F**.	99 rectangular electrodes arranged in a matrix of 9 parallel groups, with the stim section 11 groups of 3 electrodes in the middle of the matrix, and two blocking sections with 11 electrodes each positioned bilaterally to the stim section **Figure 3G**.
Qing et al., 2015. Burst-modulated waveforms optimize electrical stimuli for charge efficiency and fiber selectivity. *IEEE Trans. Neural Syst. Rehab. Eng*. 23. 6. 936–45.	Bursts of small rectangular pulses for spatially selective stim.	C fibers kept above 50% activation with activation of A fibers reduced 11% compared to nsVNS.	Charge balanced, cathode leading, alternating monophasic rectangular waveforms or burst waveforms 10 s stim followed by 10 s recovery; pulse width 40–200 μs, Max amplitude 1.5 mA, 10–20 Hz **Figure 2A,E**.	Leads spaced 1 mm apart with contact area 0.011 cm^2 for each lead.
Patel and Butera, 2015. Differential fiber-specific block of nerve conduction in mammalian peripheral nerves using kilohertz electrical stimulation. *J. Neurophysiol.* 113. 10. 3923–9.	Fiber-selective stim with KES in rats.	Able to selectively block the fast and slow components of the compound action potential.	Supramaximal cathode-first biphasic pulses 5 V, 0.2 ms KES block stimulus is continuous sinuosoid, 50–70 kHz.	Tripolar, longitudinally slit cuff. 0.75 mm between contacts, cuff diameter for 1–1.2 mm and length 3 mm, **Figure 3B**.
Plachta et al., 2016. Effect of cardiac-cycle synchronized selective vagal stimulation on heart rate and blood pressure in rats. *Advances in Therapy*. 33. 7. 1246–61.	Spatially selective stim using pulsatile stimulus synchronized to cardiac cycle. Experiments in rats.	Able to reduce BP and keep it lower without significant bradycardia.	Biphasic rectangular pulses, 100 pulses in three sets 30–50 Hz, 0.2–0.9 mA, 0.2–0.9 ms pulse width **Figure 2A**.	24 electrodes, arranged in 8 tripoles around the cuff perimeter with 45 degree spacing. Cuff length 12 mm, diameter 0.8 mm. Distance between cross-sectional electrodes 2 mm, **Figure 3D**.
Yoo et al., 2016. Modulation of heart rate by temporally patterned VN stimulation in the anesthetized dog. *Physiol. Rep.* 4:12689.	Fiber-selective stim in dogs.	Able to selectively modulate HR and laryngeal EMG. Laryngeal side effects during cardiac modulation reduced 50% compared to nsVNS.	1 s inter-burst interval, 20 s pulse train, 2–20 pulses per burst, pulse width 0.3 ms, frequency 10–50 Hz thresholds a fibers 0.08 mA, fast B 1.5 mA, slow B 4.4 mA, **Figure 2A**.	Bipolar, helical electrode **Figure 3A**.
Patel et al., 2017. Kilohertz frequency nerve block enhances anti-inflammatory effects of VN stimulation. *Nature Scientific Reports.* 7. 39810.	KES for virtual vagotomy, directionally specific block.	Successful unidirectional block in most cases, although block was sometimes incomplete.	Biphasic constant current pulses 1 mApp, 0.4 ms pulse width, 1 Hz KES at 40 kHz, 1.5–2 mA peak.	Custom, bipolar electrodes, stainless steel wire threaded through silicone tubing and spot welded to Pt-Ir contact pads **Figure 3C**.
Dali et al., 2018. Model based optimal multipolar stimulation without *a priori* knowledge of nerve structure: application to VN stimulation. *J. Neur. Eng*. 15.4. 046018.	Spatially selective stim for cardiac modulation. Experiments in sheep.	62% reduction in side effects compared to nsVNS.	Rectangular pulses acute tests: on 60 s, off 30 s; pulse width 240 μs, 25.6 Hz frequency; 4 pulses per cardiac cycle. Implant-explant: on 16 s, off 44 s; 25.6 Hz frequency; Pulse width 300 μs 0.2–1.5 mA (anesthesia), 1–3 mA (conscious) chronic: on 30 s, off 30 s; 25.6 Hz frequency pulse width 300 μs, **Figure 2A**.	Modeling of different geometries (ring, tripolar longitudinal ring (TLR), transverse tripolar (TT), transverse tripolar ring (TTR) with cathode at 0, 90, 180, and 270 degrees around the circumference **Figure 3H**.

(Continued)

TABLE 1 | Continued

Publication	sVNS Method(s)	Outcomes	Pulse parameters	Electrode geometry
McAllen et al., 2018. Calibration of thresholds for functional engagement of vagal A–C fiber groups *in vivo*. *Bioelectronic Medicine*. 1. 1. 21–27.	Fiber-selective stim. Experiments in rats.	Monitoring HR and RR while changing stimulating modality allowed for thresholds of different fiber types to be found.	Constant voltage square pulses pulse width 0.1 ms 1–2 Hz **Figure 2A**.	2 Electrodes, details of geometry not given.
Dali et al., 2019. Comparison of the efficiency of chopped and non-rectangular electrical stimulus waveforms in activating small VN fibers. *J. Neurosci. Methods.* 320. 1–8.	Fiber-selective stim. Modeling and then experiments in pigs.	Ramp-shaped pulse and sine-wave shaped chopped pulse good for targeting smaller fibers.	Chopped pulses, rectangular and ramp rectangular, ramp, quarter-sine: pulse width 350 μs chopped quarter-sine: 325 μs or 1 ms. Amplitude corresponded to charge of 1.5 nC. Frequency 2 Hz. 6 pulses with 1 s inter-pulse interval. **Figure 2E**.	Two rows of Pt-Ir electrodes with a diameter of 3 mm. Rows shorted together to form a bipolar ring. **Figure 3C**.
Aristovich et al. (2021). Model-based geometrical optimisation and in vivo validation of a spatially selective multielectrode cuff array for vagus nerve neuromodulation. *J. Neuroscience Methods.* 352. 109079.	Spatially selective stim. Modeling with FEM and experiments in sheep.	Can selectively lower RR by up to 90% without significant change in HR, and lower HR up to 27% without significant change in RR.	30 s stim, 30 s recovery square, biphasic (positive first) constant current temporal waveform with balanced current source pulse width 100 and 50 μs per phase, no interpulse interval 20 Hz frequency, 450–550 μA optimal for RR change without HR change **Figure 3A**.	Modeling of various geometries. optimal array fabricated with 14 longitudinal electrode pairs, 3 mm apart, width 0.4 mm and 0.35 mm interelectrode circumference distance, 3 mm length **Figure 3E**.

Summary of results, methods, pulse parameters and electrode geometry. RR, respiratory rate. HR, heart rate. BP, blood pressure. KES, kilohertz electrical stimulation.

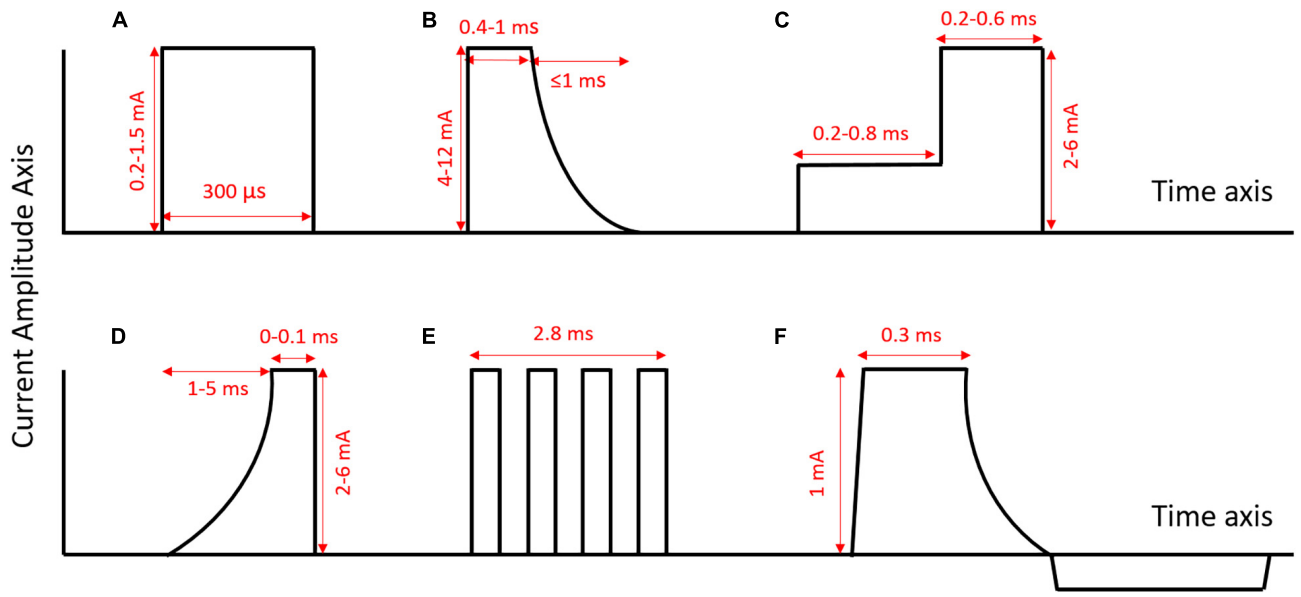

FIGURE 2 | Examples of different pulse shapes used in sVNS (axes not to scale). **(A)** Normal rectangular pulse [as used in Dali et al. (2018)]. **(B)** Anodal block pulse [as used in Vuckovic et al. (2008)]. **(C)** Depolarizing pre-pulse [as used in Vuckovic et al. (2008)]. **(D)** Slowly rising pulse [as used in Vuckovic et al. (2008)]. **(E)** Chopped pulse [as used in Dali et al. (2019)]. **(F)** Quasi-trapezoidal pulse [as used in Pečlin and Rozman (2014)]. Rectangular pulses are the standard pulse shape used in the nerve stimulation. They are easy to generate, and their symmetry makes it easier to ensure charge balance. However, pulses with more unusual shapes, such as chopped pulses or pulses with ramped parts, allow for the delivery of current throughout the pulse to be adapted to specific applications.

between rats, specifically the position of the aortic depressor nerve relative to the main trunk of the VN (Ahmed et al., 2020). The possible effects of anatomical variation must be noted when attempting to translate anodal block to human patients.

Peclin and Rozman (2009) were the first to demonstrate fiber-selective VNS in humans (Pečlin et al., 2009; Peclin and Rozman, 2009), following earlier work in a canine model (Rozman and Peclin, 2008). In the dog, they demonstrated selective control of HR and respiration rate by stimulating with sets of three electrodes at different positions around the nerve circumference (**Figures 3F,G**; Rozman and Peclin, 2008). They then applied the same technique to two human patients, reducing the HR

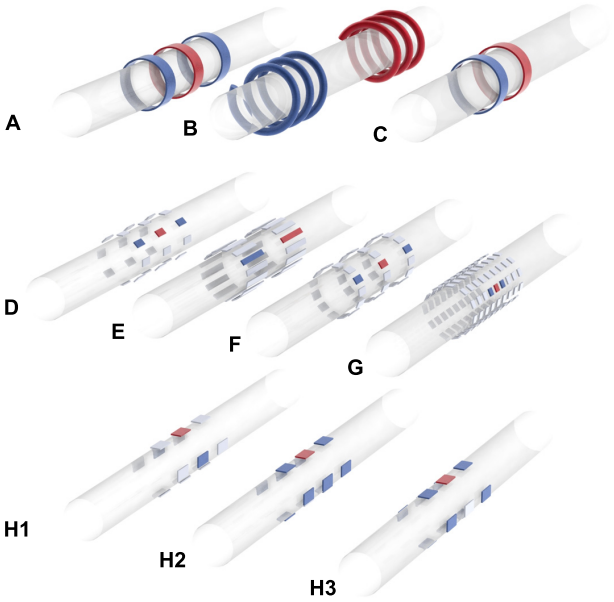

FIGURE 3 | Electrode array geometries and stimulation patterns used in major sVNS studies. **(A)** Yoo et al. (2016). **(B)** Ordelman et al. (2013), Patel and Butera (2015), Tosato et al. (2007). **(C)** Pelot and Grill (2020), Patel et al. (2017), Dali et al. (2019). **(D)** Plachta et al. (2013, 2014, 2016), Gierthmuehlen and Plachta (2016). **(E)** Aristovich et al. (2021). **(F)** Peclin and Rozman (2009). **(G)** Pečlin and Rozman (2014). **(H)** Dali et al. (2018) [**H1**: transverse tripolar (TT), **H2**: transverse tripolar ring (TTR), **H3**: tripolar longitudinal ring (TLR)]. Blue = anode, red = cathode, gray = unused. Researchers have used a range of different electrode array geometries for sVNS. Some have used rings or helical electrodes; recently there is a move toward smaller rectangular contacts that can be placed at different positions around the nerve circumference. These contacts are often arranged to allow for bipolar or tripolar stimulation.

while preferentially activating B over A fibers (Pečlin et al., 2009). Their method involves the use of "quasi-trapezoidal" pulses (**Figure 2F**), which activate A and B fibers during their square cathodal phase, before blocking A fibers during an exponentially decaying anodal phase (Pečlin and Rozman, 2014). However, in humans, this work has only been published in the form of conference abstracts and has not been peer-reviewed.

Qing et al. (2015), working in a rat model, achieved fiber-selective stimulation through the use of "chopped pulses," replacing normal rectangular waves with repeated bursts of smaller rectangular waves whose width, interval and number can be modulated (**Figure 2E**; Qing et al., 2015). The earlier pulses in the burst caused inactivation of sodium channels, primarily in large fibers, allowing smaller fibers to be preferentially excited by the later pulses. Chopped pulses are easier to produce with a normal stimulator than quasi-trapezoidal waves, and avoid the need that pre-pulses have for a precise determination of excitation threshold (Qing et al., 2015). A and C fiber activation were identified by Qing and colleagues from two separate peaks in the compound nerve action potential, with the height of the peak taken as the degree of activation. Chopped pulses and normal rectangular pulses were compared at 50% of the charge required to elicit the maximum C fiber response. At this charge level, chopped pulses where able to maintain C fibers at 50% activation while reducing activation of A fibers by 11% compared to stimulation with normal rectangular waves (Qing et al., 2015). While 11% is a significant reduction, Qing and colleagues did not investigate if it was sufficient to significantly mitigate side effects.

Yoo et al. (2016) applied a similar method in dogs, demonstrating successful HR modulation while reducing laryngeal side effects by 50% compared to nsVNS (Yoo et al., 2016). Here, the extent of laryngeal side effects was indicated by the amplitude of laryngeal electromyogram signals. The authors claim that chopped pulses displayed comparable or superior efficacy to nsVNS. However, this is not true if stimulation amplitude is held constant: their data shows that nsVNS elicits a greater reduction in HR than chopped pulses at the same frequencies when the amplitude is above the bradycardia threshold (Yoo et al., 2016); thus, selective stimulation here entailed lower efficacy.

Dali et al. (2019) compared chopped to continuous pulses, while also varying the overall pulse shape, creating a chopped-ramp (linearly increasing amplitude of each pulse within the train) and a chopped quarter-sine (amplitude of pulses within the train follows part of a sine wave). They focused on afferent gastric fibers, stimulating them distally and recording proximally at individual afferent B fibers. The threshold charge required to activate the B fibers was 19% lower for a ramp pulse than a rectangular pulse, and 15% lower for a quarter-sine pulse than a rectangular. The continuous ramp was the most energy efficient pulse shape (Dali et al., 2019).

Spatially Selective VNS

The first study to focus on spatially selective VNS was Ordelman et al. (2013), who suggested this approach as a solution to the difficulties faced by Tosato et al. (2007) in achieving full block of the targeted fiber type (Ordelman et al., 2013). Full block of a certain fiber type may be difficult to achieve if the fibers have highly varying cross-sectional position within the nerve. Ordelman and colleagues, working with a multi-contact cuff (**Figure 3B**), achieved almost double the efficacy in cardiac modulation compared to conventional VNS in pigs; 20–60 s after stimulation, HR measured by RR interval was reduced by 10% with nsVNS, and 18% with sVNS. The variance in HR reduction was quite high, however, especially with sVNS (Ordelman et al., 2013).

The same year, Plachta and colleagues presented their BaroLoop spatially selective VNS system (**Figure 3C**), demonstrating successful modulation of blood pressure (BP) in the rat; BP was reduced to 60% of the baseline value with no significant bradycardia or bradypnea (Plachta et al., 2013). It was also possible to achieve a permanent reduction in baseline BP if treatment was applied chronically. However, this study did not compare the efficacy of sVNS to nsVNS, but only compared an optimal selective paradigm to a non-optimal selective one. Nonetheless, it did provide evidence that fibers specific to BP modulation are localized to one side of the VN, since stimulation at the side directly opposite elicited bradycardia with no reduction in BP (Plachta et al., 2013).

Plachta and colleagues, who have been the main research group developing spatially selective techniques, presented similar results in 2014 (Plachta et al., 2014). In rats, they first localized the fibers responsible for BP control by measuring the response for different tripoles, before using sVNS to lower BP up to 40%. They observed no significant bradypnea and maximum 25% bradycardia, but did not prevent laryngeal side effects. In subsequent studies, they showed that the BP-reducing effects of their technique were attenuated but still significant in the presence of several major anti-hypertensive drugs (Gierthmuehlen and Plachta, 2016; Gierthmuehlen et al., 2016). However, stimulation-induced apnea was significantly increased in the presence of metoprolol (Gierthmuehlen and Plachta, 2016).

Dali et al. (2018) attempted to translate spatially selective VNS to the sheep (Dali et al., 2018). First, they conducted a modeling study with a finite element model of a nerve in order to optimize their stimulation parameters. The nerve model had 22 fascicles and was derived from cross-sectional images of a sheep VN. The Laplace equation was solved on the FEM in COMSOL, and then the optimal stimulation parameters were determined via a cost function that maximizes efficiency, selectivity and sensitivity to current amplitude. It was found that a configuration which the authors called "transverse tripolar" (TT) provided the best selectivity (**Figure 3H1**). However, when implementing sVNS *in vivo*, another configuration called "transverse tripolar + ring" (TTR) provided an optimal balance between selectivity and efficiency (**Figure 3H2**). Both were superior to the "tripolar longitudinal ring" (TLR) (**Figure 3H3**) and to the "ring" (nsVNS). With TTR, they were able to control HR while reducing side effects by 62% compared to nsVNS. However, the authors do not specify which particular side effects were included in their side effects index. It is also not clear whether any of the selective configurations was as effective as nsVNS.

Aristovich et al. (2021) aimed to further develop spatially selective VNS through optimization of the geometrical parameters in a sheep model (Aristovich et al., 2021). Initial computer modeling suggested the best geometry was a symmetrical arrangement with electrodes at the same position around the circumference (**Figure 3E**). This geometry was tested in twelve sheep, where it was possible to selectively reduce respiration rate by 90% without significant bradycardia and HR by 27% without significant bradypnea. Comparing the percentage HR and respiration rate changes across different stimulation modalities also indicated marked spatial-functional organization of the sheep VN. Laryngeal side effects were not considered by Aristovich et al. (2021).

The spatial selectivity has a limited value with respect to avoidance of the therapy-limiting side effects as they are mediated by Aα motor fibers and Aβ sensory fibers which have much lower activation thresholds (Ardell et al., 2017). For instance, it is possible that the laryngeal motor fibers would be activated during the therapeutic spatially selective stimulation even if they are located spatially on the other side of the nerve. This technique, however, can potentially be combined with directional selectivity such as anodal block (Ahmed et al., 2020) to at least partially overcome the stated limitations.

Kilohertz Electrical Stimulation Block

KES block is a technique in which an electrical stimulus of at least 5 kHz is applied to a nerve to inhibit action potential propagation (Patel and Butera, 2018). The technique was first demonstrated in the sciatic nerve of a frog, before being applied to the VN by Patel and Butera (2015). Traditionally, KES has aimed to block the entire nerve, providing only directional selectivity, although the work by Patel and Butera (2015) has shown that this kind of blocking can also achieve fiber-selective stimulation (Patel and Butera, 2015). In practice, it is rare for such directionally selective techniques to achieve a complete block even when this is their aim. It is also not clear what practical advancements KES seeks to make over anodal block.

Patel et al. (2017) used KES of the whole nerve to achieve directionally selective stimulation (Patel et al., 2017). In the rat cervical VN, they were able to selectively activate the efferent pathways while inhibiting transmission along the afferent ones (and hence simulate a vagotomy). Their aim was to improve anti-inflammatory VNS for the treatment of rheumatoid arthritis. Compared to nsVNS, full block via KES delivered an improved anti-inflammatory effect. However, when KES only achieved partial block, systemic inflammation was worse. KES also sometimes lead to severe nerve damage if parameters were not carefully chosen (Patel et al., 2017).

Neural Titration

Neural titration relies on antagonistic mechanisms within vagal control of cardiac function, as discovered by Ardell and colleagues (Ardell et al., 2015). Afferent and efferent fibers have opposite effects on the modulation of HR. Rather than attempt to avoid activation of fibers causing bradycardia, afferent and efferent fibers can be simultaneously activated to precisely the extent required for the bradycardic effects of efferent fibers to cancel out the tachycardic effects of afferent fibers (Ardell et al., 2015). Ardell and colleagues call this dynamic equilibrium "the neural fulcrum"; it is defined as the current amplitude just below that at which bradycardia is reliably evoked (bradycardia defined as a 5% decrease in HR in three consecutive stimulation sessions) (Ardell et al., 2017). Ardell and colleagues assessed the efficacy of this technique in dogs (Ardell et al., 2015). Stimulation parameters were varied to find the neural fulcrum, which remained stable for at least 14 months. However, their method had limitations. Thirty days of sessions were required to find optimal stimulation parameters for each dog, which is impractical for clinical use (although machine learning could potentially accelerate this). The dogs used in this study were healthy animals and not canine models of heart failure (Ardell et al., 2017). It is possible then that heart disease could change the behavior of the peripheral nervous system (PNS) in ways that would make neural titration more difficult to implement. Also, the controlled environment of the study likely increased the reliability of the neural titration by avoiding large changes in the animals' environment and individual physiological conditions; it is possible that a patient under non-controlled conditions may experience functional changes in their PNS that would shift the neural fulcrum on a short timescale.

CONCLUSION

The endeavor to develop sVNS has resulted in a range of promising techniques. Most studies have focused on fiber-selective stimulation, in some cases achieving an impressive reduction in laryngeal side effects (Tosato et al., 2007; Vuckovic et al., 2008). Anodal block and depolarizing pre-pulses have demonstrated the strongest mitigating effects (Tosato et al., 2007; Vuckovic et al., 2008), while chopped pulses and slowly rising pulses have been less effective (Vuckovic et al., 2008; Qing et al., 2015). More recent studies investigating the possibility of spatially selective VNS yelded more promising results (Plachta et al., 2014; Dali et al., 2018; Aristovich et al., 2021).

Fiber-selective sVNS is the only form of sVNS demonstrated in human patients (Pečlin et al., 2009), although peer-reviewed human studies are yet to emerge. Furthermore, studies on fiber-selective VNS have tended to focus on acute applications. Since the major therapeutical effects of VNS are seen chronically (Krahl, 2012), translation of fiber-selective VNS to a clinical setting would require validation of the technique chronically and with a large number of patients (in contrast to the low n numbers in animal studies). It is crucial to establish whether the efficacy of fiber-selective techniques varies significantly between patients. It is also necessary in such studies to ensure that fiber-selective techniques do not compromise electrochemical safety (an issue that has not been addressed in the sVNS literature to date).

Studies focusing on anodal block typically do not attempt to use neuromuscular blockade or nerve transection to isolate the pathway mediating respiratory side effects. This means that these studies are unable to assess the effects of possible off-target field escape (current leaking through the insulation of the stimulation apparatus). Accounting for this possibility is complicated by the fact that there may be multiple pathways whose activation can trigger respiratory side effects (such as Hering-Breuer reflex via activation of Aδ fibers, closure of glottis due to activation of Aα fibers, or a cough reflex due to activation of Aβ fibers).

Unlike fiber-selective sVNS, spatially selective sVNS takes into account evidence for a somatotopic arrangement of fibers inside the VN (Aristovich et al., 2021). Spatially selective VNS provides more precise targeting than fiber-selective VNS, and has been used successfully to elicit organ-specific responses (Aristovich et al., 2021). It has demonstrated comparable mitigation of side effects to fiber-selective VNS (Plachta et al., 2014; Dali et al., 2018), as well as increased efficacy in cardiac modulation (Ordelman et al., 2013). While studies cited here have examined the relationship between spatially selective VNS and the strength of side effects affecting the cardiovascular and respiratory system, these studies have not investigated how stimulation at different positions around the vagal circumference affects the activation of laryngeal muscles. This is a key oversight that must be addressed in future studies, since laryngeal side effects are the most common side effects experienced by patients receiving VNS. Research into spatially selective VNS also generates information on VN anatomy required for optimization of stimulation parameters (Plachta et al., 2014; Aristovich et al., 2021).

Achieving a better understanding of VN anatomy is the most important step toward improving sVNS techniques. While great progress has been made in this area (Thompson et al., 2019, 2020; Settell et al., 2020), it is still not established definitively whether fibers in the VN are arranged by fiber-type or by innervated organ, with current evidence inconclusive. If VN fibers are arranged both by fiber-type and somatotopically, then it would be necessary to develop hybrid sVNS techniques that are both fiber-selective and spatially selective.

All studies investigating the potential of sVNS to mitigate side effects must give careful consideration to the anesthetic used. Isoflurane, as used by Ordelman et al. (2013) and by Plachta et al. (2014), has a depressive effect on the PNS and on baroreflex in particular. Thus, side effects that would arise during vagal stimulation in an awake animal may be dampened or absent in an animal anesthetized with isoflurane. Isoflurane could also reduce the efficacy of VNS compared to an awake animal. Anesthetics such as urethane, α-chloralose or ketamine interfere less with peripheral nerve activity and should be used instead of isoflurane in VNS experiments.

Typically, studies that have assessed laryngeal side effects during VNS have focused on measuring EMG of a single deep neck muscle. This does not account for the possibility of current leakage through the apparatus insulation. It has also not been established whether a reduction in laryngeal EMG is associated with increased patient tolerance to the treatment. Patient tolerance must be assessed to allow for clinical translation. Moreover, since motor tolerability varies over time due to habituation, patient tolerance of laryngeal side effects during sVNS must be evaluated chronically.

How the long-term habituation may affect the efficacy of sVNS techniques is also yet to be determined. To date, all studies on sVNS in animals have been conducted acutely in anesthetized subjects. Various factors are arising after surgery that could impact the efficacy of sVNS. The formation of scar tissue could change the distance between the array and the target site as well as the pattern of current flow. Neuroplasticity could alter the response profile of the nerve. The position of the neck and the balance of fluids in the body may also have a significant impact. The design of closed-loop sVNS systems may be useful in responding to this long-term variability (Ahmed et al., 2020).

It is necessary to expand the application of sVNS beyond cardiac and respiratory therapeutic modalities. At present, the only FDA-approved clinical uses of VNS are for focal epilepsy and treatment-resistant depression (O'reardon et al., 2006; Krahl and Clark, 2012), but sVNS has not been explored for either. Focal epilepsy in particular warrants especial attention, since it has demonstrated high efficacy and is in use in a large number of patients worldwide (Krahl and Clark, 2012). The use of VNS to mitigate inflammation also remains a promising endeavor (Kwan et al., 2016; Mastitskaya et al., 2021).

The development of better sVNS techniques has the potential to benefit hundreds of thousands of patients worldwide (Johnson and Wilson, 2018), but sVNS is still a small research area. The better understanding of VN anatomy, development of more precise stimulation techniques and optimized electrode array geometries would drive the progress of sVNS research and its translation into clinical practice.

AUTHOR CONTRIBUTIONS

KA and SM conceptualized and supervised the work. AF and SM wrote the manuscript. All authors contributed to the article and approved the submitted version.

FUNDING

This work was supported by the UK Medical Research Council (MRC grant No: MR/R01213X/1) and NIH SPARC (1OT2OD026545-01).

REFERENCES

Agarwal, R., Mokelke, E., Ruble, S. B., and Stolen, C. M. (2016). Vagal nerve stimulation evoked heart rate changes and protection from cardiac remodeling. *J. Cardiovasc. Translat. Res.* 9, 67–76. doi: 10.1007/s12265-015-9668-7

Ahmed, U., Chang, Y.-C., Cracchiolo, M., Lopez, M. F., Tomaio, J. N., Datta-Chaudhuri, T., et al. (2020). Anodal block permits directional vagus nerve stimulation. *Sci. Rep.* 10:9221. doi: 10.1038/s41598-020-66332-y

Ardell, J. L., Nier, H., Hammer, M., Southerland, E. M., Ardell, C. L., Beaumont, E., et al. (2017). Defining the neural fulcrum for chronic vagus nerve stimulation: implications for integrated cardiac control. *J. Physiol.* 595, 6887–6903. doi: 10.1113/jp274678

Ardell, J. L., Rajendran, P. S., Nier, H. A., Kenknight, B. H., and Armour, J. A. (2015). Central-peripheral neural network interactions evoked by vagus nerve stimulation: functional consequences on control of cardiac function. *Am. J. Physiol. Heart Circulat. Physiol.* 309, H1740–H1752. doi: 10.1152/ajpheart.00557.2015

Aristovich, K., Donega, M., Fjordbakk, C., Tarotin, I., Chapman, CaR, et al. (2021). Model-based geometrical optimisation and in vivo validation of a spatially selective multielectrode cuff array for vagus nerve neuromodulation. *J. Neurosci. Methods* 352:109079. doi: 10.1016/j.jneumeth.2021.109079

Bawa, P. N. S., Jones, K. E., and Stein, R. B. (2014). Assessment of size ordered recruitment. *Front. Hum. Neurosci.* 8:532–532. doi: 10.3389/fnhum.2014.00532

Ben-Menachem, E. (2001). Vagus nerve stimulation, side effects, and long-term safety. *J. Clin. Neurophysiol.* 18, 415–418. doi: 10.1097/00004691-200109000-00005

Ben-Menachem, E. (2002). Vagus-nerve stimulation for the treatment of epilepsy. *Lancet Neurol.* 1, 477–482. doi: 10.1016/s1474-4422(02)00220-x

Binkley, P. F., Nunziata, E., Haas, G. J., Nelson, S. D., and Cody, R. J. (1991). Parasympathetic withdrawal is an integral component of autonomic imbalance in congestive heart failure: Demonstration in human subjects and verification in a paced canine model of ventricular failure. *JACC* 18, 464–472. doi: 10.1016/0735-1097(91)90602-6

Calvillo, L., Vanoli, E., Andreoli, E., Besana, A., Omodeo, E., Gnecchi, M., et al. (2011). Vagal stimulation, through its nicotinic action, limits infarct size and the inflammatory response to myocardial ischemia and reperfusion. *J. Cardiovasc. Pharmacol.* 58, 500–507. doi: 10.1097/FJC.0b013e31822b7204

Chapman, C. A. R., Aristovich, K., Donega, M., Fjordbakk, C. T., Stathopoulou, T.-R., et al. (2018). Electrode fabrication and interface optimization for imaging of evoked peripheral nervous system activity with electrical impedance tomography (EIT). *J. Neural Eng.* 16:016001. doi: 10.1088/1741-2552/aae868

Dali, M., Picq, C., Rossel, O., Maciejasz, P., Malbert, C. H., and Guiraud, D. (2019). Comparison of the efficiency of chopped and non-rectangular electrical stimulus waveforms in activating small vagus nerve fibers. *J. Neurosci. Methods* 320, 1–8. doi: 10.1016/j.jneumeth.2019.02.017

Dali, M., Rossel, O., Andreu, D., Laporte, L., Hernández, A., Laforet, J., et al. (2018). Model based optimal multipolar stimulation without a priori knowledge of nerve structure: application to vagus nerve stimulation. *J. Neural Eng.* 15:046018. doi: 10.1088/1741-2552/aabeb9

De Ferrari, G. M., Crijns, H. J. G. M., Borggrefe, M., Milasinovic, G., Smid, J., Zabel, M., et al. (2010). Chronic vagus nerve stimulation: a new and promising therapeutic approach for chronic heart failure. *Eur. Heart J.* 32, 847–855. doi: 10.1093/eurheartj/ehq391

Floras, J. S., and Ponikowski, P. (2015). The sympathetic/parasympathetic imbalance in heart failure with reduced ejection fraction. *Eur. Heart J.* 36, 1974–1982. doi: 10.1093/eurheartj/ehv087

Furukawa, N., and Okada, H. (1992). Effects of selective vagal stimulation on the gallbladder and sphincter of Oddi and peripheral vagal routes mediating bile evacuative responses induced by hypothalamic stimulation. *Jpn. J. Physiol.* 42, 321–334. doi: 10.2170/jjphysiol.42.321

Gierthmuehlen, M., and Plachta, D. T. (2016). Effect of selective vagal nerve stimulation on blood pressure, heart rate and respiratory rate in rats under metoprolol medication. *Hypertens Res.* 39, 79–87. doi: 10.1038/hr.2015.122

Gierthmuehlen, M., Stieglitz, T., Zentner, J., and Plachta, D. T. (2016). Haemodynamic Responses to Selective Vagal Nerve Stimulation under Enalapril Medication in Rats. *PLoS One* 11:e0147045. doi: 10.1371/journal.pone.0147045

Gold, M. R., Van Veldhuisen, D. J., Hauptman, P. J., Borggrefe, M., Kubo, S. H., Lieberman, R. A., et al. (2016). Vagus nerve stimulation for the treatment of heart failure: the INOVATE-HF trial. *JACC* 68, 149–158. doi: 10.1016/j.jacc.2016.03.525

Hammer, N., Löffler, S., Cakmak, Y. O., Ondruschka, B., Planitzer, U., Schultz, M., et al. (2018). Cervical vagus nerve morphometry and vascularity in the context of nerve stimulation - A cadaveric study. *Sci. Rep.* 8, 7997–7997. doi: 10.1038/s41598-018-26135-8

Handforth, A., Degiorgio, C. M., Schachter, S. C., Uthman, B. M., Naritoku, D. K., Tecoma, E. S., et al. (1998). Vagus nerve stimulation therapy for partial-onset seizures: a randomized active-control trial. *Neurology* 51, 48–55. doi: 10.1212/wnl.51.1.48

Hennings, K., Arendt-Nielsen, L., Christensen, S. S., and Andersen, O. K. (2005). Selective activation of small-diameter motor fibres using exponentially rising waveforms: a theoretical study. *Med. Biol. Eng. Comput.* 43, 493–500. doi: 10.1007/bf02344731

Hoffmann, T. J., Simon, B. J., Zhang, Y., and Emala, C. W. (2012). Low voltage vagal nerve stimulation reduces bronchoconstriction in guinea pigs through catecholamine release. *Neuromodulation* 15, 527–536. doi: 10.1111/j.1525-1403.2012.00454.x

Johnson, R. L., and Wilson, C. G. (2018). A review of vagus nerve stimulation as a therapeutic intervention. *J. Inflamm. Res.* 11, 203–213. doi: 10.2147/JIR.S163248

Kandel, E. R., Schwartz, J. H., and Jessell, T. M. (2020). *Principles of neural science*. New York, NY: McGraw-Hill.

Kilgore, K. L., and Bhadra, N. (2004). Nerve conduction block utilising high-frequency alternating current. *Med. Biol. Eng. Comput.* 42, 394–406. doi: 10.1007/bf02344716

Krahl, S. E. (2012). Vagus nerve stimulation for epilepsy: A review of the peripheral mechanisms. *Surg. Neurol. Int.* 3, S47–S52. doi: 10.4103/2152-7806.91610

Krahl, S. E., and Clark, K. B. (2012). Vagus nerve stimulation for epilepsy: A review of central mechanisms. *Surg. Neurol. Int.* 3, S255–S259. doi: 10.4103/2152-7806.103015

Kubin, L., Alheid, G. F., Zuperku, E. J., and Mccrimmon, D. R. (2006). Central pathways of pulmonary and lower airway vagal afferents. *J. Appl. Physiol.* 101, 618–627. doi: 10.1152/japplphysiol.00252.2006

Kwan, H., Garzoni, L., Liu, H. L., Cao, M., Desrochers, A., Fecteau, G., et al. (2016). Vagus nerve stimulation for treatment of inflammation: systematic review of animal models and clinical studies. *Bioelectr. Med.* 3, 1–6. doi: 10.15424/bioelectronmed.2016.00005

Lancashire, H. T., Vanhoestenberghe, A., Pendegrass, C. J., Ajam, Y. A., Magee, E., Donaldson, N., et al. (2016). Microchannel neural interface manufacture by stacking silicone and metal foil laminae. *J. Neural. Eng.* 13:034001. doi: 10.1088/1741-2560/13/3/034001

Li, H., and Yang, T. D. (2009). Vagus nerve stimulation may be used in the therapy of myocarditis. *Med. Hypotheses* 73, 725–727. doi: 10.1016/j.mehy.2009.04.036

Li, M., Zheng, C., Sato, T., Kawada, T., Sugimachi, M., and Sunagawa, K. (2004). Vagal nerve stimulation markedly improves long-term survival after chronic

heart failure in rats. *Circulation* 109, 120–124. doi: 10.1161/01.CIR.0000105721.71640.DA

Lv, H., Zhao, Y. H., Chen, J. G., Wang, D. Y., and Chen, H. (2019). Vagus Nerve Stimulation for Depression: A Systematic Review. *Front. Psychol.* 10:64. doi: 10.3389/fpsyg.2019.00064

Mastitskaya, S., Marina, N., Gourine, A., Gilbey, M. P., Spyer, K. M., Teschemacher, A. G., et al. (2012). Cardioprotection evoked by remote ischaemic preconditioning is critically dependent on the activity of vagal pre-ganglionic neurones. *Cardiovasc. Res.* 95, 487–494. doi: 10.1093/cvr/cvs212

Mastitskaya, S., Thompson, N., and Holder, D. (2021). Selective Vagus Nerve Stimulation as a Therapeutic Approach for the Treatment of ARDS: A Rationale for Neuro-Immunomodulation in COVID-19 Disease. *Front. Neurosci.* 15:667036. doi: 10.3389/fnins.2021.667036

McAllen, R. M., Shafton, A. D., Bratton, B. O., Trevaks, D., and Furness, J. B. (2018). Calibration of thresholds for functional engagement of vagal A-C fiber groups *in vivo*. *Bioelectron. Med.* 1, 21–27. doi: 10.2217/bem-2017-0001

Mioni, C., Bazzani, C., Giuliani, D., Altavilla, D., Leone, S., Ferrari, A., et al. (2005). Activation of an efferent cholinergic pathway produces strong protection against myocardial ischemia/reperfusion injury in rats. *Crit. Care Med.* 33, 2621–2628. doi: 10.1097/01.ccm.0000186762.05301.13

Moshé, S. L., Perucca, E., Ryvlin, P., and Tomson, T. (2015). Epilepsy: new advances. *Lancet* 385, 884–898. doi: 10.1016/s0140-6736(14)60456-6

Neligan, A., Hauser, W. A., and Sander, J. W. (2012). The epidemiology of the epilepsies. *Handb. Clin. Neurol.* 107, 113–133. doi: 10.1016/b978-0-444-52898-8.00006-9

Nicolai, E. N., Settell, M. L., Knudsen, B. E., Mcconico, A. L., Gosink, B. A., Trevathan, J. K., et al. (2020). Sources of off-target effects of vagus nerve stimulation using the helical clinical lead in domestic pigs. *J. Neural Eng.* 17:046017. doi: 10.1088/1741-2552/ab9db8

Noller, C. M., Levine, Y. A., Urakov, T. M., Aronson, J. P., and Nash, M. S. (2019). Vagus Nerve Stimulation in Rodent Models: An Overview of Technical Considerations. *Front. Neurosci.* 13:911. doi: 10.3389/fnins.2019.00911

Nuntaphum, W., Pongkan, W., Wongjaikam, S., Thummasorn, S., Tanajak, P., Khamseekaew, J., et al. (2018). Vagus nerve stimulation exerts cardioprotection against myocardial ischemia/reperfusion injury predominantly through its efferent vagal fibers. *Basic Res. Cardiol.* 113:22. doi: 10.1007/s00395-018-0683-0

Ordelman, S. C., Kornet, L., Cornelussen, R., Buschman, H. P., and Veltink, P. H. (2013). Selectivity for specific cardiovascular effects of vagal nerve stimulation with a multi-contact electrode cuff. *IEEE Trans. Neural Syst. Rehabil. Eng.* 21, 32–36. doi: 10.1109/tnsre.2012.2214058

O'reardon, J. P., Cristancho, P., and Peshek, A. D. (2006). Vagus Nerve Stimulation (VNS) and Treatment of Depression: To the Brainstem and Beyond. *Psychiatry* 3, 54–63.

Otte, C., Gold, S. M., Penninx, B. W., Pariante, C. M., Etkin, A., Fava, M., et al. (2016). Major depressive disorder. *Nat. Rev. Dis. Primers* 2:16065. doi: 10.1038/nrdp.2016.65

Patel, Y. A., and Butera, R. J. (2015). Differential fiber-specific block of nerve conduction in mammalian peripheral nerves using kilohertz electrical stimulation. *J. Neurophysiol.* 113, 3923–3929. doi: 10.1152/jn.00529.2014

Patel, Y. A., and Butera, R. J. (2018). Challenges associated with nerve conduction block using kilohertz electrical stimulation. *J. Neural Eng.* 15:031002. doi: 10.1088/1741-2552/aaadc0

Patel, Y. A., Saxena, T., Bellamkonda, R. V., and Butera, R. J. (2017). Kilohertz frequency nerve block enhances anti-inflammatory effects of vagus nerve stimulation. *Sci. Rep.* 7:39810. doi: 10.1038/srep39810

Peclin, P., and Rozman, J. (2009). A model of selective left VNS and recording in a man. *IFMBE Proc* 26, 147–148. doi: 10.1007/978-3-642-04292-8_33

Pečlin, P., and Rozman, J. (2014). Alternative paradigm of selective vagus nerve stimulation tested on an isolated porcine vagus nerve. *Sci. World J.* 2014, 310283–310283. doi: 10.1155/2014/310283

Pečlin, P., Kneževič, I., Mirkovič, T., Geršak, B., Radan, I., Podbregar, M., et al. (2009). Selective stimulation of the vagus nerve in a man. *IFMBE Proc.* 22, 1628–1631. doi: 10.1007/978-3-540-89208-3_387

Pelot, N. A., and Grill, W. M. (2020). *In vivo* quantification of excitation and kilohertz frequency block of the rat vagus nerve. *J. Neural Eng.* 17:026005. doi: 10.1088/1741-2552/ab6cb6

Plachta, D. T. T., Gierthmuehlen, M., Cota, O., Boeser, F., and Stieglitz, T. (2013). BaroLoop: using a multichannel cuff electrode and selective stimulation to reduce blood pressure. *Annu. Int. Confer. IEEE Engine. Med. Biol. Soc.* 2013, 755–758. doi: 10.1109/embc.2013.6609610

Plachta, D. T., Gierthmuehlen, M., Cota, O., Espinosa, N., Boeser, F., Herrera, T. C., et al. (2014). Blood pressure control with selective vagal nerve stimulation and minimal side effects. *J. Neural Eng.* 11:036011. doi: 10.1088/1741-2560/11/3/036011

Plachta, D. T. T., Zentner, J., Aguirre, D., Cota, O., Stieglitz, T., and Gierthmuehlen, M. (2016). Effect of cardiac-cycle synchronized selective vagal stimulation on heart rate and blood pressure in rats. *Adv. Ther.* 33, 1246–1261. doi: 10.1007/s12325-016-0348-z

Premchand, R. K., Sharma, K., Mittal, S., Monteiro, R., Dixit, S., Libbus, I., et al. (2014). Autonomic regulation therapy via left or right cervical vagus nerve stimulation in patients with chronic heart failure: Results of the ANTHEM-HF trial. *J. Cardiac Failure* 20, 808–816. doi: 10.1016/j.cardfail.2014.08.009

Purser, M. F., Mladsi, D. M., Beckman, A., Barion, F., and Forsey, J. (2018). Expected Budget Impact and Health Outcomes of Expanded Use of Vagus Nerve Stimulation Therapy for Drug-Resistant Epilepsy. *Adv. Therap.* 35, 1686–1696. doi: 10.1007/s12325-018-0775-0

Qing, K. Y., Ward, M. P., and Irazoqui, P. P. (2015). Burst-Modulated Waveforms Optimize Electrical Stimuli for Charge Efficiency and Fiber Selectivity. *IEEE Trans. Neural Syst. Rehabil. Eng.* 23, 936–945. doi: 10.1109/tnsre.2015.2421732

Qing, K. Y., Wasilczuk, K. M., Ward, M. P., Phillips, E. H., Vlachos, P. P., Goergen, C. J., et al. (2018). B fibers are the best predictors of cardiac activity during Vagus nerve stimulation: Qing, vagal B fiber activation and cardiac effects. *Bioelectron. Med.* 4:5. doi: 10.1186/s42234-018-0005-8

Rosas-Ballina, M., Olofsson, P. S., Ochani, M., Valdés-Ferrer, S. I., Levine, Y. A., Reardon, C., et al. (2011). Acetylcholine-synthesizing T cells relay neural signals in a vagus nerve circuit. *Science* 334, 98–101. doi: 10.1126/science.1209985

Rozman, J., and Peclin, P. (2008). Selective stimulation of autonomic nerves and recording of electroneurograms in a canine model. *Artif Organs* 32, 592–596. doi: 10.1111/j.1525-1594.2008.00607.x

Rozman, J., Sovinec, B., Trlep, M., and Zorko, B. (1993). Multielectrode spiral cuff for ordered and reversed activation of nerve fibres. *J. Biomed. Eng.* 15, 113–120. doi: 10.1016/0141-5425(93)90039-2

Scheffer, I. E., Berkovic, S., Capovilla, G., Connolly, M. B., French, J., Guilhoto, L., et al. (2017). ILAE classification of the epilepsies: Position paper of the ILAE Commission for Classification and Terminology. *Epilepsia* 58, 512–521. doi: 10.1111/epi.13709

Settell, M. L., Kasole, M., Skubal, A. C., Knudsen, B. E., Nicolai, E. N., Huang, C., et al. (2021). In vivo visualization of pig vagus nerve 'vagotopy' using ultrasound. *bioRxiv* 2021:424256. doi: 10.1101/2020.12.24.424256

Settell, M. L., Pelot, N. A., Knudsen, B. E., Dingle, A. M., Mcconico, A. L., Nicolai, E. N., et al. (2020). Functional vagotopy in the cervical vagus nerve of the domestic pig: implications for the study of vagus nerve stimulation. *J. Neural Eng.* 17:026022. doi: 10.1088/1741-2552/ab7ad4

Thompson, N., Mastitskaya, S., and Holder, D. (2019). Avoiding off-target effects in electrical stimulation of the cervical vagus nerve: Neuroanatomical tracing techniques to study fascicular anatomy of the vagus nerve. *J. Neurosci. Methods* 325:108325. doi: 10.1016/j.jneumeth.2019.108325

Thompson, N., Ravagli, E., Mastitskaya, S., Iacoviello, F., Aristovich, K., Perkins, J., et al. (2020). MicroCT optimisation for imaging fascicular anatomy in peripheral nerves. *J. Neurosci. Methods* 338:108652. doi: 10.1016/j.jneumeth.2020.108652

Tosato, M., Yoshida, K., Toft, E., and Struijk, J. J. (2007). Quasi-trapezoidal pulses to selectively block the activation of intrinsic laryngeal muscles during vagal nerve stimulation. *J. Neural Eng.* 4, 205–212. doi: 10.1088/1741-2560/4/3/005

Vida, G., Peña, G., Deitch, E. A., and Ulloa, L. (2011). α7-cholinergic receptor mediates vagal induction of splenic norepinephrine. *J. Immunol.* 186, 4340–4346. doi: 10.4049/jimmunol.1003722

Vuckovic, A., Tosato, M., and Struijk, J. J. (2008). A comparative study of three techniques for diameter selective fiber activation in the vagal nerve: anodal block, depolarizing prepulses and slowly rising pulses. *J. Neural Eng.* 5, 275–286. doi: 10.1088/1741-2560/5/3/002

Whitwam, J. G. (1976). Classification of peripheral nerve fibres. An historical perspective. *Anaesthesia* 31, 494–503. doi: 10.1111/j.1365-2044.1976.tb12354.x

Yoo, P. B., Liu, H., Hincapie, J. G., Ruble, S. B., Hamann, J. J., and Grill, W. M. (2016). Modulation of heart rate by temporally patterned vagus nerve stimulation in the anesthetized dog. *Physiol. Rep.* 4:12689. doi: 10.14814/phy2.12689

Zannad, F., De Ferrari, G. M., Tuinenburg, A. E., Wright, D., Brugada, J., Butter, C., et al. (2014). Chronic vagal stimulation for the treatment of low ejection fraction heart failure: results of the NEural Cardiac TherApy foR Heart Failure (NECTAR-HF) randomized controlled trial. *Eur. Heart J.* 36, 425–433. doi: 10.1093/eurheartj/ehu345

Conflict of Interest: The authors declare that the research was conducted in the absence of any commercial or financial relationships that could be construed as a potential conflict of interest.

frontiers in Neuroscience

ORIGINAL RESEARCH
published: 14 October 2021
doi: 10.3389/fnins.2021.726825

Age-Related Variation in Sympathetic Nerve Distribution in the Human Spleen

Cindy G. J. Cleypool[1], David J. Brinkman[2,3], Claire Mackaaij[1], Peter G. J. Nikkels[4], Martijn A. Nolte[5], Misha D. Luyer[3], Wouter J. de Jonge[2,6] and Ronald L. A. W. Bleys[1]*

[1] Division of Surgical Specialties, Department of Anatomy, University Medical Center Utrecht, Utrecht University, Utrecht, Netherlands, [2] Tytgat Institute for Liver and Intestinal Research, Amsterdam University Medical Center, University of Amsterdam, Amsterdam, Netherlands, [3] Department of Surgery, Catharina Hospital, Eindhoven, Netherlands, [4] Division of Laboratories, Pharmacy, Biomedical Genetics and Pathology, Department of Pathology, University Medical Center Utrecht, Utrecht, Netherlands, [5] Department of Molecular and Cellular Hemostasis, Sanquin Research and Landsteiner Laboratory, Amsterdam, Netherlands, [6] Department of Surgery, University Hospital Bonn, Bonn, Germany

Introduction: The cholinergic anti-inflammatory pathway (CAIP) has been proposed as an efferent neural pathway dampening the systemic inflammatory response via the spleen. The CAIP activates the splenic neural plexus and a subsequent series of intrasplenic events, which at least require a close association between sympathetic nerves and T cells. Knowledge on this pathway has mostly been derived from rodent studies and only scarce information is available on the innervation of the human spleen. This study aimed to investigate the sympathetic innervation of different structures of the human spleen, the topographical association of nerves with T cells and age-related variations in nerve distribution.

Materials and Methods: Spleen samples were retrieved from a diagnostic archive and were allocated to three age groups; neonates, 10–25 and 25–70 years of age. Sympathetic nerves and T cells were identified by immunohistochemistry for tyrosine hydroxylase (TH) and the membrane marker CD3, respectively. The overall presence of sympathetic nerves and T cells was semi-automatically quantified and expressed as total area percentage. A predefined scoring system was used to analyze the distribution of nerves within different splenic structures.

Results: Sympathetic nerves were observed in all spleens and their number appeared to slightly increase from birth to adulthood and to decrease afterward. Irrespective to age, more than halve of the periarteriolar lymphatic sheaths (PALSs) contained sympathetic nerves in close association with T cells. Furthermore, discrete sympathetic nerves were observed in the capsule, trabeculae and red pulp and comparable to the total amount of sympathetic nerves, showed a tendency to decrease with age. No correlation was found between the number of T cells and sympathetic nerves.

Conclusion: The presence of discrete sympathetic nerves in the splenic parenchyma, capsule and trabecular of human spleens could suggest a role in functions other than vasoregulation. In the PALS, sympathetic nerves were observed to be in proximity to T cells and is suggestive for the existence of the CAIP in humans. Since sympathetic nerve

OPEN ACCESS

Edited by:
Silvia V. Conde, New University of Lisbon, Portugal

Reviewed by:
Donald B. Hoover, East Tennessee State University, United States
Birte Steiniger, Philipps University of Marburg, Germany

****Correspondence:***
Cindy G. J. Cleypool
c.g.j.cleypool@umcutrecht.nl

Specialty section:
This article was submitted to Autonomic Neuroscience, a section of the journal Frontiers in Neuroscience

Received: *17 June 2021*
Accepted: *24 September 2021*
Published: *14 October 2021*

Citation:
Cleypool CGJ, Brinkman DJ, Mackaaij C, Nikkels PGJ, Nolte MA, Luyer MD, de Jonge WJ and Bleys RLAW (2021) Age-Related Variation in Sympathetic Nerve Distribution in the Human Spleen. Front. Neurosci. 15:726825. doi: 10.3389/fnins.2021.726825

distribution shows interspecies and age-related variation, and our general understanding of the relative and spatial contribution of splenic innervation in immune regulation is incomplete, it remains difficult to estimate the anti-inflammatory potential of targeting splenic nerves in patients.

Keywords: spleen, sympathetic innervation, neuroimmunomodulation, periarteriolar lymphatic sheath, cholinergic anti-inflammatory pathway

INTRODUCTION

The cholinergic anti-inflammatory pathway (CAIP) comprises an efferent neural pathway that dampens the systemic inflammatory response via the spleen and is suggested to involve sequential activation of the efferent vagus nerve and the splenic plexus (Reardon, 2016; Pavlov and Tracey, 2017). Others have put forward that instead of the efferent vagus nerve, this pathway involves the greater splanchnic nerve (Komega et al., 2018). Irrespective, activation of the splenic plexus results in a cascade of intrasplenic events, starting with the release of norepinephrine (NE) (Kees et al., 2003). Studies have demonstrated that NE then activates adrenergic receptors on $CD4^+$ $ChAT^+$ T lymphocytes (Rosas-Ballina et al., 2011; Vida et al., 2011, 2017), which in turn produce and secrete acetylcholine (ACh) (Borovikova et al., 2000; Rosas-Ballina et al., 2011). ACh then inhibits the release of the pro-inflammatory cytokine tumor necrosis factor alpha (TNFα) from activated macrophages via nicotinergic receptor signaling (Borovikova et al., 2000; de Jonge et al., 2005; Kox et al., 2009; Lu and Kwan, 2014).

Morphological evidence for the presence of sympathetic nerves in proximity to splenic T lymphocytes was provided earlier by Bellinger et al. (1987, 1992). In a study on rat spleens, they observed sympathetic nerves diverging into T lymphocyte specific white pulp areas, also known as periarteriolar lymphatic sheaths (PALSs). In the PALSs these nerves were in close proximity to T lymphocytes and formed synaptic connections (Felten and Olschowka, 1987). The presence of sympathetic nerves which could release NE in the proximity of T lymphocytes in the human spleen might hold potential as a therapeutic target for immune related disease and knowledge on the anatomical configuration of splenic innervation in humans is therefore essential.

The presence of sympathetic nerves at the medio adventitial junction in human spleens has been described in various studies (Heusermann and Stutte, 1977; Kudoh et al., 1979; Anagnostou et al., 2007; Verlinden et al., 2018), however, innervation of T cell specific lymphoid tissue has only been reported once (Hoover et al., 2017). In the latter study, sympathetic innervation patterns in spleens of end-stage sepsis patients were investigated and sympathetic nerves were observed to be in close association with lymphocytes in the PALS of the control group (trauma patients who died after hemorrhagic stroke). The results of this study were descriptive and it remains unclear whether this was a common feature and observed in all PALSs, or only occasionally. Since, PALS related sympathetic nerves were seldom observed in end-stage sepsis patients, the authors suggested this difference to be disease-related (Hoover et al., 2017). However, other factors, such as aging, are known to contribute to decline of sympathetic innervation as well, as shown in the rat spleen (Bellinger et al., 1987, 1992) and human cerebral arteries (Bleys and Cowen, 2001). If human splenic innervation is subject to age-related decline as well, this information is of relevance because it might determine the window of application of anti-inflammatory neuromodulation along age. Since the age profile of a substantial number of patients of the control group in the study of Hoover et al. (2017) was lacking, as well as comprehensive data on the prevalence of PALS related sympathetic nerves, our understanding of human splenic innervation remains incomplete.

Therefore, in this study, quantitative and semi-quantitative analytical methods were used to investigate the distribution of sympathetic nerves in human spleens of various age groups. Although the PALS is considered to represent the primary structure of T cell neuromodulation, T cells migrate through the spleen and exposure to NE might occur at any location they pass while entering or exiting the spleen. Therefore, blood vessels, red pulp, trabeculae and the capsule were evaluated for the presence of sympathetic nerve tissue as well.

MATERIALS AND METHODS

Tissue Samples

A total of 26 paraffin embedded splenic samples were provided the Pathology Department of the University Medical Center Utrecht. Samples were divided into three age groups, being 40 weeks of gestation (from now on referred to as neonatal), 10–25 years and 25–70 years. This study was approved by the Medical Ethical Committee (#18-167) as a "non-Medical Research Act" study and the Biobank of the University Medical Center Utrecht approved to use the rest biomaterial for this research (biobank #18-284). None of the individuals was known with immunological or splenic clinical conditions. **Table 1** contains data on age, sex, and cause of death.

Sample Processing

Samples were obtained from the splenic hilar region and were cut in the transversal plane. Paraffin embedded splenic samples were cut on a microtome (Leica 2050 Super Cut, Nussloch,

Abbreviations: ACh, acetylcholine; AR, adrenergic receptor; β, beta; BV, blood vessel; C, capsule; CAIP, cholinergic anti-inflammatory pathway; ChAT, choline acetyl transferase; HE, hematoxylin/eosin; HIER, heat induced epitope retrieval; IR, immune reactivity; NE, norepinephrine; PALS, periarteriolar lymphatic sheath; PGP9.5, protein gene product 9.5; RP, red pulp; T, trabecula; TH, tyrosine hydroxylase; TNFα, tumor necrosis factor alpha.

TABLE 1 | Patient profiles.

#	Sex	Age	Cause of death
25–70 years (*N* = 7)			
1	F	46	Pancreatic tail cyst
2	F	66	Myocardial infarct
3	F	52	Subarachnoid hemorrhage
4	F	48	Traumatic motor bike accident
5	M	66	Unknown
6	M	26	Arrhythmia
7	M	29	Long QT syndrome
10–25 years (*N* = 7)			
8	F	14	Acute unexpected death, probably due to cardiac arrest
9	M	16	Arrhythmia
10	M	11	Sudden unexpected death due to coronary artery anomaly
11	M	11	New diabetes mellitus with keto-acidosis
12	F	12	Unknown
13	M	11	Herniation of the sigmoid due to congenital mesenterial defect
14	F	24	Lung emboly
40 weeks (*N* = 12)			
15	M	40 weeks 2 days	Perinatal asphyxia
16	F	39 2/7 weeks 2 days	Perinatal asphyxia
17	M	40 weeks 1 day	Perinatal asphyxia
18	M	42 1/7 weeks 3 days	Perinatal asphyxia
19	F	41 weeks 10 days	Perinatal asphyxia
20	M	40 6/7 weeks 4 days	Perinatal asphyxia
21	M	40 2/7 weeks 1 days	Perinatal asphyxia
22	M	40 2/7 weeks 1 day	Perinatal asphyxia, congenital heart defect
23	M	40 2/7 weeks 4 days	Perinatal asphyxia
24	M	41 5/7 weeks 3 days	Perinatal asphyxia
25	F	35 weeks 1 day	Perinatal asphyxia, first born of dichorionic twin
26	M	41 6/7 weeks 7 days	Perinatal asphyxia

Age is represented in years for the 25–70 and 10–25 years age groups and in weeks of gestation and postnatal days for the 40 weeks group (e.g., 41 6/7 w 7 = 41 weeks and 6 days of gestation whereafter the newly born lived for 7 days).

Germany) and 5 μm thick sections of splenic tissue were collected on glass slides, air dried and subsequently heat fixed for 2 h on a slide drying table of 60°C (Medax, 14801, Kiel, Germany). All slides were deparaffinized, rehydrated and further processed for histochemical or immunohistochemical staining. Hematoxylin/Eosin (HE) was used to evaluate technical tissue quality, to generate a tissue overview, and to screen for general pathological changes. A double T and B cell staining, using antibodies against specific membrane proteins, being CD3 and CD20 respectively, was used to screen the white pulp for distinct pathological abnormalities. To quantify and compare the overall presence of sympathetic nerves and T cells, and the distribution of sympathetic nerves in the PALS and other splenic structures (capsule, trabeculae, rep pulp and arteries), a double staining for sympathetic nerves and T cells was performed. In this procedure antibodies against CD3 and tyrosine hydroxylase (TH), were used, the latter being an enzyme involved in the synthesis of NE. The general nerve marker, protein gene product 9.5 (PGP9.5) was used on adjacent slides to confirm neural identity of TH-immune reactive (IR) structures.

Staining Procedures

Tissue sections were dewaxed in xylene and rehydrated through graded alcohols prior to histochemical or immunohistochemical staining. Prior to immunohistochemistry, sections were pre-treated with Heat Induced Epitope Retrieval (HIER) in citrate buffer (pH6.0) for 20 min at 95°C.

Hematoxylin/Eosin Staining

Tissue sections were stained with hematoxylin for 10 min at room temperature (RT). After rinsing in running tap water, sections were dipped in ethanol 50%, stained with eosin for 1 min and dehydrated in graded alcohols and xylene. Slides were coverslipped with Entellan (Merck, Darmstadt, Germany).

Single Immunohistochemical Staining Procedures (PGP9.5 and Tyrosine Hydroxylase)

After the HIER procedure, sections were incubated with 5% Normal Human Serum (NHS) in TBS prior to incubation with rabbit anti human PGP9.5 antibody (1:2000 in TBS-T + 3% BSA, 48 h, 4°C, Dako, Glostrup, Denmark) or rabbit anti-human TH (1:1500 in TBT-T + 1% BSA, overnight RT, Pel-Freez, Rogers AR). Visualization of bound antibodies was performed with undiluted Brightvision Poly-Alkaline Phosphatase (AP) Goat-anti-Rabbit (ImmunoLogic, Amsterdam, Netherlands) and Liquid Permanent Red (LPR, Dako). All sections were counterstained with hematoxylin (Klinipath), dried on a hotplate for 15 min at 60°C and coverslipped with Entellan (Merck). Tris-buffered saline with 0.05% Tween20 (TBS-T) was used for all regular washing steps. Negative controls were obtained by incubation with TBS-3% BSA without primary antibodies. Human vagus nerve – and sympathetic trunk sections were included as a positive control for general – and sympathetic nerve tissue respectively. Both, staining procedures and positive controls, have been used in previous studies in which they proved to be valid to detect small nerves (including single nerve fibers) and to serve as proper controls, respectively (Cleypool et al., 2019, 2020).

Sequential Double Immunohistochemical Staining Procedure (CD20/CD3 and CD3/TH)

After HIER, sections were incubated with 3% Normal Goat Serum (NGS) (CD20/CD3) or 5% NHS (CD3/TH). In the first staining sequence, sections were incubated with CD20 or CD3 antibodies (details of used antibodies, including dilution, incubation time are presented in **Table 2**) and visualized with Brightvision Poly-AP Goat-anti-Mouse or Goat-anti-rabbit Mouse (ImmunoLogic) respectively followed by PermaBlue plus/AP (Diagnostics Biosystems, Pleasanton, United States). Details of the used antibodies, including dilution and incubation time are presented in **Table 2**. Prior to the second staining sequence a HIER in citrate buffer (pH6.0, 15 min RT) was performed, removing unbound antibodies but leaving

TABLE 2 | Detailed information on antibodies used in sequential double staining procedures.

Double stain	Staining sequence	Primary antibody	Host	Vendor	Dilution, incubation time and temperature	Secondary antibody	Chromogen
CD3/TH	1	CD3	Rabbit	Dako A0452	1:50, 90 min, RT	Brightvision-anti-Rabbit/AP	PermaBlue
	2	TH	Rabbit	Pel-Freez P40101	1:1500, overnight, RT	Brightvision-anti-Rabbit/AP	LPR
CD20/CD3	1	CD20	Mouse	Dako M0755	1:400, 90 min, RT	Brightvision-anti-Mouse/AP	PermaBlue
	2	CD3	Rabbit	Dako A0452	1:100, 90 min, RT	Brightvision-anti-Rabbit/AP	LPR

chromogens unhanged (Van der Loos, 2010). Sections were then incubated with 3% NGS (CD20/CD3) or 5% NHS (CD3/TH) followed by incubation with CD3 and TH antibodies, where after they were visualized with Brightvision Poly-AP Goat-anti-Rabbit (ImmunoLogic) and LPR (Dako, Glostrup, Denmark). Sections were dried on a hotplate for 15 min at 60°C and coverslipped with Entellan (Merck, Darmstadt, Germany). Tris-buffered saline with 0.05% Tween20 (TBS-T) was used for all regular washing steps. Negative controls were obtained by incubation with TBS-3% BSA without primary antibodies. Human spleen sections that were previously confirmed to show proper staining for B cells, T cells and sympathetic nerves were included as positive controls.

Microscopic Evaluation

Hematoxylin/eosin and CD3 and CD20 stain was evaluated by bright field microscopy. The chromogen LPR was used to visualize sympathetic nerves. This marker has stable fluorescent characteristics and allows the user to alternately use bright field and fluorescent microscopy on the same slide. This can be beneficial as both modalities have their own advantages, e.g., fluorescent microscopy is more sensitive allowing small nerves to be more easily recognized, whereas bright field allowed better discrimination between lymphocytes and other cells. Instead of using a band pass filter suited for LPR, a long pass filter was used which allowed emission of a broader range of wave lengths. This resulted in a green/yellow autofluorescence of connective tissue, which was used to determine if the observed nerve extended beyond, e.g., perivascular connective tissue. All samples were studied using a DM6 microscope (Leica, Nussloch, Germany) with an I3 fluorescent filter.

Image Acquisition

Single images were captured at various magnifications. These images were either brightfield or fluorescent images, depending on which modality appeared most suited to visualize the structures of interest. Both brightfield and fluorescent tile scans (stitched overlapping images) were captured for digital image analysis. Tile scans were either used to quantify the total amount of sympathetic nerves and T cells or to automatically select PALS regions which were then further studied in detail regarding their innervation (all tile scans were obtained using a 10x objective). Image acquisition was performed using a DM6 microscope with a motorized scanning stage, a I3 fluorescent filter, a DFC7000 T camera and LASX software (all from Leica, Nussloch, Germany).

Quantitative Analysis of General Sympathetic Nerve and T Cell Presence

Bright field and fluorescent tile scans of CD3 and TH stained slides, respectively, were optimized and analyzed in Fiji (ImageJ with additional plugins) (Schindelin et al., 2012). Optimization of the images included removal of irrelevant tissue (e.g., hilar connective tissue and vasculature), artifacts and large trabecular arteries with large surrounding nerves. Both the total splenic tissue area and the area of TH and CD3-IR tissue were selected using standardized thresholds and data was expressed in pixels. The overall area occupied by sympathetic nerves and T cells was expressed as area% with respect to the total tissue area. **Table 3** contains an overview of the different parameters investigated in this study, including a short description of the quantification method and how the data are expressed.

Semi Quantitative Analysis of Sympathetic Nerve Presence and Density in Various Splenic Areas

All samples contained large and small sympathetic nerves. Large nerves run with penetrating and trabecular arteries, whereas small nerves occur as discrete entities or are associated with smaller vascular structure from which they occasionally extent to the surrounding tissue. Only small nerves were evaluated in this study, since they are of relevance in regulation of local processes, such as immune cell function.

Periarteriolar Lymphatic Sheaths

For each sample a series of PALS regions was automatically selected and further studied in detail. No difference was made in types of PALS (being follicle associated PALS or non-follicle associated PALS). Automated selection was performed in Fiji, using tile scans of CD3/TH-stained slides. A threshold was set to select all CD3-IR areas, which were turned into solid regions using a blur function. Solid regions of 40.000 pixels or more were then selected. This approach resulted in a selection of 23–60 PALSs of substantial size. A maximum of 40 selected PALSs were then evaluated for the presence of sympathetic nerves. The number of positive PALSs was counted and expressed as percentage of the total number of studied PALSs. The association

TABLE 3 | Studied parameters, their method of quantification and data expression.

Quantitative analysis of:	**Method of quantification**	**Expressed as**
General sympathetic nerve presence	Automated counting of TH-IR pixels	Area %
General T cell presence	Automated counting of CD3-IR pixels	Area %
Semi-quantitative analysis of:	**Method of quantification**	**Expressed as**
# PALSs with sympathetic nerves	Automated selection of PALSs and manually counting of + PALSs	%
Sympathetic nerve density in:		
PALS	Microscopic evaluation of automated selected PALS for the relation of sympathetic nerves with T cells	Score 1–3
Capsule	General microscopic evaluation	Score 1–3
Trabeculae	General microscopic evaluation	Score 1–3
Red pulp	General microscopic evaluation	Score 1–3
Arteries	General microscopic evaluation	Score 1–3

of sympathetic nerves with T cells was then graded as follows; 1: only one or two sympathetic nerves were observed to extend beyond the connective tissue of the vessel wall and to be in close proximity to T cells immediately lining the vessel wall, 2: multiple sympathetic nerves extended beyond the connective tissue of the vessel wall and were in close proximity to T cells immediately lining the vessel wall and 3: comparable to 2, but nerves extended beyond T cells immediately lining the vessel wall.

Capsule, Trabeculae, Red Pulp and Arteries

All samples were studied microscopically using a 20x objective and alternately switching between brightfield and fluorescent microscopy for reasons described in section "Microscopic Evaluation." Nerve density in various splenic areas was quantified by means of scoring according to the following grading scale: 0: complete absence, 1: low density, 2: moderate density, and 3: high density. These scores were assigned when the observation was representative for the whole sample. With respect to the arteries, a division was made into large and small arteries. Large arteries represented penetrating arteries, also referred to as trabecular arteries (these were surrounded by a substantial amount of connective tissue). Small arteries represented arteries that could be observed in the red and white pulp.

Prior to scoring, various samples of the different age groups were evaluated by the observers in order to obtain a general idea of the extent of PALS innervation, the relation of PALS related sympathetic nerves with T cells, and to low and high nerve densities in other areas. Each sample was examined independently by two observers (CC and DB) who were blinded for the age group. When there was disagreement between the observers the samples were re-examined and scored by consensus.

Statistical Analysis

Statistical analysis and graph conception were performed using Graphpad Prism 8. A Kruskall–Wallis test was used to compare the three age groups for their general sympathetic nerve and T cell presence, and, for sympathetic nerve density in various splenic areas. An uncorrected Dunn's test was used to provide a p-value for each separate group comparison. All parameters were expressed as median followed by their inter quartile range. Association between the general presence of sympathetic nerves and T cells was tested by means of Pearson's correlation coefficient.

RESULTS

All spleens showed well defined white pulp with distinct T and B cell regions (PALS and follicles, respectively) and red pulp with well-defined splenic cords red pulp sinusoids were more indistinctly present. All samples contained blood vessels of various sizes, trabeculae and most samples contained a significant bit of capsule. No pathological abnormalities were observed. TH-IR structures showed comparable patterns to PGP9.5-IR structures in adjacent slides, confirming their nerve identity. **Figure 1** shows examples of normal splenic morphology.

General Sympathetic Nerves and T Cells Presence and Their Age-Related Variation

Sympathetic nerves were detected in 26/26 samples (100%). Nerves were mostly observed surrounding vascular structures and to a lesser extent as discrete structures in the PALS, capsule, trabeculae and red pulp. T cells were observed in all samples and were primarily present in the PALS and to a lesser extent in follicles and in the red pulp. General sympathetic nerve presence was higher in the 10–25 group (0.1 [0.09–0.18]) compared to the neonatal group (0.02 [0.01–0.07], $p = 0.0034$) as well as compared to the 25–70 group (0.04 [0.02–0.05], $p = 0.0192$) (**Figure 2A**). No significant difference in T cell presence was observed between the different age groups (**Figure 2B**). No correlation was found between sympathetic nerve and T cell presence ($r = 0.076$, $p = 0.71$). **Table 4** contains an overview of quantified median data per age group and lists age-related significant differences. Data of all separate individuals can be found in the **Supplementary Data**.

Sympathetic Nerve Presence in the Periarteriolar Lymphatic Sheaths and Its Age-Related Variation

In 25/26 subjects (96%), sympathetic nerves were occasionally observed to extend beyond the adventitial lining of the central

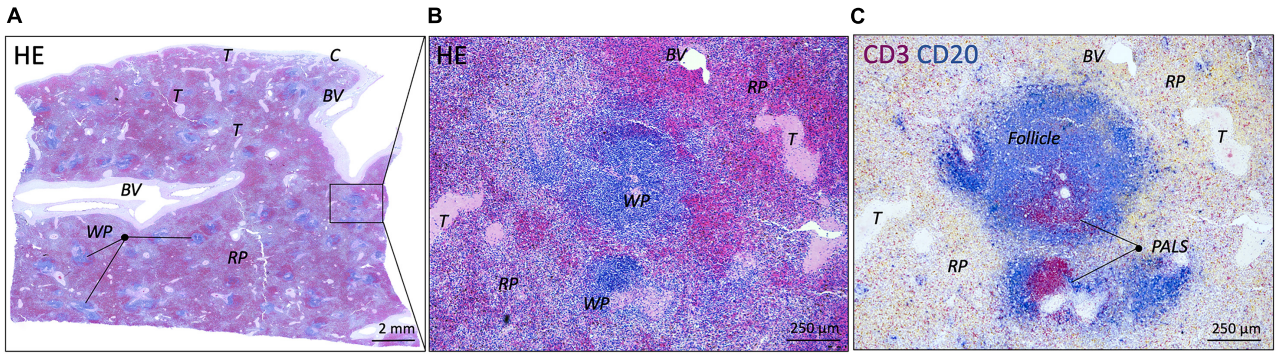

FIGURE 1 | Microscopic images of a normal spleen. **(A)** Overview image of a splenic sample of a patient from the 10–20 years group (HE staining). White and red pulp can be clearly distinguished as well as vascular structures and connective tissue structures such as trabeculae. **(B)** Close up image of the boxed splenic region in **(A)**, showing normal splenic pulp morphology with clear white and red pulp areas (HE staining). **(C)** Similar region as in **(B)**, showing the presence of T and B cells (CD3 and CD20, respectively) in periarteriolar lymphatic sheaths (PALSs) and follicles, respectively. BV, blood vessel; C, capsule; WP, white pulp; RP, red pulp; T, trabecula.

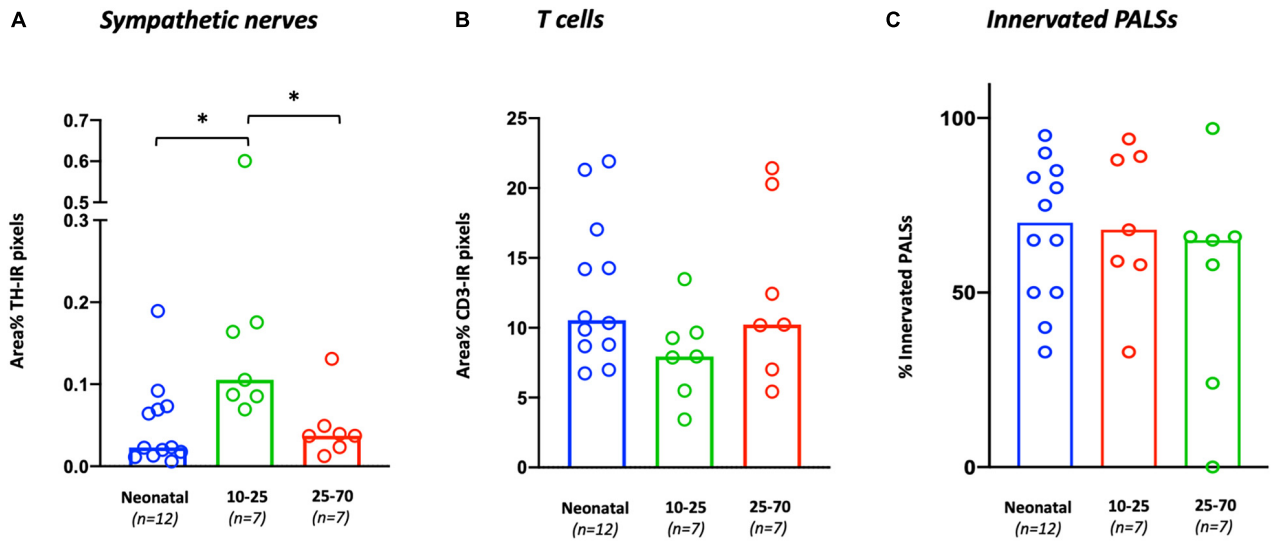

FIGURE 2 | Age-related variations in general T cell and sympathetic nerve presence and the percentage of innervated PALS. **(A)** The general presence of sympathetic nerves per sample is calculated as the number of TH positive pixels and expressed as area % with respect to the total area of each sample. **(B)** The general presence of T cells per sample is calculated as the number of CD3 positive pixels and expressed as area % with respect to the total area of each sample. **(C)** The number of sympathetic innervated PALSs per sample expressed as percentage of the total selected number of PALSs in each sample. *$P < 0.05$.

artery into the lymphatic tissue where they were in close proximity to T cells. To gain an objectified understanding of the number of innervated PALSs, a series of PALSs was automatically selected for each sample and further studied in detail (**Figure 3A**). PALSs with sympathetic nerves in close proximity to T cells were observed in 614 of the in total studied 1027 PALSs (60%). No significant difference in the percentage of innervated PALSs was observed between the different age groups (**Figure 2C**). All PALSs that contained sympathetic nerves were additionally evaluated with respect to the number of nerves that were in association with T cells and whether these nerves would travel further into the lymphatic tissue. Of the in total 1027 studied PALSs, 302 (29%) PALSs contained one paravascular nerve in proximity to T cells (score 1), 249 (24%) PALSs contained multiple nerves (score 2) and 63 (6%) PALSs contained nerves which traveled further into the lymphatic tissue (score 3) (**Figures 3B–H** contains examples of all scores). The neonatal group showed a higher percentage of PALSs with a score 1 (38 [28.5–60]) compared to the 25–70 group (21 [8–41], $p = 0.0059$). For the other scores no age-related differences were observed.

Sympathetic Nerve Density in Other Splenic Areas and Its Age-Related Variation

Capsule

In 25/26 subjects (96%) a substantial amount of capsule was present of which 15 (60%) contained sympathetic nerves. These

TABLE 4 | Age related variations of T cell and sympathetic nerve presence.

	Neonatal	10–25 years	25–70 years	Significant difference
General sympathetic nerve presence (Area %)	*0.02*	*0.10*	0.04	10–25 >neonatal $p = 0.0034$
	(0.01–0.07)	*(0.09–0.18)*	*(0.02–0.05)*	10–25 >25–70 $p = 0.0192$
General T cell presence (Area %)	10.55	7.95	10.23	NS
	(8.70–16.34)	*(5.50–9.66)*	*(7.02–20.29)*	
# PALSs with sympathetic nerves (%)	70 *(50–95)*	68 *(58–89)*	65 *(24–66)*	NS
Score 1 (%)	38	34	21	Neonatal >25–70 $p = 0.0059$
	(28.5–60)	*(21–41)*	*(8–41)*	
Score 2 (%)	10	9	8	NS
	(5–14.75)	*(4–19)*	*(1–11)*	
Score 3 (%)	4	6	9	NS
	(0–9.5)	*(0–12)*	*(0–11)*	
Sympathetic nerve density in:				
Capsule	2	0	0	Neonatal >10–25 $p = 0.0003$
	(1–2)	(0–0)	(0–1.25)	Neonatal >25–70 $p = 0.008$
Trabeculae	1	1	1	NS
	(1–2)	*(1–3)*	*(1–2)*	
Large arteries	3	2	2	Neonatal >25–70 $p = 0.0098$
	(2–3)	*(2–3)*	*(1–2)*	
Small arteries	3	2	2	NS
	(2–3)	*(2–3)*	*(1–2)*	
Red pulp	2	1	0	Neonatal >25–70 $p = 0.0016$
	(1–2)	(0–2)	(0–1)	

Data is expressed as median values (interquartile range is placed between brackets). Observed significant differences between groups are listed including their p-value.

nerves were scattered and were mainly observed in the part of the capsule which was in close proximity to the hilum, where vascular structures with surrounding nerves entered the spleen. In the hilar region, the capsule was less distinct and showed continuity with hilar specific structures such as the adventitia of incoming vascular structures or the connective tissue of suspending splenic ligaments (**Figures 4A,B**). Most observed capsular nerve tissue was present in the more superficial and middle part of the capsule (**Figures 4D–F**) and only sporadically in the deeper part, where it was in direct contact with the red pulp (**Figure 4C**).

Trabeculae

All subjects showed trabeculae which, as a result of the cutting plane of the samples, were observed either as immediate extensions of the capsule, or as discrete structures deeper in the parenchyma (**Figure 5A**). The deeper parts of the trabeculae frequently contained large vascular structures (**Figures 5C,E**). In 25/26 (96%) subjects, trabecular sympathetic nerves were present to some extent and were often observed in the deeper parts of trabeculae, whereas the trabeculae that extended immediately from the capsule were mostly devoid of nerves. Trabecular sympathetic nerves were observed as discrete structures (**Figures 5B,D,F**), or as a nerve plexus surrounding vascular structures (**Figures 5C,E**). In both cases nerves could extend up to the external border of the trabecular tissue where nerves were in proximity to the surrounding red pulp.

Arteries

All 26 subjects had clear recognizable vascular structures of various sizes which were to some extent surrounded with perivascular sympathetic nerves (**Figure 6**). In case of splenic artery branches in the hilum or large incoming trabecular arteries, nerve tissue was presented as large nerve bundles running in the adventitia or trabecular connective tissue, respectively, or as finer neural structures. In case of smaller arteries, nerves were organized in a more delicate network that were in close proximity to the vessel wall. Occasionally, perivascular nerves extended beyond the adventitial connective tissue. This was observed in central arteries, trabecular arteries and to a lesser extent in small arteries in the red pulp.

Red Pulp

The red pulp of all subjects contained clearly recognizable lymphoid tissue, also known as the splenic cords (**Figure 7A**). Sinusoids were easily recognized if they contained a substantial amount of blood, but otherwise were less distinct. Sympathetic nerves were observed in the red pulp of 20/26 (77%) subjects. These nerves comprised either small solitary nerves in between the red pulp (**Figures 7B,D**), or nerves bordering parenchymal trabeculae (**Figures 5B,E,F**, **7C**) or small vascular structures (**Figures 5F**, **7A,D,E**).

Age-Related Variations

Age-related differences were observed with respect to nerve density in the capsule, large arteries and the red pulp. The neonatal group showed a significant higher nerve density in its capsule compared to both the 10–25 and 25–70 group, and, surrounding its large arteries and in its red pulp when compared to the 25–70 group. No age-related differences were

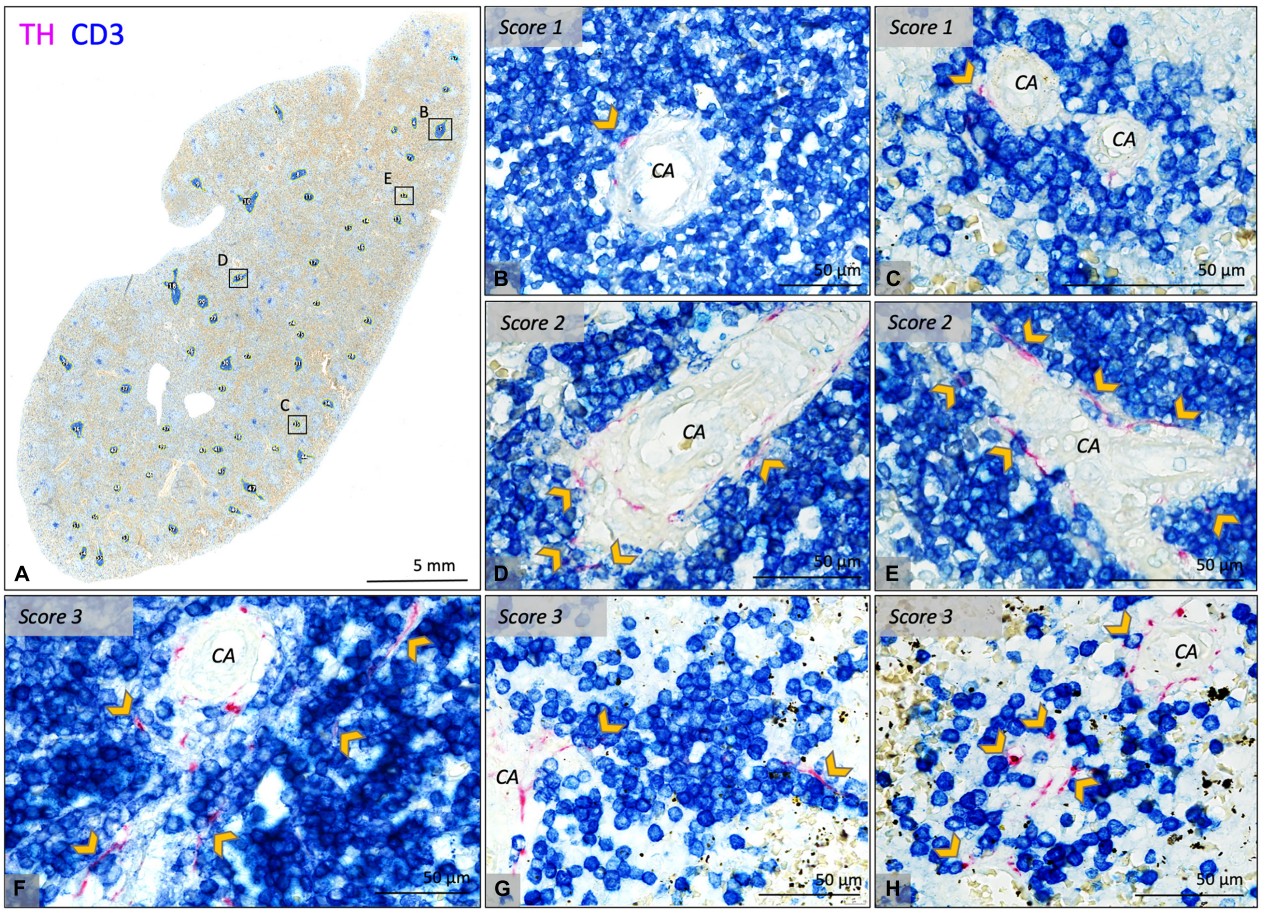

FIGURE 3 | Bright field microscopic images of PALS related sympathetic nerves in CD3/TH double stained splenic tissue slides of various neonatal individuals. **(A)** Overview image of a splenic sample showing automatically selected T cell regions which were further investigated for the presence of sympathetic nerves and their relation with T cells. **(B–E)** Close up images of the marked regions in **(A)** representing PALSs with a score 1 or 2. **(F–H)** Close up images of PALSs with a score 3 (all from different neonatal individuals). Score 1: Only one or two sympathetic nerves were observed to extend beyond the connective tissue of the vessel wall of the central artery (CA) and to be in close proximity with T cells immediately lining the vessel wall. Score2: multiple sympathetic nerves extended beyond the connective tissue of the CA and were in close proximity with T cells immediately lining the vessel wall. Score 3: comparable to 2, but nerves extended beyond T cells immediately lining the vessel wall. CA, central artery; Arrow heads: pointing out sympathetic nerves that are in close proximity with T cells, but might be obscured by the blue stain.

observed in trabeculae and small arteries. **Table 4** contains detailed information on median group data and *p*-values.

DISCUSSION

This study shows that the human spleen contains sympathetic nerves, not only associated with the splenic vasculature, but also as discrete structures in the PALS, capsule, trabeculae and red pulp. Furthermore, the presence of sympathetic nerves shows a mild tendency to decrease with age. These findings are of relevance for understanding the role of splenic sympathetic nerves in regulation of the systemic immune response in humans and for the development of neuromodulatory anti-inflammatory therapies.

Sympathetic nerves were observed in all spleens but their presence was most prominent in the 10–25 age group, suggesting that from birth their number increases whereafter it decreases from adulthood on. This observation fits in with the fact that organ systems, including the peripheral nervous system, mature after birth until the onset of adulthood whereafter they subsequently show signs of aging (Verdú et al., 2000). More specifically, animal studies have shown that an age-related decline applies for splenic sympathetic innervation as well (Bellinger et al., 1987, 1992; Madden et al., 1997).

A decrease in T cell presence has been put forward as another explanation for a decrease in sympathetic nerve abundance (Hoover et al., 2017). The authors observed the presence of T cells to correlate to that of sympathetic nerves and suggested the lack of specific nerve growth factors produced by these T cells to be of relevance. In the current study, however, no correlation between the general presence of sympathetic nerves and T cells (both expressed as area%) was found, thereby further

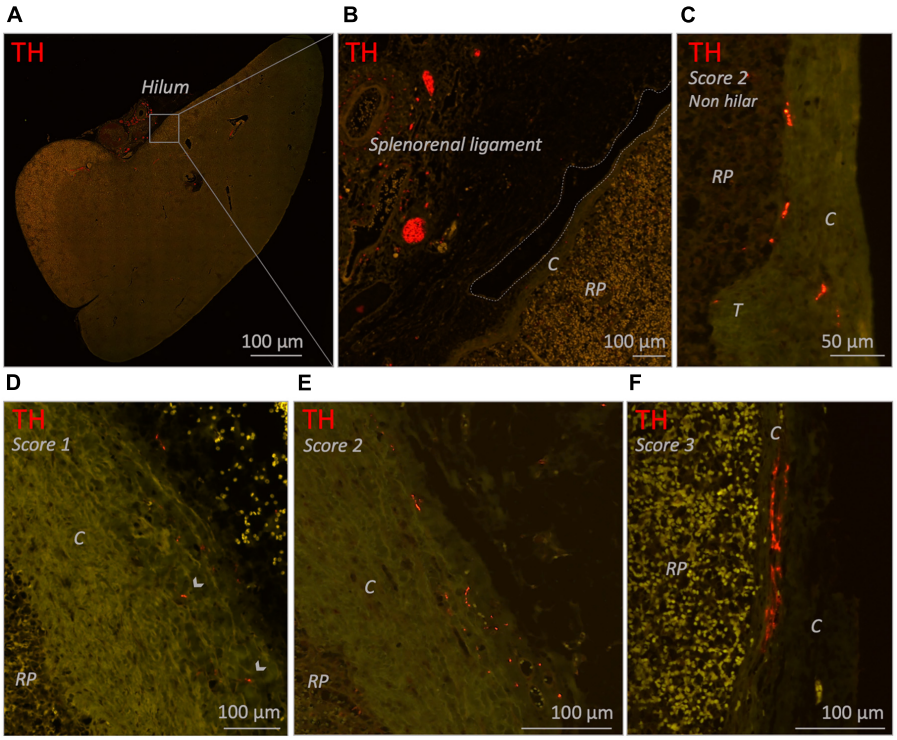

FIGURE 4 | Fluorescence microscopic images of various capsule related sympathetic nerve densities (TH staining). **(A)** Overview image of a neonatal spleen. Large blood vessels with a perivascular nerve plexus reside in the splenorenal ligament and enter the spleen at the hilum. **(B)** Close up images of the boxed region in **(A)**. The splenorenal ligament contains connective tissue, vascular structures and sympathetic nerves. The lining of the splenorenal ligament reflects over the hilar capsule and on its distal continuation thins out (dotted line shows the lining of the ligament). **(C)** Close up image of a part of a capsule obtained from a non-hilar part of a neonatal spleen. A moderate density (score 2) of sympathetic nerves can be observed. **(D,E)** Close up images of hilar capsule samples of spleens of individuals from the 25–70 years age group containing a low (score 1) and moderate (score 2) density of sympathetic nerves, respectively. **(F)** Close up image of hilar capsule sample of a neonatal spleen with a high (score 3) density of sympathetic nerves. Capsular nerves were mostly observed in the more superficial and middle part of the capsule and only sporadically in the deeper part where they were in direct contact with the red pulp (as shown in **C**). C, capsule; RP, red pulp; T, trabecula. Arrow heads: small capsular nerves.

emphasizing aging to be the most plausible explanation for the observed decline of sympathetic innervation in spleens of healthy persons.

In 96% of the studied individuals, PALSs were observed to contain sympathetic nerves that extended beyond the adventitia of central arteries and to be in apposition with T cells. So far PALS innervation in humans have only been reported once (Hoover et al., 2017). The authors, however, did not supply information on the number of innervated PALSs per individual, deeming it impossible to estimate whether PALS innervation represented a structural entity of normal healthy spleens or a more coincidental heterogenous finding. The current study shows that human PALSs innervation was observed in 60% of the in total 1027 studied PALSs and therefore represents a structural phenomenon. Furthermore, no significant age-related differences could be determined with respect to the innervation of the number of PALSs, or the extent to which sympathetic nerves were in proximity to T cells.

Sympathetic innervation patterns observed so far in human PALSs, however, seem to differ significantly from rodent species. In rats, mice and rabbits, nerves were more densely present and also traveled further into the parenchyma (Felten et al., 1987, 1997; Bellinger et al., 1992). This questions whether splenic plexus stimulation in humans, with only a few T cells of the PALS in direct contact with sympathetic nerves, would target enough of these cells to establish a similar systemic anti-inflammatory effect as observed in rodents. It is, however, known that vagus nerve stimulation in humans results in a systemic anti-inflammatory response (Koopman et al., 2016). Since vagus nerve stimulation activates the splenic plexus (Reardon, 2016; Pavlov and Tracey, 2017) this effect must be elicited by splenic sympathetic nerves, potentially involving different components and/or locations than what is known for the prevailing CAIP NE-Ach-TNF mechanism. In the following part various alternative options for explaining this effect will be discussed in the light of our findings.

Most T cells are migratory cells and reside in the PALS for only a certain amount of time whereafter they disseminate to the red pulp and return to the systemic circulation. If, during this migration, enough $CD4^{+}$T cells pass sympathetic nerves and short term synaptic connections are formed,

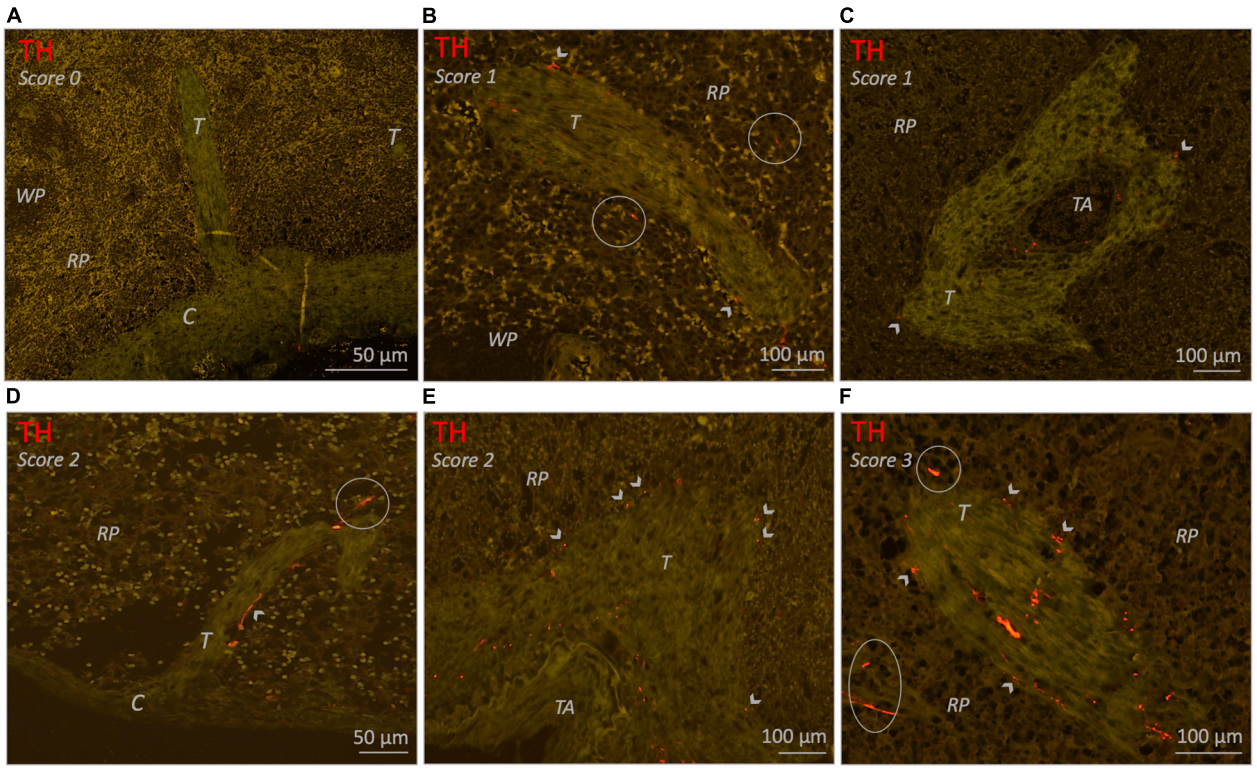

FIGURE 5 | Fluorescence microscopic images of various trabecula related sympathetic nerve densities (TH staining) in different neonatal individuals. **(A)** Spleen without trabecular sympathetic nerves (score 0). **(B)** Trabecula with a low density (score 1) of sympathetic nerves. A few small nerves are present within the connective tissue of the trabecular and a few nerves can be observed on its outer margin where they are in proximity to the RP. **(C)** Trabecula with a low density (score 1) of sympathetic nerves. Perivascular nerves can be observed in the adventitia of a small blood vessel (trabecular artery) and in the connective tissue of the trabecula from where it diverges to its outer margins where a few nerves are bordering the RP. **(D)** Trabecula extending from the capsule with a moderate density (score 2) of sympathetic nerves. Most nerves are in proximity to the RP and on its cranial site a nerve extents into the RP. Sympathetic nerves in parts of trabeculae directly extending from the capsule were very sparse. **(E)** Comparable to **(C)** but this figure contains a larger trabecular artery and shows a moderate density (score 2) of sympathetic nerves. **(F)** Trabecula with a high density (score 3) of sympathetic nerves which diverge to the trabecula's outer border to be in proximity to the RP.

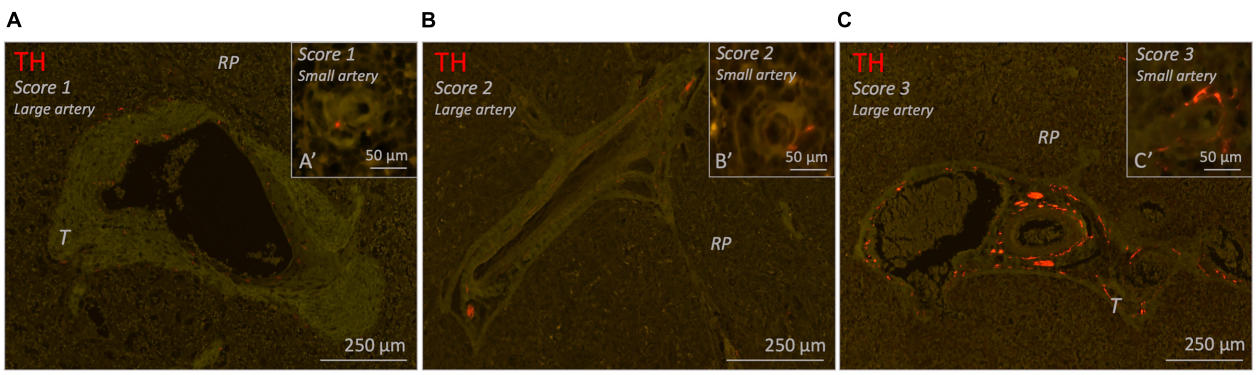

FIGURE 6 | Fluorescence microscopic images of various of blood vessel related sympathetic nerve densities (TH staining) in different 25–70 years age group individuals. Each figure contains a representative example of a large vessel and a small vessel with a specific amount of sympathetic nerves (score 1–3). **(A–C)** Splenic samples with a low, moderate or high density of sympathetic nerves surrounding large arteries (score 1-3). (A'–C') Splenic samples with a low, moderate, or high density of sympathetic nerves surrounding small arteries (score 1–3). RP, red pulp; T, trabecula.

a phenomenon referred to as short term plasticity (Song et al., 2018), a significant amount of adrenergic receptors on CD4 $^{+}$T cells might indeed get activated. Another potential mechanism to overcome this issue might be volume transmission; a process wherein a neurotransmitter is not released in a synaptic cleft but is expelled into the

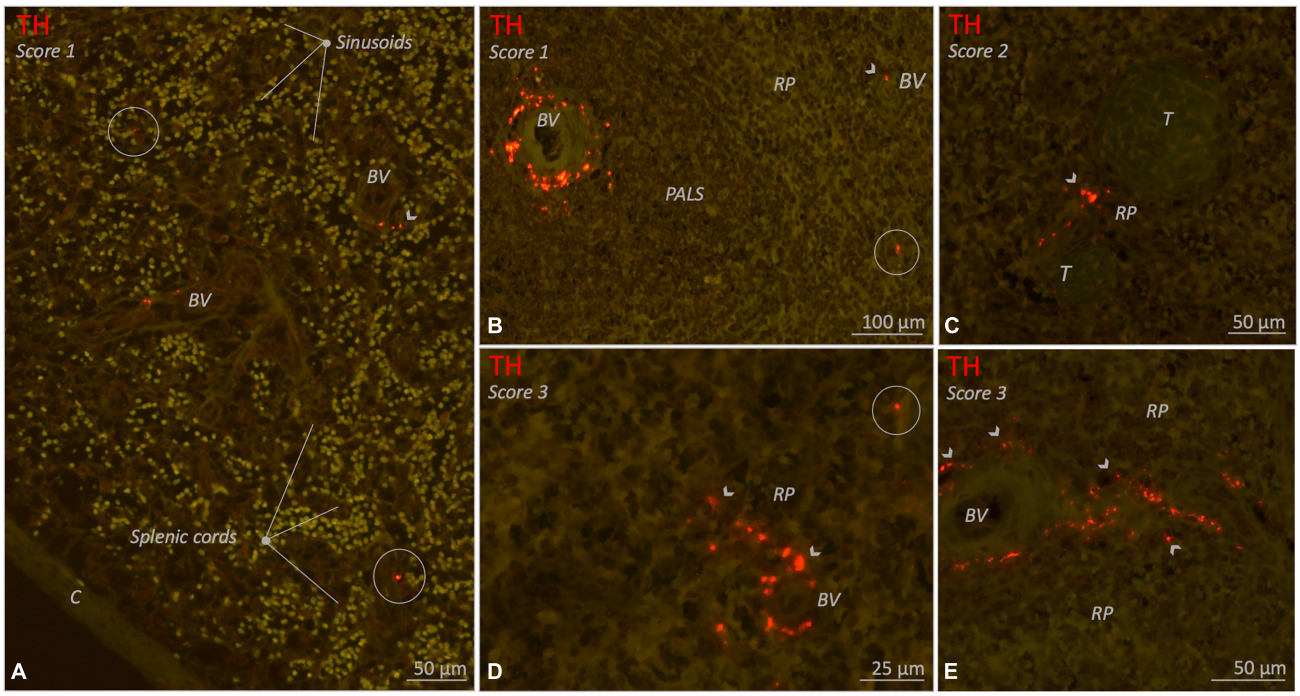

FIGURE 7 | Fluorescence microscopic images of various red pulp related sympathetic nerve densities (TH staining) in different 10–25 year age group individuals. Sympathetic nerves are present as discrete structures running in the splenic cords (encircled structures) or as nerves that originate from a perivascular or trabecular plexus and from there diverge further into the red pulp (RP) (arrow heads). **(A)** Splenic sample with clear splenic cords and sinusoids and a low density (score 1) of sympathetic nerves. **(B–E)** Various examples of spleens with RP related nerves either as a low density (score 1), a moderate density (score 2) or a high (score 3) RP related sympathetic nerve density. C, capsule; BV, blood vessel; PALS, periarteriolar lymphatic sheath; RP, red pulp; T, trabecula.

extracellular matrix and reaches its effector cells by diffusion (Fuxe et al., 2013). Volume transmission of NE could result in adrenergic activation in increased numbers and more distant T cells other than the ones in direct contact with sympathetic nerves. Furthermore, the splenic white pulp appears to contain low amounts of acetylcholinesterase (Hoover et al., 2020), and volume transmission of Ach (secreted by activated T cells in the PALS) might occur as well, thereby further expanding the indirect effector scope of sympathetic nerves.

Other studies have casted doubt on the prevailing mechanisms of the cholinergic anti-inflammatory pathway involving the sequence of NE release, ACh production, and subsequent TNFα reduction through cholinergic receptor activation on macrophages, both with respect to the mechanism itself and with respect to its location (Rosas-Ballina et al., 2008; Murray et al., 2017). In a recent study wherein the relationship between sympathetic neurons and $ChAT^+$ lymphocytes were mapped in complete mouse spleens, it was shown that overall few $ChAT^+$ T cells were juxtaposed to sympathetic fibers and that their distance to these fibers exceeded that of traditional synapses (Murray et al., 2017). Moreover, the authors showed that sympathetic innervation was involved in homing of $ChAT^+$T cells to appropriate physical regions in the spleen by increasing the expression of the chemokine CXCL13 in stromal cells (Murray et al., 2017). Such homing processes are vital as it conjoins the right cells for a properly aligned immune response (reviewed by Zhao et al., 2015). In case of conjoining the key mediators of the intrasplenic NE-ACh-TNFα mechanism, this requires homing of $ChAT^+$T cells towards macrophage rich areas such as the marginal zone and the red pulp, where adrenergic receptors on these T cells need to be activated prior to release of ACh in proximity to these macrophages. Interestingly, vagus nerve stimulation in mice specifically attenuated TNFα production by splenic macrophages in these two areas 30 minutes after endotoxin administration (Rosas-Ballina et al., 2008). The authors observed nerve terminals adjacent to these TNFα producing macrophages, but did not provide information on the local presence of $ChAT^+$ T cells. With the above discussed topics in mind, it would be more plausible that the intrasplenic NE-Ach-TNFα mechanism occurs in the marginal zone and red pulp, instead of the PALS. Further support for favoring the red pulp and marginal zone over the PALS as designated immune regulation areas, is the difference in T cell transit time. T cell passage through the red pulp and marginal zone takes 5 and 50 min respectively whereas passage through the PALS (from the perivascular area to the macrophage rich marginal zone/red pulp) takes 2.5–6 h (Hammond, 1975; Ford, 1979; Ganusov and Auerbach, 2014) and the latter may take too long to provoke the fast systemic response which peaks at 90 min after electrical stimulation (Rosas-Ballina et al., 2008; Komega et al., 2018; Guyot et al., 2019).

According to recent literature, human spleens do not have a marginal zone but their red pulp is considered to be morphologically and functionally comparable to mice and rats (reviewed by Steiniger, 2015). In contrast to previous studies (Heusermann and Stutte, 1977; Kudoh et al., 1979; Anagnostou et al., 2007; Verlinden et al., 2018) the current study showed that, although rare, red pulp innervation is present in all age groups albeit it more prominent in younger individuals. Sporadically, discrete nerves were observed within the red pulp, but most of the red pulp innervation was supplied either by trabecular nerves which extended to the outer margins of the trabecular connective tissue, or by nerves positioned outside the connective tissue surrounding small red pulp vascular structures. These nerves always remained in proximity to the trabeculae and vascular structures and never traveled deeper into the red pulp. In human fetuses, capsular nerves have also been observed to extend into the red pulp (Anagnostou et al., 2007). In the current study, however, capsular nerves have been observed in all age groups, but only rarely extended into the red pulp or reached the inner capsular margins contacting the red pulp and therefore were not considered to generally contribute to red pulp innervation.

Thus, comparable to the PALS, the red pulp in humans contains significant less sympathetic innervation when compared to other animals in which red pulp innervation was already considered sparse (Bellinger et al., 1987). Therefore, again one could question whether splenic plexus stimulation in humans would target a sufficient amount of red pulp effector cells to provoke the effect observed in animals (Rosas-Ballina et al., 2008). While searching the literature for the role of the stromal cells in immune regulation, a more elegant and subtle mechanism, which potentially requires little direct innervation of red pulp immune cells, was found. In the spleen stromal cells reside in both the white and red pulp where they represent the main cellular components of the reticular framework, a connective tissue scaffold which provides support for splenic immune cells and guidance for their migration (Perez-Shibayama et al., 2019). As shown by a transmission electron microscopic study in guinea pigs, the reticular framework is composed enveloping reticular cells which enclose connective tissue components and occasionally a sympathetic axon or free nerve endings (Saito, 1990). The connective tissue space of the framework was shown to be continuous and to contain meshwork like spaces (Saito, 1990). The author referred to these meshwork like spaces as catecholamine canals since he hypothesized them to facilitate diffusion of released sympathetic neurotransmitters over larger distances throughout the reticular framework. With the exception of follicles, the reticular cells of the reticular framework are represented by contractile myofibroblasts (Pinkus et al., 1986). Contraction of these myofibroblasts results in exposure of migrating immune cells to the content of catecholamine canals; sympathetic nerve endings or previously secreted and diffused NE (Saito, 1990). Adrenergic signaling can than modulate the immune response, which in case of diffused NE does not require direct immune cell innervation. The reticular framework might equal the more recent discovered splenic conduit system in mice; an interconnected tubular network that functions as a transport system for fluid, small molecules and particles (including antigens) and is covered with fibroblast reticular cells which support migratory lymphocytes (Nolte et al., 2003; Roozendaal et al., 2008). Whether the human spleen contains catecholamine cannals or a conduit system has not been established yet.

Overall, it can be concluded that, apparent age-related and interspecies differences in splenic sympathetic nerve distribution and density exists. It is, however, uncertain if and to what extent these differences are of significance for NE-ACh-TNFα mechanism based anti-inflammatory therapies in humans. Although experimental studies have shown an indisputable role for sympathetic nerves, $ChAT^{+}$ T cells and macrophages, it is, however, not completely understood how and where the various elements of the prevailing intrasplenic NE-ACh-TNFα mechanism interact and whether unknown intermediate elements are required. In order to be able to extrapolate experimental data to humans and to estimate whether targeting splenic sympathetic nerves in humans could be beneficial, additional experimental and morphological studies are required and alternative or additional mechanisms should be taken into consideration.

Study Limitations

The use of single tissue sections will result in a 2D representation of sympathetic nerves in relation with surrounding structures. This makes it difficult to truly estimate whether the evaluated sympathetic nerves represent small, local tissue innervating (discrete) nerves or that they might be part of larger *en route* nerves. This bias should be kept in mind when interpretating data on sympathetic nerve quantification. However, since the same bias applies to all samples, we consider its influence on group comparison data negligible.

CONCLUSION

Although less extensive when compared to other animals, human spleens contain sympathetic nerves, not only associated with vascular structures but also as discrete entities. In the PALS, these nerves were in proximity to T cells, suggesting the potential existence of a CAIP in humans. Alternative locations involved in neuroimmune regulation might be represented by the capsule, trabeculae and red pulp since these structures contain discrete sympathetic nerves as well. Since splenic sympathetic nerve distribution and density shows interspecies variation and our general understanding of the relative and spatial contribution of splenic innervation in immune regulation is incomplete, it remains difficult to estimate the anti-inflammatory potential of targeting splenic sympathetic nerves in humans. Future studies should focus on the anti-inflammatory efficacy of targeting these nerves in humans and further characterize the underlying mechanism. Splenic sympathetic innervation density slightly decreases from adulthood on and these age-related variations might be of relevance when developing sympathetic nerve based anti-inflammatory therapies.

DATA AVAILABILITY STATEMENT

The original contributions presented in the study are included in the article/**Supplementary Material**, further inquiries can be directed to the corresponding author/s.

ETHICS STATEMENT

The studies involving human participants were reviewed and approved by the Medical Ethical Committee (#18-167) as a "non-Medical Research Act" study and the Biobank of the University Medical Center Utrecht approved to use the rest biomaterial for this research (biobank #18-284). Written informed consent to participate in this study was provided by the participants' legal guardian/next of kin.

AUTHOR CONTRIBUTIONS

CC: study design, sample preparation, image analysis, data interpretation, and manuscript writing. DB: study design, sample preparation, data interpretation, and manuscript writing. MN, WJ, and RB: manuscript revision. PN, ML, and RB: sample collection and manuscript revision. RB: manuscript revision and project supervision. All authors contributed to the article and approved the submitted version.

SUPPLEMENTARY MATERIAL

The Supplementary Material for this article can be found online at: https://www.frontiersin.org/articles/10.3389/fnins.2021.726825/full#supplementary-material

Supplementary Table 1 | Data of separate individuals.

REFERENCES

Anagnostou, V. K., Doussis-Anagnostopoulou, I., Tiniakos, D. G., Karandrea, D., Agapitos, E., Karakitsos, P., et al. (2007). Ontogeny of intrinsic innervation in the human thymus and spleen. *J. Histochem. Cytochem.* 55, 813–820. doi: 10.1369/jhc.6A7168.2007

Bellinger, D. L., Ackerman, K. D., Felten, S. Y., and Felten, D. L. (1992). A longitudinal study of age-related loss of noradrenergic nerves and lymphoid cells in the rat spleen. *Exp. Neurol.* 116, 295–311.

Bellinger, D. L., Felten, T. J., Collier, T. J., and Felten, D. L. (1987). Noradrenergic sympathetic innervation of the spleen: IV. Morphometric analysis i adult and aged F344 rats. *J. Neurosci. Res.* 18, 55–63. doi: 10.1002/jnr.490180109

Bleys, R. L. A. W., and Cowen, T. (2001). Innervation of cerebral blood vessels: morphology, plasticity, age-related, and alzheimer ' s disease-related. *Neurodegeneration* 118, 106–118.

Borovikova, L. V., Ivanova, S., Zhang, M., Yang, H., Botchkina, G. I., Watkins, L. R., et al. (2000). Vagus nerve stimulation attenuates the systemic inflammatory response to endotoxin. *Nature* 405, 458–462. doi: 10.1038/35013070

Cleypool, C. G. J., Lotgerink Bruinenberg, D., Roeling, T., Irwin, E., and Bleys, R. L. A. W. (2020). Splenic artery loops: potential splenic plexus stimulation sites for neuroimmunomodulatory-based anti-inflammatory therapy? *Clin. Anat.* 34, 371–380. doi: 10.1002/ca.23643

Cleypool, C. G. J., Schurink, B., Van Der Horst, D. E. M., and Bleys, R. L. A. W. (2019). Sympathetic nerve tissue in milky spots of the human greater omentum. *J. Anat.* 236, 156–164. doi: 10.1111/joa.13077

de Jonge, W. J., van der Zanden, E. P., The, F. O., Bijlsma, M. F., van Westerloo, D. J., Bennink, R. J., et al. (2005). Stimulation of the vagus nerve attenuates macrophage activation by activating the Jak2-STAT3 signaling pathway. *Nat. Immunol.* 6, 844–851. doi: 10.1038/ni1229

Felten, D. L., Ackerman, K. D., Wiegand, S. J., and Felten, S. Y. (1987). Noradrenergic sympathetic innervation of the spleen: I. nerve fibers associate with lymphocytes and macrophages in specific compartments of the splenic white pulp. *J. Neurosci. Res.* 18, 28–36. doi: 10.1002/jnr.490180107

Felten, D. L., Felten, S. Y., Carlson, S. L., Olschowka, J. A., and Livnat, S. (1997). Noradrenergic and peptidergic innervation of lymphoid organs. *J. Immunol.* 135, 755–765. doi: 10.1159/000058655

Felten, S. Y., and Olschowka, J. (1987). Noradrenergic sympathetic innervation of the spleen: II. tyrosine hydroxylase (TH)-positive nerve terminals form synapticlike contacts on lymphocytes in the splenic white pulp. *J. Neurosci. Res.* 18, 37–48. doi: 10.1002/jnr.490180108

Ford, W. L. (1979). Lymphocytes. 3. distribution. distribution of lymphocytes in health. *J. Clin. Pathol. Suppl.* 13, 63–69. doi: 10.1136/jcp.s3-13.1.63

Fuxe, K., Borroto-Escuela, D. O., Romero-Fernandez, W., Zhang, W. B., and Agnati, L. F. (2013). Volume transmission and its different forms in the central nervous system. *Chin. J. Integr. Med.* 19, 323–329. doi: 10.1007/s11655-013-1455-1

Ganusov, V. V., and Auerbach, J. (2014). Mathematical modeling reveals kinetics of lymphocyte recirculation in the whole organism. *PLoS Comput. Biol.* 10:e1003586. doi: 10.1371/journal.pcbi.1003586

Guyot, M., Simon, T., Panzolini, C., Ceppo, F., Daoudlarian, D., Murris, E., et al. (2019). Brain, behavior, and immunity apical splenic nerve electrical stimulation discloses an anti-in fl ammatory pathway relying on adrenergic and nicotinic receptors in myeloid cells. *Brain Behav. Immun.* 80, 238–246. doi: 10.1016/j.bbi.2019.03.015

Hammond, B. J. (1975). A compartmental analysis of corculatory lymphocytes in the spleen. *Cell Tissue Kinet.* 8, 153–169.

Heusermann, U., and Stutte, H. J. (1977). Electron microscopic studies of the innervation of the human spleen. *Cell Tissue Res.* 184, 225–236. doi: 10.1007/BF00223070

Hoover, D. B., Brown, T. C., Miller, M. K., Schweitzer, J. B., and Williams, D. L. (2017). Loss of sympathetic nerves in spleens from patients with end stage sepsis. *Front. Immunol.* 8:e01712. doi: 10.3389/fimmu.2017.01712

Hoover, D. B., Poston, M. D., Brown, S., Lawson, S. E., Bond, C. E., Downs, A. M., et al. (2020). Cholinergic leukocytes in sepsis and at the neuroimmune junction in the spleen. *Int. Immunopharmacol.* 81:106359. doi: 10.1016/j.intimp.2020.106359

Kees, M. G., Pongratz, G., Kees, F., Schölmerich, J. U., and Straub, R. H. (2003). Via β-adrenoceptors, stimulation of extrasplenic sympathetic nerve fibers inhibits lipopolysaccharide-induced TNF secretion in perfused rat spleen. *J. Neuroimmunol.* 145, 77–85. doi: 10.1016/j.jneuroim.2003.09.011

Komega, E. N., Farmer, D. G. S., Brooks, V. L., McKinley, M. J., McAllen, R. M., and Martelli, D. (2018). Vagal afferent activation suppresses systemic in flammation via the splanchnic anti-inflammatory pathway. *Brain Behav. Immun.* 73, 441–449. doi: 10.1016/j.bbi.2018.06.005

Koopman, F. A., Chavan, S. S., Miljko, S., Grazio, S., Sokolovic, S., Schuurman, P. R., et al. (2016). Vagus nerve stimulation inhibits cytokine production and attenuates disease severity in rheumatoid arthritis. *Proc. Natl. Acad. Sci. U.S.A.* 113, 8284–8289. doi: 10.1073/pnas.1605635113

Kox, M., van Velzen, J. F., Pompe, J. C., Hoedemaekers, C. W., van der Hoeven, J. G., and Pickkers, P. (2009). GTS-21 inhibits pro-inflammatory cytokine release independent of the Toll-like receptor stimulated via a transcriptional mechanism involving JAK2 activation. *Biochem. Pharmacol.* 78, 863–872. doi: 10.1016/j.bcp.2009.06.096

Kudoh, G., Hoshi, K., and Murakami, T. (1979). Fluorescence of the microscopic and enzyme spleen histochemical studies innervation of the human. *Arch. Histol. Cytol.* 42, 169–180.

Lu, B., and Kwan, K. (2014). α7 Nicotinic acetylcholine receptor signaling inhibits inflammasome activation by preventing mitochondrial DNA Release. *Mol. Med.* 20, 350–358. doi: 10.2119/molmed.2013.00117

Madden, K. S., Bellinger, D. L., Felten, S. Y., Snyder, E., Maida, M. E., and Felten, D. L. (1997). Alterations in sympathetic innervation of thymus and spleen in aged mice. *Mech. Ageing Dev.* 94, 165–175. doi: 10.1016/s0047-6374(96)01858-1

Murray, K., Godinez, D. R., Brust-Mascher, I., Miller, E. N., Gareau, M. G., and Reardon, C. (2017). Neuroanatomy of the spleen: mapping the relationship between sympathetic neurons and lymphocytes. *PLoS One* 12:e0182416. doi: 10.1371/journal.pone.0182416

Nolte, M. A., Beliën, J. A., Schadee-Eestermans, I., Jansen, W., Unger, W. W., van Rooijen, N., et al. (2003). A conduit system distributes chemokines and small blood borne molecules through the splenic white pulp. *Exp. Med.* 198, 505–512. doi: 10.1084/jem.20021801

Pavlov, V. A., and Tracey, K. J. (2017). Neural regulation of immunity: molecular mechanisms and clinical translation. *Nat. Neurosci.* 20, 156–166. doi: 10.1038/nn.4477

Perez-Shibayama, C., Gil-Cruz, C., and Ludewig, B. (2019). Fibroblastic reticular cells at the nexus of innate and adaptive immune responses. *Immunol. Rev.* 289, 31–41. doi: 10.1111/imr.12748

Pinkus, G. S., Warhol, M. J., O'Connor, E. M., Etheridge, C. L., and Fujiwara, K. (1986). Immunohistochemical localization of smooth muscle myosin in human spleen, lymph node, and other lymphoid tissues. Unique staining patterns in splenic white pulp and sinuses, lymphoid follicles, and certain vasculature, with ultrastructural correlations. *Am. J. Pathol.* 123, 440–453.

Reardon, C. (2016). Neuro-immune interactions in the cholinergic anti-inflammatory reflex. *Immunol. Lett.* 178, 92–96. doi: 10.1016/j.imlet.2016.08.006

Roozendaal, R., Mebius, R. E., and Kraal, G. (2008). The conduit system of the lymph node. *Int. Immunol.* 20, 1483–1487. doi: 10.1093/intimm/dxn110

Rosas-Ballina, M., Ochani, M., Parrish, W. R., Ochani, K., Harris, Y. T., Huston, J. M., et al. (2008). Splenic nerve is required for cholinergic antiinflammatory pathway control of TNF in endotoxemia. *Proc. Natl. Acad. Sci. U.S.A.* 105, 11008–11013. doi: 10.1073/pnas.0803237105

Rosas-Ballina, M., Olofsson, P. S., Ochani, M., Valdes-Ferrer, S. I., Levine, Y. A., Reardon, C., et al. (2011). Acetylcholine-synthesizing T cells relay neural signals in a vagus nerve circuit. *Science* 334, 98–101. doi: 10.1126/science.1209985

Saito, H. (1990). Innervation of the guinea pig spleen studied by electron microscopy. *Am. J. Anat.* 189, 213–215.

Schindelin, J., Arganda-Carreras, I., Frise, E., Kaynig, V., Longair, M., Pietzsch, T., et al. (2012). Fiji: an open-source platform for biological-image analysis. *Nat. Methods* 9, 676–682. doi: 10.1038/nmeth.2019

Song, D., Robinson, B. S., and Berger, T. W. (2018). Identification of short-term and long-term functional synaptic plasticity from spiking activities. *Adapt. Learn. Methods Nonlinear Syst. Model.* 2018, 289–312.

Steiniger, B. S. (2015). Human spleen microanatomy: Why mice do not suffice. *Immunology* 145, 334–346. doi: 10.1111/imm.12469

Van der Loos, C. M. (2010). Chromogens in multiple immunohistochemical staining used for visual assessment and spectral imaging: the colorful future. *J. Histotechnol.* 33, 31–40. doi: 10.1179/his.2010.33.1.31

Verdú, E., Ceballos, D., Vilches, J. J., and Navarro, X. (2000). Influence of aging on peripheral nerve function and regeneration. *J. Peripher. Nerv. Syst.* 5, 191–208. doi: 10.1046/j.1529-8027.2000.00026.x

Verlinden, T. J. M., Van Dijk, P., Hikspoors, J., Herrler, A., Lamers, W. H., and Köhler, S. E. (2018). Brain, behavior, and immunity innervation of the human spleen: a complete hilum-embedding approach. *Brain Behav. Immun.* 77, 92–100. doi: 10.1016/j.bbi.2018.12.009

Vida, G., Peña, G., Deitch, E. A., and Ulloa, L. (2011). alpha7-cholinergic receptor mediates vagal induction of splenic norepinephrine. *J. Immunol.* 186, 4340–4346. doi: 10.4049/jimmunol.1003722

Vida, G., Pena, G., Kanashiro, A., del Rocio Thompson-Bonilla, M., Palange, D., Deitch, E. A., et al. (2017). β2-adrenoreceptors of regulatory lymphocytes are essential for vagal neuromodulation of the innate immune system. *FASEB J.* 25, 4476–4485. doi: 10.1096/fj.11-191007

Zhao, L., Liu, L., Guo, B., and Zhu, B. (2015). Regulation of adaptive immune responses by guiding cell movements in the spleen. *Front. Microbiol.* 6:645. doi: 10.3389/fmicb.2015.00645

Conflict of Interest: The authors declare that the research was conducted in the absence of any commercial or financial relationships that could be construed as a potential conflict of interest.

Publisher's Note: All claims expressed in this article are solely those of the authors and do not necessarily represent those of their affiliated organizations, or those of the publisher, the editors and the reviewers. Any product that may be evaluated in this article, or claim that may be made by its manufacturer, is not guaranteed or endorsed by the publisher.

frontiers in Neuroscience

ORIGINAL RESEARCH
published: 25 November 2021
doi: 10.3389/fnins.2021.676680

In vivo Visualization of Pig Vagus Nerve "Vagotopy" Using Ultrasound

Megan L. Settell[1,2], Aaron C. Skubal[1,2], Rex C. H. Chen[1,2], Maïsha Kasole[1,2], Bruce E. Knudsen[1,2], Evan N. Nicolai[1,2,3], Chengwu Huang[4], Chenyun Zhou[4,5], James K. Trevathan[1,2], Aniruddha Upadhye[6,7], Chaitanya Kolluru[6,7], Andrew J. Shoffstall[6,7], Justin C. Williams[1,2,8], Aaron J. Suminski[1,2,8], Warren M. Grill[9,10,11,12], Nicole A. Pelot[9], Shigao Chen[4†] and Kip A. Ludwig[1,2,8†]*

[1] Department of Biomedical Engineering, University of Wisconsin-Madison, Madison, WI, United States, [2] Wisconsin Institute of Neuroengineering (WITNe), University of Wisconsin-Madison, Madison, WI, United States, [3] Mayo Clinic Graduate School of Biomedical Sciences, Mayo Clinic, Rochester, MN, United States, [4] Department of Radiology, Mayo Clinic, Rochester, MN, United States, [5] Department of Ultrasound, West China Hospital of Sichuan University, Chengdu, China, [6] Department of Biomedical Engineering, Case Western Reserve University, Cleveland, OH, United States, [7] Louis Stokes Cleveland VA Medical Center, Cleveland, OH, United States, [8] Department of Neurosurgery, University of Wisconsin-Madison, Madison, WI, United States, [9] Department of Biomedical Engineering, Duke University, Durham, NC, United States, [10] Department of Electrical and Computer Engineering, Duke University, Durham, NC, United States, [11] Department of Neurobiology, Duke University, Durham, NC, United States, [12] Department of Neurosurgery, Duke University, Durham, NC, United States

Background: Placement of the clinical vagus nerve stimulating cuff is a standard surgical procedure based on anatomical landmarks, with limited patient specificity in terms of fascicular organization or vagal anatomy. As such, the therapeutic effects are generally limited by unwanted side effects of neck muscle contractions, demonstrated by previous studies to result from stimulation of (1) motor fibers near the cuff in the superior laryngeal and (2) motor fibers within the cuff projecting to the recurrent laryngeal.

Objective: Conventional non-invasive ultrasound, where the transducer is placed on the surface of the skin, has been previously used to visualize the vagus with respect to other landmarks such as the carotid and internal jugular vein. However, it lacks sufficient resolution to provide details about the vagus fascicular organization, or detail about smaller neural structures such as the recurrent and superior laryngeal branch responsible for therapy limiting side effects. Here, we characterize the use of ultrasound with the transducer placed in the surgical pocket to improve resolution without adding significant additional risk to the surgical procedure in the pig model.

Methods: Ultrasound images were obtained from a point of known functional organization at the nodose ganglia to the point of placement of stimulating electrodes within the surgical window. Naïve volunteers with minimal training were then asked to use these ultrasound videos to trace afferent groupings of fascicles from the nodose to their location within the surgical window where a stimulating cuff would normally be placed. Volunteers were asked to select a location for epineural electrode placement away from the fascicles containing efferent motor nerves responsible for therapy limiting side effects. 2-D and 3-D reconstructions of the ultrasound were directly compared to *post-mortem* histology in the same animals.

OPEN ACCESS

Edited by:
Silvia V. Conde,
New University of Lisbon, Portugal

Reviewed by:
David S. Holder,
University College London,
United Kingdom
Nicole Thompson,
University College London,
United Kingdom, in collaboration
with reviewer DH
Daniel Chew,
Galvani Bioelectronics Limited,
United Kingdom
Ana Fernandes,
Champalimaud Foundation, Portugal

***Correspondence:**
Kip A. Ludwig
kip.ludwig@wisc.edu

[†] These authors share senior authorship

Specialty section:
This article was submitted to Autonomic Neuroscience, a section of the journal Frontiers in Neuroscience

Received: 05 March 2021
Accepted: 01 November 2021
Published: 25 November 2021

Citation:
Settell ML, Skubal AC, Chen RCH, Kasole M, Knudsen BE, Nicolai EN, Huang C, Zhou C, Trevathan JK, Upadhye A, Kolluru C, Shoffstall AJ, Williams JC, Suminski AJ, Grill WM, Pelot NA, Chen S and Ludwig KA (2021) In vivo Visualization of Pig Vagus Nerve "Vagotopy" Using Ultrasound. Front. Neurosci. 15:676680. doi: 10.3389/fnins.2021.676680

Results: High-resolution ultrasound from the surgical pocket enabled 2-D and 3-D reconstruction of the cervical vagus and surrounding structures that accurately depicted the functional vagotopy of the pig vagus nerve as confirmed via histology. Although resolution was not sufficient to match specific fascicles between ultrasound and histology 1 to 1, it was sufficient to trace fascicle groupings from a point of known functional organization at the nodose ganglia to their locations within the surgical window at stimulating electrode placement. Naïve volunteers were able place an electrode proximal to the sensory afferent grouping of fascicles and away from the motor nerve efferent grouping of fascicles in each subject (n = 3).

Conclusion: The surgical pocket itself provides a unique opportunity to obtain higher resolution ultrasound images of neural targets responsible for intended therapeutic effect and limiting off-target effects. We demonstrate the increase in resolution is sufficient to aid patient-specific electrode placement to optimize outcomes. This simple technique could be easily adopted for multiple neuromodulation targets to better understand how patient specific anatomy impacts functional outcomes.

Keywords: vagotopy, histology, vagus nerve, vagus nerve stimulation, bioelectronic medicine, electroceutical, neuromodulation, ultrasound

INTRODUCTION

The therapeutic effects of vagus nerve stimulation (VNS) for epilepsy and heart failure, while significant in some patients, are often limited by intolerable side effects including throat tightening or pain, voice changes, hoarseness, cough, and dyspnea (Morris and Mueller, 1999; Howland, 2014). The inadvertent stimulation of somatic nerve branches extending from the vagus, such as the superior and recurrent laryngeal nerve (SLN and RLN, respectively), has been implicated as the cause of these side effects (Tosato et al., 2007; Yoo et al., 2013; Nicolai et al., 2020). These nerve branches are either activated through stimulation of fascicles within the stimulating cuff (RLN), or by current escaping the cuff (SLN) (Boon et al., 2009; Castoro et al., 2011; Nicolai et al., 2020). The SLN and RLN innervate neck muscles involved in many of the therapy-limiting side effects and therefore avoiding stimulation of these nerve fibers is paramount.

The vagus nerve (VN) contains a topographical organization (Settell et al., 2020), or vagotopy, that has the potential to be visualized using ultrasound. Previous work in a pig model of VNS demonstrated a bimodal functional organization in the VN. In the nodose ganglia (NG), pseudo-unipolar cell bodies (predominately sensory afferents) are grouped into a large fascicle, distinct from a separate, smaller grouping of nerve fibers. This secondary grouping of nerve fibers gives rise to the superior and recurrent laryngeal nerve branches (Settell et al., 2020). This bimodal arrangement of fascicles could be used to strategically place VNS cuffs to avoid the neuronal projections that innervate muscles implicated in side effects. Current clinical VNS cuffs wrap approximately 270° around the vagus nerve, and thus stimulate the circumference of the trunk mostly indiscriminately. Strategic placement of small electrodes and utilization of a current steering stimulation protocol, to target sensory over motor regions, could minimize therapy-limiting activation of the neck muscles, and optimize clinical efficacy.

Visualization of peripheral nerves using ultrasound could be an effective intraoperative method to identify fascicular organization and pertinent anatomical information *in vivo*. Ultrasound offers higher resolution, and is more cost-effective than other imaging modalities such as magnetic resonance imaging (MRI) (Zaidman et al., 2013). The use of ultrasound for neuropathology was first reported in the 1980s, with improvements in capabilities over the last thirty years (Cartwright et al., 2017). Non-invasive ultrasound has been completed in patients on a variety of superficial nerves demonstrating fascicular resolution. The sciatic nerve has been visualized in patients using ultrasound during popliteal sciatic nerve block for hallux valgus surgery (bunionectomy), with clear visualization of the epineurium through the skin (Karmakar et al., 2013). The median, radial and ulnar nerves, are more superficial than the sciatic nerve and have been visualized through the skin during carpal tunnel evaluation with slightly better resolution of fascicles (Marciniak et al., 2013; Taylor et al., 2016). In 2016, the FDA approved a high frequency ultrasound device for human-use, which further improved imaging of superficial nerve fascicles such as those in the median nerve (Cartwright et al., 2017).

Despite the ability to visualize these superficial nerves, visualizing fascicular organization of the VN with ultrasound poses a unique problem, as it is below several layers of skin, fat, and muscle. Current capabilities of the clinical transducers do not allow for high-resolution, non-invasive visualization of the fascicular organization of deep nerves such as the VN (Brown et al., 2016; Inamura et al., 2017; Ottaviani et al., 2020). Though non-invasive ultrasound of the VN has been established in the clinical setting for diagnosis of masses of the neck (Giovagnorio and Martinoli, 2001), the depth of penetration is not sufficient to

observe fascicular organization, and resolution tends to be poor (Inamura et al., 2017). In humans, the VN is 36.2 ± 9.4 mm (mean ± SD) from the surface of the skin, with no differences between sides or sexes (Hammer et al., 2018). Given the depth of the VN, we propose a novel approach for visualizing vagotopy by placing the ultrasound transducer within the surgical pocket to improve resolution without increasing surgical risk.

Here, we demonstrate this simple intraoperative methodology for visualization of the vagotopy of the pig VN using a high frequency (50 MHz) ultrasound transducer within the surgical pocket. We characterize the utility of ultrasound placed within the surgical pocket to (1) identify the bimodal organization between the pseudo-unipolar cell bodies (sensory afferents) and the secondary fascicle grouping giving rise to the SLN and RLN at the level of the nodose ganglia, (2) resolve the bimodal organization of fascicles within the surgical window, and (3) obtain additional information about the fascicular organization of the SLN and RLN themselves that may be useful in seeding computational models to inform off-target activation. Ultrasound images at selected locations were compared to histological images to confirm underlying vagotopy.

To test the utility of this information for aiding in surgical placement of epineural electrodes, ultrasound images were provided to a group of volunteers, with minimal training, who were asked to follow the sensory afferents from the pseudo-unipolar cell plane to a region where the VNS cuff is usually placed. Volunteers were asked to place the center of the stimulating contact as far from the motor efferents as possible at the specified VNS cuff location, within the surgical window. Thus, demonstrating the feasibility of using ultrasound to optimize contact placement near sensory afferents intended for therapy and to prevent off-target, therapy-limiting side effects (motor-efferents). These results demonstrate that real-time ultrasound can be collected, analyzed, and used to inform electrode cuff placement. This simple approach could lead to patient-specific, optimized placement of implanted electrodes for a variety of neuromodulation targets, resulting in reduced effects on off-target fibers and potentially more efficacious stimulation.

MATERIALS AND METHODS

Subjects

All study procedures were approved by the University of Wisconsin—Madison and Mayo Clinic Institutional Animal Care and Use Committee. Additionally, procedures completed at the Mayo Clinic were conducted under the guidelines of the American Association for Laboratory Animal Science in accordance with the National Institutes of Health Guidelines for Animal Research (Guide for the Care and Use of Laboratory Animals). Subjects included 3 healthy domestic (Yorkshire/Landrace crossbreed) swine (2F/1M; mean ± SD = 41 ± 1.71 kg). All subjects were housed individually (21°C and 45% humidity) with ad libitum access to water and were fed twice a day. Each subject was given an intramuscular injectable induction anesthesia: telazol (6 mg/kg), xylazine (2 mg/kg), and glycopyrrolate (0.006 mg/kg). An intramuscular injection of buprenorphine was given as an analgesic (0.03 mg/kg). A blood pressure catheter was placed in the femoral artery (Millar, Inc., Houston, TX, Model # SPR-350S), and an intravenous catheter placed in the peripheral ear vein for drug and fluid administration. Subjects were endotracheally intubated and maintained with a mechanical ventilator using 1.5–3% isoflurane. All vital signs including temperature, heart rate, CO2, and respiration were continuously collected and recorded every 15 minutes and used to monitor depth of anesthesia. To aid in the quantification of fascicular structure, an additional set of 3 swine (2F/1M; mean ± SD = 33 ± 14.7 kg were scanned post-mortem, and will hereby be referred to as cadaver studies. These subjects underwent all surgical and ultrasound methods as listed below unless otherwise noted.

Surgical Methods

The surgical approach for exposing the VN and microdissection procedures have been described previously (Settell et al., 2020). Briefly, in a dorsal recumbence position, a ventral incision was made on the subject's right side, just lateral and parallel to midline starting at the level of the mandible. Tissue was divided to locate the carotid sheath which was incised to expose the carotid artery, internal jugular vein, and VN. The VN was bluntly dissected from the nodose ganglion to approximately 10 cm caudal; careful measures were taken to avoid disturbing any of the surrounding branches, such as the SL or sympathetic trunk (ST). This exposed region spans the equivalent location for cervical VNS implantation in a patient, as identified by a practicing neurosurgeon (Nicolai et al., 2020; Settell et al., 2020). The incision site was kept moist with 0.9% sterile saline until the completion of experiment. In the additional cadaver experiments the surgical pocket was extended cranially to expose the superior cervical ganglion (SCG) to locate the branching of the ST.

Ultrasound

The ultrasound approach for this study was described previously (Huang et al., 2019). Briefly, after the surgical procedure, all ultrasound images were collected using a Vevo® 3100 (live) or Vevo® 2100 (cadaver) high frequency imaging system (FUJIFILM VisualSonics Inc., Toronto, Canada). The high frequency 50 MHz linear array transducer (MX700, 35 μm nominal axial resolution, 70 μm nominal lateral resolution, 9 mm × 10 mm imaging window) was placed within the surgical pocket (**Figure 1A**), 1–2 mm above the VN to obtain axial cross sections (**Figures 1B,C**). The surgical pocket was filled with mineral oil (live subjects) or room temperature saline (cadaver experiments, live to cadaver comparison subject) to increase coupling between the transducer and nerve, and the vagus nerve suspended from surrounding tissue using vessel loops to limit movement artifact and improve image quality. The transducer was attached to a linear stepper motor (P/N 11484, VisualSonics Inc.) connected to the Vevo® integrated rail system to allow for smooth acquisition of images along the length of the nerve, without the need for manual manipulation. The transducer was directed to move along the length of the VN in the cranial to caudal direction, starting at the nodose ganglion or SCG (**Figure 1C**) and extending the length of the surgical window (approximately 10–12 cm in length), with image collection including the typical VNS cuff location. 3-D plane-by-plane

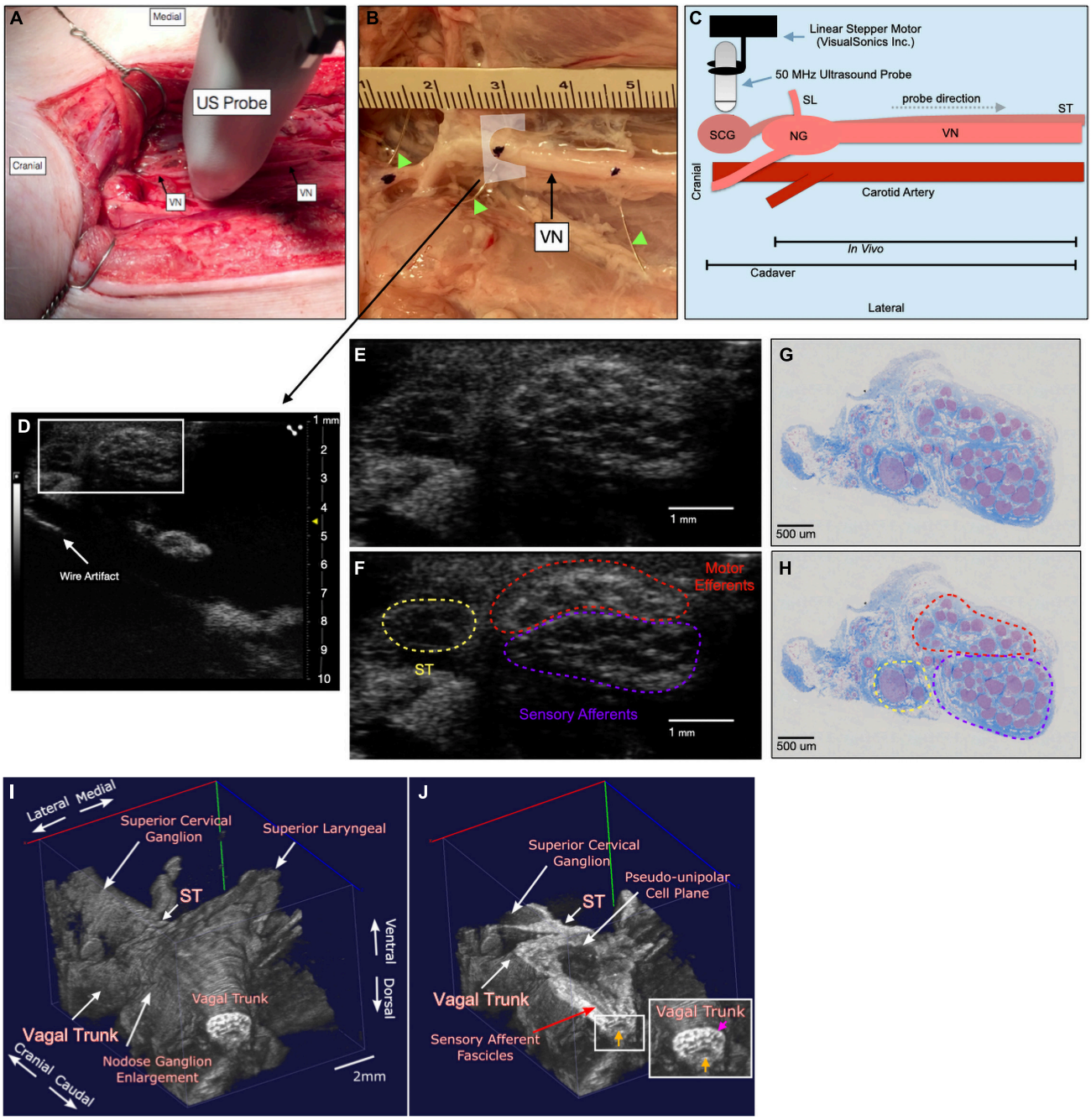

FIGURE 1 | Ultrasound method for visualizing the vagus nerve in a representative subject **(A)** the swine surgical window includes the right vagus nerve (VN) and the carotid artery, as well as the 50 MHz ultrasound probe (US probe) moving in the cranial to caudal direction. Skin, muscle, and fat were retracted in this acute preparation. **(B)** Representative VN in one of the cadaver subjects showing fiducial wire (green arrow heads) and histology dye as well as cross section of US plane **(D)**. **(C)** Schematic of the probe direction (gray dashed arrow) as it scanned from the nodose ganglion (NG) (*in vivo*) or superior cervical ganglion (SCG) (cadaver) moving caudally, approximately 10 cm. **(D)** Ultrasound cross section demonstrating bimodal fascicular organization within the surgical window, with wire fiducial marker and zoom of nerve indicated with white box **(E,F)**. **(E,F)** Zoomed region of ultrasound still (white box, **D**) demonstrating sensory and motor bimodal arrangement (purple and red regions, respectively) as traced from the pseudo-unipolar cell plane of the nodose ganglion (See **Supplementary Video**, Cadaver Subject 1 for the full ultrasound video) The sympathetic trunk (ST), as traced from the SCG is indicated in yellow **(G,H)** A representative, paired histology section (5 μm, Gomori's trichrome) showing the bimodal organization of the vagus nerve within the surgical window, at the wire fiducial marker, indicating the bimodal sensory and motor fascicular organization, as indicated by the purple and red regions, respectively. The ST is indicated in yellow. **(I)** Subject 1 3D ultrasound data clearly showing the nodose ganglion and superior laryngeal extending ventromedially, and vagal trunk extending in the cranial and caudal direction. The superior cervical ganglion is just cranial to the nodose ganglion, with the sympathetic trunk (ST) running parallel to the vagus nerve along the dorsomedial aspect. **(J)** Coronal plane (ventral to dorsal) of vagus nerve showing axons extending from the pseudo-unipolar cell plane to the sensory afferent mode of the vagal trunk. In the zoomed region of the vagal trunk, sensory afferent fascicles are indicated by the yellow arrow, and motor efferent fascicles are indicated by the pink arrow.

volumetric B-mode images were collected (**Figures 1D–F**). Data associated with this study (Settell et al., 2021), were collected as part of the Stimulating Peripheral Activity to Relieve Conditions (SPARC) program and are available through the SPARC Portal (RRID: SCR_017041) under a CC-BY 4.0 license.

To aid in the confirmation of sensory afferent vs. motor efferent fascicles in ultrasound data we used a system of wire fiducials paired with histology dye to indicate specific regions along the vagus nerve; (1) SCG (2) NG (3) the region of cervical vagus nerve (cVN) where the clinical stimulating cuff is placed (**Figure 1B**). Wire fiducials placed underneath the vagus nerve created artifacts in the ultrasound images, allowing us to directly pair these ultrasound images with their corresponding histology slices as indicated by histology dye (**Figures 1B,D–H**). Additionally, 3-D reconstructions of ultrasound data were created (**Figures 1I,J**, see Ultrasound Video Analysis for Methods).

Histology and Microdissection

At the completion of ultrasound scanning, the VN was exposed further to identify clearly branches extending from the main trunk, including the ST which courses parallel to the VN, and the RLN bifurcation at the level of the subclavian artery. Connective tissue was removed, and histological dye was placed along the lateral and ventral edges of the vagus nerve to maintain orientation information (Bradley Products, Inc., Davidson Marking System, Bloomington, MN).

The VN was then excised from just cranial to the nodose ganglion to the RLN bifurcation (*in vivo*) or from just cranial to the SCG to the cVN (cadaver). The vagus nerves were placed in 10% neutral buffered formalin for approximately 48 h at 4°C. Samples were then placed in a Research and Manufacturing Paraffin Tissue Processor (RMC Ventana Renaissance PTP 1530, Ventana Medical Systems, Oro Valley, AZ), and they underwent a series of standard processing steps to dehydrate, clear, and infiltrate with paraffin wax (see Settell et al., 2020 for details). Embedded samples were sectioned at 5 μm, mounted on charged slides, and stained using Gomori's trichrome. Slides were imaged at 20x using a Zeiss Axio Imager 2 with a Zeiss digital camera (**Figures 1G,H**).

Ultrasound Video Analysis

To provide quantification of the ultrasound data to evaluate its utility in tracking sensory afferent fascicles from the nodose ganglia to the region of stimulation, we obtained data in an additional three cadavers. We then created a set of tutorial videos to train naïve ultrasound users on how to identify key markers in the ultrasound video; (1) SCG, (2) NG (as identified by pseudo-unipolar cell plane), (3) motor efferent fascicles, (4) SLN, and the (5) sensory afferents projecting from the pseudo-unipolar cell plane of the nodose ganglia (**Supplementary Tutorial Videos 1–3**). Volunteers were then instructed on how to trace the grouping of sensory fibers from the NG to the region of the stimulating cuff (as noted by the wire artifact). Once volunteers felt comfortable with the process, they were asked to make an attempt at placing a hypothetical stimulating contact on the remaining two subject's ultrasound videos they had not previously viewed. The only guidance provided in the remaining two videos was an analog clock face placed over the nerve at the correct cervical level, so volunteers could provide a time to indicate their selected location (**Supplementary Test Videos 1–3**). To confirm whether volunteers successfully located sensory vs. afferent grouping, histological slices corresponding to the wire fiducials for the selected location were compared for each subject. This blinded process allowed us to evaluate the feasibility of the technique for aiding in identifying the specific locations of fascicles, using both modalities. Additionally, data was converted into 3-D volumetric videos (**Supplementary 3D Cadaver Videos**). Ultrasound images were exported in B-mode from the Vevolab software and imported into Fiji to convert them into v3draw format. Images were then converted to 3-D data using vaa3D (Peng et al., 2010, 2014a,b).

RESULTS

Ultrasound of the Vagus Nerve to Identify Key Anatomical Features

Ultrasound videos were of sufficient resolution to generate 3-D reconstructions suitable to identify key features at a place of known functional organization at the nodose ganglia, and trace associated fascicles to their location at the stimulating cuff region (**Figure 1I**). The pseudo-unipolar cells of the nodose were identified via ultrasound as a single large fascicle, or large circular hypoechoic region within the nodose ganglia (**Figure 2**). The region of fascicles above the pseudo-unipolar cell region have previously been traced to the superior laryngeal and recurrent laryngeal in histology, and are putatively mainly motor and parasympathetic efferent fibers (Settell et al., 2020). Therefore, using ultrasound we were able to trace the afferent fascicles arising from the pseudo-unipolar cell groupings, beginning at the nodose ganglia into the cervical region of the vagus nerve. This bimodal organization, while previously shown in histology, could be visualized at various points along the length of the cervical VN [see **Supplementary Material** for the full 3D ultrasound videos, $n = 3$ (live), and $n = 3$ (cadaver)].

Despite visualization of fascicular structure, further quantification and evaluation of this technique for its utility in clinical applications was warranted. We repeated this approach in cadaver swine to allow for the placement of wire fiducials in an expanded surgical pocket ($n = 3$). To ensure that fascicular structure and organization in both live and cadaver models was clear and easily identifiable, we directly compared the vagus nerve of one subject both pre and *post-mortem* (**Figure 3**).

Ultrasound of the Superior and Recurrent Laryngeal Branches

We assessed whether ultrasound could be used during the surgical procedure to visualize the RLN and SLN branches of the vagus nerve, as these are implicated in off-target activation of the deep neck muscles that produce therapy-limiting side effects (Nicolai et al., 2020). Despite these branches being smaller in diameter than the compound VN, we were able to locate both within the surgical window both visually and using ultrasound, with clear visualization of fascicular structure.

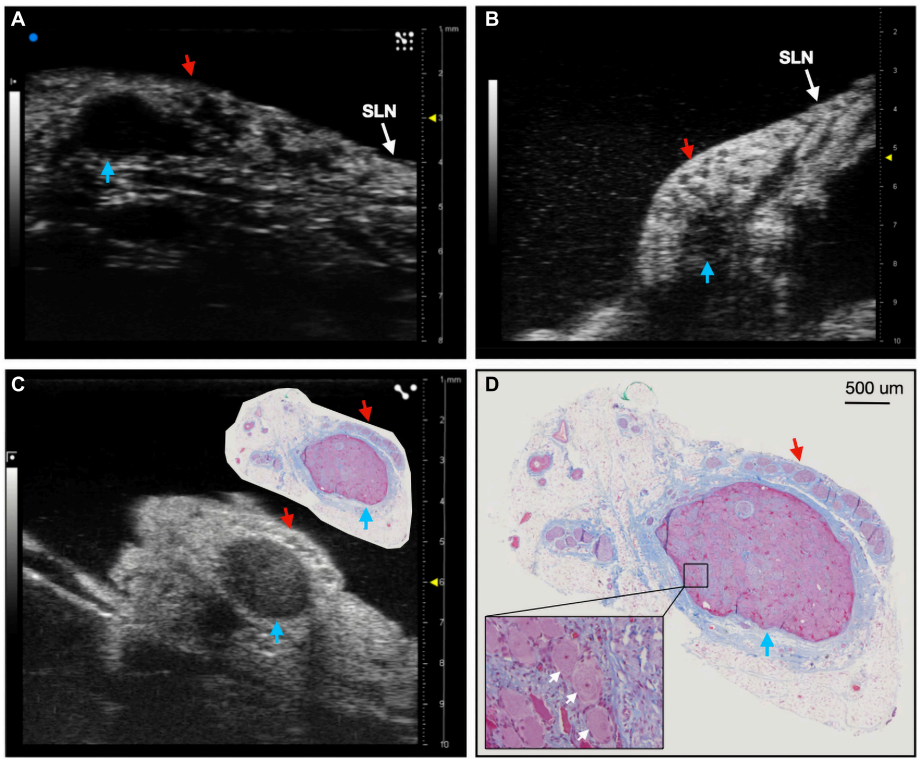

FIGURE 2 | Ultrasound of the nodose ganglia in two live, and one cadaver subject (*n* = 3). Blue arrows indicate the hypoechoic pseudo-unipolar cell region of the nodose ganglia, red arrows indicate the motor efferent region fascicles. **(A,B)** Ultrasound of the nodose ganglia and superior laryngeal nerve (SLN) *in vivo.* **(C)** Ultrasound of the nodose ganglion in a cadaver with paired histology slice demonstrating the pseudo-unipolar cell region **(D)** Histology slice at a larger scale with zoomed region of pseudo-unipolar cells (white arrows) and surrounding satellite cells.

The SLN extends ventromedially from the NG to innervate the cricoarytenoid (internal branch of the superior laryngeal) and cricothyroid (external branch of the superior laryngeal) muscles of the throat (**Figure 4A**; Hayes et al., 2013; Settell et al., 2020). The RLN was identified as running parallel to the vagus nerve along the esophagus and inserting into the cricoarytenoid muscle. It contained far fewer fascicles, but was clearly visible (**Figure 4B**).

Quantification of Fascicular Organization Using Volunteers

We next sought to determine if volunteers with minimal prior training could trace the axonal projections from the pseudo-unipolar cell plane of the nodose ganglia into the cervical region of the vagus nerve, where the stimulating cuff would traditionally be placed from an ultrasound video to which they were naïve (**Table 1**). In subject 1 and 2, five of six volunteers were able to successfully trace the sensory afferent region from the nodose ganglia (**Figures 5A**, **6A**); with the average contact placed well within the sensory afferent region as identified via histology, opposite the motor efferent grouping of fascicles (**Figures 5B,C**, **6B,C**). Electrode placements were largely consistent across evaluators in these two subjects, with one clear outlier, likely placed in error, on the opposite mode. As can be seen in **Figures 5**, **6** the placement by the remaining evaluators was tightly clustered around the ideal placement point as identified by histology.

In the third subject, there was an extensive amount of undissected fat and connective tissue, as can be seen in the ultrasound video, that was subsequently dissected to perform histology. This additional tissue would make it problematic to place an electrode on the epineural surface at the approximate mid-point of the sensory mode close to these fascicles. Therefore, despite the "optimal placement" (10:15) being distant from the group (8:00), the most accessible placement *in vivo,* would be closer to 7 o'clock. Four out of six volunteers were able to correctly place the stimulating cuff for subject three, with these placements clustered at the only realistic location an electrode could be placed (**Figure 7A**). Across all six evaluators the average placement was still within the sensory afferent region of the nerve (**Figures 7B,C**).

DISCUSSION

Toward Improving Intraoperative Placement of Vagus Nerve Stimulation Cuffs

Surgical implantation of VNS devices has limited patient specificity (Reid, 1990; Terry et al., 1990, 1991). Briefly, in the

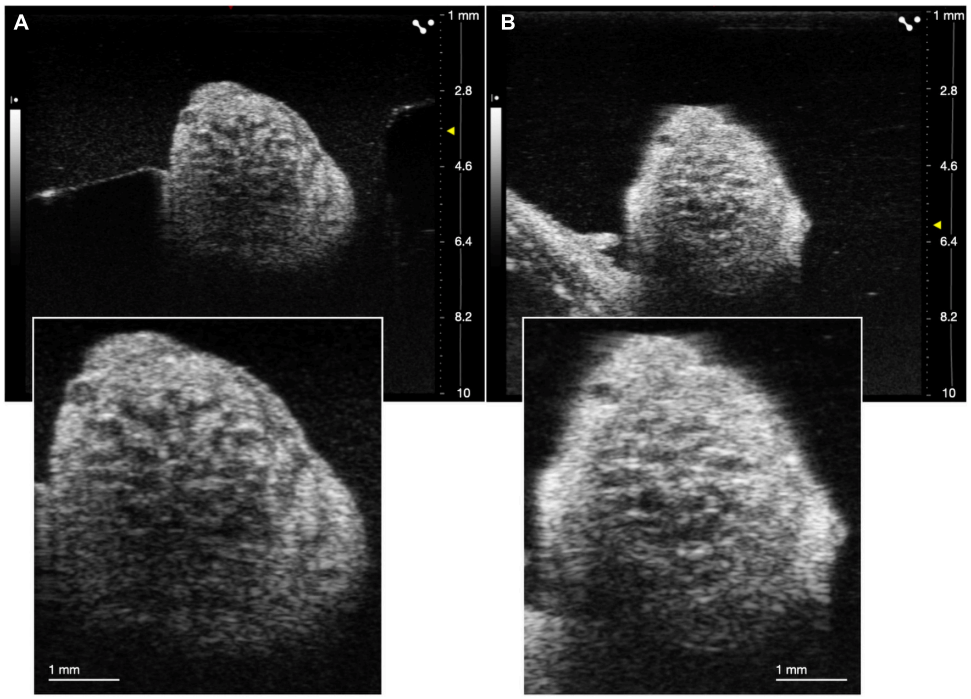

FIGURE 3 | Comparison of ultrasound in live **(A)** and cadaver **(B)** swine. Insets are demonstrating clear visualization of fascicles in both states.

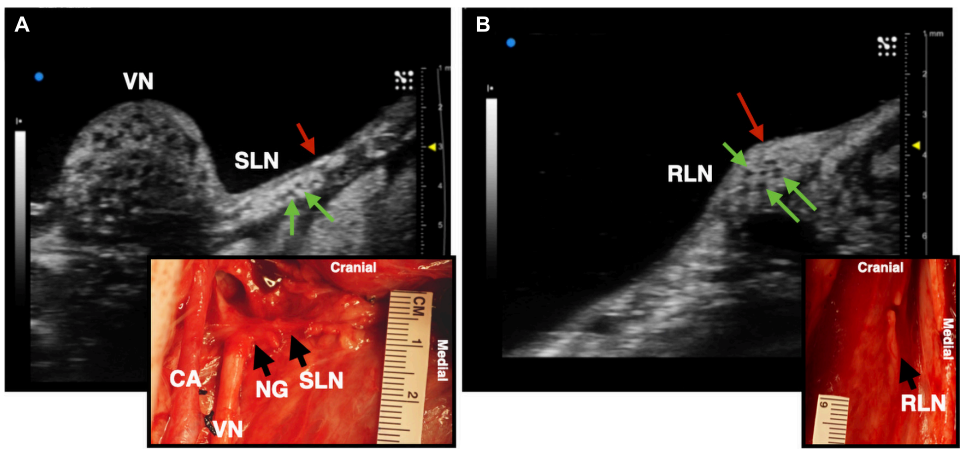

FIGURE 4 | Ultrasound images of the superior laryngeal nerve (SLN) and recurrent laryngeal nerve (RLN) branches of the vagus nerve (VN) in one live representative subject (n = 1). **(A)** The SLN (red arrow) branching ventromedially off of the nodose ganglion (NG). Green arrows indicate fascicles within the nerve. **(B)** The RLN (red arrow), running along the esophageal groove. Green arrows indicate fascicles. Photograph insets in both **(A,B)** depict the corresponding ultrasound region within the surgical pocket; carotid artery (CA).

current clinical surgical method, the carotid sheath is located medial to the muscle and undergoes blunt dissection and is opened approximately 7 cm to expose the carotid artery, internal jugular vein, and VN. Vessel loops are used to suspend the VN while approximately 3 cm are dissected from any surrounding tissue to allow for proper placement of cuff electrodes. Three helical cuffs are then placed around the nerve (two stimulating electrodes and an anchor) (Giordano et al., 2017). The simple and widely deployable introduction of ultrasound into this VNS implantation process could significantly aid in identifying (1) fascicular organization of the VN, (2) branches extending from the VN implicated in producing side effects, and (3) optimized locations for cuff placement based on patient-specific anatomy.

Using anatomical landmarks, ultrasound is effective for clinical evaluation of superficial somatic peripheral nerves (Lawande et al., 2014) and has greater sensitivity for detection of neuropathologies than MRI (Zaidman et al., 2013). The median nerve can be consistently visualized from the mid-upper arm to

TABLE 1 | Responses for the location of the stimulating contact from each volunteer, based on the subject videos provided.

	Stimulating contact location		
Volunteer	**Subject 1**	**Subject 2**	**Subject 3**
1	6:00	Tutorial	8:00
2	5:00	Tutorial	5:30
3	7:00	6:00	Tutorial
4	Tutorial	1:30	8:00
5	7:00	5:00	Tutorial
6	Tutorial	5:00	8:00
7	6:45	5:45	Tutorial
8	Tutorial	6:00	8:00
9	1:00	Tutorial	5:00
Average	5:27	4:52	7:05
Standard deviation	2:18	1:42	1:25
Approximate best location	6:45	5:00	10:15

*Stimulating contact location refers to the analog clock face placed over the vagus nerve in the ultrasound video (see **Supplementary Tutorial and Test Videos**). Average responses are given with standard deviation for each of the three subjects, along with the approximate best location as determined by histology (yellow rows).*

the wrist using high frequency, linear-array transducers (Brown et al., 2016). *Post-mortem* visualization of the RLN via ultrasound is used in studying neuropathologies such as vocal cord paralysis (Solbiati et al., 1985). Ultrasound has also been used clinically for detection of pathologies in peripheral nerves such as tumors and leprosy (Martinoli et al., 2000). Non-invasive imaging of the VN has been conducted both in patients (Park et al., 2011) and cadavers (Knappertz et al., 1998), with visualization of the carotid artery, jugular vein, and VN. However, resolution tends to be poor and the only visually obvious components tend to be the jugular vein and carotid artery, with the VN difficult to identify (Knappertz et al., 1998). There has been significant work in creating a database of ultrasound images of the VN to provide neurosurgeons with a resource for predicting the location of the VN and the distribution of the depths of the nerve from the skin's surface (Inamura et al., 2017). Though the use of ultrasound in this manner highlights the ability to view the VN non-invasively in relation to the carotid artery and jugular vein, it also demonstrates the poor resolution for viewing fascicular structure, and other pertinent branches (external branch of the SLN, RLN). Current literature suggests that resolution is just clear enough to visualize nerves based on surrounding anatomical landmarks, such as the internal jugular vein for identification of the vagus nerve; and quantitative measurements are usually in the form of cross-sectional area (Curcean et al., 2020; Horsager et al., 2021). Thus, there is a clear gap in datasets for understanding fascicular organization as it pertains to clinical stimulation. Here we address this, by placing the high frequency transducer within the surgical pocket and utilizing the increased resolution to determine fascicular organization based on known anatomical landmarks such as the nodose ganglion.

We used a pig VNS model to validate the concept of using high frequency ultrasound within the surgical pocket, to improve resolution. The ultrasound transducer was placed in the surgical pocket of anesthetized pigs that were undergoing VNS experiments. The skin incision in the pig model (10–12 cm) is slightly larger than that of the human preparation (∼7 cm), and the skin, fat, and muscle were retracted in the animal model to optimize transducer placement. The cavity was filled with mineral oil (*in vivo, n* = 3) or saline (*in vivo, n* = 1; cadaver, *n* = 3) to improve coupling to the nerve. The VN was visible in the ultrasound with clear, identifying, features in both the live and cadaver models. From the ultrasound images, we visualized the fascicular organization with sufficient resolution to identify the pseudo-unipolar cell region of the nodose ganglion (**Figure 2**), the bimodal organization (**Figures 5–7**), and the SLN and RLN branches (**Figure 4**). When these images were compared to *post-mortem* histology, it was determined that this approach is not only easily deployable during the procedure but captures the anatomical organization in real-time. Volunteers, not practiced in reading ultrasound were able to visualize the organization of the vagus nerve, based on a single training video. This suggests that in the clinical setting, this technique could be very useful in the initial placement of the stimulating cuff to avoid motor efferent fibers and limit off-target effects. This information could also be used to inform patient programming at future clinical visits. Finally, fascicular variance from subject to subject, or even within subject, may play a key role in therapeutic efficacy; data obtained via ultrasound intraoperatively could be used to assess the relationship between responder/non-responder and subject specific fascicular organization.

Avoiding Off-Target Effects by Identifying Off-Target Nerves

The SLN and RLN are implicated in many of the off-target effects of VNS (Nicolai et al., 2020). We aimed to evaluate the utility of ultrasound as a tool for visualizing the SLN and RLN within the surgical pocket, and identify fascicular organization. As compared to the pig model, the human SLN—which branches at the level of the nodose (inferior ganglion)—may be more difficult to discern, as the nodose ganglion is typically cranial to the surgical window, and therefore simply tracing the vagus nerve back to its point of origination is not feasible. Though the SLN is smaller and contains fewer fascicles than the vagal trunk, ultrasound could potentially be used as a quick confirmation for identifying the nerve within the surgical window (**Figure 4A**), and for seeding computational models to inform off-target activation. As the SLN innervates several muscles of the neck that are implicated in side effects of VNS (Yoo et al., 2013; Nicolai et al., 2020), it is imperative that intraoperative placement of the VNS cuff not be in a region where current escape could activate the SLN resulting in off-target activation.

The anatomy of the SLN can vary between patients (Whitfield et al., 2010). Injuries to the external branch of the superior laryngeal (ESL) nerve, which innervates the cricothyroid muscle, result in voice changes, a common side effect of VNS (Whitfield et al., 2010). The classic anatomy of the ESL, and its relationship to traditional landmarks such as the superior thyroid artery or superior pole of the thyroid, is highly variable (Whitfield et al., 2010). Before placing the VNS cuff, the use of ultrasound to

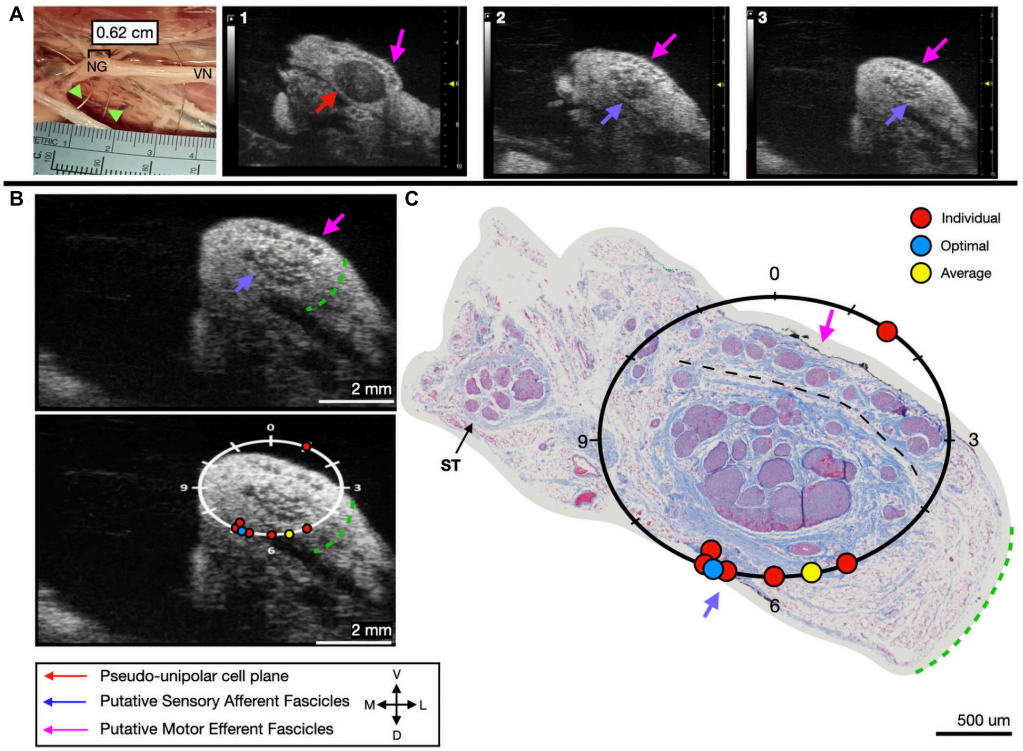

FIGURE 5 | Subject 1 **(A)** From Left to Right: Location of wire fiducials within the surgical pocket. (Note, this subject's surgical photo does not contain histology dye, however, it was placed on the nerve before removal from the pocket). The location of the paired ultrasound video and required placement of stimulating contact is at wire fiducial two [0.62 cm from the superior laryngeal coming off of the nodose ganglion (NG)]. **(A1–3)** Progressive ultrasound images in the cranial to caudal direction from the NG to the cervical vagus nerve (VN), and location where volunteers were requested to place the stimulating contact (1–3, respectively). Red arrow indicates pseudo-unipolar cell region of the NG, pink arrows indicate motor efferent region, purple arrow indicates sensory afferent region, as confirmed via histology. **(B)** Ultrasound cross sections of wire fiducial two, where volunteers were asked to trace the sensory afferent axons from the NG. Top panel: pink arrows note motor efferent region, purple arrow indicates the sensory afferent fascicle grouping, green dashed line indicates area of transected connective tissue during removal for histology. Bottom panel: analog clock face placed on test video to give volunteers locations to place the hypothetical stimulating contact based on their tracing task, green dashed line indicates area of transected connective tissue during removal for histology. **(C)** Histology slice from wire fiducial two, as indicated with histology dye, with analog clock face to demonstrate stimulating contact locations as placed by volunteers in the ultrasound video. Green dashed line indicates area of transected connective tissue during removal for histology. **(B,C)** Red circles indicate each volunteer's placement of the stimulating contact, the yellow circle indicates the average response, and the blue circle indicates the optimal contact location. Sympathetic trunk (ST), medial (M), ventral (V), dorsal (D), lateral (L).

identify the ESL, which extends into the surgical window, could aid in minimizing some of the off-target effects that occur. Data from this study demonstrate visualization of the VN, SLN, and RLN can be achieved through imaging within the surgical pocket to store 3-D reconstructions for future analyses.

Our study demonstrates the degree to which ultrasound information within the surgical window could be personalized, not only in terms of VN location, and fascicular organization, but the location of surrounding structures. A patient-specific surgical approach, tailored by ultrasound, would allow the surgeon to consider variations in vagal branching and location, or potential variances in vagal fascicular orientation. Adding the ultrasound component to the current surgical approach, would not only aid in patient-specific cuff placement, but introduces minimal risk, as the time needed to scan the nerve is minimal (minutes) once the surgical area is prepared. Additionally, patient-specific ultrasound images could inform computational models of VNS. Computational models are critical for the development and application of neurostimulation devices, specifically in terms of optimizing the post-surgical programming process. Individualized models, seeded by patient-specific fascicular organization obtained from ultrasound could increase the speed and process of programming, and may be critical for practically programming multi-contact electrode designs in the future. Existing models for non-invasive VNS are based on high-resolution MRI and focus solely on the activation of specific targeted fiber types (Mourdoukoutas et al., 2018). However, it has been shown that ultrasound imaging provides greater resolution and sensitivity than MRI for peripheral nerves (Zaidman et al., 2013).

Future computational models should consider off-target activation for better quantitative predictions of the potential side effects of VN activation. Greater consideration must be given to the SLN and RLN in future models for VNS, which can be achieved through visualizing vagotopy and the region surrounding the implant using ultrasound. Current three dimensional MRI and finite element-based models of compound peripheral nerves incorporate realistic geometries, as well as

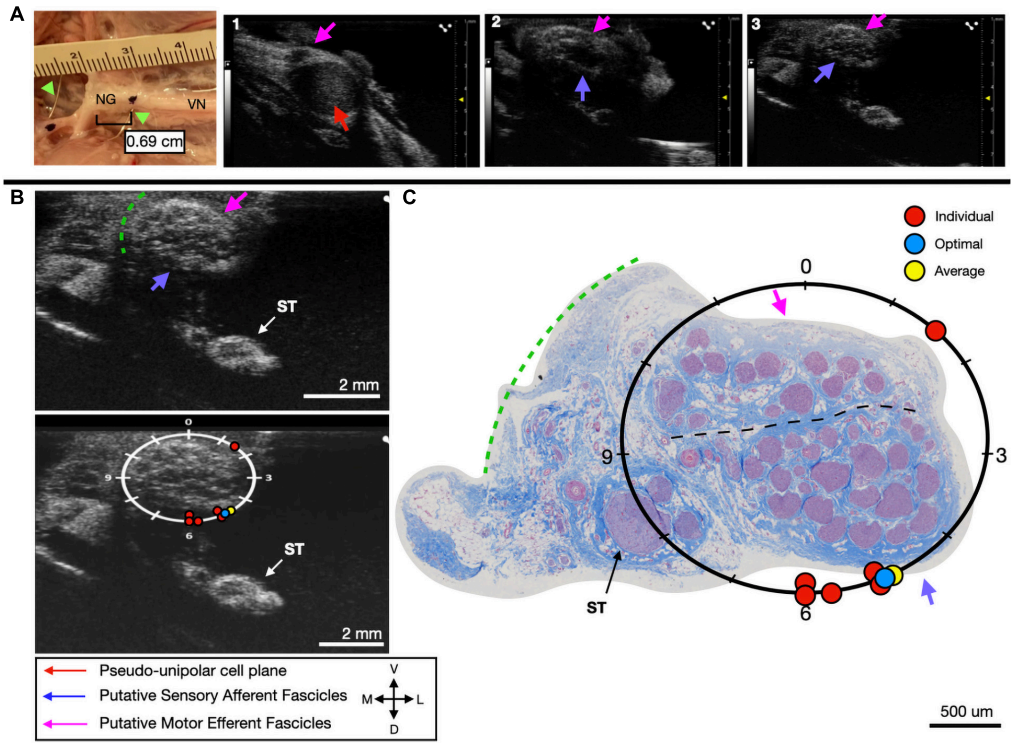

FIGURE 6 | Subject 2 **(A)** From Left to Right: Location of wire fiducials and histology dye within the surgical pocket. The location of the paired ultrasound video and required placement of stimulating contact is at wire fiducial two [0.69 cm from the superior laryngeal coming off of the nodose ganglion (NG)]. **(A1–3)** Progressive ultrasound images in the cranial to caudal direction from the NG to the cervical vagus nerve (VN), and location where volunteers were requested to place the stimulating contact (1–3, respectively). Red arrow indicates pseudo-unipolar cell region of the NG, pink arrows indicate motor efferent region, purple arrow indicates sensory afferent region, as confirmed via histology. **(B)** Ultrasound cross sections of wire fiducial two, where volunteers were asked to trace the sensory afferent axons from the NG. Top panel: pink arrows note motor efferent region, purple arrow indicates the sensory afferent fascicle grouping, green dashed line indicates area of transected connective tissue during removal for histology. Bottom panel: analog clock face placed on test video to give volunteers locations to place the hypothetical stimulating contact based on their tracing task, green dashed line indicates area of transected connective tissue during removal for histology. **(C)** Histology slice from wire fiducial two, as indicated with histology dye, with analog clock face to demonstrate stimulating contact locations as placed by volunteers in the ultrasound video. Green dashed line indicates area of transected connective tissue during removal for histology. **(B,C)** Red circles indicate each volunteer's placement of the stimulating contact, the yellow circle indicates the average response, and the blue circle indicates the optimal contact location. Sympathetic trunk (ST), medial (M), ventral (V), lateral (L), dorsal (D).

inhomogeneous and anisotropic electrical properties of specific nerve elements such as the perineurium and endoneurium (Mourdoukoutas et al., 2018; Pelot et al., 2018). In the future, existing finite element modeling can be used to develop more realistic VN models through consideration of VN fascicular structure, gathered from ultrasound images.

Additionally, this work highlights the opportunity for improved electrode design. Clinical VNS cuffs currently stimulate a large portion of the nerve (270°), therefore despite improved placement to avoid motor efferents, electrodes may still activate unwanted regions. Future electrode designs may include smaller, multi-contact electrodes that encompass all 360°, allowing for clinicians to stimulate differing pairs of contacts, driven by patient-specific imaging data, to improve patient outcomes.

Limitations

There are several limitations to this study that should be taken into consideration. While the pig VN is similar in size to that of the human VN (Settell et al., 2020), it is at a different depth and requires a different surgical approach. The pig surgical window contains much more fat and muscle than typical human necks and therefore requires more retraction. The retracted surgical preparation allowed for the placement of the ultrasound transducer directly above the nerve (1–2 mm), something that may need to be modified in the clinical setting. Additionally, the cadaver subjects underwent a more extensive surgical opening, allowing for imaging more cranial than in a normal preparation. Furthermore, connective tissue was removed, and the nerve was positioned perpendicular to the ultrasound probe to obtain clear images. This may be more difficult in the clinical setting as care is taken to disrupt the nerve as little as possible, however, given the length of nerve exposed for cuff placement, orientation should not be as much of a barrier. Given the fascicle size in the human vagus is on average larger than the pig, presumably making them easier to resolve via ultrasound, this advantage in humans may offset some of the aforementioned limitations (Pelot et al., 2020; Settell et al., 2020).

A slight difference in resolution of fascicles was noted between a few subjects, independent of live or *post-mortem* state, and is most likely attributed to the acoustic impedance of tissue

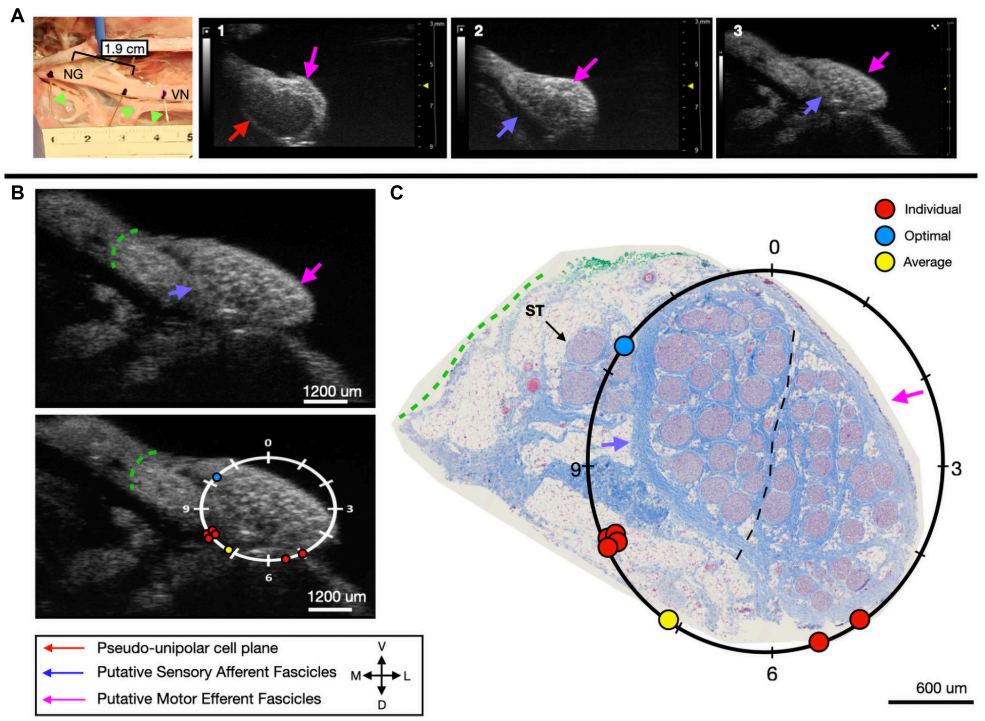

FIGURE 7 | Subject 3 **(A)** From Left to Right: Location of wire fiducials and histology dye within the surgical pocket. The location of the paired ultrasound video and required placement of stimulating contact is at wire fiducial two [1.9 cm from the superior laryngeal coming off of the nodose ganglion (NG)]. **(A1–3)** Progressive ultrasound images in the cranial to caudal direction from the NG to the cervical vagus nerve (VN), and location where volunteers were requested to place the stimulating contact (1–3, respectively). Red arrow indicates pseudo-unipolar cell region of the NG, pink arrows indicate motor efferent region, purple arrow indicates sensory afferent region, as confirmed via histology. **(B)** Ultrasound cross sections of wire fiducial two, where volunteers were asked to trace the sensory afferent axons from the NG. Top panel: pink arrows note motor efferent region, purple arrow indicates the sensory afferent fascicle grouping, green dashed line indicates area of transected connective tissue during removal for histology. Bottom panel: analog clock face placed on test video to give volunteers locations to place the hypothetical stimulating contact based on their tracing task, green dashed line indicates area of transected connective tissue during removal for histology. **(C)** Histology slice from wire fiducial two, as indicated with histology dye, with analog clock face to demonstrate stimulating contact locations as placed by volunteers in the ultrasound video. Green dashed line indicates area of transected connective tissue during removal for histology. **(B,C)** Red circles indicate each volunteer's placement of the stimulating contact, the yellow circle indicates the average response, and the blue circle indicates the optimal contact location. Sympathetic trunk (ST), medial (M), ventral (V), lateral (L), dorsal (D).

(temperature, water content, blood flow etc.), or potentially the amount of connective tissue surrounding the nerve. However, in both states, fascicles were clearly identifiable and motor efferent and sensory afferent groupings could be traced into the cVN. As the state of the vagus nerve effects acoustic impedance, future studies involving formalin fixed human cadavers should consider effects on resolution (Sawhney et al., 2017).

In addition to variations in anatomy, the process of preparing the histology may cause the nerve to shrink (Stickland, 1975), which may affect the appearance of the histology, despite being paired to ultrasound via wire fiducials and histology dye. However, the overall appearance of fascicles in the high resolution ultrasound was clear enough that the vagotopy was visible throughout both modalities.

Furthermore, the nodose ganglion in humans is located near the base of the skull in the jugular foramen, more cranial from the surgical window than in a pig model. However, the hypoechoic region of pseudo-unipolar cells is quite large in pigs and could potentially be identified in humans either non-invasively (pre- or intra-operatively) or by aiming the transducer toward the ganglion. This could allow identification of the bimodal organization and subsequent tracking to the surgical window. The feasibility of the translation of this imaging method from pigs to humans may be evaluated in cadavers.

CONCLUSION

Vagus nerve stimulation is FDA-approved for several indications, including epilepsy and depression, and holds promise for many other indications. However, for improved clinical VNS efficacy, fascicular organization of the VN should be considered for each patient. Ultrasound is an established method for visualization of these characteristics in somatic nerves and could be implemented during the surgical implantation of the VNS lead to inform placement of cuff electrodes and to inform patient-specific computational models.

Our findings demonstrated the ability to identify the vagotopy of the pig VN intraoperatively with a high-resolution transducer placed in the surgical pocket. We identified the pseudo-unipolar

cell aggregation of the nodose ganglia and were able to visualize bimodal organization of fascicular bundles through the cervical trunk where a VNS electrode would be placed. Our subset of cadaver ultrasound data were paired with *post-mortem* histology to confirm fascicular organization, and the technique verified by a set of naïve volunteers. This work highlights the potential for an intraoperative technique that could improve VNS cuff placement, aid in limiting unwanted side effects, and therefore hold promise for enabling patient-specific computational models to inform stimulation paradigms. The simple method of using the surgical pocket to place the ultrasound transducer closer to the nerve target of interest, without increasing patient risk, could also be readily applied to numerous other neuromodulation therapies.

DATA AVAILABILITY STATEMENT

The raw data supporting the conclusions of this article will be made available by the authors, without undue reservation.

ETHICS STATEMENT

The animal studies were reviewed and approved by the Mayo Clinic and University of Wisconsin-Madison Institutional Animal Care and Use Committees.

AUTHOR CONTRIBUTIONS

MS: conceptualization, methodology, data curation, writing—original draft and edited draft, and data analysis. AS: methodology, data curation, writing—original draft and edited draft, and data analysis. RC: methodology, data curation, writing—edited draft, and data analysis. MK: writing—original draft and data analysis. BK, CH, CZ, AU, and CK: methodology, data curation, writing—original draft, and data analysis. EN: conceptualization, methodology, and data curation. JT: methodology, writing, edited draft, and data analysis, AJSh and AJSu: conceptualization, methodology, data curation, writing—original draft, and data analysis. JW: conceptualization, funding acquisition, and writing—original draft. WG and NP: conceptualization, data analysis, writing—original draft. SC: methodology, data curation, writing—original draft, and data analysis. KL: conceptualization, methodology, funding acquisition, supervision, writing—original draft and edited draft, and data analyses.

FUNDING

This work was supported by the National Institutes of Health SPARC Program (OT2 OD025340).

ACKNOWLEDGMENTS

We would like to acknowledge the Cancer Center Support Grant: NCI P30 CA014520, University of Wisconsin Small Animal Imaging and Radiotherapy Facility and VisualSonics US/PA SIG: NIH S10-OD018505 for supporting this work. We would also like to acknowledge Jamie Van Gompel (Mayo Clinic) for his instruction on electrode placement procedures, Andrea McConico (Mayo Clinic) for her assistance during surgical procedures, and Ashley Weichmann for her assistance during ultrasound. We would like to thank our volunteers for their time and participation in evaluating the ultrasound videos: AJSu, JT, Nishant Verma, MK, Maria LaLuzerne, BK, EN, Stephan Blanz, and Ashlesha Deshmukh.

SUPPLEMENTARY MATERIAL

The Supplementary Material for this article can be found online at: https://www.frontiersin.org/articles/10.3389/fnins.2021.676680/full#supplementary-material

REFERENCES

Boon, P., Raedt, R., Herdt, V., Wyckhuys, T., and Vonck, K. (2009). Electrical stimulation for the treatment of epilepsy. *Neurotherapeutics* 6, 218–227. doi: 10.1016/j.nurt.2008.12.003

Brown, J. M., Yablon, C. M., Morag, Y., Brandon, C. J., and Jacobson, J. A. (2016). US of the Peripheral Nerves of the Upper Extremity: A Landmark Approach. *Radio Graphics* 36, 452–463. doi: 10.1148/rg.2016150088

Cartwright, M. S., Baute, V., Caress, J. B., and Walker, F. O. (2017). Ultrahigh-frequency ultrasound of fascicles in the median nerve at the wrist. *Muscle Nerve* 56, 819–822. doi: 10.1002/mus.25617

Castoro, M. A., Yoo, P. B., Hincapie, J. G., Hamann, J. J., Ruble, S. B., Wolf, P. D., et al. (2011). Excitation properties of the right cervical vagus nerve in adult dogs. *Exp. Neurol.* 227, 62–68. doi: 10.1016/j.expneurol.2010.09.011

Curcean, A. D., Rusu, G. M., and Dudea, S. M. (2020). Ultrasound appearance of peripheral nerves in the neck: Vagus, hypoglossal and greater auricular. *Med. Pharm. Rep.* 93, 39–46. doi: 10.15386/mpr-1273

Giordano, F., Zicca, A., Barba, C., Guerrini, R., and Genitori, L. (2017). Vagus nerve stimulation: Surgical technique of implantation and revision and related morbidity. *Epilepsia* 58, 85–90. doi: 10.1111/epi.13678

Giovagnorio, F., and Martinoli, C. (2001). Sonography of the Cervical Vagus Nerve: Normal Appearance and Abnormal Findings. *Am. J. Roentgenol.* 176, 745–749. doi: 10.2214/ajr.176.3.1760745

Hammer, N., Löffler, S., Cakmak, Y. O., Ondruschka, B., Planitzer, U., Schultz, M., et al. (2018). Cervical vagus nerve morphometry and vascularity in the context of nerve stimulation—A cadaveric study. *Scient. Rep.* 8:7997. doi: 10.1038/s41598-018-26135-8

Hayes, D., Nicol, K. K., Tobias, J. D., Chicoine, L. G., Duffy, V. L., Mansour, H. M., et al. (2013). Identification of the Nodose Ganglia and TRPV1 in Swine. *Lung* 191, 445–447. doi: 10.1007/s00408-013-9496-y

Horsager, J., Walter, U., Fedorova, T. D., Andersen, K. B., Skjærbæk, C., Knudsen, K., et al. (2021). Vagus Nerve Cross-Sectional Area in Patients With Parkinson's Disease—An Ultrasound Case-Control Study. *Front. Neurol.* 12:844. doi: 10.3389/fneur.2021.681413

Howland, R. H. (2014). Vagus Nerve Stimulation. *Curr. Behav. Neurosci. Rep.* 1, 64–73. doi: 10.1007/s40473-014-0010-5

Huang, C., Lowerison, M. R., Lucien, F., Gong, P., Wang, D., Song, P., et al. (2019). Noninvasive Contrast-Free 3D Evaluation of Tumor Angiogenesis with Ultrasensitive Ultrasound Microvessel Imaging. *Scient. Rep.* 9:4907. doi: 10.1038/s41598-019-41373-0

Inamura, A., Nomura, S., Sadahiro, H., Imoto, H., Ishihara, H., and Suzuki, M. (2017). Topographical features of the vagal nerve at the cervical level in an aging population evaluated by ultrasound. *Interdiscipl. Neurosurg.* 9, 64–67. doi: 10.1016/j.inat.2017.03.006

Karmakar, M. K., Shariat, A. N., Pangthipampai, P., and Chen, J. (2013). High-Definition Ultrasound Imaging Defines the Paraneural Sheath and the Fascial Compartments Surrounding the Sciatic Nerve at the Popliteal Fossa. *Reg. Anesthesia Pain Med.* 38, 447–451. doi: 10.1097/AAP.0b013e31829ffcb4

Knappertz, V. A., Tegeler, C. H., Hardin, S. J., and McKinney, W. M. (1998). Vagus Nerve Imaging with Ultrasound: Anatomic and in Vivo Validation. *Otolaryngol. Head Neck Surg.* 118, 82–85. doi: 10.1016/S0194-5998(98)70379-1

Lawande, A. D., Warrier, S. S., and Joshi, M. S. (2014). RECENT ADVANCES IN MSK. Role of ultrasound in evaluation of peripheral nerves. *Ind. J. Radiol. Imag.* 24, 254–258. doi: 10.4103/0971-3026.137037

Marciniak, C., Caldera, F., Welty, L., Lai, J., Lento, P., Feldman, E., et al. (2013). High-Resolution Median Nerve Sonographic Measurements. *J. Ultrasound Med.* 32, 2091–2098. doi: 10.7863/ultra.32.12.2091

Martinoli, C., Bianchi, S., and Derchi, L. E. (2000). Ultrasonography of Peripheral Nerves. *Curr. Neurol. Neurosci. Rep.* 9:328.

Morris, G. L., and Mueller, W. M. (1999). Long-term treatment with vagus nerve stimulation in patients with refractory epilepsy. *Neurology* 53, 1731–1731. doi: 10.1212/WNL.53.8.1731

Mourdoukoutas, A. P., Truong, D. Q., Adair, D. K., Simon, B. J., and Bikson, M. (2018). High-Resolution Multi-Scale Computational Model for Non-Invasive Cervical Vagus Nerve Stimulation. *Neuromodulation* 21, 261–268. doi: 10.1111/ner.12706

Nicolai, E. N., Settell, M., Knudsen, B. E., McConico, A. L., Gosink, B. A., Trevathan, J. K., et al. (2020). Sources of off-target effects of vagus nerve stimulation using the helical clinical lead in domestic pigs. *J. Neural Engin.* 17:046017. doi: 10.1088/1741-2552/ab9db8

Ottaviani, M. M., Wright, L., Dawood, T., and Macefield, V. G. (2020). In vivo recordings from the human vagus nerve using ultrasound-guided microneurography. *J. Physiol.* 598, 3569–3576. doi: 10.1113/JP280077

Park, J. K., Jeong, S. Y., Lee, J.-H., Lim, G. C., and Chang, J. W. (2011). Variations in the Course of the Cervical Vagus Nerve on Thyroid Ultrasonography. *Am. J. Neuroradiol.* 32, 1178–1181. doi: 10.3174/ajnr.A2476

Pelot, N. A., Behrend, C. E., and Grill, W. M. (2018). On the parameters used in finite element modeling of compound peripheral nerves. *J. Neural Engin.* 16:016007. doi: 10.1088/1741-2552/aaeb0c

Pelot, N. A., Goldhagen, G. B., Cariello, J. E., Musselman, E. D., Clissold, K. A., Ezzell, J. A., et al. (2020). Quantified Morphology of the Cervical and Subdiaphragmatic Vagus Nerves of Human, Pig, and Rat. *Front. Neurosci.* 14:1148. doi: 10.3389/fnins.2020.601479

Peng, H., Bria, A., Zhou, Z., Iannello, G., and Long, F. (2014a). Extensible visualization and analysis for multidimensional images using Vaa3D. *Nat. Protocols* 9, 193–208. doi: 10.1038/nprot.2014.011

Peng, H., Tang, J., Xiao, H., Bria, A., Zhou, J., Butler, V., et al. (2014b). Virtual finger boosts three-dimensional imaging and microsurgery as well as terabyte volume image visualization and analysis. *Nat. Commun.* 5:4342. doi: 10.1038/ncomms5342

Peng, H., Ruan, Z., Long, F., Simpson, J. H., and Myers, E. W. (2010). V3D enables real-time 3D visualization and quantitative analysis of large-scale biological image data sets. *Nat. Biotechnol.* 28, 348–353. doi: 10.1038/nbt.1612

Reid, S. A. (1990). Surgical Technique for Implantation of the Neurocybernetic Prosthesis. *Epilepsia* 31, S38–S39. doi: 10.1111/j.1528-1157.1990.tb05847.x

Sawhney, C., Lalwani, S., Ray, B. R., Sinha, S., and Kumar, A. (2017). Benefits and Pitfalls of Cadavers as Learning Tool for Ultrasound-guided Regional Anesthesia. *Anesthesia Essays Res.* 11, 3–6. doi: 10.4103/0259-1162.186607

Settell, M. L., Kasole M., Skubal, A. C., Knudsen, B. E., Nicolai, E. N., Huang, C., et al. (2021). *In vivo Visualization of Pig Vagus Nerve 'vagotopy' Using Ultrasound. Version 1 [Data set]. Pennsieve Discover.* doi: 10.1101/2020.12.24.424256

Settell, M. L., Pelot, N. A., Knudsen, B. E., Dingle, A. M., McConico, A. L., Nicolai, E. N., et al. (2020). Functional vagotopy in the cervical vagus nerve of the domestic pig: Implications for the study of vagus nerve stimulation. *J. Neural Engin.* 17:026022. doi: 10.1088/1741-2552/ab7ad4

Solbiati, L., De Pra, L., Ierace, T., Bellotti, E., and Derchi, L. (1985). High-resolution sonography of the recurrent laryngeal nerve: Anatomic and pathologic considerations. *Am. J. Roentgenol.* 145, 989–993. doi: 10.2214/ajr.145.5.989

Stickland, N. C. (1975). A Detailed Analysis of the Effects of Various Fixatives on Animal Tissue with Particular Reference to Muscle Tissue. *Stain Technol.* 50, 255–264. doi: 10.3109/10520297509117068

Taylor, T., Meer, J., and Beck, S. (2016). Ultrasound-Guided Ulnar, Median, and Radial Nerve Blocks. *Emerg. Med.* 48, 321–324. doi: 10.12788/emed.2016.0043

Terry, R., Tarver, W. B., and Zabara, J. (1990). An Implantable Neurocybernetic Prosthesis System. *Epilepsia* 31, S33–S37. doi: 10.1111/j.1528-1157.1990.tb05846.x

Terry, R. S., Tarver, W. B., and Zabara, J. (1991). The Implantable Neurocybernetic Prosthesis System. *Pacing Clin. Electrophysiol.* 14, 86–93. doi: 10.1111/j.1540-8159.1991.tb04052.x

Tosato, M., Yoshida, K., Toft, E., and Struijk, J. J. (2007). Quasi-trapezoidal pulses to selectively block the activation of intrinsic laryngeal muscles during vagal nerve stimulation. *J. Neural Engin.* 4, 205–212. doi: 10.1088/1741-2560/4/3/005

Whitfield, P., Morton, R. P., and Al-Ali, S. (2010). Surgical anatomy of the external branch of the superior laryngeal nerve. *ANZ J. Surg.* 80, 813–816. doi: 10.1111/j.1445-2197.2010.05440.x

Yoo, P. B., Lubock, N. B., Hincapie, J. G., Ruble, S. B., Hamann, J. J., and Grill, W. M. (2013). High-resolution measurement of electrically-evoked vagus nerve activity in the anesthetized dog. *J. Neural Engin.* 10:026003. doi: 10.1088/1741-2560/10/2/026003

Zaidman, C. M., Seelig, M. J., Baker, J. C., Mackinnon, S. E., and Pestronk, A. (2013). Detection of peripheral nerve pathology: Comparison of ultrasound and MRI. *Neurology* 80, 1634–1640. doi: 10.1212/WNL.0b013e3182904f3f

Conflict of Interest: JW and KL were scientific board members and have stock interests in NeuroOne Medical Inc., a company developing next generation epilepsy monitoring devices. JW also has an equity interest in NeuroNexus technology Inc., a company that supplies electrophysiology equipment and multichannel probes to the neuroscience research community. KL was also a paid member of the scientific advisory board of Cala Health, Blackfynn, Abbott and Battelle. KL was also a paid consultant for Galvani and Boston Scientific. KL was a consultant to and co-founder of Neuronoff Inc. None of these associations are directly relevant to the work presented in this manuscript.

The remaining authors declare that the research was conducted in the absence of any commercial or financial relationships that could be construed as a potential conflict of interest.

Publisher's Note: All claims expressed in this article are solely those of the authors and do not necessarily represent those of their affiliated organizations, or those of the publisher, the editors and the reviewers. Any product that may be evaluated in this article, or claim that may be made by its manufacturer, is not guaranteed or endorsed by the publisher.

frontiers in Neuroscience

ORIGINAL RESEARCH
published: 10 January 2022
doi: 10.3389/fnins.2021.780841

Blocking Ocular Sympathetic Activity Inhibits Choroidal Neovascularization

Juan Carlos Martinez-Camarillo[1,2], Christine K. Spee[3], Gloria Paulina Trujillo-Sanchez[1,2], Anthony Rodriguez[3], David R. Hinton[2,3], Alessandra Giarola[4], Victor Pikov[4], Arun Sridhar[4], Mark S. Humayun[1,2] and Andrew C. Weitz[1,2]*

[1] USC Roski Eye Institute, Keck School of Medicine, University of Southern California, Los Angeles, CA, United States, [2] USC Ginsburg Institute for Biomedical Therapeutics, University of Southern California, Los Angeles, CA, United States, [3] Department of Pathology, Keck School of Medicine, University of Southern California, Los Angeles, CA, United States, [4] Galvani Bioelectronics, Stevenage, United Kingdom

Purpose: To investigate how modulating ocular sympathetic activity affects progression of choroidal neovascularization (CNV), a hallmark feature of wet age-related macular degeneration (AMD).

Methods: In the first of two studies, Brown Norway rats underwent laser-induced CNV and were assigned to one of the following groups: daily eye drops of artificial tears (n = 10; control group); daily eye drops of the β-adrenoreceptor agonist isoproterenol (n = 10); daily eye drops of the β-adrenoreceptor antagonist propranolol (n = 10); sympathetic internal carotid nerve (ICN) transection 6 weeks prior to laser-induced CNV (n = 10). In the second study, rats underwent laser-induced CNV followed by ICN transection at different time points: immediately after the laser injury (n = 6), 7 days after the laser injury (n = 6), and sham surgery 7 days after the laser injury (n = 6; control group). All animals were euthanized 14 days after laser application. CNV development was quantified with fluorescein angiography and optical coherence tomography (*in vivo*), as well as lesion volume analysis using 3D confocal reconstruction (postmortem). Angiogenic growth factor protein levels in the choroid were measured with ELISA.

Results: In the first study, blocking ocular sympathetic activity through pharmacological or surgical manipulation led to a 75% or 70% reduction in CNV lesion volume versus the control group, respectively ($P < 0.001$). Stimulating ocular sympathetic activity with isoproterenol also led to a reduction in lesion volume, but only by 27% versus controls ($P < 0.05$). VEGF protein levels in the choroid were elevated in the three treatment groups ($P < 0.01$). In the second study, fluorescein angiography and CNV lesion volume analysis indicated that surgically removing the ocular sympathetic supply inhibited progression of laser-induced CNV, regardless of whether ICN transection was performed on the same day or 7 days after the laser injury.

Conclusion: Surgical and pharmacological block of ocular sympathetic activity can inhibit progression of CNV in a rat model. Therefore, electrical block of ICN activity could be a potential bioelectronic medicine strategy for treating wet AMD.

Keywords: wet AMD, internal carotid nerve, choroidal neovascularization, ocular sympathetic activity, laser-induced CNV, β-adrenoreceptor modulation

OPEN ACCESS

Edited by:
Pietro Enea Lazzerini, University of Siena, Italy

Reviewed by:
Michael B. Powner, City, University of London, United Kingdom
Claudio Punzo, University of Massachusetts Chan Medical School, United States

***Correspondence:**
Mark S. Humayun
humayun@med.usc.edu

Specialty section:
This article was submitted to Autonomic Neuroscience, a section of the journal Frontiers in Neuroscience

Received: *21 September 2021*
Accepted: *14 December 2021*
Published: *10 January 2022*

Citation:
Martinez-Camarillo JC, Spee CK, Trujillo-Sanchez GP, Rodriguez A, Hinton DR, Giarola A, Pikov V, Sridhar A, Humayun MS and Weitz AC (2022) Blocking Ocular Sympathetic Activity Inhibits Choroidal Neovascularization. Front. Neurosci. 15:780841. doi: 10.3389/fnins.2021.780841

INTRODUCTION

Age-related macular degeneration (AMD) is among the most common causes of vision loss in developed countries (Campochiaro, 2013). Exudative (wet) AMD is a form of the disease in which an imbalance between angiogenic and antiangiogenic factors, such as vascular endothelial growth factor (VEGF), leads to choroidal neovascularization (CNV) (Van Lookeren Campagne et al., 2014). Anti-VEGF therapies are the gold standard therapy for wet AMD, but these drugs must be injected into the eye every 2–6 weeks (Menon and Walters, 2009).

The sympathetic nervous system may play a role in regulating endpoints related to wet AMD. Sympathetic innervation of the eye originates from the superior cervical ganglion (SCG) (Smith and Reddy, 1990). Prior studies in rat have shown a role for the SCG in regulating choroidal vascularity, with removal of the SCG leading to an increase in vascularization within weeks (Steinle et al., 2002; Steinle and Smith, 2003) accompanied by changes in angiogenic growth factors (Lashbrook and Steinle, 2005; Steinle and Lashbrook, 2006; Wiley et al., 2006). Our group recently demonstrated similar effects through transection of the internal carotid nerve (ICN), a branch of the SCG that is the eye's only source of sympathetic input (Martinez-Camarillo et al., 2019). We reported that ICN transection led to increased choroidal vascularity and levels of angiogenic factors, including VEGF and tumor necrosis factor-alpha (TNF-α). These results indicate potential involvement of the sympathetic system in CNV and therefore in wet AMD.

The most widely accepted animal model of wet AMD is the laser photocoagulation model (Pennesi et al., 2012). The model works by burning Bruch's membrane with a laser, which causes growth of new blood vessels from the choroid into the subretinal space (Lambert et al., 2013). This growth is accompanied by upregulation of VEGF (Yi et al., 1997; Wada et al., 1999) and TNF-α (Shi et al., 2006; Jasielska et al., 2010). Maximal changes are observed 1–2 weeks following the laser injury, with involution of the CNV and recovery of the retinal pigment epithelium occurring thereafter (Hoerster et al., 2012; Pennesi et al., 2012). Although the laser-induced CNV animal model was originally developed in non-human primates (Ryan, 1979), rodent models have emerged as the most employed species for neovascular AMD research (Pennesi et al., 2012). While the laser photocoagulation model doesn't replicate the complete pathophysiology of AMD, it is still the most commonly used animal model for developing wet AMD therapies (Shah et al., 2015; Lin et al., 2019).

Expression of β-adrenergic receptors as part of the sympathetic pathway within the choroid has been described previously (Casini et al., 2014). Propranolol, a non-selective β-adrenoceptor (β-AR) blocker, has been used as an antiangiogenic compound for treating choroidal diseases such as choroidal hemangioma (Thapa and Shields, 2013; O'Bryhim et al., 2019). Prior studies using the laser photocoagulation model in mouse have demonstrated that systemic (Lavine et al., 2013) or intraocular (Nourinia et al., 2015) delivery of propranolol causes a reduction in CNV lesion size. These findings support manipulation of ocular sympathetic activity as a potential therapy for wet AMD. However, they appear to contradict our prior findings that ICN transection (i.e., blocking sympathetic activity) is proangiogenic (Martinez-Camarillo et al., 2019).

The field of bioelectronic medicine has recently emerged with a goal of treating diseases caused by autonomic disbalance (Birmingham et al., 2014). These therapies typically involve electrical stimulation or blocking of autonomic nerves to selectively affect the function of individual organs innervated by those nerves. We have hypothesized that chronic electrical modulation (stimulation or block) of ICN activity can slow, stop, or even reverse progression of wet AMD by normalizing expression of angiogenic growth factors that regulate blood vessel proliferation (Martinez-Camarillo et al., 2019). In the present study, we tested this hypothesis by using pharmacological or surgical manipulation of ocular sympathetic activity as a proxy for ICN electrical modulation and the rat laser photocoagulation model as a proxy for wet AMD. Outcome measures included quantification of CNV development and measurement of choroidal VEGF levels.

MATERIALS AND METHODS

Animals and Study Design

A total of 58 Brown Norway rats, aged postnatal day (P) 100 ± 5 days, were included in two consecutive studies. In the first study, 40 female rats were assigned into one of the following four groups (n = 10 per group): (1) laser injury followed by 14 days topical therapy with artificial tears (control group); (2) laser injury followed by 14 days topical therapy of 50 mM isoproterenol eye drop formulation (β-AR agonist group); (3) laser injury followed by 14 days topical therapy with 2% propranolol eye drop formulation (β-AR antagonist group); (4) bilateral ICN transection 6 weeks prior to laser injury followed by 14 days topical therapy with artificial tears (ICNx group). Female animals were used to be consistent with prior studies (Steinle et al., 2002, 2005; Steinle and Smith, 2003; Lashbrook and Steinle, 2005; Steinle and Lashbrook, 2006; Wiley et al., 2006; Martinez-Camarillo et al., 2019). In the second study, 18 male Brown Norway rats were assigned to the following three groups (n = 6 per group): (1) bilateral ICN sham surgery 7 days after laser therapy (control group); (2 and 3) bilateral ICN transection immediately after or 7 days after laser therapy. Male animals were used to avoid possible confounding effects from the menstrual cycle on angiogenic growth factor levels. All animals were euthanized 14 days after laser application. CNV development was quantified *in vivo* with fluorescein angiography (FA) and spectral-domain optical coherence tomography (SD-OCT), as well as postmortem with lesion volume analysis using 3D confocal reconstruction. VEGF protein levels in the choroid were measured with ELISA. **Table 1** indicates which of these outcome measures were analyzed in each study. Unpaired t-tests were used for all statistical comparisons. Investigators who performed data analysis were blinded to the treatment group. All animals received the same anesthesia protocol, which included an intraperitoneal injection of ketamine/xylazine. All experiments were performed in accordance with the University of Southern California Institutional Animal Care and Use Committee

TABLE 1 | Analyses performed to track CNV progression following laser injury (day 0).

	Analysis	Time point(s)	Measurement method
Study 1	CNV leakiness	Day 14	FA
	Lesion volume (*ex vivo*)	Postmortem	3D confocal reconstruction
	Choroidal VEGF protein levels	Postmortem	ELISA
Study 2	Lesion volume and edema (*in vivo*)	Days 3, 7, 10, and 14	SD-OCT
	CNV leakiness	Days 3, 7, 10, and 14	FA
	Lesion volume (*ex vivo*)	Postmortem	3D confocal reconstruction

(IACUC) approval and guidelines on animal use and with the Association for Research in Vision and Ophthalmology (ARVO) statement for the Use in Ophthalmic and Vision Research.

Internal Carotid Nerve Transection

A subset of animals underwent bilateral transection of the ICN, using a technique previously published by our group (Martinez-Camarillo et al., 2019). This surgical approach selectively disrupts sympathetic supply to the eye, while preserving the other SCG branches. Following transection, the skin incision was closed with a non-absorbable suture (nylon 6-0), and antibiotic ointment was applied. Success of the surgery was verified by monitoring eyelid and eyeball position over the subsequent days (Savastano et al., 2010; Martinez-Camarillo et al., 2019).

Laser Photocoagulation Injury

With the animals under anesthesia, eye drops were instilled (1% tropicamide and 2.5% phenylephrine HCl) to induce full pupil dilation. Rats were treated with a 532-nm OcuLight GL green diode laser (IRIDEX, Toronto, ON, Canada). Laser settings were: 150–160 mW power, 50 ms duration, and 75 μm diameter. In study 1, half of the rats in each experimental group received 4 burns per eye (one burn per quadrant) and were used for evaluating CNV development with FA scoring and lesion volume analysis using 3D confocal reconstruction (He et al., 2005). The other half received 12 burns in a single eye (one burn per clock hour) and were used for evaluating choroidal VEGF protein levels (Chan et al., 2005) (Twelve burns is considered a blinding procedure, so only one eye could be treated according to animal care guidelines). In study 2, all rats were treated with 4 laser burns per eye. Care was taken to avoid the retinal vessels. Rupture of Bruch's membrane was confirmed by the presence of a retinal bubble.

Eye Drops

Following the laser injury, animals in study 1 received daily eye drops between 9:00 and 11:00 am each day for 14 days. Two drops (∼40 μL each) were instilled per eye. Artificial tears were applied in the control and ICNx groups. The β-AR agonist group received 50 mM isoproterenol (Jiang et al., 2010) dissolved in artificial tears, and the β-AR antagonist group received 2% propranolol (Dal Monte et al., 2013) dissolved in artificial tears. Isoproterenol is known to be subject to oxidation, especially at pH levels ≥6.5, which can lead to chemical degradation (Leach et al., 1977). However, the pH of the eye drops could not be adjusted below 6.5 since that would irritate the eyes. In order to mitigate degradation, isoproterenol and propranolol drops were freshly prepared once per week in plastic vials and stored at 4°C. UV spectra of the isoproterenol drops were measured over time to confirm drug stability (Siva et al., 2012).

Fluorescein Angiography

All animals underwent FA to assess leakage from newly formed vessels resulting from the laser injury. Rats in study 1 received FA 14 days after laser therapy (prior to being euthanized), while rats in study 2 received FA 3, 7, 10, and 14 days after laser injury. With the animals fully anesthetized and their eyes dilated, a 0.01 mL intraperitoneal injection of 10% sodium fluorescein dye was applied. Sequential posterior pole images were taken using a RetCam 3 Retinal Camera (Clarity Medical Systems, Pleasanton, CA, United States) with an 80° lens. The intensity of fluorescein staining in late-phase FA was scored according to an established grading scale (Takehana et al., 1999). Lesions were given a score of 0 (no staining), 1 (slightly stained), 2 (moderately stained), or 3 (strongly stained). The scores of all lesions within each treatment group were averaged. Lesions that scored a 0 were excluded from analysis, since those lesions likely represented laser impacts that did not result in CNV (Lambert et al., 2013).

3D Confocal Reconstruction

Animals with 4 burns per eye were used for quantifying CNV lesion volume postmortem. Rats were euthanized at least 4–5 h after FA imaging, in order to allow the fluorescein enough time to clear from the circulatory system. Eyes were enucleated, and the cornea, lens, and retina were removed. The sclera-choroid complex was fixed overnight in 4% formalin at 4°C. Tissue was washed the next day and permeabilized with 0.5% Triton-X for 4 h. The eye cups were blocked with 1% BSA for 2 h and placed in 1:50 fluorescein-labeled GSL I isolectin B4 (endothelial cell and macrophage marker; Vector Laboratories, Burlingame, CA, United States) at 4°C overnight. Samples were washed and mounted on slides with mounting media (VECTASHIELD; Vector Laboratories), while making incisions in the eye cups to flatten them. Flat mounts were visualized using the 10x objective of an UltraVIEW spinning disk confocal microscope (PerkinElmer, Waltham, MA, United States). The image stacks were generated in the z-plane, with the microscope set to excite at 488 nm and to detect at 505–530 nm. Images were processed using the microscope's software, by closely circumscribing and digitally extracting the fluorescent lesion areas throughout the entire image stack (He et al., 2005). Each extracted lesion was processed through the topography software to generate a

digital topographic image representation of the lesion, which was measured to indicate the CNV lesion volume.

Optical Coherence Tomography

In the second study, SD-OCT was used to monitor CNV progression *in vivo* after laser therapy. OCT imaging was performed with an Envisu Bioptigen system (Leica Microsystems, Wetzlar, Germany), with each lesion imaged using 100 horizontal raster scans spaced 16 μm apart, over an area of 1.6 × 1.6 mm. We used a stereological method (three-dimensional interpretation of two-dimensional cross sections) to reconstruct the OCT images in 3D and calculate lesion size, as described previously (Trujillo-Sanchez et al., 2018).

Angiogenic Growth Factor Levels

In study 1, animals with 12 laser burns were used for evaluating choroidal VEGF protein levels. Posterior poles were isolated from each laser-treated eye and pooled within each of the four experimental groups. Tissues were homogenized in buffer containing mixed protease inhibitors for protein extraction. Total protein concentration was determined by a Bio-Rad protein assay (Bio-Rad Laboratories, Hercules, CA, United States). VEGF protein in the posterior poles was assessed in triplicate with a VEGF ELISA kit (detection range of 3–500 pg/mL; R&D Systems, Minneapolis, MN, United States) (Chan et al., 2005). Protein concentrations were normalized by the total protein.

RESULTS

Study 1

In the first study, we measured the effects of pharmacological or surgical manipulation of ocular sympathetic activity on development of laser-induced CNV. Animals were subjected to laser injury and were split into four groups: (1) daily eye drops of artificial tears (control group); (2) daily eye drops of isoproterenol (β-AR agonist group); (3) daily eye drops of propranolol (β-AR antagonist group); (4) bilateral ICN transection 6 weeks prior to the laser injury, followed by daily eye drops of artificial tears (ICNx group). The 6-week delay before the laser injury was chosen to be consistent with prior studies that assessed effects of sympathetic denervation on choroidal vascularity and related measures (Steinle et al., 2002; Steinle and Smith, 2003; Steinle and Lashbrook, 2006; Martinez-Camarillo et al., 2019). Animals were euthanized 14 days after laser application. As described in **Table 1** and section "Materials and Methods," outcome measures included CNV leakiness (*in vivo*), CNV lesion volume (*ex vivo*), and choroidal VEGF protein levels.

Fluorescein Angiography

Leakiness of CNV lesions was assessed with FA scoring, 14 days after laser therapy. Average FA scores for all groups fell between 1.5 and 2.0, indicating moderate staining (**Figure 1**). Lesions in rats receiving daily β-AR eye drops (propranolol or isoproterenol) were slightly less leaky than lesions in the control group; however, scores were not significantly different among these groups ($P > 0.05$). In rats that underwent ICN transection 6 weeks prior to laser injury, FA scores were 17% lower than scores in the control group ($P = 0.02$).

3D Confocal Reconstruction

Confocal analysis of lesion volumes revealed smaller lesions in the three treatment groups than in the control group (**Figure 2**). Blocking β-AR activity with propranolol or through ICN transection led to reductions in lesion volume by 75 and 70%, respectively ($P < 0.001$). Application of the β-AR agonist isoproterenol also reduced lesion volume versus the control group, but by only 27% ($P < 0.05$).

Angiogenic Growth Factor Levels

ELISA testing indicated elevated choroidal VEGF protein levels in the three treatment groups versus the control group ($P < 0.01$; **Figure 3**). VEGF levels in the control group were relatively low (Martinez-Camarillo et al., 2019), suggesting a return to baseline in this group.

Study 2

The second study was designed to further investigate the effects of ICN transection in the rat laser-induced CNV model. Results

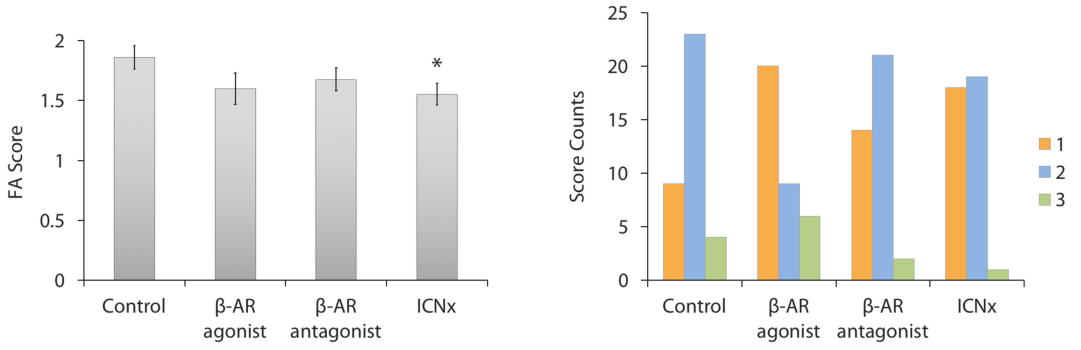

FIGURE 1 | FA scores 14 days after laser injury in each experimental group ($n \geq 35$ lesions per group from five animals per group). Four laser burns were made per eye. **(Left)** Average lesion score in each group. Scores in the ICN transection group were significantly lower than scores in the control group (*$P < 0.05$). Error bars indicate SEM. **(Right)** Histogram showing the distribution of FA scores in each group.

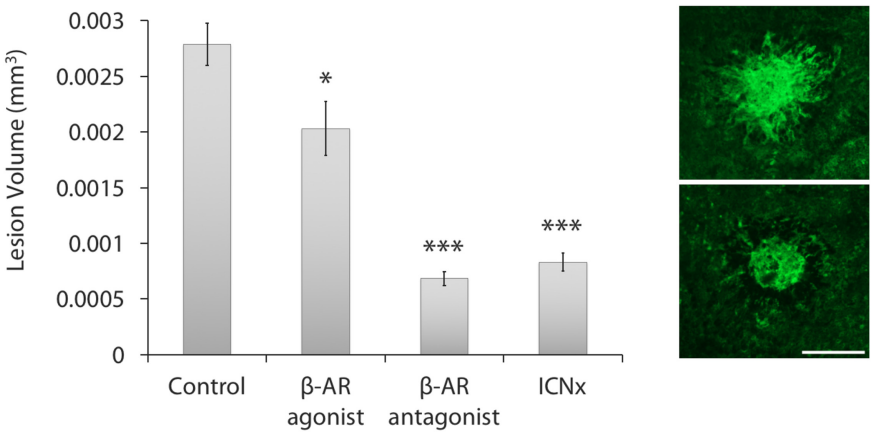

FIGURE 2 | β-AR modulation leads to smaller laser-induced CNV lesions. **(Left)** All three treatment groups had statistically smaller lesions than the control group ($n \geq 30$ lesions per group from five animals per group; $^{***}P < 0.001$; $^{*}P < 0.05$). Lesions in the propranolol and ICN transection groups were statistically similar in size ($P = 0.16$). Error bars represent SEM. **(Right)** Images of CNV membranes, stained with FITC-labeled isolectin-B4, showing representative lesions from the control group (top) and ICN transection group (bottom). Scale bar = 200 μm.

from study 1 revealed that blocking ocular sympathetic activity in this model inhibited progression of laser-induced CNV (see **Figures 1**, **2**), supporting ICN block as a potential therapy for wet AMD. However, ICN transection was performed 6 weeks prior to the laser injury. A therapy for wet AMD would not commence until after a patient presents with CNV; therefore, a better animal model of the clinical situation would be to perform ICN transection *after* the laser injury. This was the purpose of study 2.

Rats were subjected to laser injury and split into three groups: (1) bilateral ICN sham surgery 7 days after the laser injury (control group); (2) bilateral ICN transection immediately after the laser injury ($ICNx_0$ group); (3) bilateral ICN transection 7 days after the laser injury ($ICNx_7$ group). Animals were euthanized 14 days after laser application. Outcome measures included CNV leakiness (*in vivo*) and CNV volume (*in vivo* and *ex vivo*), as described in **Table 1** and section "Materials and Methods."

Fluorescein Angiography

Figure 4 shows the FA scores in each experimental group at 3, 7, 10, and 14 days after the laser injury. Scores in all groups were statistically similar on days 3 and 7, with the average score increasing from ∼0.2 to ∼0.9 over this time period. Scores in each group increased again on days 10 and 14, indicating steady CNV development throughout the 2-week monitoring period. On days 10 and 14, FA scores in both ICNx groups were lower than those of the control group, with the $ICNx_7$ group exhibiting the lowest average scores. The average FA score in the $ICNx_7$ group increased from ∼0.9 to ∼1.1 between days 7 and 14, signifying limited CNV progression over this time period.

Lesion Volume Analysis

Figure 5 summarizes the results from the OCT and confocal lesion volume measurements. Lesions in all three groups shrank between days 3 and 7 after the laser injury, due to resolution of edema during this time period. Between days 7 and 10, lesion sizes remained relatively stable. Average lesion sizes in all groups were statistically similar through day 10, with just one exception (see **Figure 5**, *left*). By day 14, however, lesions in the control group had grown, while lesion sizes in the two ICNx groups remained stable. Both OCT and confocal imaging revealed significantly smaller lesion sizes in the ICNx groups versus the control group on day 14 ($P < 0.001$). According to the confocal measurements, average lesion volume in the $ICNx_0$ and $ICNx_7$ groups was 30 and 45% smaller than that of the control group, respectively.

DISCUSSION

Outcomes from our two studies indicate a direct role for the sympathetic nervous system, and the β-AR receptors in

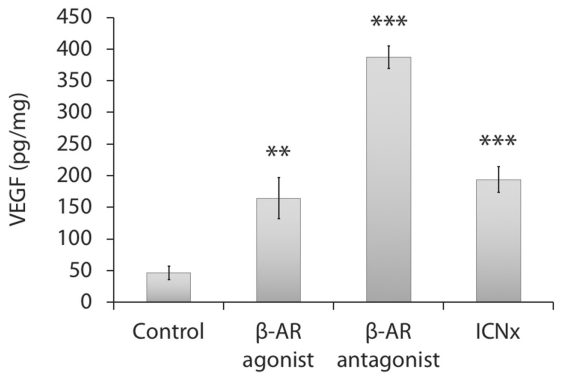

FIGURE 3 | Choroidal VEGF protein levels 14 days after laser injury in each experimental group ($n = 5$ animals per group). Twelve laser burns were made in a single eye. VEGF levels in the treatment groups were significantly higher than levels in the control group. Units represent VEGF protein normalized to total protein. Error bars represent SD. $^{***}P < 0.001$; $^{**}P < 0.01$.

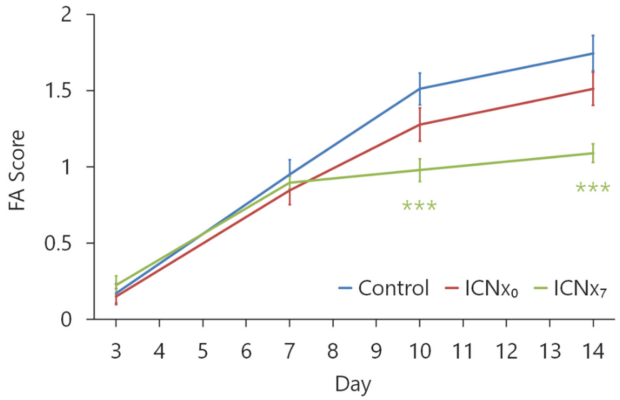

FIGURE 4 | FA scores at 3, 7, 10, and 14 days after laser injury in each experimental group ($n \geq 45$ lesions per group from six animals per group). Four laser burns were made per eye. Beginning 10 days after laser treatment, scores in the animals that underwent ICN transection on day 7 were significantly lower than scores in the animals that received sham surgery (***$P < 0.001$). Error bars indicate SEM.

particular, in regulating the development of laser-induced CNV. In the first study, inhibiting sympathetic activity by either pharmacological or surgical manipulation led to reductions in lesion volume by 70–75%. In agreement with the FA data (see **Figure 1**), these results suggest that blocking ocular sympathetic activity generated an anti-angiogenic response. Unexpectedly, application of the β-AR agonist isoproterenol also led to a reduction in lesion volume versus the control group, but only by 27%. This may be attributed to β-AR desensitization or downregulation caused by prolonged application of isoproterenol, as reported by others (Gonzalez-Brito et al., 1988; Gambarana et al., 1991; Brouri et al., 2002; Dal Monte et al., 2012).

Though no studies have investigated the effect of β-AR agonists on the progression of laser-induced CNV, several studies in mice have reported that systemic or intraocular delivery of β-AR antagonists causes a reduction in CNV lesion size (Lavine et al., 2013, 2017; Nourinia et al., 2015; Omri et al., 2019). Lavine et al. (2013) measured lesion areas (as opposed to volumes) 14 days after laser photocoagulation and found that daily intraperitoneal injection of propranolol (20 mg/kg/day) led to a 50% reduction in lesion size. Omri et al. (2019) also treated mice with daily administration of intraperitoneal propranolol (6 mg/kg/day) and observed ∼70% reduced lesion areas after 14 days. Nourinia et al. (2015) measured lesion areas 28 days after laser photocoagulation and found that a single intravitreal injection of propranolol (0.3 μg) at the time of laser application led to a 79% reduction in lesion size, similar to what we observed. Lavine et al. (2017) tested effects of a single intravitreal injection of the β_2-AR antagonist ICI 118,551 at the time of laser application and found a 35% reduction in lesion area after 14 days, indicating that the anti-angiogenic effects reported in these studies are at least partially due to β_2 receptor blockade (as opposed to other β-AR subtypes).

To further demonstrate the inhibitory effect of delayed ocular sympathetic block on laser-induced CNV in rats, the second study showed that surgical ICN transection led to smaller CNV lesion sizes, even when transection was performed at 0 and 7 days after the laser injury. Unexpectedly, we found that ICN transection 7 days after the laser injury was more effective than immediately after the laser injury (see **Figures 4**, **5**). This finding may arise from use of relatively small sample sizes ($n = 6$ animals per group). In support of this hypothesis, it would be expected that 7 days after the laser injury, CNV lesions in the $ICNx_7$ group (prior to undergoing surgery) would be similar in size to lesions in the control group. However, as shown in **Figure 5**, $ICNx_7$ lesions were smaller than control group lesions on day 7. Nevertheless, the FA and lesion volume results from both studies indicate that surgically removing the ocular sympathetic supply inhibits progression of laser-induced CNV. Surgical ICN block was more effective when performed 6 weeks prior to laser injury versus after laser injury (70% reduction in lesion volumes versus 30–45% reduction, respectively). For comparison, a mouse study with the FDA-approved anti-VEGF

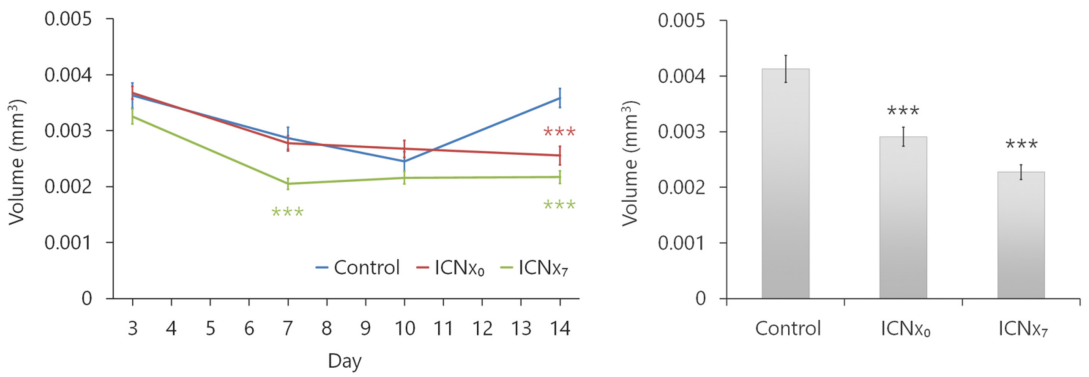

FIGURE 5 | ICN transection leads to smaller laser-induced CNV lesions. Lesion volumes were measured with SD-OCT at 3, 7, 10, and 14 days after laser treatment (left). Following euthanasia on day 14, volumes were measured *ex vivo* with confocal microscopy (right). By day 14, animals that underwent ICN transection had statistically smaller lesions than the animals that received sham surgery ($n \geq 44$ lesions per group from six animals per group; ***$P < 0.001$). This was true regardless of whether ICN transection was performed immediately after or 7 days after laser therapy. Error bars represent SEM.

agent aflibercept (Eylea; VEGF-TRAP$_{R1R2}$) demonstrated that a single intravitreal injection of the drug at the time of laser application led to a ∼30% reduction in lesion size after 14 days (Saishin et al., 2003).

Given our finding that pharmacological and surgical block of ocular sympathetic activity inhibited CNV progression, it would be expected that these interventions would also cause reduced choroidal VEGF levels. However, we found just the opposite; choroidal VEGF was elevated in the treatment groups (see **Figure 3**). There are a couple potential explanations for this surprising result: First, VEGF was measured 14 days after the laser injury, which may not have been the appropriate time point [for example, systemic VEGF levels in mouse peak 7 days after laser injury and return to baseline after 14 days (Kase et al., 2010)]. Second, VEGF levels are affected by several factors including inflammation, ischemia, and hypoxia (Ramakrishnan et al., 2014); it is possible that drug administration and/or ICN transection surgery caused these side effects.

Our observation that blocking ocular sympathetic activity in the laser-induced CNV model is anti-angiogenic appears to contradict our prior finding that ICN transection in naive rats (not subjected to laser injury) causes increased choroidal vascularity after 6 weeks, as measured by histomorphometry (Martinez-Camarillo et al., 2019). One possible explanation, as proposed previously, is that this increased vascularity may have been indirectly caused by a long-term vasodilation due to a loss of sympathetic tone (Martinez-Camarillo et al., 2019). Another possibility is that the contradictory findings arise from use of different experimental models and rat strains: naive Sprague Dawley (albino) in our prior study and laser-treated Brown Norway (pigmented) in the present studies (The laser-induced CNV model requires pigmented animals, since pigment is needed for absorbing the laser energy to create a burn). Yet another possibility is that sympathetic activity plays different roles in the intact versus leaky blood vessels, which is supported by a pro-angiogenic sympathetic role in tumor neovascularization (Mulcrone et al., 2017; Hanns et al., 2019; Kamiya et al., 2019; Stavropoulos et al., 2020). In a comprehensive review of the role of the β-adrenergic system on ocular neovascularization, Casini et al. (2014) concluded that "in different experimental models, a decrease of the β-adrenergic function may result either in reduction or in exacerbation of the vascular changes, thus suggesting possible dual effects of β-AR modulation depending on the experimental setting." Because the laser-induced CNV model is the gold standard for testing new treatments for wet AMD (Pennesi et al., 2012), future studies should focus on this model.

In summary, our results demonstrate that blocking ocular sympathetic activity inhibits CNV. Even when ICN transection was performed 1 week after laser injury, inhibition of CNV progression was still observed. This suggests that electrical blocking of ICN activity could be an effective bioelectronic medicine strategy for treating wet AMD.

DATA AVAILABILITY STATEMENT

The raw data supporting the conclusions of this article will be made available by the authors, without undue reservation.

ETHICS STATEMENT

The animal study was reviewed and approved by the USC Institutional Animal Care and Use Committee.

AUTHOR CONTRIBUTIONS

JCM-C, MH, DH, and AW contributed to conception and design of the study. JCM-C, CS, GT-S, AR, AG, VP, AS, and AW conducted the experiments and organized the database. AW performed the statistical analysis. JCM-C wrote the first draft of the manuscript. CS, AR, and AW wrote sections of the manuscript. All authors contributed to manuscript revision, read, and approved the submitted version.

FUNDING

Supported by a grant from Galvani Bioelectronics as well as unrestricted departmental support to the USC Roski Eye Institute from Research to Prevent Blindness.

REFERENCES

Birmingham, K., Gradinaru, V., Anikeeva, P., Grill, W. M., Pikov, V., McLaughlin, B., et al. (2014). Bioelectronic medicines: a research roadmap. *Nat. Rev. Drug Discov.* 13, 399–400. doi: 10.1038/nrd4351

Brouri, F., Findji, L., Mediani, O., Mougenot, N., Hanoun, N., Le Naour, G., et al. (2002). Toxic cardiac effects of catecholamines: role of β-adrenoceptor downregulation. *Eur. J. Pharmacol.* 456, 69–75. doi: 10.1016/S0014-2999(02)02643-2

Campochiaro, P. A. (2013). Ocular neovascularization. *J. Mol. Med.* 91, 311–321. doi: 10.1007/s00109-013-0993-5

Casini, G., Dal Monte, M., Fornaciari, I., Filippi, L., and Bagnoli, P. (2014). The β-adrenergic system as a possible new target for pharmacologic treatment of neovascular retinal diseases. *Prog. Retin Eye Res.* 42, 103–129. doi: 10.1016/j.preteyeres.2014.06.001

Chan, C. K., Pham, L. N., Zhou, J., Spee, C., Ryan, S. J., and Hinton, D. R. (2005). Differential expression of pro- and antiangiogenic factors in mouse strain-dependent hypoxia-induced retinal neovascularization. *Lab Investig.* 85, 721–733. doi: 10.1038/labinvest.3700277

Dal Monte, M., Casini, G., la Marca, G., Isacchi, B., Filippi, L., and Bagnoli, P. (2013). Eye drop propranolol administration promotes the recovery of oxygen-induced retinopathy in mice. *Exp. Eye Res.* 111, 27–35. doi: 10.1016/j.exer.2013.03.013

Dal Monte, M., Martini, D., Latina, V., Pavan, B., Filippi, L., and Bagnoli, P. (2012). Beta-adrenoreceptor agonism influences retinal responses to hypoxia in a model of retinopathy of prematurity. *Invest Ophthalmol. Vis. Sci.* 53, 2181–2192. doi: 10.1167/iovs.11-9408

Gambarana, C., Ordway, G. A., Hauptmann, M., Tejani-Butt, S., and Frazer, A. (1991). Central administration of 1-isoproterenol *in vivo* induces

a preferential regulation of β2-adrenoceptors in the central nervous system of the rat. *Brain Res.* 555, 141–148. doi: 10.1016/0006-8993(91)90870-2

Gonzalez-Brito, A., Reiter, R., Menendez-Pelaez, A., Guerrero, J. M., Santana, C., and Jones, D. J. (1988). Darkness-induced changes in noradrenergic input determine the 24 hour variation in beta-adrenergic receptor density in the rat pineal gland: *in vivo* physiological and parmacological evidence. *Life Sci.* 43, 707–714.

Hanns, P., Paczulla, A. M., Medinger, M., Konantz, M., and Lengerke, C. (2019). Stress and catecholamines modulate the bone marrow microenvironment to promote tumorigenesis. *Cell Stress* 3, 221–235. doi: 10.15698/cst2019.07.192

He, S., Ding, Y., Zhou, J., Krasnoperov, V., Zozulya, S., Kumar, S. R., et al. (2005). Soluble EphB4 regulates choroidal endothelial cell function and inhibits laser-induced choroidal neovascularization. *Investig. Ophthalmol. Vis. Sci.* 46, 4772–4779. doi: 10.1167/iovs.05-0502

Hoerster, R., Muether, P. S., Vierkotten, S., Schröder, S., Kirchhof, B., and Fauser, S. (2012). *In-vivo* and *ex-vivo* characterization of laser-induced choroidal neovascularization variability in mice. *Graefe's Arch. Clin. Exp. Ophthalmol.* 250, 1579–1586. doi: 10.1007/s00417-012-1990-z

Jasielska, M., Semkova, I., Shi, X., Schmidt, K., Karagiannis, D., Kokkinou, D., et al. (2010). Differential role of tumor necrosis factor (TNF)-alpha receptors in the development of choroidal neovascularization. *Invest. Ophthalmol. Vis. Sci.* 51, 3874–3883. doi: 10.1167/iovs.09-5003

Jiang, Y., Walker, R. J., Kern, T. S., and Steinle, J. J. (2010). Application of isoproterenol inhibits diabetic-like changes in the rat retina. *Exp. Eye Res.* 91, 171–179. doi: 10.1016/j.exer.2010.04.014

Kamiya, A., Hayama, Y., Kato, S., Shimomura, A., Shimomura, T., Irie, K., et al. (2019). Genetic manipulation of autonomic nerve fiber innervation and activity and its effect on breast cancer progression. *Nat. Neurosci.* 22, 1289–1305. doi: 10.1038/s41593-019-0430-3

Kase, S., He, S., Sonoda, S., Kitamura, M., Spee, C., Wawrousek, E., et al. (2010). αB-crystallin regulation of angiogenesis by modulation of VEGF. *Blood* 115, 3398–3406. doi: 10.1182/blood-2009-01-197095

Lambert, V., Lecomte, J., Hansen, S., Blacher, S., Gonzalez, M. L., Struman, I., et al. (2013). Laser-induced choroidal neovascularization model to study age-related macular degeneration in mice. *Nat. Protoc.* 8, 2197–2211. doi: 10.1038/nprot.2013.135

Lashbrook, B. L., and Steinle, J. J. (2005). Beta-adrenergic receptor regulation of pigment epithelial-derived factor expression in rat retina. *Aut. Neurosci.* 121, 33–39.

Lavine, J. A., Farnoodian, M., Wang, S., Darjatmoko, S. R., Wright, L. S., Gamm, D. M., et al. (2017). β2–adrenergic receptor antagonism attenuates CNV through inhibition of VEGF and IL-6 expression. *Investig. Ophthalmol. Vis. Sci.* 58, 299–308. doi: 10.1167/iovs.16-20204

Lavine, J. A., Sang, Y., Wang, S., Ip, M. S., and Sheibani, N. (2013). Attenuation of choroidal neovascularization by β2-Adrenergic receptor antagonism. *JAMA Ophthalmol.* 131, 376–382. doi: 10.1001/jamaophthalmol.2013.1476. Attenuation

Leach, J. K., Strickland, R. D., Millis, D. L., Stremsterfer, C. E., and Skipper, B. J. (1977). Biological activity of dilute isoproterenol solution stored for long periods in plasgic bags. *Am. J. Hosp. Pharmcists* 34, 709–712.

Lin, X., Wang, Q., and He, M. (2019). Repeated retinal photocoagulation in monkeys for the optimization of a laser-induced choroidal neovascularization model. *Exp. Eye Res.* 184, 1–7. doi: 10.1016/j.exer.2019.03.020

Martinez-Camarillo, J. C., Spee, C. K., Chen, M., Rodriguez, A., Nimmagadda, K., Trujillo-Sanchez, G. P., et al. (2019). Sympathetic effects of internal carotid nerve manipulation on choroidal vascularity and related measures. *Investig. Ophthalmol. Vis. Sci.* 60, 4303–4309. doi: 10.1167/iovs.18-25613

Menon, G., and Walters, G. (2009). New paradigms in the treatment of wet AMD: the impact of anti-VEGF therapy. *Eye* 23, S1–S7. doi: 10.1038/eye.2009.13

Mulcrone, P. L., Campbell, J. P., Clément-Demange, L., Anbinder, A. L., Merkel, A. R., Brekken, R. A., et al. (2017). skeletal colonization by breast cancer cells is stimulated by an osteoblast and β2AR-Dependent neo-angiogenic switch. *J. Bone Miner. Res.* 32, 1442–1454. doi: 10.1002/jbmr.3133

Nourinia, R., Kanavi, M. R., Kaharkaboudi, A., Taghavi, S. I., Aldavood, S. J., Darjatmoko, S. R., et al. (2015). Ocular safety of intravitreal propranolol and its efficacy in attenuation of choroidal neovascularization. *Investig. Ophthalmol. Vis. Sci.* 56, 8228–8235. doi: 10.1167/iovs.15-17169

O'Bryhim, B. E., Li, A. S., Bayliss, S. J., Tychsen, L., Lueder, G. T., and Rajagopal, R. (2019). Successful treatment of an exudative choroidal hemangioma with oral propranolol in a 10-year-old boy. *J. Aapos.* 23, 236–238. doi: 10.1016/j.jaapos.2019.02.004

Omri, S., Tahiri, H., Pierre, W. C., Desjarlais, M., Lahaie, I., Loiselle, S. E., et al. (2019). Propranolol attenuates proangiogenic activity of mononuclear phagocytes: implication in choroidal neovascularization. *Investig. Ophthalmol. Vis. Sci.* 60, 4632–4642. doi: 10.1167/iovs.18-25502

Pennesi, M. E., Neuringer, M., and Courtney, R. J. (2012). Animal models of age related macular degeneration. *Mol. Aspects Med.* 33, 487–509. doi: 10.1016/j.mam.2012.06.003

Ramakrishnan, S., Anand, V., and Roy, S. (2014). Vascular endothelial growth factor signaling in hypoxia and inflammation. *J. Neuroimmune Pharmacol.* 9, 142–160. doi: 10.1007/s11481-014-9531-7.Vascular

Ryan, S. J. (1979). The development of an experimental model of subretinal neovascularization in disciform macular degeneration. *Trans. Am. Ophthalmol. Soc.* 77, 707–745.

Saishin, Y., Saishin, Y., Takahashi, K., Lima e Silva, R., Hylton, D., Rudge, J. S., et al. (2003). VEGF-TRAPR1R2suppresses choroidal neovascularization and VEGF-induced breakdown of the blood-retinal barrier. *J. Cell Physiol.* 195, 241–248. doi: 10.1002/jcp.10246

Savastano, L. E., Castro, A. E., Fitt, M. R., Rath, M. F., Romeo, H. E., and Muñoz, E. M. (2010). A standardized surgical technique for rat superior cervical ganglionectomy. *J. Neurosci. Methods* 192, 22–33. doi: 10.1016/j.jneumeth.2010.07.007

Shah, R. S., Soetikno, B. T., Lajko, M., and Fawzi Amani, A. A. (2015). A mouse model for laser-induced choroidal neovascularization. *J. Vis. Exp.* 2015, 1–7. doi: 10.3791/53502

Shi, X., Semkova, I., Müther, P. S., Dell, S., Kociok, N., and Joussen, A. M. (2006). Inhibition of TNF-?? reduces laser-induced choroidal neovascularization. *Exp. Eye Res.* 83, 1325–1334. doi: 10.1016/j.exer.2006.07.007

Siva, S., Venkatesh, G., Prabhu, A. A. M., Sankaranarayanan, R. K., and Rajendiran, N. (2012). Absorption and fluorescence spectral characteristics of norepinephrine, epinephrine, isoprenaline, methyl dopa, terbutaline and orciprenaline drugs. *Phys. Chem. Liq.* 50, 434–452. doi: 10.1080/00319104.2011.597029

Smith, P. G., and Reddy, H. (1990). Reorganization of cranial sympathetic pathways following neonatal ganglionectomy in the rat. *J. Comp. Neurol.* 301, 490–500. doi: 10.1002/cne.903010311

Stavropoulos, I., Sarantopoulos, A., and Liverezas, A. (2020). Does sympathetic nervous system modulate tumor progression? a narrative review of the literature. *J. Drug Assess.* 9, 106–116. doi: 10.1080/21556660.2020.1782414

Steinle, J. J., and Lashbrook, B. L. (2006). Cervical sympathectomy regulates expression of key angiogenic factors in the rat choroid. *Exp. Eye Res.* 83, 16–23. doi: 10.1016/j.exer.2005.11.006

Steinle, J. J., and Smith, P. G. (2003). Sensory but not parasympathetic nerves are required for ocular vascular remodeling following chronic sympathectomy in rat. *Auton Neurosci. Basic Clin.* 109, 34–41. doi: 10.1016/j.autneu.2003.09.004

Steinle, J. J., Lindsay, N. L., and Lashbrook, B. L. (2005). Cervical sympathectomy causes photoreceptor-specific cell death in the rat retina. *Auton Neurosci. Basic Clin.* 120, 46–51. doi: 10.1016/j.autneu.2005.03.004

Steinle, J. J., Pierce, J. D., Clancy, R. L., and Smith, P. G. (2002). Increased ocular blood vessel numbers and sizes following chronic sympathectomy in rat. *Exp. Eye Res.* 74, 761–768. doi: 10.1006/exer.2002.1182

Takehana, Y., Kurokawa, T., Kitamura, T., Tsukahara, Y., Akahane, S., Kitazawa, M., et al. (1999). Suppression of laser-induced choroidal neovascularization by oral tranilast in the rat. *Investig. Ophthalmol. Vis. Sci.* 40, 459–466.

Thapa, R., and Shields, C. L. (2013). Oral propranolol therapy for management of exudative retinal detachment from diffuse choroidal hemangioma in Sturge-Weber syndrome. *Eur. J. Ophthalmol.* 23, 922–924. doi: 10.5301/ejo.5000322

Trujillo-Sanchez, G. P., Martinez-Camarillo, J. C., Spee, C. K., Hinton, D. R., Humayun, M. S., and Weitz, A. C. (2018). Stereological method in optical coherence tomography for *in vivo* evaluation of laser-induced choroidal

neovascularization. *Ophthalmic Surg Lasers Imaging Retin.* 49, e65–e74. doi: 10.3928/23258160-20180907-09

Van Lookeren Campagne, M., Lecouter, J., Yaspan, B. L., and Ye, W. (2014). Mechanisms of age-related macular degeneration and therapeutic opportunities. *J. Pathol.* 232, 151–164. doi: 10.1002/path.4266

Wada, M., Ogata, N., Otsuji, T., and Uyama, M. (1999). Expression of vascular endothelial growth factor and its receptor (KDR/flk-1) mRNA in experimental choroidal neovascularization. *Curr. Eye Res.* 18, 203–213. doi: 10.1076/ceyr.18.3.203.5368

Wiley, L. A., Berkowitz, B. A., and Steinle, J. J. (2006). Superior cervical ganglionectomy induces changes in growth factor expression in the rat retina. *Investig. Opthalmol. Vis. Sci.* 47:439. doi: 10.1167/iovs.05-0656

Yi, X., Ogata, N., Komada, M., Yamamoto, C., Takahashi, K., Omori, K., et al. (1997). Vascular endothelial growth factor expression in choroidal neovascularization in rats. *Graefe's Arch. Clin. Exp. Ophthalmol.* 235, 313–319. doi: 10.1007/BF01739641

Conflict of Interest: AG, VP, and AS were employed by the company Galvani Bioelectronics.

The remaining authors declare that the research was conducted in the absence of any commercial or financial relationships that could be construed as a potential conflict of interest.

The authors declare that this study received funding from Galvani Bioelectronic. The funder had the following involvement in the study: Study design and interpretation of data.

Publisher's Note: All claims expressed in this article are solely those of the authors and do not necessarily represent those of their affiliated organizations, or those of the publisher, the editors and the reviewers. Any product that may be evaluated in this article, or claim that may be made by its manufacturer, is not guaranteed or endorsed by the publisher.

frontiers in Neuroscience

ORIGINAL RESEARCH
published: 10 January 2022
doi: 10.3389/fnins.2021.725751

Blood Pressure Regulation by the Carotid Sinus Nerve: Clinical Implications for Carotid Body Neuromodulation

Silvia V. Conde[1†], Joana F. Sacramento[1], Bernardete F. Melo[1], Rui Fonseca-Pinto[2], Mario I. Romero-Ortega[3] and Maria P. Guarino[1,2*†]*

[1] Faculdade de Ciências Médicas, Chronic Disease Research Center (CEDOC), NOVA Medical School, Universidade NOVA de Lisboa, Lisbon, Portugal, [2] ciTechCare, School of Health Sciences, Polytechnic of Leiria, Leiria, Portugal, [3] Department of Biomedical Engineering, University of Houston, Houston, TX, United States

OPEN ACCESS

Edited by:
Thiago S. Moreira,
University of São Paulo, Brazil

Reviewed by:
M. Teresa Perez-Garcia,
University of Valladolid, Spain
Josiane Campos Cruz,
Federal University of Paraiba, Brazil

***Correspondence:**
Silvia V. Conde
silvia.conde@nms.unl.pt
Maria P. Guarino
maria.guarino@ipleiria.pt

[†]These authors share senior authorship

Specialty section:
This article was submitted to Autonomic Neuroscience, a section of the journal Frontiers in Neuroscience

Received: 15 June 2021
Accepted: 24 November 2021
Published: 10 January 2022

Citation:
Conde SV, Sacramento JF, Melo BF, Fonseca-Pinto R, Romero-Ortega MI and Guarino MP (2022) Blood Pressure Regulation by the Carotid Sinus Nerve: Clinical Implications for Carotid Body Neuromodulation. Front. Neurosci. 15:725751. doi: 10.3389/fnins.2021.725751

Chronic carotid sinus nerve (CSN) electrical modulation through kilohertz frequency alternating current improves metabolic control in rat models of type 2 diabetes, underpinning the potential of bioelectronic modulation of the CSN as a therapeutic modality for metabolic diseases in humans. The CSN carries sensory information from the carotid bodies, peripheral chemoreceptor organs that respond to changes in blood biochemical modifications such as hypoxia, hypercapnia, acidosis, and hyperinsulinemia. In addition, the CSN also delivers information from carotid sinus baroreceptors—mechanoreceptor sensory neurons directly involved in the control of blood pressure—to the central nervous system. The interaction between these powerful reflex systems—chemoreflex and baroreflex—whose sensory receptors are in anatomical proximity, may be regarded as a drawback to the development of selective bioelectronic tools to modulate the CSN. Herein we aimed to disclose CSN influence on cardiovascular regulation, particularly under hypoxic conditions, and we tested the hypothesis that neuromodulation of the CSN, either by electrical stimuli or surgical means, does not significantly impact blood pressure. Experiments were performed in Wistar rats aged 10–12 weeks. No significant effects of acute hypoxia were observed in systolic or diastolic blood pressure or heart rate although there was a significant activation of the cardiac sympathetic nervous system. We conclude that chemoreceptor activation by hypoxia leads to an expected increase in sympathetic activity accompanied by compensatory regional mechanisms that assure blood flow to regional beds and maintenance of hemodynamic homeostasis. Upon surgical denervation or electrical block of the CSN, the increase in cardiac sympathetic nervous system activity in response to hypoxia was lost, and there were no significant changes in blood pressure in comparison

to control animals. We conclude that the responses to hypoxia and vasomotor control short-term regulation of blood pressure are dissociated in terms of hypoxic response but integrated to generate an effector response to a given change in arterial pressure.

Keywords: carotid body, carotid sinus nerve, hypoxia, blood pressure, neuromodulation

INTRODUCTION

Carotid sinus nerve (CSN) denervation improves glucose homeostasis in insulin-resistant and glucose-intolerant rats (Ribeiro et al., 2013; Sacramento et al., 2017, 2018). Electrical modulation of the CSN through kilohertz frequency alternating current is also shown to revert dysmetabolism metabolic in animal models of type 2 diabetes (Sacramento et al., 2018). In the context of an innovative therapeutic approach, termed bioelectronic medicines, in which individual nerve fibers are targeted in pathological conditions to restore functionality, the CSN emerges with a vast therapeutic potential in cardiometabolic disorders (Sacramento et al., 2018; Conde et al., 2020). Still, the positive effects of CSN blockade may be hindered by adverse effects associated with permanent loss of function (Conde, 2018). The CSN carries sensory information from the carotid bodies (CB), peripheral chemoreceptor organs that respond to changes in blood biochemical modifications such as hypoxia, hypercapnia, acidosis, and hyperinsulinemia (Gonzalez et al., 1994; Conde et al., 2014). In addition, the CSN also delivers information from carotid sinus baroreceptors, mechanoreceptor sensory neurons directly involved in the control of blood pressure (Marshall, 1998; Chapleau et al., 2001). The CB is implicated in the pathophysiology of several cardiovascular diseases, such as chronic heart failure (Del Rio et al., 2013; Schultz et al., 2013) and several forms of hypertension (Prabhakar and Peng, 2004; Abdala et al., 2012; Paton et al., 2013) playing a fundamental role in the genesis and maintenance of these diseases. It is shown that CSN inputs from the CB contribute to the elevated systemic sympathetic tone being critical for the genesis and maintenance of hypertension in spontaneously hypertensive rats (Abdala et al., 2012; McBryde et al., 2013). Also, it is shown that rats with chronic heart failure develop increased CB chemoreflex drive and chronic central presympathetic neuronal activation, increased sympathetic outflow, increased breathing variability, and apnea incidence as well as desensitization of the baroreflex, these effects being reduced by CB ablation (Del Rio et al., 2013). Together, these results confirm the role of the CB in regulating blood pressure and cardiac performance via sympathetic nervous system (SNS) activation. The interaction between these powerful reflex systems—chemoreflex and baroreflex—whose sensory receptors are in anatomical proximity, might represent a shortcoming to the development of selective bioelectronic tools to modulate the CSN.

The chemoreflex and baroreflex control the cardiovascular system via the profound influences they exert on autonomic outflow (Marshall, 1994). Disclosing the interdependency between these two reflex responses, particularly in the presence of stimuli such as hypoxia or ischemia (Marshall, 1998), is required to address pathophysiological mechanisms and therapeutics in cardiometabolic diseases. Although chemoreceptors are known for their role in the control of ventilation, they also modulate cardiovascular, endocrine, and renal systems. In contrast with the respiratory responses, the cardiovascular responses to CB stimulation are surrounded by a lot of controversies. They were extensively studied in the 70's and 80's although, as pointed out by Marshall (1994), multiple confounding factors contribute to an uneven interpretation of results, such as hyperventilation, hypocapnia, pulmonary stretch/vagal activation, central respiratory drive, baroreceptor involvement, circulating catecholamines, and the preparation studied (specie, awake/anesthetized animal, among others). The baroreceptors, on the other hand, are mechanoreceptor sensory neurons that respond to mechanical deformation of the nerve endings during distension of the arterial wall (Chapleau et al., 2001). They provide information to the solitary nucleus in the medulla oblongata to influence cardiac output and systemic vascular resistance through a negative feedback system called the baroreflex. Baroreceptor activation induces hypotension, and baroreceptor resection results in systemic hypertension (Irigoyen et al., 1991; Kougias et al., 2010). Baroreflex sensitivity is decreased in numerous pathological states, including chronic arterial hypertension, heart failure, obesity, and diabetes mellitus (Chapleau et al., 2001; Limberg et al., 2015). There is still debate in the literature regarding the interdependency between these two reflex responses, particularly in the presence of stimuli such as hypoxia.

Our group is dedicated to understanding the physiology of the CB chemoreceptors and to look at the CSN as a bioelectronic medicine target. Herein, we designed experiments to explore the crosstalk between CB-mediated blood pressure responses using different stimuli to the CSN from hypoxic hypoxia to ischemic hypoxia and electrical stimulation or high-frequency blocking. The primary objective of the study is to determine if electrical neuromodulation of CSN affects systemic blood pressure and cardiac autonomic function in both normoxic and hypoxic conditions.

MATERIALS AND METHODS

Animals

All animal experimental and care procedures were approved by the Ethics Committee and by the Animal Welfare Body of Faculdade de Ciências Médicas| Nova Medical School and by the Direcção Geral de Veterinária, Portugal. Principles of laboratory care were followed following the European Union Directive

for Protection of Vertebrates Used for Experimental and Other Scientific Ends (2010/63/EU). Experiments were performed in male Wistar Han rats (220–260 g) at 10–12 weeks old obtained from the vivarium of the Faculdade de Ciências Médicas, Universidade Nova de Lisboa, Lisboa, Portugal. Animals were kept under controlled temperature and humidity (21 ± 1°C; 55 ± 10% humidity) with a 12 h light/dark cycle and *ad libitum* access to food and water. In protocols requiring anesthesia, rats were anesthetized with sodium pentobarbital (60 mg kg^{-1} i.p.) and supplemented intravenously with 10% of the initial dose as necessary to make them areflexic to a nociceptive stimulus (effects of corneal reflexes and pinch to the front paw on the rise in arterial blood pressure). Body temperature was maintained close to 37 ± 1°C using a heated underblanket controlled by a rectal thermistor probe.

Evaluation of Blood Pressure and Heart Rate Responses to Acute Hypoxia in Conscious and Anesthetized Animals

To perform the set of experiments in conscious animals, rats were implanted with telemetry devices for blood pressure and heart rate (HR) continuous recording (HD-S10, Data Sciences Corporation, United States) under ketamine [75 mg/kg body weight (i.p.), Nimatek, Dechra, Northwich, United Kingdom]/metedomidine [0.5 mg/kg body weight (i.p.), Sedator®, Dechra, Northwich, United Kingdom] anesthesia and buprenorphine (10 μg/kg, Bupaq®, Richter Pharma AG, Wels, Austria) analgesia. In brief, the abdominal aorta was exposed via a ventral midline incision in the abdominal cavity, and the radio telemetry transmitter was implanted aseptically and sealed with a drop of tissue adhesive (Vetbound, 3M Company, St. Paul, MN, United States). The body of the transmitter was then placed on top of the intestines and secured to the abdominal muscle. Anesthesia was reversed with atipamezole [0.25 mg/kg in 2 ml (i.p.), Antisedan®, Zoetis, New Jersey, United States]. Animals were treated for 3 days with the non-steroidal anti-inflammatory drug carprofen [5 mg/kg/ml (s.c.), Rimadyl™, Pfizer, New York, United States] and allowed to recover from surgery for 15 days. Blood pressure, HR, and autonomic responses to hypoxic hypoxia were evaluated in conscious animals implanted with telemeters by placing the animals in a polypropylene cage equipped with gas injectors and sensors for oxygen (O_2). The hypoxic hypoxia protocol consisted of submitting the animals to 30 min baseline recording at normoxia (20% O_2 balanced N_2) followed by 15 min hypoxia (10% O_2 balanced N_2), followed by 10 min normoxia. Systolic (SBP), diastolic (DBP), and mean blood pressure (MBP) and HR were obtained via radio frequency signals through the Data Acquisition System from Data Sciences International (DSI, St. Paul, MN). Blood pressure and HR measurements were obtained during 1-s sampling periods and averaged. For measurement of blood pressure and HR in an anesthetized setting, animals were administered sodium pentobarbital (60 mg kg-1 i.p.), and the femoral artery and vein were catheterized under a dissection microscope. The femoral artery catheter was connected to a pressure transducer (−50, + 300 mmHg) and amplifier (Emka Technologies, Paris, France) to measure arterial blood pressure, and the venous catheter served to administer anesthetic supplements. To study the effect of ischemic hypoxia on blood pressure, SBP, DBP, and time elapsed between two successive R-waves of the QRS signal on the electrocardiogram—RR intervals—were recorded in spontaneously breathing anesthetized rats submitted to bilateral occlusion of the common carotid artery (OCC) for either 5 or 1 5 s. MBP was calculated using the values of SBP and DBP by the Iox 2.9.5.73 software (Emka Technologies, Paris, France) using the following mathematical formula: MAP = [SBP + 2 (DBP)]/3.

Assessment of Blood Pressure and Heart Rate Regulation in Response to Hypoxia After Carotid Sinus Nerve Bilateral Denervation

To test the influence of CSN on blood pressure responses to hypoxia, rats were anesthetized with sodium pentobarbital (60 mg kg-1 i.p.), the carotid artery bifurcations were located, bilaterally, and CSNs were identified and sectioned. The femoral artery and vein were catheterized to measure arterial blood pressure and to administer anesthetic supplements, respectively. SBP, DBP, HR, and time elapsed between two successive R-waves of the QRS signal on the electrocardiogram—RR intervals—were continuously recorded during ischemic hypoxia induced by bilateral OCC during either 5 or 15 s. Mean RR intervals were plotted vs. SBP, DBP, and MBP. One animal implanted with a telemetry blood pressure transducer, as described above, was anesthetized and tilted at an angle of 75°, and blood pressure changes were acquired using the Data Acquisition System from Data Sciences International (DSI, St. Paul, MN, United States) before and after acute CSN resection.

Assessment of Blood Pressure and Heart Rate Regulation in Response to Kilohertz Frequency Alternate Current Modulation of the Carotid Sinus Nerve

To evaluate the impact of acute Kilohertz frequency alternate current (KHFAC) modulation of the CSN on blood pressure and hypoxic responses, animals were implanted with bipolar sling cuff electrodes (90% platinum and 10% iridium, 100 μm inner diameter × 1 mm length, electrode surface area 0.4 × 0.5 mm^2, 0.45 mm interelectrode center-to-center distance, CorTec, Freiburg, Germany). Fibrin glue (Tisseel, Baxter Healthcare, Compton, Newbury, United Kingdom) was used to secure the cuff to the CSN and to prevent current spread from the ends of the cuff. The effect of KHFAC modulation (blocking and stimulation) on respiratory rate, HR, blood pressure, and cardiorespiratory responses evoked by hypoxia was evaluated by applying to the cuff electrodes bilaterally as rectangular pulses a current of 2 mA for 20 Hz (CSN stimulation) and 50 kHz (blocking) as previously described (Sacramento et al., 2018). KHFAC was applied using a commercial current source (Keithley 6221, Tektronix, Bracknell, United Kingdom) for 10 s for CSN stimulation and 1 min for CSN blocking. To ensure near-equal current split, the cuff electrode impedances were

measured in saline (154 mmol/l NaCl) before implantation, and the cuffs were matched for each animal based on < 10% difference in their impedance values. The current values are reported as peak-to-peak for each cuff, assuming an equal 50/50 split from the current source output. The impact of CSN blocking on cardiorespiratory responses to hypoxia was tested by delivering hypoxia (10% O_2 balanced N_2) through a mask to the animal for 1 min. Respiratory frequency and HR were recorded to determine the efficacy of KHFAC modulation of the CSN. Respiratory and cardiac variables were measured utilizing intercostal platinum wires for electromyography (EMG) and ECG placed subcutaneously across the diaphragm as previously described (Sacramento et al., 2018). EMG and ECG data were differentially recorded using Digidata Low Noise Data Acquisition System (Molecular Devices, Wokingham, United Kingdom). Blood pressure was measured through a catheter placed at the femoral artery and connected to a pressure transducer (–50, + 300 mmHg) and amplifier (Emka Technologies, Paris, France). At the end of experiments, animals were euthanized by an intracardiac overdose of pentobarbital. Death was confirmed by cervical dislocation.

Evaluation of Cardiac Autonomic Nervous System

Analysis of heart rate variability (HRV) is a non-invasive indirect method to assess the cardiac sympatho-vagal balance and herein was used both in freely moving and anesthetized rats to evaluate autonomic neural regulation of heart rate. Power spectral analysis of HRV was performed to evaluate the balance between the sympathetic and parasympathetic components of the cardiac autonomic nervous system (Thireau et al., 2008; Fonseca-Pinto, 2011; Silva et al., 2017). In anesthetized animals, the femoral artery was cannulated under a dissection microscope, and the animals were transferred to a heating pad to maintain body temperature at 37.5 ± 0.5°C, thus avoiding cold stress sympathetic activation. The catheter was connected to a pressure transducer and amplifier to acquire MAP (model 603, HSE-HA GmgH, Harvard Apparatus, Madrid, Spain). HR was derived from the mean arterial pressure (MAP) curve obtained by HSE-Harvard Pulmodyn W software with an acquisition frequency of 500 Hz. The tachogram containing the RR signal was obtained after the identification of the peak of MAP in each cardiac cycle. In conscious animals, blood pressure was assessed by a radiotelemetry device placed in the abdomen. Animals were gentled for 10 min daily for 1 week prior to surgery to minimize any discomfort related to the experimental manipulation and to reduce data variability from indwelling blood pressure telemeter instrumentation. After transmitter implantation surgery, the animals were allowed to recover for 10 days before any measurements were recorded. HR and RR intervals were obtained using Iox 2.9.5.73 software (Emka Technologies, Paris, France) with an acquisition frequency of 500 Hz. Blood pressure recordings to calculate LF/HF index were selected using 300 s of stable recording before and after the interventions except for the KHFAC neuromodulation experimental setting, in which the intervals chosen were of 30 s, corresponding to the neurostimulation period chosen to avoid central hypoxia.

The RR plots obtained in both groups were interpolated at 10 Hz (a frequency suitable to catch all oscillations from heart rhythm in rats) using cubic splines. The algorithm used to obtain spectral non-parametric HRV indices was created in Matlab Software (MATLAB version 7.10.0. Natick, Massachusetts, United States: The MathWorks Inc.), using a fast fourier transform approach (Thireau et al., 2008) by Welch spectral estimation considering a 256-point window and 50% overlapped. Beyond the relative power obtained by the area under the spectral curve associated with slow (High Frequencies–Hf) and Fast (Low Frequencies-Lf) oscillations, the sympathovagal balance was also calculated using the ratio between Lf and Hf. Hf power represents the vagal control of the heart, modulated by breathing, whereas Lf power (more precisely, its normalized version) reflects primarily the sympathetic modulation of heart rate (Thireau et al., 2008). Frequencies are presented in normalized units, and graphs were obtained using Kubios Software (Thireau et al., 2008). In rodents, the lack of a standard protocol has been conducted in recent years to a set of studies regarding methodological issues (Silva et al., 2017). Concerning the particular issue of defining the frequency bands associated with Lf and Hf frequency ranges, data obtained in the 90's suggest different frequency bands for rats (with limits from 0.195–0.6 Hz (Lf band) to 0.6–2.5 Hz (Hf band) and a ratio between Lf and Hf bands of 0.32 and from 0.02 to 0.195 Hz (Lf band) to 0.195 to 0.6 Hz (Hf band) and a ratio of 3–5 (Aubert et al., 1999); however, based in more recent findings in rodents, it is suggested the use of Lf in (0.15–1.5 Hz) and Hf in (1.5–4 Hz) as a good compromise to gauge the sympathetic and parasympathetic components of HRV (Thireau et al., 2008; Silva et al., 2017). These frequency ranges were used in this work.

Statistical Analysis

Statistical analyses were performed using Prism version 8 (GraphPad Software Inc., La Jolla, CA, United States). Data are presented as mean ± SEM. Shapiro–Wilk normality tests were performed. The significance of the differences between the mean values was calculated by two-tailed Student's *t*-test and two-way ANOVA with Bonferroni multiple comparison tests. Differences were considered significant at $p < 0.05$.

RESULTS

Evaluation of Blood Pressure and Heart Rate Responses to Acute Hypoxic Hypoxia and Ischemic Hypoxia in Conscious and Anesthetized Animals

Hypoxic hypoxia (10% O_2) during 15 min in conscious animals (**Figure 1A**) did not significantly change SBP, DBP, and MBP although a decreasing trend was observed (*normoxia*: SBP = 114.13 ± 4.85 mmHg, DBP = 92.31 ± 6.41 mmHg, MBP = 103.51 ± 5.57 mmHg; *hypoxia:* SBP = 106.60 ± 5.01 mmHg, DBP = 83.92 ± 3.68 mmHg, MBP = 95.37 ± 4.25 mmHg, $n = 4$) (**Figure 1B**). In the same

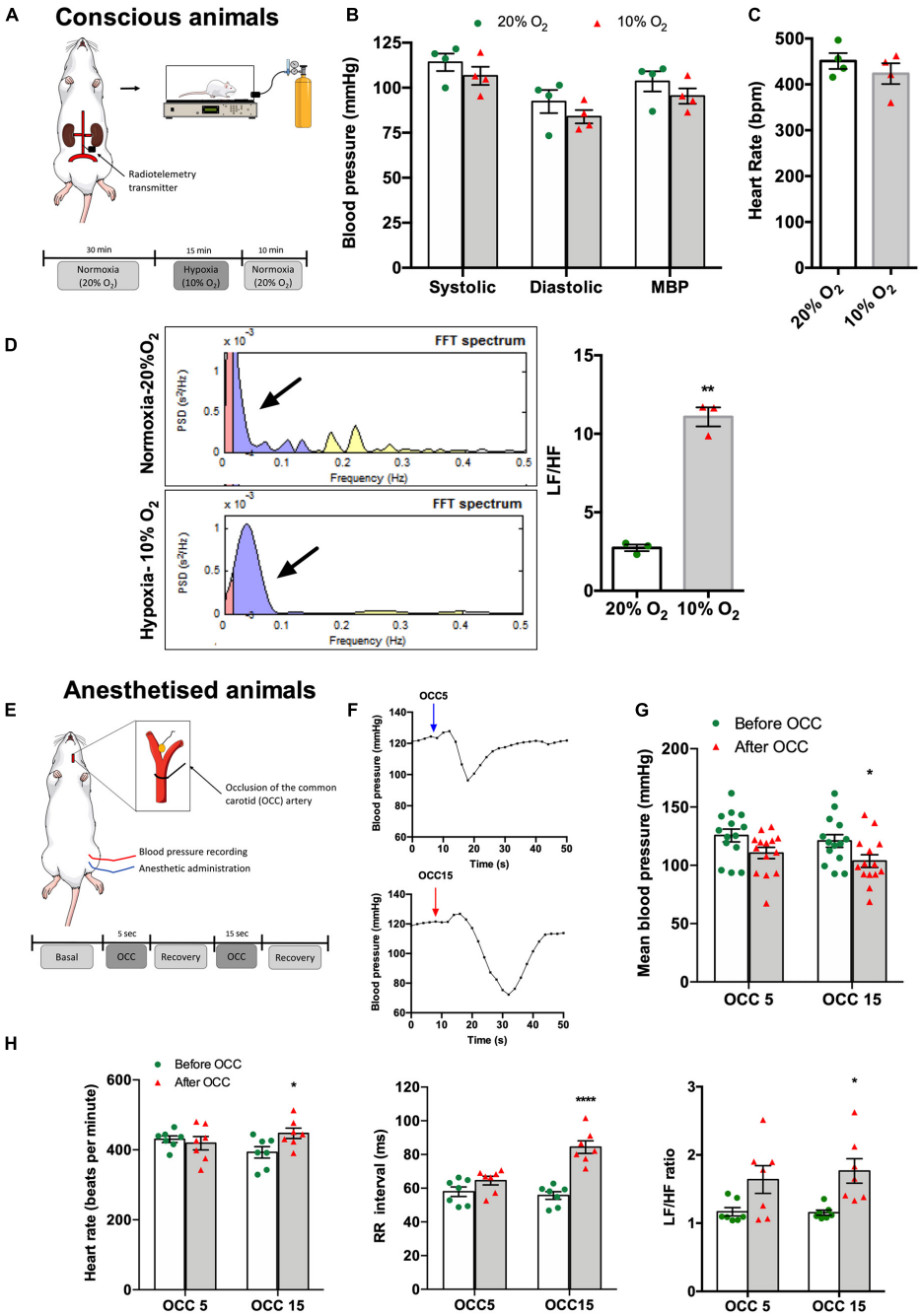

FIGURE 1 | Effect of hypoxic and ischemic hypoxia on blood pressure, HR, and autonomic nervous system activity in conscious **(A–D)** and anesthetized animals **(E–H)**. **(A)** Schematic representation of the experimental protocol used to assess the effect of hypoxic hypoxia on physiological variables recorded in four conscious animals. Animals implanted with telemetry devices for blood pressure recording were submitted to 15 min of 10% O_2 (balanced N_2) after 30 min of baseline recording at normoxia (20% O_2 balanced N_2), $n = 4$. **(B)** Effect of hypoxic hypoxia on SBP, DBP, and MBP when compared with normoxia. **(C)** Effect of hypoxic hypoxia on HR ($n = 4$). **(D)** Effect of 15 min exposure to hypoxic hypoxia on autonomic function assessed by spectral analysis of HR. The left panel shows control examples of power spectral density in normoxia, $n = 4$ (top), and hypoxia, $n = 3$ (bottom). Frequencies are presented in normalized units. The right panel shows mean values of autonomic function assessed by the ratio between the percentage of Lf that represents the sympathetic component of the autonomic nervous system and the percentage of Hf that represents the parasympathetic component of the autonomic nervous system. **(E)** Schematic representation of the experimental protocol used to assess the effect of ischemic hypoxia on anesthetized animals. **(F)** Typical blood pressure responses to ischemic hypoxia assessed as OCC of 5 (top) and 15 s (bottom) of intensities. **(G)** Effect of 5 and 15 s OCC on MBP ($n = 14$). **(H)** Effect of 5 and 15 s of ischemic hypoxia on HR (left panel), on the RR intervals (middle panel), and autonomic function assessed by the spectral analysis of the HR and expressed as the ratio between the Lf and Hf of the spectra (right panel) ($n = 7$). Bars represent mean ± SEM. Shapiro–Wilk normality tests were performed, and all groups passed normality test. Whenever two groups were compared, two-tailed Student's *t*-test was executed **(C,D)**, and when more than two groups were compared, two-way ANOVA with Bonferroni's multiple comparison test was performed **(B,G,H)**; $^{*}p < 0.05$, $^{**}p < 0.01$, $^{****}p < 0.0001$ comparing values before and after the OCC.

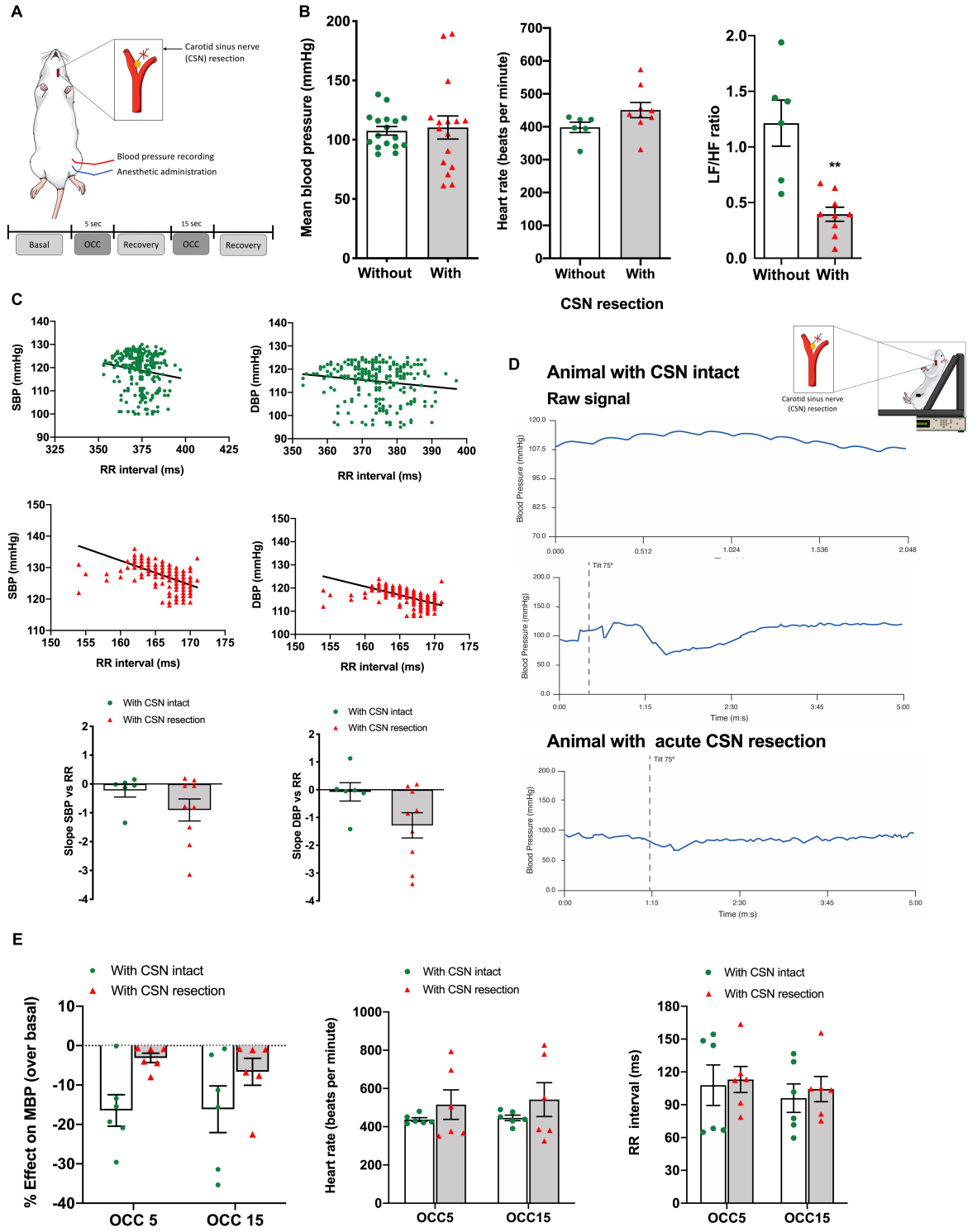

FIGURE 2 | Effect of CSN acute resection on blood pressure, HR, autonomic function, baroreflex sensitivity, and blood pressure responses in basal conditions and in response to ischemic hypoxia in anesthetized animals. **(A)** Schematic representation of the protocol used to assess the impact of CSN on the physiological variables evaluated in basal conditions (normoxic atmosphere) and in response to ischemic hypoxia assessed as OCC of 5 and 15 s, **(B)** respectively, from left to right, the effect of bilateral CSN denervation on MBP (left panel), HR (middle panel), and autonomic function (right panel) assessed by the spectral analysis of the HR and expressed as the ratio between the Lf and Hf of the spectra in anesthetized rats (control; n = 17; CSN denervated, n = 16). **(C)** Top graphs show representative SBP and DBP correlations with the RR intervals in rats with CSN intact (green, n = 6) and with CSN resection (red, n = 9) obtained in the experimental setting shown in **(A)**.

(Continued)

FIGURE 2 | Graphs on the bottom show the mean values of the slope of the correlations between SBP and DBP and RR intervals. **(D)** Typical response to a tilt test in conscious animals implanted with telemetry devices for blood pressure recording. Top panel shows raw signal of MBP in a rat with CSN intact. Middle and bottom panels show, respectively, a tilt test performed in a rat with CSN intact and with bilateral resection of the CSN. **(E)** Effect of CSN denervation on MBP (left panel), HR (middle panel), and RR intervals (right panel in response to ischemic hypoxia of 5 and 15 s of intensity, $n = 6$). Bars represent mean ± SEM. Shapiro–Wilk normality tests were performed, and all groups passed normality test. Two-tailed Student's *t*-test was accomplished **(B,C)** when comparing values with and without CSN denervation. When more than two groups were compared, two-way ANOVA with Bonferroni multicomparison test was performed **(E)**; $^{**}p < 0.01$.

line, hypoxic hypoxia did not modify HR ($n = 4$; **Figure 1C**). In contrast, hypoxia increased the Lf band in the power spectrum of the HR variability (**Figure 1D**, left panel) as shown by a 305% increase in the Lf/Hf cardiac index (Lf/Hf normoxia = 2.73 ± 0.21, $n = 4$; Lf/Hf hypoxia = 11.08 ± 0.60, $n = 3$, **Figure 1D**, right panel), meaning that acute hypoxia promoted an increase in cardiac SNS activity.

Figures 1E–H show the effect of ischemic hypoxia assessed by OCC during 5 and 15 s on blood pressure, HR, and cardiac autonomic function in anesthetized animals ($n = 7$). Ischemic hypoxia produced a transient increase in MBP followed by a hypotensive effect as shown in the typical recordings presented in **Figure 1F**. Whereas the hypotensive effect produced by the OCC5 was non-significant (MBP: before OCC5 = 125.61 ± 5.50 mmHg, OCC5 = 110.56 ± 4.87 mmHg, $n = 7$), OCC15 significantly decreased MBP by 14.27% (MBP: before OCC15 = 120.88 ± 5.46 mmHg, OCC15 = 103.65 ± 5.46 mmHg, $n = 7$) (**Figure 1G**). In agreement, OCC5 did not change HR or RR intervals although producing a non-significant increase in Lf/Hf cardiac index of 21.50%, whereas OCC15 produced a significant increase of 13.83% in HR, of 34.04% in RR intervals, and of 53.00% in the Lf/Hf cardiac index (**Figure 1H**).

Assessment of Blood Pressure and Heart Rate Regulation in Response to Hypoxia After Carotid Sinus Nerve Bilateral Denervation

Figure 2 depicts the effect of acute CSN resection (**Figure 2A**) on blood pressure and HR regulation in both baseline and response to ischemic hypoxia as well as the result of a single experiment on the effect of CSN resection on the baroreflex. Acute CSN bilateral resection did not modify either MBP (**Figure 2B**, MBP without CSN resection = 107.50 ± 3.65 mmHg, $n = 17$; MBP with CSN resection = 110.3 ± 9.71 mmHg, $n = 16$) or HR (HR without CSN resection = 398.1 ± 15.75 beats per min, $n = 17$; HR with CSN resection = 450.6 ± 22.92, $n = 16$) but decreased sympathetic activation as shown by a significant decrease in Lf/Hf cardiac index of 67.19% (**Figure 2B**). Top panels of **Figure 2C** shows representative correlations between SBP and DBP and the RR intervals in animals with the CSN intact (green) and animals with bilateral resection of the CSN (**Figure 2C**). CSN resection showed a tendency, although non-statistically significant, to alter the slope of the correlation between SBP and DBP and the RR intervals [slope SBP vs. RR without CSN resection = −0.22 ± 0.22, $n = 6$; slope SBP vs. RR with CSN resection = −0.90 ± 0.30, $n = 9$ ($p = 0.206$); slope DBP vs. RR without CSN resection = −0.07 ± 0.33, $n = 6$; slope DBP vs. RR with CSN resection = −1.28 ± 0.45, $n = 9$ ($p = 0.0748$)] suggesting that CSN denervated animals exhibit significantly altered baroreflex sensitivity. To clarify these findings, baroreflex sensitivity was evaluated by measuring blood pressure and RR interval variation during a postural challenge, the tilt test (**Figure 2D**). **Figure 2D** shows typical recordings of blood pressure in anesthetized rats with (bottom panel) and without (middle panel) CSN resection, submitted to a tilt test, in which the animal was suspended at an angle of 75° (middle panel). Note that CSN resection alters the variations in MBP produced by tilting the animal, suggesting altered baroreflex sensitivity caused by denervation of the CSN. The effect of CSN resection was tested also in the MBP, HR, and RR intervals in response to ischemic hypoxia. Acute CSN denervation attenuated the decrease in MBP produced by ischemic hypoxia of 5 and 15 s (**Figure 2E**, left panel) in a non-significant manner ($n = 6$) without altering either HR or RR intervals (**Figure 2E**, middle and right panels).

Assessment of Blood Pressure and Heart Rate Regulation in Response to Kilohertz Frequency Alternate Current Modulation of the Carotid Sinus Nerve

Figure 3 shows the effect of CSN electrical neuromodulation on respiratory frequency, blood pressure, and HR in normoxic conditions and response to hypoxic hypoxia in anesthetized animals (**Figure 3A**). Typical EMG recordings of respiratory frequency in response to hypoxic hypoxia, CSN stimulation, and CSN high frequency blocking are shown in **Figure 3B**. As expected, 1 min hypoxic hypoxia (10% O_2) significantly increased respiratory frequency by 47.66% (*normoxia* = 47.78 ± 4.28 bpm; *hypoxia* = 70.56 ± 4.98 bpm; $n = 6$) (**Figure 3C**). Electrical stimulation of the CSN significantly increased respiratory frequency, confirming that the electrodes were correctly placed (respiratory frequency 20 Hz = 116.70 ± 8.82 bpm, $n = 6$). As previously described (Sacramento et al., 2018) and as shown in **Figure 3C**, high frequency blocking of the CSN (50 kHz, 2 mA) did not modify respiratory frequency in normoxia (respiratory frequency 50 kHz = 51.67 ± 5.53 bpm, $n = 6$) but abolished the ventilatory hypoxic response (respiratory frequency 50 kHz + 10% O_2 = 53.33 ± 4.91 bpm, $n = 6$). Hypoxic hypoxia applied for 1 min decreased MBP by 53.6% (normoxic MBP = 100.8 ± 8.56 mmHg: hypoxia MBP = 46.77 ± 8.15 mmHg, $n = 6$, **Figure 3D**). Likewise, stimulation of CSN with 20 Hz frequency produced a decrease in blood pressure of 24.1% (MBP 20 Hz = 65.0 ± 11.92 mmHg) (**Figure 3D**). Similarly, to the effect of high frequency blocking on respiratory frequency, electrical blocking of the CSN blocking did not modify MBP

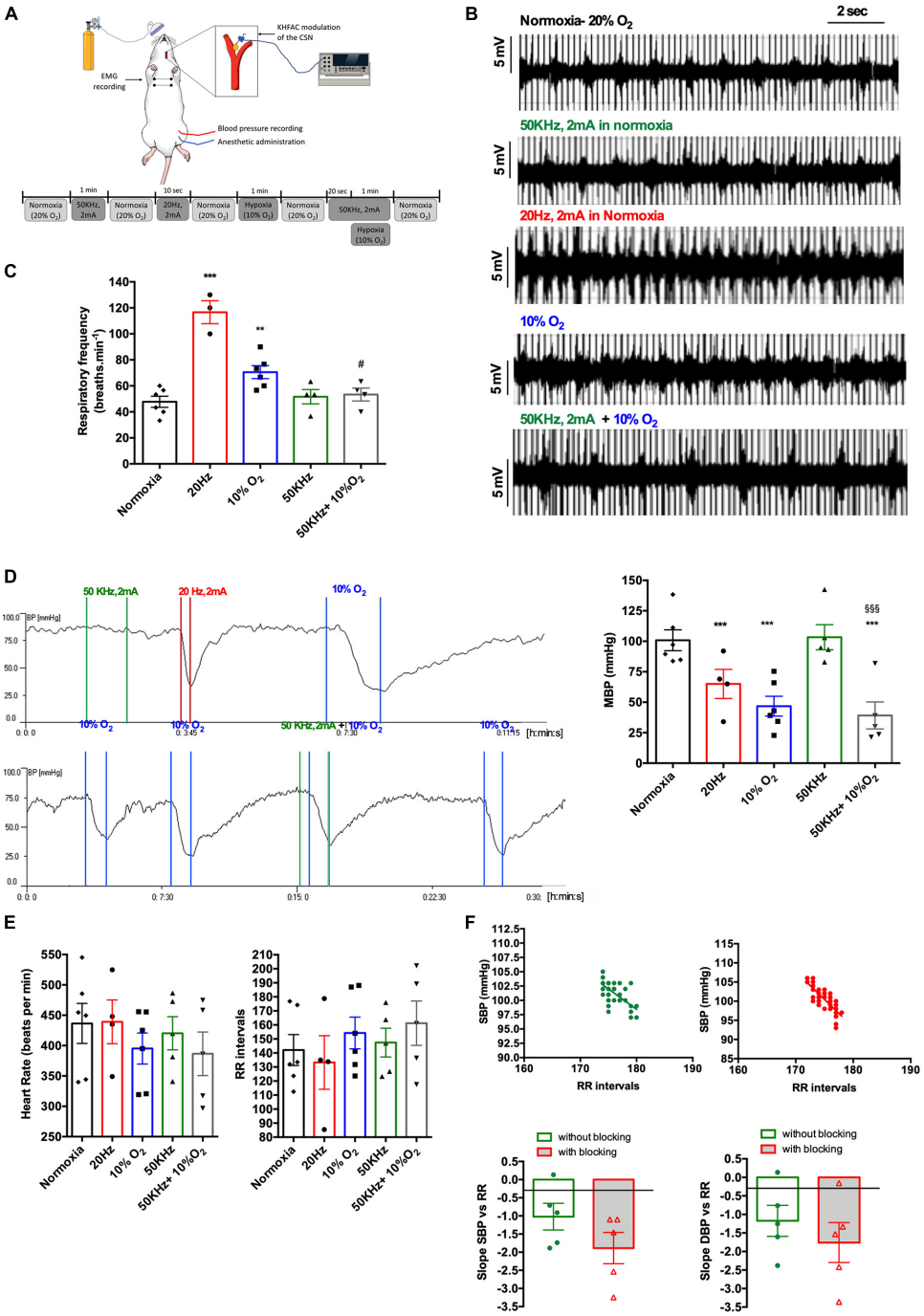

FIGURE 3 | Effect of acute CSN electrical modulation on baseline cardiorespiratory variables and the cardiorespiratory response to hypoxic hypoxia in anesthetized rats. **(A)** Schematic representation of the experimental setting and protocol used to evaluate the effect of electrical blocking of the CSN on the physiological variables; **(B)** panel shows, respectively, from top to bottom, EMG representative recordings of animals in normoxia (n = 6; 20% O_2 balanced N_2), under electrical blocking (n = 6; 50 kHz, 2 mA, 1 min), under electrical stimulation (n = 6, 20 Hz, 2 mA, 10 s), in response to hypoxia (n = 6, 10% O_2 balanced N_2, 1 min), and under electrical block plus hypoxia (n = 6; 50 kHz, 2 mA plus 10% O_2). **(C)** Shows the effect of CSN neuromodulation–stimulation (20 Hz, 2 mA, 10 s, n = 4) and blocking (50 kHz, 2 mA, 1 min, n = 4) on baseline respiratory frequency and respiratory frequency evoked by hypoxic hypoxia (10% O_2 balanced N_2, 1 min, n = 6) expressed as bpm. **(D)** Left panel shows a typical recording of the effect of electrical blocking (50 kHz, 2 mA, 1 min) and stimulation (20 Hz, 2 mA, 10 s) of the CSN and the effect of hypoxic hypoxia (10% O_2 balanced N_2, 1 min) on MBP measured at the femoral artery. Right panel show the mean values for the effect of electrical blocking on MBP in normoxia and hypoxia. Note that electrical blocking did not modify MBP and that CSN stimulation elicited a hypotensive response such as the produced by hypoxic hypoxia. The panel at the bottom shows the effect of blocking (50 kHz, 2 mA, 1 min) on MBP response to hypoxic hypoxia (10% O_2 balanced N_2, 1 min). Note that electrical blocking of CSN does not seem to affect blood pressure response to hypoxic hypoxia. CSN electrical modulation was applied bilaterally to the CSN through

(Continued)

FIGURE 3 | electrode cuffs. Stimuli were applied between colored lines, and colors represent, respectively, green—electrical blocking (50 kHz, 2 mA, 1 min), red—electrical stimulation (20 KHz, 2 mA, 10 s), and blue—hypoxic hypoxia (10% O_2 balanced N_2, 1 min). To test CSN electrical blocking plus hypoxia, the current was initiated 30 s before submitting the animals to hypoxia. **(E)** Effect of CSN neuromodulation–stimulation (20 Hz, 2 mA, 10 s, $n = 4$) and blocking (50 kHz, 2 mA, 1 min, $n = 4$) and hypoxia ($n = 6$) on HR and RR intervals. **(F)** Top panel shows correlations between SBP and RR intervals in animals without CSN electrical blocking (green, $n = 6$) and when submitted to electrical blocking (red, $n = 6$). Correlations were performed with values obtained during 1 min at a sampling rate of 1,000 Hz. Bottom panels show the impact of electrical neuromodulation of the CSN on the mean values of the slope of the correlations between SBP and DBP and RR intervals. Bars represent mean ± SEM. Shapiro–Wilk normality tests were performed, and all groups passed normality test. One-way ANOVA with Bonferroni's multiple comparisons test was executed in series depicted in **(C–E)**; $^{**}p < 0.01$, $^{***}p < 0.001$ vs. normoxia; $^{\#}p < 0.05$, $^{\$\$\$}p < 0.001$ vs. hypoxia. Whenever two groups were compared a two-tailed Student's *t*-test was performed **(F)**.

in normoxia (MBP 50 KHz = 103.3 ± 10.29 mmHg, $n = 6$, **Figure 3D**). In contrast, it did not produce any alteration in MBP in response to hypoxic hypoxia (MBP 50 KHz + 10% O_2 = 39.14 ± 11.09, **Figure 3D**), indicating a possible decoupling of CB-mediated ventilatory and blood pressure responses to hypoxia. Note also that the high frequency blocking of the CSN did not modify both HR and the RR intervals (**Figure 3E**). The effect of electrical blocking was also tested on the correlations between SBP and DBP and the RR intervals (**Figure 3F**). The top panel of **Figure 3F** shows correlations between SBP and RR intervals in CSN without electrical stimulation (green) and when the animals were submitted to electrical blocking for 1 min (red) (**Figure 3F**, top panel). High frequency electrical blocking of the CSN did not change the correlation between SBP and DBP and the RR intervals [slope SBP vs. RR without CSN blocking = −1.02 ± 0.37; slope SBP vs. RR with CSN electrical blocking = −1.89 ± 0.43 ($n = 6$, $p = 0.17$); slope DBP vs. RR without CSN electrical blocking = −1.173 ± 0.342; slope DBP vs. RR with CSN resection = −1.759 ± 0.54 ($n = 6$, $p = 0.42$)].

DISCUSSION

This study assessed the impact of the CSN in systemic blood pressure under normoxic and hypoxic conditions, aiming for a better understanding of the crosstalk between the chemoreceptors and blood pressure control systems. Our study confirms that functional ablation of the CSN, either surgically or through electrical neuromodulation, does not significantly influence baseline hemodynamic parameters nor blood pressure modulation by hypoxic/ischemic challenges despite a decreased sympathetic tone induced by loss of CSN function. We hypothesize that bilateral denervation/electrical blockade of the CSN and subsequent abolition of CB afferent chemoreflex and carotid-sinus baroreflex are compensated by redundant mechanisms that respond to acute changes in blood gases, independently of the autonomic resetting that occurs upon hindrance of CSN transmission.

It was previously shown that that baseline values of respiratory and cardiovascular parameters do not differ before and after unilateral chemoreceptor deactivation through ligation and sectioning of the left CB artery for Katayama et al. (2019).

The same authors observed that unilateral electrical stimulation of the carotid sinus and the CSN activates both the carotid baroreflex and chemoreflex as previously described (Gonzalez et al., 1994; Marshall, 1994, 1998), resulting in hypotension in conscious animals (Katayama et al., 2015). Additionally, it was also demonstrated that the hypotensive response after electrical stimulation of the carotid sinus was enhanced by carotid chemoreceptor deactivation (Katayama et al., 2015), suggesting that an intact bilateral chemoreflex counteracts the hypotensive effects carotid sinus stimulation.

Herein, we performed bilateral surgical or electrical ablation of the CSN, thus preventing complete conveying of the information from carotid chemo and baroreceptors to the central nervous system, and we observed no changes in blood pressure or HR despite a significant decrease in cardiac sympathetic activity in both normoxic and hypoxic conditions.

Looking at the correlation between the SBP and DBP and RR intervals, we observed no significant differences between the slopes, suggesting that CSN resection does not affect the feedback loop among blood pressure and HR in basal conditions. Pijacka et al. (2018) report that CSN denervation resulted in abolishment of the baroreceptor reflex, which was not perceivable after selective CB resection. The single experiment we performed in a CSN-resected animal submitted to a head-up tilt test showed a less pronounced drop in blood pressure when comparing the pre-denervation period with the post-denervation period, indicating that despite causing no significant changes in systemic blood pressure control, CSN-denervated animals may present an impaired hemodynamic response to head-up tilting, also observed by Pijacka et al. (2018).

Immediate cardiovascular responses to acute hypoxia are known to be species-dependent, primarily mediated by the aortic bodies with a smaller contribution of the CB and followed by hypoxic vasodilatory response controlled by local autoregulatory mechanisms at peripheral vascular beds (Marshall, 1998; Rohlicek et al., 2002; Cowburn et al., 2017). In humans, CBs play a critical role in adapting ventilation and maintaining arterial pressure during hypoxia, whereas the HR response is mainly mediated by aortic bodies (Niewinski et al., 2014; Pijacka et al., 2018). In anesthetized rats, hypoxic hypoxia (10% O_2 in N_2), which stimulates both CBs and aortic bodies, and carbon monoxide hypoxia (30% O_2 in N_2 with CO addition) that stimulates only the aortic bodies, induced an increase in cardiac output, cardiac contractility, SBP/DBP, aortic blood pressure, total peripheral resistance, and pulmonary arterial pressure (Fitzgerald et al., 2013) with the CBs having a higher effect in the majority of these variables except for blood pressure—whose major control seems to be assured by the aortic bodies (Fitzgerald et al., 2013). In contrast, sustained or chronic hypoxia leads to distinct ventilatory and hemodynamic responses that are not easily attributed to chemoreflex or baroreflex independently and involve resetting of the feedback loops (Niewinski et al., 2014;

Lohmeier et al., 2016; Pijacka et al., 2018). However, the relation of the CBs with sympathetic tone is irrefutable in either acute conditions or response to chronic stimuli (Prabhakar et al., 2005; McBryde et al., 2017; Sacramento et al., 2020) with a clear involvement of these organs in long-term increase in sympathetic vasoconstrictor outflow in several disease states (Conde et al., 2014; Pijacka et al., 2018).

Herein, we observed no significant effects of acute hypoxic hypoxia in baseline hemodynamic parameters in conscious animals implanted with continuous blood pressure monitoring telemeters although there was a significant activation of the SNS as assessed by HR variability analysis. In a setting of ischemic hypoxia, we also observed no changes in blood pressure although there was an increase in sympathetic activation, significant only for a 15-s ischemia period.

To assess the role of the CB chemoreceptors in acute blood pressure control in response to hypoxia, we surgically denervated the CSN and evaluated acute changes in BP, sympathetic activity in hypoxic hypoxia conditions. We observed that blood pressure was not significantly modified in acutely CSN denervated animals, but the increase in SNS activity in response to ischemic hypoxia was lost in animals submitted to CSN denervation. Acute CSN resection also diminished the hypotensive effect evoked by hypoxia. In these animals, the decrease in BP in response to hypoxia was lower than in animals with intact CSN. To confirm these findings, we functionally abolished CSN activity by KHFAC (50 kHz, 2 mA) and observed that neither baseline blood pressure nor the adaptive blood pressure response to hypoxic hypoxia was affected by the electrical blockade. Our results support that functional or surgical blockade of the CSN does not impact basal blood pressure or basal ventilation in contrast to electrical stimulation of the CSN that mimics the ventilatory and hemodynamic responses evoked by hypoxic and ischemic hypoxia.

We concluded that, in acute settings, the chemoreflex and baroreflex control of blood pressure are dissociated in terms of hypoxic response but integrated to generate an effector response to a given change in arterial pressure. Chemoreceptor activation caused by acute hypoxic or ischemic hypoxia increased sympathetic activity in both conscious and anesthetized animals. However, baseline blood pressure was not affected by acute hypoxia except for sustained hypoxic challenges, namely, OCC for 15 s, indicating that hemodynamic compensatory regional mechanisms triggered by acute hypoxia are effective in maintaining blood pressure for short-term stimuli but not for longer challenges. Paton's group recently reported that CSN sparing selective ablation of the CBs assures functional integrity of the carotid sinus baroreceptors in spontaneously hypertensive rats, demonstrating the importance of CBs in the hemodynamic response to hypoxia and hypercapnia in hypertension (Pijacka et al., 2018). Regarding the contribution of the CB to the development and maintenance of hypertension, our work agrees with previous results obtained by other groups in which it was observed that carotid sinus denervation prevented arterial pressure from reaching hypertensive levels and decreased sympathetic activity in spontaneous hypertensive young rats (Pijacka et al., 2018).

To conclude, chemoreflex and baroreflex short-term regulation of blood pressure are dissociated in terms of hypoxic response but integrated to generate an effector response to a given change in arterial pressure. Based on our findings, we postulate that the clinical use of Hf stimulation to modulate CSN activity is devoid of hypoxic-induced pressure fluctuations.

DATA AVAILABILITY STATEMENT

The raw data supporting the conclusions of this article will be made available by the authors upon request, without undue reservation.

ETHICS STATEMENT

The animal study was reviewed and approved by the Animal Welfare Body of Faculdade de Ciências Médicas | Nova Medical School and by the Direcção Geral de Veterenária (DGAV), Portugal.

AUTHOR CONTRIBUTIONS

SC, MG, and MR-O designed the experiments. SC, JS, BM, and MG performed the experiments. SC, JS, BM, MG, RF-P, and MR-O analyzed the data. SC, BM, RF-P, and MG contributed to manuscript preparation. SC and MG wrote the manuscript. All authors reviewed and accepted the manuscript.

FUNDING

This study was partially supported by the GlaxoSmithKline Bioelectronics R&D –Innovation Challenge. JS and BM were supported by a contract and a Ph.D. Grant from the Portuguese Foundation for Science and Technology Reference CEECIND/02428/2018 and PD/BD/128336/2017, respectively. This study received funding from the Fundação para a Ciência e Tecnologia (FCT) (UIDB/05704/2020).

REFERENCES

Abdala, A. P., McBryde, F. D., Marina, N., Hendy, E. B., Engelman, Z. J., Fudim, M., et al. (2012). Hypertension is critically dependent on the carotid body input in the spontaneously hypertensive rat. *J. Physiol.* 590, 4269–4277. doi: 10.1113/jphysiol.2012.237800

Aubert, A. E., Ramaekers, D., Beckers, F., Breem, R., Denef, C., Van de Werf, F., et al. (1999). The analysis of heart rate variability in unrestrained rats. Validation

of method and results. *Comput. Methods Programs Biomed.* 60, 197–213. doi: 10.1016/s0169-2607(99)00017-6

Chapleau, M. W., Li, Z., Meyrelles, S. S., Ma, X., and Abboud, F. M. (2001). Mechanisms determining the Physiolisvity of baroreceptor afferents in health and disease. *Ann. N. Y. Acad. Sci.* 940, 1–19. doi: 10.1111/j.1749-6632.2001.tb03662.x

Conde, S. V. (2018). Ablation of the carotid bodies in disease: meeting its adverse effects. *J. Physiol.* 596:2955. doi: 10.1113/JP275796

Conde, S. V., Sacramento, J. F., and Martins, F. O. (2020). Immunity and the carotid body: implications for metabolic diseases. *Bioelectron. Med.* 6:24. doi: 10.1186/s42234-020-00061-5

Conde, S. V., Sacramento, J. F., Guarino, M. P., Gonzalez, C., Obeso, A., Diogo, L. N., et al. (2014). Carotid body, insulin, and metabolic diseases: unraveling the links. *Front. Physiol.* 5:418. doi: 10.3389/fphys.2014.00418

Cowburn, A. S., Macias, D., Summers, C., Chilvers, E. R., and Johnson, R. S. (2017). Cardiovascular adaptation to hypoxia and the role of peripheral resistance. *Elife* 6:e28755.

Del Rio, R., Marcus, N. J., and Schultz, H. D. (2013). Carotid chemoreceptor ablation improves survival in heart failure: rescuing autonomic control of cardiorespiratory function. *J. Am. Coll. Cardiol.* 62, 2422–2430. doi: 10.1016/j.jacc.2013.07.079

Fitzgerald, R. S., Dehghani, G. A., and Kiihl, S. (2013). Autonomic control of the cardiovascular system in the cat during hypoxemia. *Auton. Neurosci.* 174, 21–30. doi: 10.1016/j.autneu.2012.11.005

Fonseca-Pinto, R. (2011). "A new tool for nonstationary and nonlinear signals: the Hilbert-Huang transform in biomedical applications, biomedical engineering," in *Trends in Electronics, Communications and Software*, ed. A. Laskovski (London: InTech), 481–504.

Gonzalez, C., Almaraz, L., Obeso, A., and Rigual, R. (1994). Carotid body chemoreceptors: from natural stimuli to sensory discharges. *Physiol. Rev.* 74, 829–898. doi: 10.1152/physrev.1994.74.4.829

Irigoyen, M. C., Moreira, E. D., Cestari, I. A., and Krieger, E. M. (1991). The relationship between renal sympathetic nerve activity and arterial pressure after selective denervation of baroreceptors and chemoreceptors. *Braz. J. Med. Biol. Res.* 24, 219–222.

Katayama, P. L., Castania, J. A., Dias, D. P., Patel, K. P., Fazan, R. Jr., and Salgado, H. C. (2015). Role of chemoreceptor activation in hemodynamic responses to electrical stimulation of the carotid sinus in conscious rats. *Hypertension* 66, 598–603. doi: 10.1161/HYPERTENSIONAHA.115.05316

Katayama, P. L., Castania, J. A., Fazan, R. Jr., and Salgado, H. C. (2019). Interaction between baroreflex and chemoreflex in the cardiorespiratory responses to stimulation of the carotid sinus/nerve in conscious rats. *Auton. Neurosci.* 216, 17–24. doi: 10.1016/j.autneu.2018.12.001

Kougias, P., Weakley, S. M., Yao, Q., Lin, P. H., and Chen, C. (2010). Arterial baroreceptors in the management of systemic hypertension. *Med. Sci. Monit.* 16, RA1–RA8.

Limberg, J. K., Dube, S., Kuijpers, M., Farni, K. E., Basu, A., Rizza, R. A., et al. (2015). Effect of hypoxia on heart rate variability and baroreflex sensitivity during hypoglycemia in type 1 diabetes mellitus. *Clin. Auton. Res.* 25, 243–250. doi: 10.1007/s10286-015-0301-2

Lohmeier, T. E., Iliescu, R., Tudorancea, I., Cazan, R., Cates, A. W., Georgakopoulos, D., et al. (2016). Chronic interactions between carotid baroreceptors and chemoreceptors in obesity hypertension. *Hypertension* 68, 227–235. doi: 10.1161/HYPERTENSIONAHA.116.07232

Marshall, J. M. (1994). Peripheral chemoreceptors and cardiovascular regulation. *Physiol. Rev.* 74, 543–594. doi: 10.1152/physrev.1994.74.3.543

Marshall, J. M. (1998). Chemoreceptors and cardiovascular control in acute and chronic systemic hypoxia. *Braz. J. Med. Biol. Res.* 31, 863–888. doi: 10.1590/s0100-879x1998000700002

McBryde, F. D., Abdala, A. P., Hendy, E. B., Pijacka, W., Marvar, P., Moraes, D. J., et al. (2013). The carotid body as a putative therapeutic target for the treatment of neurogenic hypertension. *Nat. Commun.* 4:2395. doi: 10.1038/ncomms3395

McBryde, F. D., Hart, E. C., Ramchandra, R., and Paton, J. F. (2017). Evaluating the carotid bodies and renal nerves as therapeutic targets for hypertension. *Auton. Neurosci.* 204, 126–130. doi: 10.1016/j.autneu.2016.08.002

Niewinski, P., Janczak, D., Rucinski, A., Tubek, S., Engelman, Z. J., Jazwiec, P., et al. (2014). Dissociation between blood pressure and heart rate response to hypoxia after bilateral carotid body removal in men with systolic heart failure. *Exp. Physiol.* 99, 552–561. doi: 10.1113/expphysiol.2013.075580

Paton, J. F., Sobotka, P. A., Fudim, M., Engelman, Z. J., Hart, E. C., McBryde, F. D., et al. (2013). The carotid body is a therapeutic target for the treatment of sympathetically mediated diseases. *Hypertension* 61, 5–13. doi: 10.1161/HYPERTENSIONAHA.111.00064

Pijacka, W., Katayama, P. L., Salgado, H. C., Lincevicius, G. S., Campos, R. R., McBryde, F. D., et al. (2018). Variable role of carotid bodies in cardiovascular responses to exercise, hypoxia and hypercapnia in spontaneously hypertensive rats. *J. Physiol.* 596, 3201–3216. doi: 10.1113/JP275487

Prabhakar, N. R., and Peng, Y. J. (2004). Peripheral chemoreceptors in health and disease. *J. Appl. Physiol.* 96, 359–366. doi: 10.1152/japplphysiol.00809.2003

Prabhakar, N. R., Peng, Y. J., Jacono, F. J., Kumar, G. K., and Dick, T. E. (2005). Cardiovascular alterations by chronic intermittent hypoxia: importance of carotid body chemoreflexes. *Clin. Exp. Pharmacol. Physiol.* 32, 447–449. doi: 10.1111/j.1440-1681.2005.04209.x

Ribeiro, M. J., Sacramento, J. F., Gonzalez, C., Guarino, M. P., Monteiro, E. C., and Conde, S. V. (2013). Carotid body denervation prevents the development of insulin resistance and hypertension induced by hypercaloric diets. *Diabetes* 62, 2905–2916. doi: 10.2337/db12-1463

Rohlicek, C. V., Matsuoka, T., and Saiki, C. (2002). Cardiovascular response to acute hypoxemia in adult rats hypoxemic neonatally. *Cardiovasc. Res.* 53, 263–270. doi: 10.1016/s0008-6363(01)00475-8

Sacramento, J. F., Andrzejewski, K., Melo, B. F., Ribeiro, M. J., Obeso, A., and Conde, S. V. (2020). Exploring the mediators that promote carotid body dysfunction in type 2 diabetes and obesity related syndromes. *Int. J. Mol. Sci.* 21:5545. doi: 10.3390/ijms21155545

Sacramento, J. F., Chew, D. J., Melo, B. F., Donegá, M., Dopson, W., Guarino, M. P., et al. (2018). Bioelectronic modulation of carotid sinus nerve activity in the rat: a potential therapeutic approach for type 2 diabetes. *Diabetologia* 61, 700–710. doi: 10.1007/s00125-017-4533-7

Sacramento, J. F., Ribeiro, M. J., Rodrigues, T., Olea, E., Melo, B. F., Guarino, M. P., et al. (2017). Functional abolition of carotid body activity restores insulin action and glucose homeostasis in rats: key roles for visceral adipose tissue and the liver. *Diabetologia* 60, 158–168. doi: 10.1007/s00125-016-4133-y

Schultz, H. D., Marcus, N. J., and Del Rio, R. (2013). Role of the carotid body in the pathophysiology of heart failure. *Curr. Hypertens. Rep.* 15, 356–362.

Silva, L. E. V., Geraldini, V. R., De Oliveira, B. P., Silva, C. A. A., Porta, A., and Fazan, R. (2017). Comparison between spectral analysis and symbolic dynamics for heart rate variability analysis in the rat. *Sci. Rep.* 7:8428. doi: 10.1038/s41598-017-08888-w

Thireau, J., Zhang, B. L., Poisson, D., and Babuty, D. (2008). Heart rate variability in mice: a theoretical and practical guide. *Exp. Physiol.* 93, 83–94. doi: 10.1113/expphysiol.2007.040733

Conflict of Interest: Part of this study, in particular **Figures 1**, **3** were funded by GlaxoSmithKline Bioelectronics R&D unit. The funder had the following involvement with the study: decision to publish.

The authors declare that the research was conducted in the absence of any commercial or financial relationships that could be construed as a potential conflict of interest.

frontiers in Neuroscience

ORIGINAL RESEARCH
published: 17 February 2022
doi: 10.3389/fnins.2022.816106

The Effect of Non-invasive Spinal Cord Stimulation on Anorectal Function in Individuals With Spinal Cord Injury: A Case Series

*Evgeniy Kreydin[1,2,3], Hui Zhong[2,4], Igor Lavrov[5,6], V. Reggie Edgerton[4,7,8,9] and Parag Gad[2,3,4]**

[1] Keck School of Medicine, Institute of Urology, University of Southern California, Los Angeles, CA, United States, [2] Rancho Los Amigos National Rehabilitation Center, Rancho Research Institute, Downey, CA, United States, [3] SpineX Inc., Los Angeles, CA, United States, [4] Department of Neurobiology, University of California, Los Angeles, Los Angeles, CA, United States, [5] Department of Neurology, Department of Biomedical Engineering, Mayo Clinic, Rochester, NY, United States, [6] Institute of Fundamental Medicine and Biology, Kazan Federal University, Kazan, Russia, [7] Department of Neurosurgery, University of California, Los Angeles, Los Angeles, CA, United States, [8] Brain Research Institute, University of California, Los Angeles, Los Angeles, CA, United States, [9] Institut Guttmann, Hospital de Neurorehabilitació, Institut Universitari Adscrit a la Universitat Autònoma de Barcelona, Barcelona, Spain

OPEN ACCESS

Edited by:
Arun Sridhar, Independent Researcher, Milton Keynes, United Kingdom

Reviewed by:
Victor Pikov, Medipace Inc., United States
Robert A. Gaunt, University of Pittsburgh, United States

***Correspondence:**
Parag Gad
paraggad@ucla.edu

Specialty section:
This article was submitted to Autonomic Neuroscience, a section of the journal Frontiers in Neuroscience

Received: 16 November 2021
Accepted: 20 January 2022
Published: 17 February 2022

Citation:
Kreydin E, Zhong H, Lavrov I, Edgerton VR and Gad P (2022) The Effect of Non-invasive Spinal Cord Stimulation on Anorectal Function in Individuals With Spinal Cord Injury: A Case Series. Front. Neurosci. 16:816106. doi: 10.3389/fnins.2022.816106

Spinal cord injury (SCI) is a devastating condition that impacts multiple organ systems. Neurogenic bowel dysfunction (NBD) frequently occurs after a SCI leading to reduced sensation of bowel fullness and bowel movement often leading to constipation or fecal incontinence. Spinal Neuromodulation has been proven to be a successful modality to improve sensorimotor and autonomic function in patients with spinal cord injuries. The pilot data presented here represents the first demonstration of using spinal neuromodulation to activate the anorectal regions of patients with spinal cord injuries and the acute and chronic effects of stimulation. We observed that spinal stimulation induces contractions as well as changes in sensation and pressure profiles along the length of the anorectal region. In addition, we present a case report of a patient with a SCI and the beneficial effect of spinal neuromodulation on the patient's bowel program.

Keywords: non-invasive spinal cord stimulation, spinal cord injury, stroke, multiple sclerosis, neurogenic bladder, overactive bladder urodynamics

INTRODUCTION

Neurogenic bowel dysfunction (NBD) is a significant source of morbidity after a spinal cord injury (SCI). After an SCI, many patients develop the inability to empty the bowels spontaneously and become reliant on onerous and time-consuming bowel programs to manage constipation and stool retention. Others may develop stool incontinence secondary to obstipation or anal sphincter weakness. As a result, NBD has a marked deleterious effect on patients' health and quality of life. Indeed, several survey studies of SCI patients have demonstrated that recovery of bowel function is one of the top rehabilitation priorities in this population (Anderson, 2004; Bloemen-Vrencken et al., 2005; Ditunno et al., 2008).

Despite such significant impact on a patient's life, treatment options for NBD are limited. Rectal suppositories and oral stool softeners and laxatives are the mainstays of therapy but have

a limited efficacy in decreasing the time devoted to bowel programs and do little to normalize bowel function and stool transit. Surgical interventions, such as creation of colostomy or Malone Antegrade Continence Enema (MACE) are morbid and can have a negative impact on an already-impaired body image in patients with SCI (Waddell et al., 2020). More recently, neuromodulation has begun to be explored as a therapy for NBD. Techniques such as functional electrical stimulation, magnetic stimulation, sacral nerve stimulation, dorsal genital nerve stimulation and transcutaneous interferential electrical stimulation have been attempted as a therapy for NBD in adults (SCI) and children (myelomeningocele) with promising results (Deng et al., 2018; Parittotokkaporn et al., 2020).

We have developed and implemented a novel Spinal Cord Neuromodulator (SCONE^{TM}, SpineX Inc., Los Angeles, CA, United States) as a non-invasive stimulation modality to facilitate functional recovery after SCI. This approach delivers an electrical stimulation to the spinal cord without eliciting significant cutaneous discomfort by incorporating a high-frequency carrier current. We have previously demonstrated that non-invasive spinal cord neuromodulation can improve lower (Gad et al., 2015; Gerasimenko Y. P. et al., 2015; Parag Gad and Reggie Edgerton, 2019), upper extremity (Gad P. et al., 2018; Inanici et al., 2018), trunk stability (Rath et al., 2018), respiratory (Gad et al., 2020) and lower urinary tract function (Gad P. N. et al., 2018; Kreydin et al., 2020; Gad et al., 2021b) in patients with SCI. In this study, we used anorectal manometry (ARM) to determine the effect of acute SCONE^{TM} stimulation on anorectal physiology in three chronically paralyzed patients and the effect of chronic stimulation on bowel program times in one patient.

MATERIALS AND METHODS

Patient Recruitment

This study was approved by the Institutional Review Board of Rancho Research Institute, the research arm of Rancho Los Amigos National Rehabilitation Center, Downey, CA, United States. The research participants signed an informed consent form before the start of the study and consented to the data being used in future publications and presentations. The patient demographics and injury characteristics were as follow: Acute Stimulation Patient 1 (ASP1) was a 39-year-old male who sustained a SCI at C5 (AIS A) 9 years prior to study. ASP2 was a 29-year-old male who sustained a SCI at T6 (AIS A) 5 years prior to the study. ASP3 was a 28-year-old female who sustained a SCI at T6 (AIS A) 2 years prior to the study. Finally, the patient who underwent chronic stimulation [Chronic Stimulation Patient 1 (CSP1)] was a 32-year-old female who sustained a SCI at T6 (AIS A) 2 years prior to the study.

Spinal Stimulation

Spinal stimulation was delivered using a proprietary SCONE^{TM} device (SpineX Inc., Los Angeles, CA, United States). The stimulation was delivered either as single test pulses or as therapeutic pulses. The test pulse waveform consisted of a monophasic pulse at 0.5 Hz with a high frequency carrier frequency (10 KHz) with a pulse width of 1 ms. The therapeutic waveform consisted of two alternating pulses of opposite polarities separated by a 1 uS delay forming a delayed biphasic waveform. The pulses consisted of a high frequency biphasic carrier pulse (10 KHz) combined with a low frequency (30 Hz) burst pulse each with a pulse width of 1 ms. Stimulation was applied using an adhesive electrode over the interspinous ligaments of T11 and L1 serving as the cathode and two adhesive electrodes over the iliac crests as the anodes (**Figure 1**). The intensity of stimulation during acute mapping studies (0.5 Hz) were set at a supra sensory and motor threshold, i.e., the lowest intensity at which contractions were visible on the pressure probes. At this intensity all patients also noted contractions of several lower extremity muscles. The intensity of stimulation during therapeutic stimulation (30 Hz) was set at a supra-sensory and sub-motor threshold level, i.e., at 80% of the intensity that generated a visible contraction on the pressure probes. At this intensity, patients could feel the stimulation but did not note any lower extremity muscles contractions and tolerated the stimulation well.

Anorectal Manometry and Mapping

Acute stimulation patients were asked to perform an enema at home at least 6 h prior to the study. Anorectal manometry (ARM) probe was placed in the anorectal region. The probe consisted of four sensors around the periphery of the tip. A balloon was positioned at the proximal end of the catheter. The anorectum was mapped by positioning the catheter at specific distances from the anal verge starting at 2 cm and continuing up to 10 cm in increments of 1 cm. At each catheter location, stimulation test pulses were delivered starting at 10 mA and increasing to 200 mA in increments of 10 mA. A minimum of five pulses were delivered at each intensity. A minimum of 3 mins pause was taken prior to moving the catheter to the next position. Anorectal profiles were created by slowly withdrawing the catheter at a constant speed of 0.5–1 cm/s. These profiles were created with the patient in a relaxed position (relax) and while attempting to generate a bowel movement (squeeze) on command. Following test stimulation, tonic submotor stimulation was applied and anorectal pressure profiles were generated in an identical manner. Finally, to test anorectal sensation, the catheter was placed at 5 cm from the anal verge, the balloon was slowly filled with air using an external syringe at a rate of 60 ml/min without and with sub-motor threshold stimulation. The patient was asked to report when they experienced rectal sensation and the 1st volume, at which this occurred, was recorded.

Chronic Spinal Stimulation

The chronic stimulation patient (CSP1) was recruited to study the effect of chronic spinal stimulation on bowel function. This patient needed external digital stimulation to assist bowel movement and relied on rectal suppositories to move her bowels every 1–2 days. She was asked to monitor the duration of her bowel program for the duration of the study. The therapeutic waveform consisted of two alternating pulses of

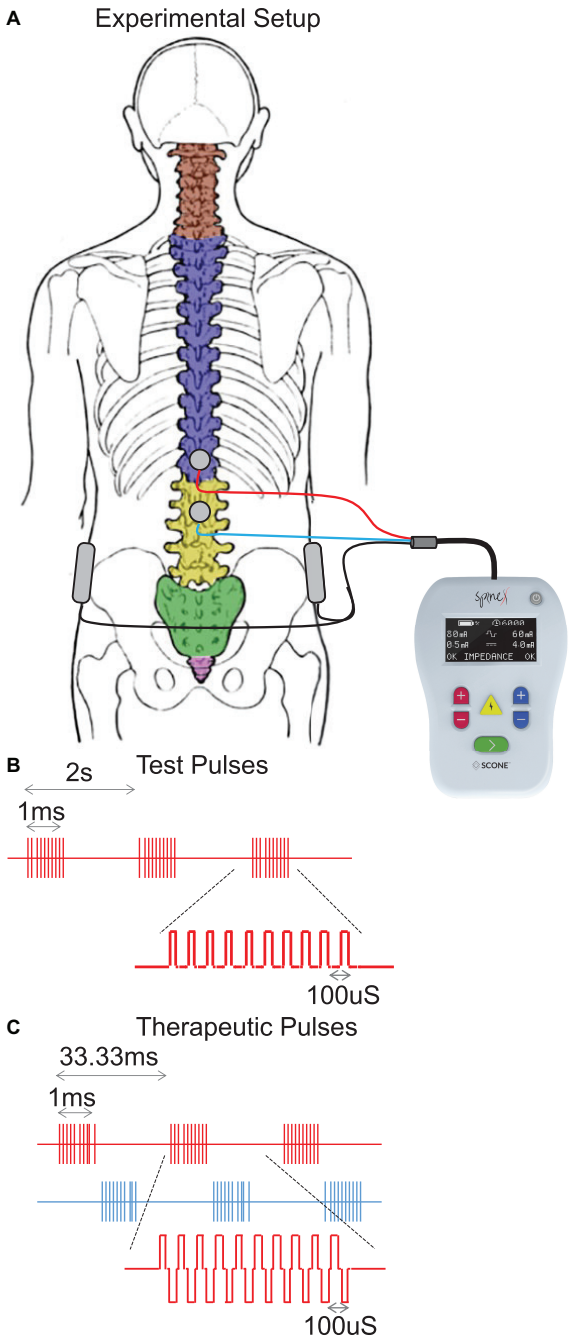

FIGURE 1 | (A) Experimental setup demonstrating the stimulation electrodes over T11-12 and L1-2 vertebral levels and return electrodes over the iliac crests. **(B)** Test pulses showing the train of monophasic pulses including the high frequency (10 KHz) pulses on for a period of 1 ms and low frequency (0.5 Hz, repeating every 2 s) pulses and **(C)** Therapeutic pulses showing the train of biphasic pulses including the high frequency (10 KHz) pulse on for a period of 1 ms and low frequency (30 Hz, repeating every 33.33 ms) pulses.

opposite polarities separated by a 1 uS delay forming a delayed biphasic waveform. The pulses consisted of a high frequency biphasic carrier pulse (10 KHz) combined with a low frequency (30 Hz) burst pulse each with a pulse width of 1 ms (**Figure 1**). Stimulation was applied using an adhesive electrode over the interspinous ligaments of T11 and L1 serving as the cathode and two adhesive electrodes over the iliac crests as the anodes. She received 1 h of stimulation 5 days a week for 5 weeks. On the days that the patient had a bowel program, she completed the bowel program 1–3 h prior to receiving stimulation. For the first 18 days, stimulation was delivered at a therapeutic level whereas during the last 18 days, stimulation intensity was reduced to an amplitude not expected to generate any physiological response based on our previous studies (sham stimulation). The patient was blinded by the intensity of stimulation at all times.

RESULTS

Acute Stimulation

Single pulses delivered over the lumbosacral spinal cord generated contractions in the anorectum of all three acute stimulation patients. The latency of contraction varied from 100 to 200 ms post stimulation pulse. The response amplitude varied based on the location. In addition, responses between 4 and 6 cm demonstrated a more complex response consisting of a second component with a longer latency (200–300 ms) (**Figure 2A**). However, location that generated the maximal amplitude occurred either between 1 and 3 cm or between 4 and 6 cm (**Figure 2B**).

The pressure profile across the anorectal region peaked between 4 and 6 cm (**Figure 3**) in all patients while the patients were relaxed and while they attempted to push as if to attempt a bowel movement. With tonic sub-motor threshold stimulation at T11 and L1, the pressure profile demonstrated a more consistent curve with high responses occurring between 3 and 8 cm. In addition, while the patient attempted to empty their bowels, the amplitude of response further increased between 3 and 8 cm. The change in pressure across the profile was higher while the patient was attempting to defecate and with the stimulation On (**Figure 3**).

Without stimulation, one patient was able to sense a filled balloon in the rectum, whereas two patients were unable to sense it up to a volume of 300 ml, which was established as a safe upper limit by the clinician (**Figure 4A**). Upon initiation of tonic sub-motor threshold stimulation at T11 and L1, the sensate patient reported rectal sensation at a lower balloon volume, and one of the insensate patients reported new onset sensation with balloon distention of the rectum (**Figure 4B**).

Chronic Stimulation

The chronic stimulation patient was asked to record the amount of time needed to complete her bowel program. Prior to initiation of the study and during the first few days, her bowel program time was consistently approximately 75 mins. After completing 1 week of daily stimulation, her bowel program time reduced to 15 mins. Over the course of the next 18 days, sham stimulation was delivered, and her bowel program time increased to between 45 and 65 mins (**Figure 5**). No adverse effects of stimulation were reported by the patient or noted by the study staff.

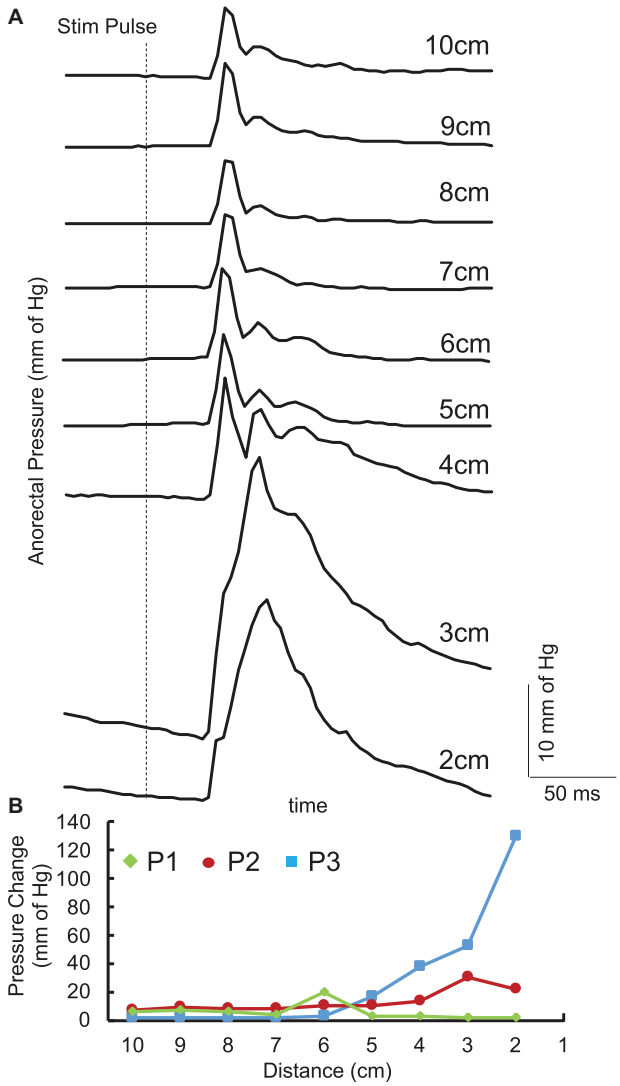

FIGURE 2 | (A) Average (n = 5) pulses spinally evoked pressure change with singe pulses at 150 mA in the anorectal region 10 cm to 2 cm from the anus from a representative SCI (P1) patient. **(B)** Pressure changes across the anorectal region 10 cm to 2 cm from the anus from the three patients enrolled in the study.

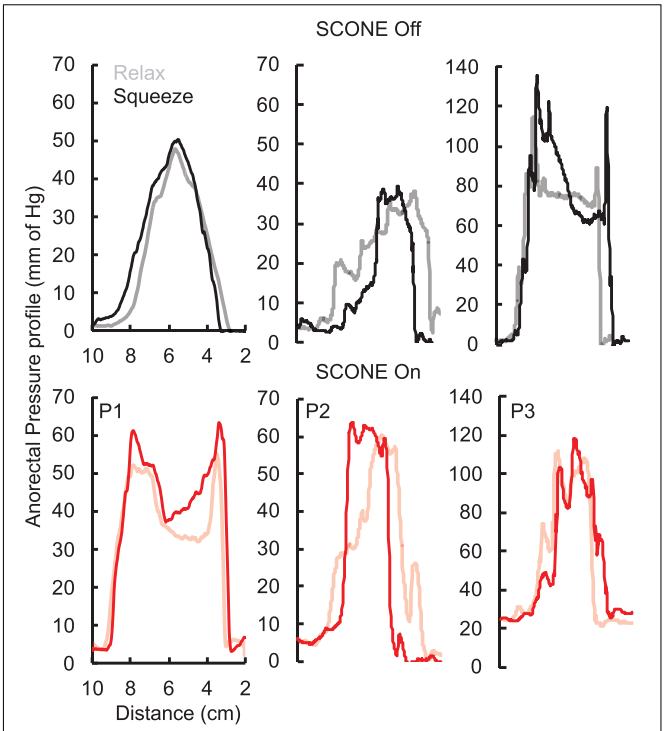

FIGURE 3 | Anorectal pressure profile without (black) and with (ref) SCONE^{TM} at T11 from the three SCI patients while the patients were relaxed (light) or squeezing (bold) their anus trying to assist a bowel movement.

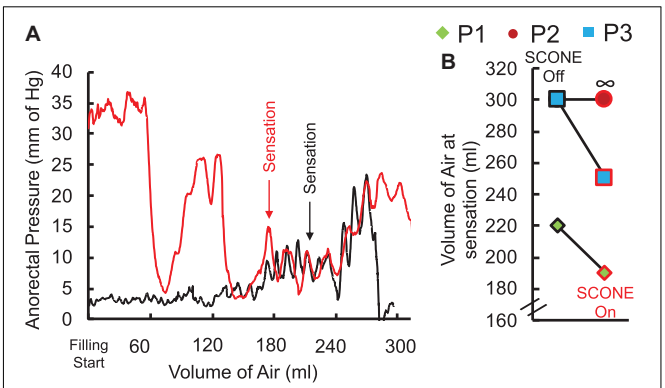

FIGURE 4 | (A) Anorectal pressure recorded while manually filling the rectal balloon with air without (black) and with (red) spinal stimulation at T11 in a representative SCI patient (P1) AIS A at C5 without and with SCONE^{TM}. Note the sensation of filling appears at lower volume with compared to without SCONE^{TM} (190 ml vs. 220 ml). **(B)** Threshold of sensation without and with SCONE^{TM} from the three patients enrolled in the study. ∞ represents a case when the patient was unable to detect the filled air (mm Hg).

DISCUSSION

In this pilot study we demonstrate that spinal neuromodulation can acutely change motor and sensory function of the anorectum. Additionally, in a case report of one patient, we show that spinal neuromodulation delivered over the course of several weeks may improve bowel function by decreasing the time required to perform a bowel program. SCONE^{TM} is a non-invasive neuromodulation modality initially developed to promote lower extremity functional recovery after SCI. In our previous work, we have demonstrated that SCONE^{TM} also appears to facilitate changes in lower urinary tract function in SCI individuals, promoting higher bladder capacity and decreasing detrusor overactivity (Gad P. N. et al., 2018; Kreydin et al., 2020). Although the bowel and the bladder differ markedly in function and control, their spinal and peripheral innervation share common origins. Parasympathetic innervation of both the anorectum and lower urinary tract (LUT) originates in the sacral parasympathetic nucleus located at the S2–S5 levels of the spinal

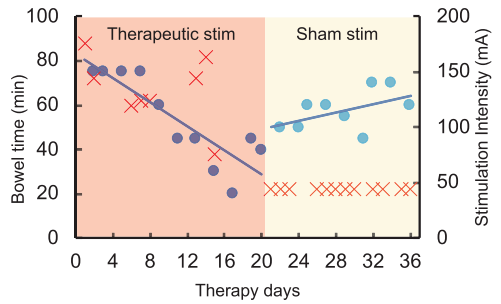

FIGURE 5 | Time required to complete bowel program (blue) in an SCI patient (T4 AIS A) over 35 therapy days with varying intensities of stimulation (red). Note the decrease in bowel time over the first 18 days during higher intensity therapeutic stimulation (red region). However, the bowel program time increased close to baseline during the second half of the study with sham stimulation (yellow region).

cord (T12-L1 vertebral level). Onuf's nucleus, which serves as the origin of the pudendal nerve, is located at the same level of the spinal cord and provides innervation of the skeletal external urethral and anal sphincters. Finally, sympathetic innervation of the anorectum and the LUT arises in the sympathetic chain at spinal levels T11-L2 (vertebral levels T7–T11) (de Groat et al., 2015; Callaghan et al., 2018). Thus, stimulation at levels T11 and L1 exerts an effect on all three components of the nervous system involved in bladder and bowel regulation. Just as with locomotion and LUT function, we hypothesize that spinal neuromodulation at these levels provides a signal to the relevant spinal centers, separated from the brain and brainstem by an injury, and allows acute and chronic changes to anorectal activity, that eventually lead to improvement in function.

An increase in anorectal pressure in response to SCONE^{TM} was an effect we observed in each participant, with two participants exhibiting the strongest response in the region of the anal canal. This region is the location of the external (EAS) and internal (IAS) anal sphincters, with the puborectalis muscle located more proximally and giving rise to the former (Kaiser and Ortega, 2002). Thus, one of the two participants exhibited the strongest response at the level of the puborectalis (3.5 cm above the anal verge), while the other exhibited the strongest response at the level of the superficial EAS (0.5–2 cm above the anal verge), suggesting the pudendal nerve as the ultimate element that mediates the response as part of a spinal reflex arc (see discussion below). Other authors have demonstrated similar effects in response to transcutaneous magnetic stimulation of the sacral regions of patients with SCI. Morren et al. (2001) delivered transcutaneous magnetic stimulation laterally to the midline at S2–S4 vertebral levels, targeting the sacral spinal nerves as they exit the sacral foramina, and hypothesized that the strong pressure response noted in the anal canal was due to direct excitation of this nerve. An elevation in rectal pressure was also seen with transcutaneous magnetic stimulation of the cauda equina (L3–L5 vertebral levels) in studies by Lin et al. (2001) (both healthy controls and patients with SCI) and Shafik and El-Sibai (2000) (healthy individuals only). Interestingly, one participant exhibited the strongest pressure response in a more rostral location of the rectum, 6 cm above the anal verge. This location is considerably proximal to the skeletally innervated puborectalis and EAS, suggesting that this increase in pressure may be mediated by excitation of the autonomic nerves responsible for rectal function. Morren et al. (2001) also noted changes in rectal pressure (i.e., proximal to the puborectalis and the EAS) with transcutaneous magnetic stimulation and hypothesized that this was likely due to a reflex arc, whereby stimulation of large caliber somatic sensory nerves led to the excitation of autonomic fibers at the level of the lumbosacral spine.

While the exact neural structure, with which spinal neuromodulation interacts, remains to be determined, the relatively prolonged latencies and the multipeak nature of the pressure response suggest that the effect is not due to the direct stimulation of the pudendal nerve (causing anal sphincter contraction) but rather to a polysynaptic or reflex-mediated phenomenon. A similar response was noted by Fowler et al. (2000) and Schurch et al. (2003), when the S3 nerve root was percutaneously stimulated in able-bodied and SCI participants, respectively. A direct motor response would be expected to occur at a sub-10 ms timescale; on the other hand, the response we observed occurred at least 100 ms after pulse adminstration with a second component occurring up to 300 ms after. Similarly, a pudendo-anal reflex would be expected to occur with a latency of less than 40 ms (Cavalcanti Gde et al., 2007). Although latencies observed in this study could be mediated by an afferent spino-bulbospinal mechanism, this is less likely as the spinobulbar pathways are expected to be disrupted after an SCI. Nonetheless, it is possible that spinal neuromodulation promotes communication along damaged but anatomically persistent pathways. The other possibility is that the response we observed is mediated by a reflex of spinal origin. The latter possibility is supported by the persistence of the response even in patents with AIS A injuries both with acute and chronic stimulation.

In other applications of spinal neuromodulation, it was noted that stimulation improves not only motor activity, but also sensory function in patients with SCI (Gerasimenko et al., 2016; Gad P. N. et al., 2018), stroke and multiple sclerosis (Kreydin et al., 2020), and children with cerebral palsy (Edgerton et al., 2021; Gad et al., 2021a). Here we observed a similar phenomenon, whereby rectal sensation changed during application of stimulation, enabling two of the three participants to sense inflation of a rectal balloon at a lower volume than in the absence of stimulation. The mechanism by which spinal neuromodulation alters conscious sensation is not fully understood. As in our experience with urinary storage and locomotion, however, we hypothesized that SCONE^{TM} may activate intact (but dormant) neural fibers at the injury site even in cases of functionally complete SCI and promote restoration of conscious sensation in a retrograde fashion. Alternatively, SCONE^{TM} may lead to the excitation of sympathetic fibers, thus allowing rectal distention to elicit a sympathetic response at a lower volume. The participant may then appreciate this response as "rectal sensation." Although it is unclear why Participant 2 did not exhibit this change in sensation, it is possible that this

individual had a more complete injury and the reflex arc between rectal sensory fibers and the sympathetic chain/higher sensory centers was more significantly disrupted.

Finally, the finding that the participant who underwent daily SCONE^{TM} sessions noted a gradual decrease in the time required to complete the bowel program suggests that SCONE^{TM} stimulation may be a useful technique to promote functional improvement in patients with NBD. Several previous studies have assessed neuromodulation as a means of improving bowel function after SCI. Tsai et al. (2009) studied seven patients with supraconal SCI and assessed the effect of a 3-week course of daily transcutaneous magnetic stimulation at T9 and L3 on bowel function. A statistically significant decrease in colonic transit time and an improvement in questionnaire-measured bowel function were noted. Lin et al. (2001) reported similar findings in subjects who underwent transcutaneous magnetic stimulation of the cauda equina and exhibited a significant decrease in colonic transit time. In addition, subjects reported restoration of some sensory function and decreased reliance on digital stimulation to empty their bowels (Lin et al., 2001). Implantable sacral neuromodulation (Medtronic Interstim®, Minnesota, MN, United States) was assessed as a means to improve bowel function in patients with incomplete SCI by Jarrett et al. (2005) and was found to improve bowel continence and sensation of incomplete bowel emptying. Because patients with SCI suffer from abnormally prolonged bowel transit times and dyssenergic defecation, correction of these parameters would be expected to reduce the time required to complete a bowel movement. While the mechanism by which neuromodulation achieves these effects remains to be elucidated, we hypothesize that the stimulation signal interacts with neural fibers that remain after an injury to correct or improve end organ function.

Traditionally, non-invasive electrical spinal stimulation has been thought to be ineffective for stimulation of neural structures in the spinal cord because, unlike magnetic stimulation, significant signal attenuation occurs when an electrical impulse is applied to highly resistant tissues, such as skin, fat and bone that overlie the spinal cord. However, this study adds to the existing evidence that the unique dual frequency paradigm delivered by spinal neuromodulation can affect the function of neural structures in the spinal cord (Gerasimenko Y. et al., 2015). We hypothesize that the relatively high amplitude of stimulation afforded by spinal neuromodulation allows electrical charge to penetrate the investing tissues of the spinal cord and modulate the activity of spinal reflex arcs important for limb, lower urinary tract, respiratory and bowel control. Interestingly, interferential electrical current stimulation uses frequencies in the same order of magnitude as spinal neuromodulation and has been found to be effective in improving both clinical and physiological parameters of neurogenic bowel in pediatric patients with spina bifida (Kajbafzadeh et al., 2012).

While the results observed are significant, our study has from several limitations. First, the small number of patients limits the generalizability of the results. However, the activation of the anorectum across all three participants, and similar findings by other authors utilizing magnetic stimulation suggest that we observed a true physiologic effect. Secondly, our participants were fairly heterogeneous with varying levels and years post SCI. It is possible that with a more homogeneous cohort, more consistent effects of SCONE^{TM} would have been observed. Future studies will need to determine how injury characteristics impact SCONE^{TM} response and to identify biomarkers that modulate its effect. Finally, SCONE^{TM} mediated improvement in bowel function after SCI requires further evaluation and confirmation in a rigorous sham-controlled setting.

DATA AVAILABILITY STATEMENT

The raw data supporting the conclusions of this article will be made available by the authors, without undue reservation.

ETHICS STATEMENT

The studies involving human participants were reviewed and approved by the Rancho Research Institute. The patients/participants provided their written informed consent to participate in this study.

AUTHOR CONTRIBUTIONS

PG, EK, and VE designed the study. EK, PG, and HZ performed the experiments. All authors edited and approved the manuscript.

FUNDING

This research was funded in part by the NIH/NINDS 1U01NS113871-01, NIH/NIDDK 01R44DK129164-01A1, and NSF 2112366, the Dana and Albert R. Broccoli Charitable Foundation, Nanette and Burt Forester, including matching by PwC LLP, Roberta Wilson, and BEL13VE in Miracles Jack Jablonski Foundation.

REFERENCES

Anderson, K. D. (2004). Targeting recovery: priorities of the spinal cord-injured population. *J. Neurotrauma* 21, 1371–1383.

Bloemen-Vrencken, J. H., Post, M. W., Hendriks, J. M., De Reus, E. C., and De Witte, L. P. (2005). Health problems of persons with spinal cord injury living in the Netherlands. *Disabil. Rehabil.* 27, 1381–1389. doi: 10.1080/09638280500164685

Callaghan, B., Furness, J. B., and Pustovit, R. V. (2018). Neural pathways for colorectal control, relevance to spinal cord injury and treatment: a narrative review. *Spinal Cord* 56, 199–205. doi: 10.1038/s41393-017-0026-2

Cavalcanti Gde, A., Bruschini, H., Manzano, G. M., Giuliano, L. P., Nobrega, J. A., and Srougi, M. (2007). Urethral sensory threshold and urethro-anal reflex latency in continent women. *Int. Urol. Nephrol.* 39, 1061–1068. doi: 10.1007/s11255-007-9177-y

de Groat, W. C., Griffiths, D., and Yoshimura, N. (2015). Neural control of the lower urinary tract. *Compr. Physiol.* 5, 327–396.

Deng, Y., Dong, Y., Liu, Y., Zhang, Q., Guan, X., Chen, X., et al. (2018). A systematic review of clinical studies on electrical stimulation therapy for patients with neurogenic bowel dysfunction after spinal cord injury. *Medicine (Baltimore)* 97:e12778. doi: 10.1097/MD.0000000000012778

Ditunno, P. L., Patrick, M., Stineman, M., and Ditunno, J. F. (2008). Who wants to walk? Preferences for recovery after SCI: a longitudinal and cross-sectional study. *Spinal Cord* 46, 500–506. doi: 10.1038/sj.sc.3102172

Edgerton, V. R., Hastings, S., and Gad, P. N. (2021). Engaging spinal networks to mitigate supraspinal dysfunction after CP. *Front. Syst. Neurosci.* 15:643463. doi: 10.3389/fnins.2021.643463

Fowler, C. J., Swinn, M. J., Goodwin, R. J., Oliver, S., and Craggs, M. (2000). Studies of the latency of pelvic floor contraction during peripheral nerve evaluation show that the muscle response is reflexly mediated. *J. Urol.* 163, 881–883. doi: 10.1016/s0022-5347(05)67826-3

Gad, P., Zhong, H., Edgerton, V. R., and Kreydin, E. (2021b). Home-based SCONE^{TM} therapy improves symptoms of neurogenic bladder. *Neurotrauma Rep.* 2, 165–168. doi: 10.1089/neur.2020.0061

Gad, P., Hastings, S., Zhong, H., Seth, G., Kandhari, S., and Edgerton, V. R. (2021a). Transcutaneous spinal neuromodulation reorganizes neural networks in patients with cerebral palsy. *Neurotherapeutics* 18, 1953–1962. doi: 10.1007/s13311-021-01087-6

Gad, P., Lee, S., Terrafranca, N., Zhong, H., Turner, A., Gerasimenko, Y., et al. (2018). Non-invasive activation of cervical spinal networks after severe paralysis. *J. Neurotrauma* 35, 2145–2158. doi: 10.1089/neu.2017.5461

Gad, P. N., Gerasimenko, Y. P., Zdunowski, S., Sayenko, D., Haakana, P., Turner, A., et al. (2015). Iron 'ElectriRx' man: overground stepping in an exoskeleton combined with noninvasive spinal cord stimulation after paralysis. *Annu. Int. Conf. IEEE Eng. Med. Biol. Soc.* 2015, 1124–1127. doi: 10.1109/EMBC.2015.7318563

Gad, P. N., Kreydin, E., Zhong, H., and Edgerton, V. R. (2020). Enabling respiratory control after severe chronic tetraplegia: an exploratory case study. *J. Neurophysiol.* 124, 774–780. doi: 10.1152/jn.00320.2020

Gad, P. N., Kreydin, E., Zhong, H., Latack, K., and Edgerton, V. R. (2018). Non-invasive neuromodulation of spinal cord restores lower urinary tract function after paralysis. *Front. Neurosci.* 12:432. doi: 10.3389/fnins.2018.00432

Gerasimenko, Y., Gad, P., Sayenko, D., McKinney, Z., Gorodnichev, R., Puhov, A., et al. (2016). Integration of sensory, spinal, and volitional descending inputs in regulation of human locomotion. *J. Neurophysiol.* 116, 98–105. doi: 10.1152/jn.00146.2016

Gerasimenko, Y., Gorodnichev, R., Moshonkina, T., Sayenko, D., Gad, P., and Reggie Edgerton, V. (2015). Transcutaneous electrical spinal-cord stimulation in humans. *Ann. Phys. Rehabil. Med.* 58, 225–231.

Gerasimenko, Y. P., Lu, D. C., Modaber, M., Zdunowski, S., Gad, P., Sayenko, D. G., et al. (2015). Noninvasive reactivation of motor descending control after paralysis. *J. Neurotrauma* 32, 1968–1980. doi: 10.1089/neu.2015.4008

Inanici, F., Samejima, S., Gad, P., Edgerton, V. R., Hofstetter, C. P., and Moritz, C. T. (2018). Transcutaneous electrical spinal stimulation promotes long-term recovery of upper extremity function in chronic tetraplegia. *IEEE Trans. Neural Syst. Rehabil. Eng.* 26, 1272–1278. doi: 10.1109/TNSRE.2018.2834339

Jarrett, M. E., Matzel, K. E., Christiansen, J., Baeten, C. G., Rosen, H., Bittorf, B., et al. (2005). Sacral nerve stimulation for faecal incontinence in patients with previous partial spinal injury including disc prolapse. *Br. J. Surg.* 92, 734–739. doi: 10.1002/bjs.4859

Kaiser, A. M., and Ortega, A. E. (2002). Anorectal anatomy. *Surg. Clin. North Am.* 82, 1125–1138.

Kajbafzadeh, A. M., Sharifi-Rad, L., Nejat, F., Kajbafzadeh, M., and Talaei, H. R. (2012). Transcutaneous interferential electrical stimulation for management of neurogenic bowel dysfunction in children with myelomeningocele. *Int. J. Colorectal Dis.* 27, 453–458. doi: 10.1007/s00384-011-1328-z

Kreydin, E., Zhong, H., Latack, K., Ye, S., Edgerton, V. R., and Gad, P. (2020). Transcutaneous electrical spinal cord neuromodulator (TESCoN) improves symptoms of overactive bladder. *Front. Syst. Neurosci.* 14:1. doi: 10.3389/fnsys.2020.00001

Lin, V. W., Nino-Murcia, M., Frost, F., Wolfe, V., Hsiao, I., and Perkash, I. (2001). Functional magnetic stimulation of the colon in persons with spinal cord injury. *Arch. Phys. Med. Rehabil.* 82, 167–173. doi: 10.1053/apmr.2001.18215

Morren, G. L., Walter, S., Hallbook, O., and Sjodahl, R. (2001). Effects of magnetic sacral root stimulation on anorectal pressure and volume. *Dis. Colon Rectum* 44, 1827–1833. doi: 10.1007/BF02234462

Parag Gad, Y. G., and Reggie Edgerton, V. (2019). "Tetraplegia to overground stepping using non-invasive spinal neuromodulation," in *Proceedings of the 2019 9th International IEEE/EMBS Conference on Neural Engineering (NER)*, San Francisco, CA, 89–92.

Parittotokkaporn, S., Varghese, C., O'Grady, G., Svirskis, D., Subramanian, S., and O'Carroll, S. J. (2020). Non-invasive neuromodulation for bowel, bladder and sexual restoration following spinal cord injury: a systematic review. *Clin. Neurol. Neurosurg.* 194:105822. doi: 10.1016/j.clineuro.2020.105822

Rath, M., Vette, A. H., Ramasubramaniam, S., Li, K., Burdick, J., Edgerton, V. R., et al. (2018). Trunk stability enabled by noninvasive spinal electrical stimulation after spinal cord injury. *J. Neurotrauma* 35, 2540–2553. doi: 10.1089/neu.2017.5584

Schurch, B., Reilly, I., Reitz, A., and Curt, A. (2003). Electrophysiological recordings during the peripheral nerve evaluation (PNE) test in complete spinal cord injury patients. *World J. Urol.* 20, 319–322. doi: 10.1007/s00345-002-0299-7

Shafik, A., and El-Sibai, O. (2000). Effect of magnetic stimulation on the contractile activity of the rectum in humans. *Am. Surg.* 66, 491–494.

Tsai, P. Y., Wang, C. P., Chiu, F. Y., Tsai, Y. A., Chang, Y. C., and Chuang, T. Y. (2009). Efficacy of functional magnetic stimulation in neurogenic bowel dysfunction after spinal cord injury. *J. Rehabil. Med.* 41, 41–47. doi: 10.2340/16501977-0280

Waddell, O., McCombie, A., and Frizelle, F. (2020). Colostomy and quality of life after spinal cord injury: systematic review. *BJS Open* 4, 1054–1061. doi: 10.1002/bjs5.50339

Conflict of Interest: VE holds shareholder interest in Onward and hold certain inventorship rights on intellectual property licensed by The Regents of the University of California to Onward. VE, EK, and PG holds shareholder interest in SpineX Inc., and hold certain inventorship rights on intellectual property licensed by The Regents of the University of California to SpineX Inc.

The remaining authors declare that the research was conducted in the absence of any commercial or financial relationships that could be construed as a potential conflict of interest.

Publisher's Note: All claims expressed in this article are solely those of the authors and do not necessarily represent those of their affiliated organizations, or those of the publisher, the editors and the reviewers. Any product that may be evaluated in this article, or claim that may be made by its manufacturer, is not guaranteed or endorsed by the publisher.

frontiers | Frontiers in Neuroscience

ORIGINAL RESEARCH
published: 16 May 2022
doi: 10.3389/fnins.2022.726467

Renal Nerve Activity and Arterial Depressor Responses Induced by Neuromodulation of the Deep Peroneal Nerve in Spontaneously Hypertensive Rats

*Maria Alejandra Gonzalez-Gonzalez[1], Kevin Romero[1], John Beitter[2], David Lloyd[1], Danny V. Lam[2], Ana Guadalupe Hernandez-Reynoso[2], Aswini Kanneganti[2], Han-Kyul Kim[3], Caroline K. Bjune[4], Scott Smith[3,5], Wanpen Vongpatanasin[3] and Mario I. Romero-Ortega[1]**

[1] Department of Biomedical Engineering and Biomedical Sciences, University of Houston, Houston, TX, United States, [2] Department of Biomedical Engineering, The University of Texas at Dallas, Dallas, TX, United States, [3] Hypertension Section, Department of Internal Medicine, University of Texas Southwestern Medical Center, Dallas, TX, United States, [4] Draper Laboratory, Boston, MA, United States, [5] Applied Clinical Research, University of Texas Southwestern Medical Center, Dallas, TX, United States

OPEN ACCESS

Edited by:
Stephen Lewis,
Case Western Reserve University,
United States

Reviewed by:
Tymoteusz Zera,
Medical University of Warsaw, Poland
Mazher Mohammed,
University of Florida, United States

***Correspondence:**
Mario I. Romero-Ortega
miromeroortega@uh.edu

Specialty section:
This article was submitted to Autonomic Neuroscience, a section of the journal Frontiers in Neuroscience

Received: 16 June 2021
Accepted: 21 March 2022
Published: 16 May 2022

Citation:
Gonzalez-Gonzalez MA, Romero K, Beitter J, Lloyd D, Lam DV, Hernandez-Reynoso AG, Kanneganti A, Kim H-K, Bjune CK, Smith S, Vongpatanasin W and Romero-Ortega MI (2022) Renal Nerve Activity and Arterial Depressor Responses Induced by Neuromodulation of the Deep Peroneal Nerve in Spontaneously Hypertensive Rats. Front. Neurosci. 16:726467. doi: 10.3389/fnins.2022.726467

Hypertension is a main cause of death in the United States with more than 103 million adults affected. While pharmacological treatments are effective, blood pressure (BP) remains uncontrolled in 50–60% of resistant hypertensive subjects. Using a custom-wired miniature electrode, we previously reported that deep peroneal nerve stimulation (DPNS) elicited acute cardiovascular depressor responses in anesthetized spontaneously hypertensive rats (SHRs). Here, we further study this effect by implementing a wireless system and exploring different stimulation parameters to achieve a maximum depressor response. Our results indicate that DPNS consistently induces a reduction in BP and suggests that renal sympathetic nerve activity (RSNA) is altered by this bioelectronic treatment. To test the acute effect of DPNS in awake animals, we developed a novel miniaturized wireless microchannel electrode (w-μCE), with a Z-shaped microchannel through which the target nerves slide and lock into the recording/stimulation chamber. Animals implanted with w-μCE and BP telemetry systems for 3 weeks showed an average BP of 150 ± 14 mmHg, which was reduced significantly by an active DPNS session to 135 ± 8 mmHg ($p < 0.04$), but not in sham-treated animals. The depressor response in animals with an active w-μCE was progressively returned to baseline levels 14 min later (164 ± 26 mmHg). This depressor response was confirmed in restrained fully awake animals that received DPNS for 10 days, where tail-cuff BP measurements showed that systolic BP in SHR lowered 10% at 1 h and 16% 2 h after the DPNS when compared to the post-implantation baseline. Together, these results support the use of DPN neuromodulation as a possible strategy to lower BP in drug-resistant hypertension.

Keywords: hypertension, neuromodulation, spontaneously hypertensive rats, renal nerve activity, deep peroneal nerve

INTRODUCTION

Hypertension is an important risk factor in the development of cardiovascular and kidney disease and stroke and heart failure, affecting more than 103.3 million people in the United States (Muntner et al., 2020). The American College of Cardiology/American Heart Association 2018 guidelines classified average systolic blood pressure (BP) > 130 mmHg and diastolic BP > 80 mmHg, on at least two separate occasions, as hypertension (Flack et al., 2018). Broadly used pharmaceuticals for this condition include renin-angiotensin inhibitors, angiotensin-converting enzyme inhibitors, and angiotensin II receptor blockers. Others include thiazide diuretics, beta-blockers, and calcium antagonists, depending on co-morbidities (Mendoza et al., 2021). Unfortunately, despite the use of multiple antihypertensive drugs in combination, BP remains poorly controlled in 50–60% of the hypertensive population (Carey et al., 2018), and approximately 12–18% of them develop resistant hypertension (RH); defined as BP > 140/90 mmHg despite the use of three antihypertensive drugs of complementary mechanisms, including a diuretic agent (Chia et al., 2020). Alternative treatments aim at reducing the renal sympathetic tone, or the hyper-reflex sympathetic signals from the carotid body, which are sensitive to oxygen and blood flow. For the former, renal denervation has been shown to reduce mean arterial pressure (MAP) in six placebo-controlled trials (systolic BP−5.53 mmHg), although with high variability, and the possible kidney reinnervation (Lauder et al., 2020). For the latter, unilateral resection of the carotid body in 15 patients with RH was shown to reduce ambulatory BP in 8 subjects, although serious adverse events were reported in two of them (Narkiewicz et al., 2016).

Several medical devices have been developed for RH (Lauder et al., 2020), such as the Rheos (CVRx) system, with bilateral electrodes implanted near the aortic arch to stimulate the baroreceptors, which exert an inhibitory influence on sympathetic nerve activity (Groenland and Spiering, 2020). This baroreflex activation therapy was reported in an open-label study to reduce in-office MAP in patients with RH, but not ambulatory RH (Bakris et al., 2012). In addition, a double-blind, randomized pivotal study with 265 patients was failed to meet efficacy endpoints, and 25% showed adverse surgical complications (Ewen et al., 2017). A second generation of the Rheos device has provided promising results, although side effects due to high stimulation intensities remain (Mahfoud et al., 2021).

Alternative treatments include electroacupuncture based either on Qi hypotheses or mechanistic information, where controlled clinical trials have shown a significantly lower 24-h ambulatory MAP ($\geq$6 mmHg), correlated with reductions in circulating norepinephrine, renin, and aldosterone (Flachskampf et al., 2007; Li et al., 2015). We previously reported that stimulation of the deep peroneal nerve (DPNS), a fascicle of the sciatic nerve in proximity to the acupuncture point ST-36, induced a 23 mmHg reduction in MAP in anesthetized spontaneously hypertensive rats (SHRs) (Kim and Romero-Ortega, 2012; Kim et al., 2014). However, confirming the depressor effect in freely moving animals who underwent DPNS has remained a challenge, given the small size of the rat peroneal nerve (≈200 μm OD) and the need for fully implantable miniature wireless stimulators to avoid nerve injury and/or discomfort to the animal during ambulation. Here, we report studies that refined stimulation parameters for optimal MAP reduction by DPNS in SHR animals. We previously developed a miniature wireless microchannel electrode (w-μCE) with inductive stimulator circuit and an external power/command control (Freeman et al., 2017; Hernandez-Reynoso et al., 2019), here we improved it with a novel nerve attachment microchannel that facilitates implantation and anchor of the device into small nerves and allowed sub-chronic DPNS in awake animals. The results support the notion that wireless neuromodulation devices can be used to deliver bioelectronic treatment to lower MAP in a rat model of hypertension and show promise as a treatment for RH.

MATERIALS AND METHODS

Animals

A total of 26 adult male SHRs (300–350 g, 12–14 weeks old, Charles River, Wilmington, MA, United States) were used in this study. SHRs are considered an established model of primary hypertension due to an overactivated sympathetic drive (Shanks et al., 2013; Gu et al., 2020). The animals were divided into three separate study phase cohorts, which are as follows: (I) evaluation of acute pulse duration effect in anesthetized breathing-assisted rats (n = 5), (II) confirmation of optimized stimulation parameters in anesthetized spontaneous breathing animals (n = 8; **Figure 1**), and (III) testing sub-chronic DPNS in awake animals (n = 13). Animals were anesthetized with vaporized isoflurane (2%) in a constant oxygen flux (2 L/min) delivered by a calibrated vaporizer, placed on a warm pad, and body temperature, cardiac rate, and respiration were monitored constantly. Nerve stimulation in Phase I and II cohorts was done using a wired hook platinum electrode, whereas Phase III evaluation used fully implantable w-μCE stimulators and included a sham group implanted with non-functional electrodes.

Tracheotomy

Animals participating in Phase I of the study underwent a tracheotomy for assisted mechanical ventilation. The trachea was exposed by a midline incision in the neck (1.5–2 cm), and an endotracheal tube (1.72 mm diameter) was inserted into the airway. A respirator (Model 683, Harvard Apparatus) was used with a tidal volume of 2.5 ml/breath and respiratory rate of 70 breaths/min throughout the experiment.

Deep Peroneal Nerve Stimulation

A 2.0 cm incision on the hind-limb below the femur exposed the biceps femoris and vastus lateralis muscles, which were bluntly dissected to expose the DPN branch from the sciatic nerve and gently isolated from surrounding connective tissue using a glass rod and kept hydrated with warm physiological saline solution (pH 7.2). Either wired hook platinum electrodes (Phase I and II studies) or a wireless stimulator (Phase III studies) were used.

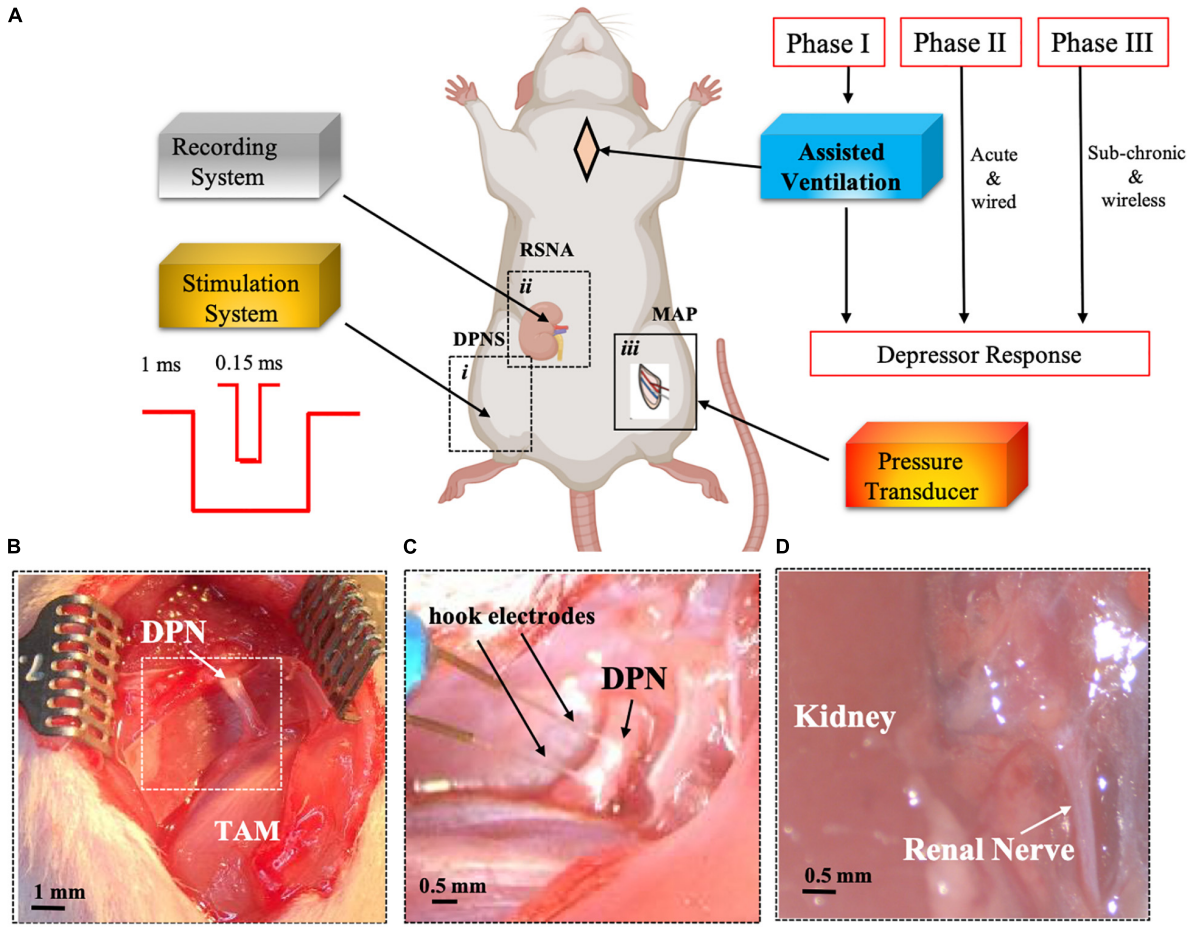

FIGURE 1 | Experimental set-up for DPNS to modulate MAP. Adult SRH rats were anesthetized. Phase I animals received assisted ventilation (n = 5), and phase II did not (n = 8), and phase III the MAP was measured by telemetry and DPNS with a wireless system (n = 11). The effect of DPNS on RSNA and MAP was evaluated, **(A)** Animal setup: a stimulator system with a pulse generator for short (0.15 ms) or long (1 ms) pulses was connected to a hook electrode placed on the DPN *(i)*. A second electrode was placed on the renal nerve to record neural activity *(ii)*. A catheter was implanted in the femoral artery and connected to a pressure transducer to monitor MAP *(iii)*. Dotted-line inserts *(i* and *ii)* show the site where pictures in panels **(B–D)** were obtained. Photographs of the DPN before **(B)** and after **(C)** electrode implantation are displayed. Insert in panel **B** is magnified in panel **C** after electrode placement. **(D)** Identification of renal nerve. SHR, spontaneous hypertensive rats; RSNA, renal sympathetic nerve activity; DPNS, Deep peroneal nerve stimulation; DPN, deep peroneal nerve: MAP, mean arterial pressure; TAM, tibialis anterior muscle.

For Phase III studies, the wound was closed after implantation of the w-μCE electrode onto the DPN, topical antibiotics were applied, and antibiotic and analgesic were administrated (cefazolin, 5 mg/kg and buprenorphine sustained-release [SR], 1 mg/kg; respectively). These animals were recovered for 3 weeks before applying wireless DPN neuromodulation.

Stimulation Parameters in Acute Studies

Stimulation parameters were evaluated for maximum depressor responses, using either voltage (0.2–1.2 mV, n = 11 tests; 2 animals) or current (0.06–2.0 mA, n = 17 tests; 3 animals) 0.15 and 1.0 ms cathodic monophasic pulses, applied with a PlexStim Electrical Stimulator System (Plexon Inc). The effect was confirmed by the evoked contraction of the tibialis anterior (TA) muscle and digits, which was videotaped and used to determine the threshold and effectiveness of DPN stimulation. The frequency for pulses was maintained at 2 Hz for 30 ± 15 s. The effect of DPN stimulation on the blood pressure was evaluated by implanting an arterial pressure sensor.

Sub-Chronic Deep Peroneal Nerve Neuromodulation

A miniature implantable w-μCE neural stimulator was developed using a sub-millimeter radiofrequency (RF) stimulator circuit (150-turn coil with a Nickel-Zinc ferrite core, a 7.0 pF capacitor tuned at 10.9 MHz, a Schottky diode, and a 100 pF shunt capacitor (Hernandez-Reynoso et al., 2019)), integrated into a 3D printed nerve-attachment device with a Z-shaped microchannel, leading to a stimulation chamber containing platinum trace electrodes. This new design facilitates nerve implantation by placing it underneath the nerve and gently lifting it over the microchannel. This causes a transient longitudinal elongation and transverse compression of the nerve, which then allows it to

pass through a smaller microchannel (internal diameter 20–30% less than the DPN diameter) and into the electrode chamber. Lowering the device, release the tension in the nerve allowing it to expand to its original size and locking it in place. Seven electrodes were used for this study and were electrochemically characterized before use, with an average impedance value of 250.63 ± 53.42 KΩ at 1 kHz frequency. During stimulation, we used an external RF antenna, with an electrical field ranging from 16.87 to 27.5 A/m, at 2–10 cm from the implanted w-μCE stimulator. The limits of exposure to electromagnetic fields were established to meet the Federal Communications Commission (Bassen et al., 2005). Three weeks after recovery, animals implanted with w-μCE stimulators onto the DPN were stimulated for 8 min with 200 mV square monophasic pulses (200 μs) at 2 Hz, using a pulse generator (Agilent 81110A) that was connected to an external RF amplifier, and a transmission antenna with a 10.0 MHz carrier frequency (AG 1012, T&C Power Conversion, Inc).

Renal Sympathetic Nerve Activity (RSNA)

A 2.5 cm midline abdominal incision was made to visualize the kidney. Using a dissecting microscope, a 2 mm segment of the renal nerve was gently dissected from the artery and interfaced with a bipolar stainless-steel wire electrode (Bioflex wire AS633; Cooner Wire). A thin layer of medical-grade silicone (Kwik-Sil; World Precision Instruments, Sarasota, FL, United States) was added over the nerve for insulation and mechanical stability. The RSNA was recorded at 1 kHz sampling rate using a Neuro Amp EX (AD-Instruments). The full-wave was rectified and averaged in 1 s intervals for analysis. Baseline values were determined by averaging 30 s of recorded data before DPN stimulation. Baseline RSNA values were considered as 100%, and experimental values were expressed as a change in percentage of the baseline (ΔRSNA,%). Hexamethonium bromide (60 mg/kg), an autonomic ganglia nicotinic acetylcholine receptor antagonist (Touw et al., 1980), was administered intravenously at the end of the experiments to confirm that RSNA signals were recorded from post-ganglionic renal fibers. Neural activity was further confirmed by the abolition of the recorded signal 30-min after euthanasia.

Blood Pressure Measurements

For animals in Phase I and II studies, the BP was recorded acutely in anesthetized animals using a wired pressure sensor that was attached to a cannula implanted into the femoral artery. For animals in Phase III, BP was measured using a tail cuff in awake and restrained animals (n = 4), or a telemetry BP system implanted into the femoral artery (n = 9).

Wired Blood Pressure Recording

A 1.5–2 cm incision was made in the inner part of the left leg to expose the femoral artery, where a heparinized (20 IU/ml) cannula (0.6 mm outer diameter) was inserted and secured using 4.0 silk sutures. The cannula was connected to a calibrated pressure transducer (AD-Instruments, MLT1199) and coupled to a bridge amplifier and power supply (AD-Instruments, FE221 and ML826, respectively). BP measurements were obtained continuously during the acute studies and exported at 1,000 and 100 bits per second, respectively. A PowerLab data acquisition system and LabChart Pro software (both from AD Instruments, Colorado Springs, CO, United States) were used to digitalize and visualize the data.

Tail-Cuff Blood Pressure Measuring

For non-invasive measurements in fully awake animals, the rats were placed in an animal holder (HLD-RM, Kent Scientific), and a tail-cuff BP system based on volume pressure recording (VPR) sensor technology (CODA, Kent Scientific) was used to measure the systolic and diastolic BP.

Telemetry Blood Pressure Monitoring

A wireless BP sensor (HD-S11-F2, DSI Harvard Bioscience, Inc.) was implanted in a cohort of animals in Phase III studies. The device battery was implanted in the abdominal cavity and fixed with sutures to the abdominal walls. The pressure catheter was implanted in the femoral artery. An ambient pressure reference (APR-2, DSI) was used for calibration during measurements (accuracy ± 1 mmHg). The measurements were obtained every 15 s using the PONEMAH software 6.51.

Ethics Statement

All protocols and surgical procedures were designed to prevent animal discomfort and suffering. These were approved by the University of Texas at Dallas, University of Texas Southwestern Medical Center, and the University of Houston, Institutional Animal Care and Use Committees, following the guidelines provided by the National Institute of Health (NIH).

Spectrogram Analysis

In a small cohort of SHR animals (n = 3), MATLAB R2020a was used with a hamming window with a length of 128 samples, 64 samples of overlap, and 128 samples for fast Fourier transform (FFT). A 10-s window from before, during, and after stimulation was selected. Frequencies below 50 Hz were considered related to RSNA and from 50–100 Hz related to stimulation artifact. The intensity of the short-time Fourier transform was averaged over each 2-s window and converted to decibels, divided by the maximum spectrogram frequency to calculate spectral density in dB/Hz.

Histology

At the end of the studies, the animals were euthanized with an overdose of sodium pentobarbital (120 mg/kg, intraperitoneal [ip]). The DPN was harvested and fixed in cold 4% paraformaldehyde in phosphate-buffered saline (PBS; pH 7.2) for 24 h, cryoprotected in 30% sucrose, embedded in optimal cutting temperature (OCT) media, and cut in 35 μm cross-sections in a cryostat. The sections were rinsed, blocked, and incubated with primary antibodies as described previously (Gonzalez-Gonzalez et al., 2018). Beta III tubulin (1:400, Sigma, T4026), myelin glycoprotein zero, (P0 1:400; Millipore, AB9352), and the 110 kDa activated macrophages glycoprotein maker ED1 (1:200 Abcam, 31630). Secondary antibodies coupled to Alexa Fluor 488 or 555 (Invitrogen; 1:200 dilution) or Cy5 bis-NHS ester (Jackson ImmunoResearch; 1:400 dilution) were used for visualization. The sections were imaged in a confocal microscope (Nikon, eclipse Ti®).

Statistical Analysis

Evaluation of pulse duration in voltage-controlled stimulation was achieved by a mixed effect analysis followed by a Sidak multiple comparison test. The effect of stimulation intensity was evaluated using an unpaired Student's *t*-test. For the spectral density analysis, an ANOVA test was performed with 2-s window from before, during, and after stimulation selected for all frequencies. The intensity (as decibels) was averaged for each time window. To calculate spectral density in dB/Hz, values were divided by the maximum spectrogram frequency (500 Hz). *Post hoc* Tukey's multiple comparison test was applied to assess pairwise comparison between means. One-way ANOVA followed by Dunnett's test was used for the evaluation of the BP differences. Statistical analysis was performed using the GraphPad Prism software version 9.1.2 and MATLAB R2020a.

RESULTS

Consistent Cardiovascular Depressor Responses Induced by Deep Peroneal Nerve Stimulation

An immediate and reproducible arterial depressor effect was observed with a concomitant increase in heart rate (HR) in response to electrical stimulation of the DPN in anesthetized animals with ventilation support (**Figure 2A**). Pulse duration, tested with 0.2–0.4 mV stimuli at 2 Hz for 30 s, showed a maximal depressor response with 1 ms pulses (−16 mmHg) as compared to 0.15 ms (−8 mmHg; $p < 0.05$; unpaired *t*-test $n = 4$; **Figure 2B**). Stimulation intensity tested using monophasic cathodic 1 ms pulses showed a higher depressor response evoked by 1 mA (−23 mmHg) compared that elicited by 0.6 mA stimuli (−7 mmHg, respectively; $p < 0.005$ unpaired *t*-test; $n = 5$; **Figure 2C**). The DPNS depressor responses were found to be highly reproducible over repetitive stimulations. **Figure 2D** shows MAP changes induced by two consecutive DPNS stimulation events, and **Figure 2E** demonstrates consistently evoked depressor responses in 5 individual animals over 3 sequential treatments.

The optimized parameters, 1 mA, 1 ms cathodic monophasic pulses, were used at 2 Hz for 30 s in anesthetized SHR animals without ventilation support to confirm their efficacy. These DPNS parameters efficiently induced a cardiovascular depressor response in all animals (**Figure 2F**), reducing the average baseline MAP from 108–132 mmHg to 92–120 mmHg (**Figure 2G**, Student's *t*-test, $p = 0.02$, $n = 8$).

Modulation of Renal Sympathetic Nerve Activity by Deep Peroneal Nerve Stimulation

A notable increase in RSNA was observed during DPNS with the similar onset and offset as the electrical stimulation. Overlapping the MAP with the RSNA showed an initial pressor response of about 3 s, followed by a 10 s of continued depressor response, which was reversed to baseline at the end of stimulation (**Figure 3A**). This activity was different from the stimulation artifact as the onset of RSNA was not synchronous with that of the electrical stimulation, showing a delay of 100–200 ms after the first stimulation pulse (**Figures 3B,B'**). The ganglion blocker hexamethonium blunted the RSNA activity, demonstrating that these neural signals were sympathetic (Janssen et al., 1989; **Figure 3C**). Furthermore, the frequency observed in renal nerve activity (10–50 Hz) was differentiated from the 2-Hz stimulus pulses delivered to the DPNS, from the evoked paw movement, and from the stimulation artifact registered above 50 Hz. Power analysis allowed to confirm different signals, unlike the stimulation artifact showed minimal average power density at baseline (0.7 dB/Hz) with some increase during DPNS to 11.2 dB/Hz at frequencies > 50 Hz, the SRNA signals showed regular spiking activity before stimulation and with a power density of 11.2 dB/Hz. This RSNA increased to 37.8 dB/Hz during DPNS (>50 Hz frequency band) and showed a tendency to decrease for 5 s, albeit not significantly compared to baseline (**Figures 3D,E**). One-way ANOVA followed by Bonferroni's test showed that these changes in power density were significant only in the low-frequency range ($^{**}p < 0.001$, $n = 3$; **Figure 3E**). We then used principal component analysis to test if waveforms present at baseline were modulated by DPNS. Two waveforms were identified with evoked activity at 0.5–2.5 Hz and were presented only during the stimulation period. Another one was active before the stimulation and was negatively modulated after the stimulation (**Figure 3F**). Finally, we looked at peak-to-peak amplitude in the spontaneous RSNA activity before and after DPNS and found that increasing the stimulation current from 0.06 to 1.0 mA significantly increased the amplitude of the evoked RSNA activity 83 ± 8%, from 3.19 ± 0.61 μA to 5.84 ± 0.56 μA ($^{**}p < 0.004$ paired *t*-test, $n = 5$; **Figure 3G**). Together, these data indicate that DPNS induced changes in RSNA, suggesting a possible role of the renal nerve in the reduction of MAP by this neuromodulation approach.

Wireless Deep Peroneal Nerve Stimulation Induces a Depressor Response in Awake Animals

Small w-μCE electrodes were implanted onto the DPN of SHR rats and were externally controlled and powered by a radio-magnetic antenna at a carrier frequency of 10.3 MHz (**Figure 4A**). This device uses a slide-and-lock approach where the nerve passes through a microchannel, 20–30% smaller than the outside diameter of the target nerve, and is placed in an electrode chamber where it expands to its original size, fitting the stimulation chamber tightly (**Figure 4a'**). The w-μCE was implanted by placing it under the nerve and slightly pulling it upward to stretch it slightly reducing its diameter, allowing it to slide through the Z-shape microchannel and into the electrode chamber (**Figure 4B**). The output voltage of the w-μCE neural stimulator is a function of the electromagnetic field strength, which is determined by the RF antenna power, and its distance from the implanted device. The devices generated an average of 1.4 V at a 45.6 A/m magnetic field, delivering 0.6–1 mA cathodic pulses at 2 cm from the external antenna

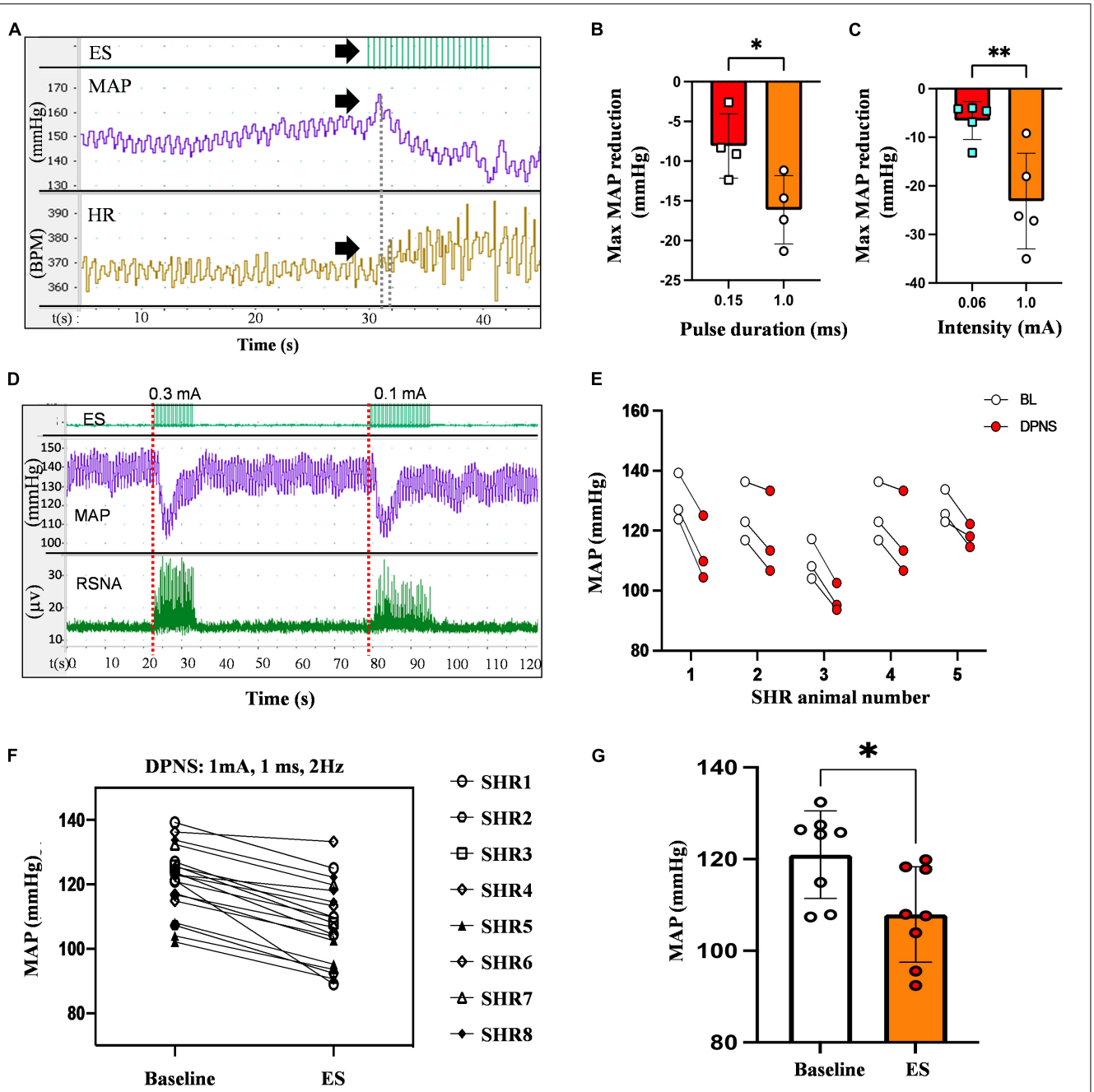

FIGURE 2 | Reduction in MAP by DPNS. **(A)** Stimulation of the DPN at 2 Hz (arrows) evokes a reduction in MAP and increases the SRNA (red dotted lines). **(B)** 1 ms pulse duration and **(C)** 1 mA pulse amplitude induced more effective MAP depressor responses (unpaired t-test; $^{*}p < 0.05$; $^{**}p < 0.008$, $n = 4$–5). **(D)** Reproducible MAP reduction evoked by two sequential DPNS trains. **(E)** MAP reduction evoked by three consecutive trains of DPNS in five individual SHR animals. **(F,G)** 1 ms pulses induced a reduction in MAP in each animal and a significant reduction in MAP compared to baseline (unpaired *t*-test; $^{**}p < 0.02$, $n = 8$). ES, electrical stimulation, MAP, mean arterial pressure; HR, heart rate; BPM, beats per minute; RSNA, renal sympathetic nerve activity; DPN, deep peroneal nerve.

(**Figure 4C**). During active stimulation, the w-μCE on the DPN evoked contraction of the TA muscle producing paw dorsiflexion (**Figure 4D**). We confirmed that magnetic fields of 17.3–45.6 A/m were able to power the implanted w-μCE devices in 6 SHR animals and videotaped the motor responses produced by DPNS.

The hind-limb was color labeled in the ankles and toes to trace the movement of paw dorsiflexion evoked by the external antenna at 28.16 A/m (**Figure 4E**) and monophasic cathodic pulses at 2 Hz at 0–50% power intensity. **Figure 4F** displays the pixels obtained from the video as an x, y trajectory of the limb movements evoked at increasing power levels from the external

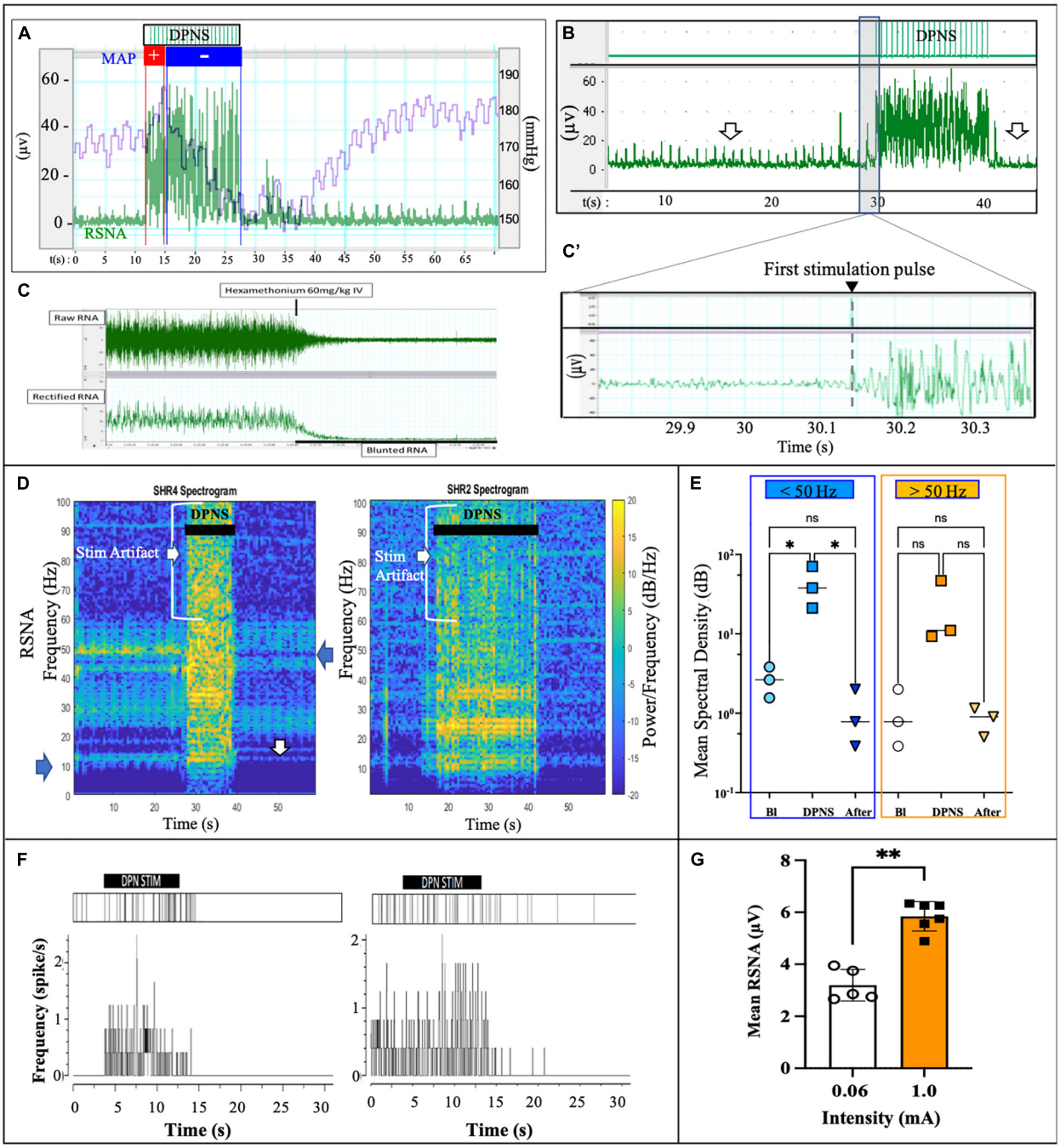

FIGURE 3 | DPNS neuromodulation of RSN activity. **(A)** Spontaneous RSNA (green) increased in amplitude and frequency during the 10 s DPNS. Concurrently, the MAP decreases (blue). **(B,B')** The onset of RSNA was observed at approximately 0.2 s after the first DPNS stimulation pulse. Arrows point before and after RSNA, to highlight the decrease in amplitude. **(C)** Nicotinic receptor blocker hexamethonium (60 mg/kg) confirmed RSNA activity. **(D)** Power spectral analysis in two different SHR animals after 10 and 20 s of DPNS showed the RSNA band at 10–50 Hz; arrows point signals and stimulus artifact. **(E)** Compared to baseline (Bl), the mean SSD showed a significant increase in the RSNA range (ANOVA $^{*}p < 0.05$, $n = 3$), but not 10 s after stimulation. **(F)** Raster plots of two waveforms from RSNA, one was evoked during the stimulation and the second was present before stimulation and reduced thereafter. **(G)** 1 mA stimulation pulses increased the amplitude of the evoked RSNA ($^{**}p < 0.004$, paired *t*-test, $n = 5$). ES, electrical stimulation; DPN, deep peroneal nerve; DPNS, deep peroneal nerve stimulation; RSNA, renal sympathetic nerve activity.

RF antenna. Threshold limb activity was observed at 20% of power and the maximal response at 40%, with magnetic fields below the 1.6 W/Kg SAR limit.

In Phase III, a cohort of 9 SHR animals was also implanted with telemetry BP measurement systems (**Figure 5A**), evaluated for active DPNS implanted with functional w-μCE stimulators

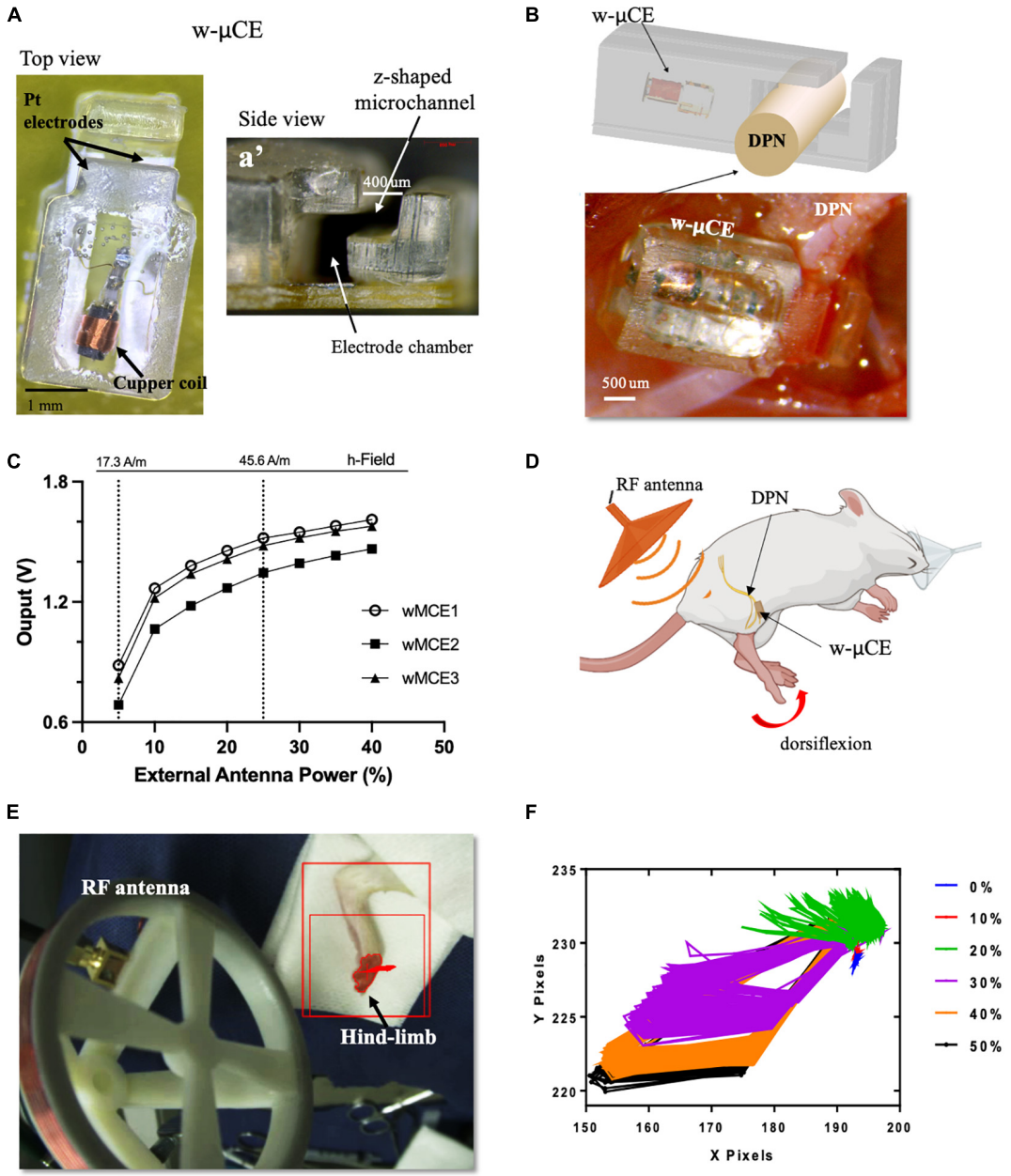

FIGURE 4 | w-μCE for sub-chronic DPNS. **(A)** Picture of the w-μCE top view. **(A')** Side view of the insertion z-shaped channel and electrode chamber. **(B)** Schematic and picture of the w-μCE implanted onto the DPN. **(C)** Voltage output from the w-μCE as a function of power from the external antenna (n = 3). **(D)** Illustration of the device implanted in the DPN and evoked dorsiflexion. **(E)** Placement of the external antenna, 3–4 cm from the w-μCE; the hind-limb was stained to facilitate dynamic pixel tracking during videotaping. **(F)** Pixels tracked from the video recorded during DPNS sessions are displayed in an X/Y graph. The evoked movement was directly proportional to the RF power (0–50%). w-μCE, wireless multichannel electrode; DPNS, deep peroneal nerve stimulation; RF, radio frequency.

(n = 6), and compared to sham-treated animals that are implanted with not-functional devices (n = 3). Three weeks after recovery, all animals were exposed to the external RF treatment and telemetry MAP data were recorded before and after the stimulation. The data show averaged MAP per animal at 15-s intervals, demonstrating a decrease in BP in all SHR animals with an active stimulator (DPNS treatment), but not in those with inactive devices and sham treatment (**Figure 5B**). Active DPNS showed a depressor response that persisted for 12 min before returning to mean baseline values (**Figure 5C**). At baseline, all animals showed MAP values of 150 ± 14 mmHg (n = 9; **Figure 5D**), but at 8 min after the stimulation, MAP values were similar in sham animals (150 ± 13 mmHg; n = 3), but were significantly reduced ($^*p < 0.04$, one-way ANOVA followed by Dunnett's test) in the DPNS-treated group (135 ± 8 mmHg; n = 6; **Figure 5D**). The depressor response in animals with an

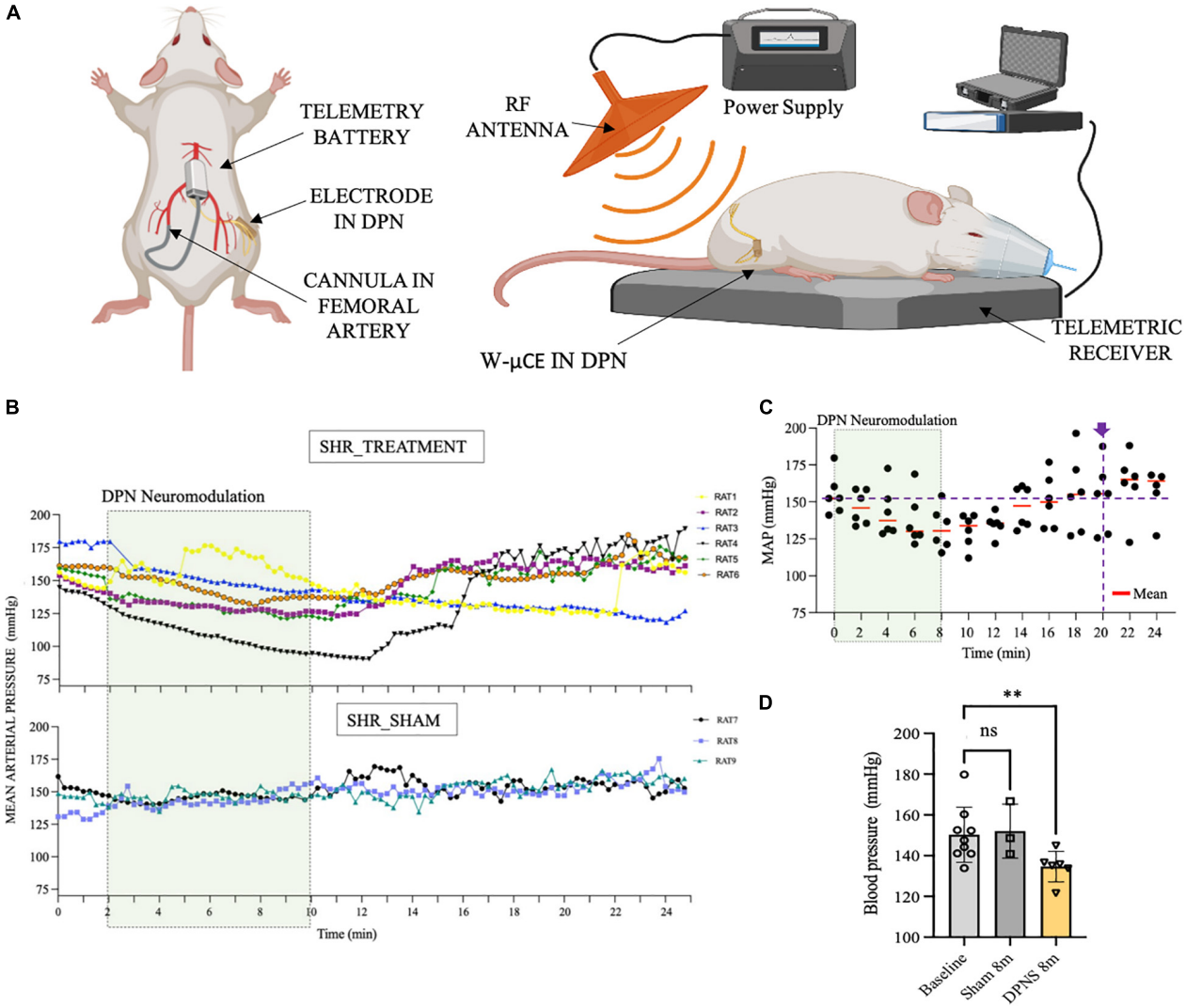

FIGURE 5 | Effect of sub-chronic DPNS on mean arterial pressure in SHR animals. **(A)** Experimental setup; mean arterial pressure was measured with a telemetric device from the femoral artery. The external RF antenna delivered pulses to the w-mCE on the DPN. **(B)** Mean arterial pressure modulation by DPN stimulation, at day 21 of implantation (n = 6 SHR animals treated, n = 3 SHR sham). At baseline, all animals showed MAP values of (150 ± 14 mmHg; n = 9); the shadowed square represents the period of stimulation. SHR treated showed a decrease from 159 to 128 mmHg (n = 6), while the sham group maintained a MAP of 150 ± 13 mmHg (n = 3). **(C)** Individual datapoints of SHR with an active w-μCE (n = 6) with their means obtained every 2 min. The depressor response progressively returned to baseline levels at minute 20 from the start of the stimulation (164 ± 26 mmHg). **(D)** Effect of DPN stimulation at minute 8 significantly reduced the MAP (**p < 0.004 one-way ANOVA followed by Dunnett's test) in the DPNS-treated group (135 ± 8 mm Hg; n = 6), while MAP values were similar in sham animals (150 ± 13 mm Hg; n = 3). DPN, deep peroneal nerve; DPNS, DPN stimulation; RF, radio frequency; SHR, spontaneous hypertense rats; w-mCE, wireless micro-channel electrode.

active w-μCE was progressively returned to baseline levels 14 min later (164 ± 26 mmHg). Maximal reduction in BP in the DPNS group was observed 2 min after the end of stimulation, which showed a reduction from 159 mmHg prior to stimulation to 128 mmHg after. These data confirmed that stimulation of the DPN using a fully implantable device can reproducibly induce a MAP depressor response.

To evaluate the effect of DPNS treatment in fully awake animals, a separate cohort of four SHR animals was acclimated and stimulated for 10 min while restrained in a cylindrical enclosure, repeated daily for 10 days. In these animals, BP was measured by tail-cuff before and 1 and 2 h after the bioelectronic treatment. Evoked hindlimb movements by DPNS were used to confirm the treatment and showed that it failed in two animals during the first week, but remained effective in the other two animals during the 2 weeks test period.

This group of animals showed BP measurements comparable with previous groups with telemetric device implantation, where the systolic blood pressure average was 139 ± 5 mmHg and 10 days after recovery was 142 ± 1 mmHg (**Figure 6A**).

Fifteen days after daily DPNS significantly lowered the systolic (**Figure 6B**) and diastolic (**Figure 6C**) BP, at 1 and 2 h post-electrical stimulation (128 ± 7 and 119 ± 1 mmHg; respectively) when compared to baseline. The reduction in systolic BP was estimated at −10% at 1 h and −16% at 2 h after the DPNS when compared to the post-implantation baseline. These changes were found to be significant using a two-ANOVA followed by Tukey's multiple comparison test despite the low sample number, given that 15–20 measurements of MAP were taken per animal at each time point.

Gross Anatomy and Histology

The foreign body response to the w-μCE on the DPN was evaluated in four SHR animals 30 days after implantation. The gross histological observation did not show signs of hematoma, inflammation, nerve compression, and tissue damage in the area of the implanted device. The nerve appeared normal and the device was not displaced despite being placed near the knee, an area of high mobility (**Figure 7A**). After device removal, the nerve had a normal and healthy appearance (**Figure 7B**). This agrees with observations of these animals during the 2-week testing, that showed normal gait behavior, and no signs of pain or discomfort during normal walking or after stimulation were noted, despite the clear observation of evoked paw movement.

The DPN tissue was processed for immunofluorescence to visualize axonal marked b-tubulin, and the myelin protein P0 marker, in the control non-implanted side (**Figures 7C,D'**) when compared to the side implanted with the w-μCE device (**Figures 7E,F'**). Cross sections of the nerve segment implanted in the middle of the device showed either normal shapes or slight deformations when compared to the normal contralateral side. Axon and myelin staining showed an absence of nerve fiber loss or demyelination in the implanted nerve, being comparable to the non-implanted side. We also stained the tissue with antibodies that label activated macrophage (ED-1) markers to evaluate the possibility of inflammation. The numbers of activated macrophages per cross-section range were estimated at 44 ± 20 ED1 + cells and were similar to that seen in not-implanted controls (n = 4 each group, t-test $p < 0.01$). Together, the histological evaluation of the tissue indicated that placement of this miniature wireless stimulator did not cause harm to the nerve.

DISCUSSION

Cardiovascular depressor responses have been previously reported after stimulation of the sciatic nerve or its deep peroneal branch (Baum et al., 1966; Kim and Romero-Ortega, 2012). This report further elucidates that pulses of 1 ms duration are more effective when compared to shorter ones in mediating the reduction of MAP and that the depressor response can be reproduced with sequential stimulation events in anesthetized and ventilation-assisted animals. We also confirmed in anesthetized animals without breathing support, that DPNS was lowered 12 mmHg ($p < 0.02$) in MAP, suggesting that this effect is independent of respiratory-sympathetic pathways. While this is a tempting interpretation, the interaction between the cardiovascular and respiratory systems during DPNS is certainly complex and deserves further investigation. Long stimulation pulses are known to recruit more axons, particularly of medium and large diameters, including those that mediate antidiuresis in the renal nerve, when compared to short pulses or increased amplitude, which recruit small unmyelinated axons involved in renal vasoconstriction (DiBona et al., 1996). This observation suggests that increasing both amplitude and pulse duration, additional renal axons are recruited. The renal nerve is known to play an important role in cardiovascular homeostasis (Ricksten et al., 1979; Veiga et al., 2021), and it contains both efferent sympathetic and afferent sensory axons from the kidney to the dorsal root ganglia, which project centrally to the brain (Leal et al., 2012; Mizuno et al., 2014; Pettigrew et al., 2017). It has been reported that denervation of the sinoaortic baroreceptors results in an immediate increase in RSNA, HR, and MAP (Dibona and Jones, 2001). In this study, DPNS induced an initial increase in RSNA during the first 2–3 s, followed by a reduction in renal activity and MAP, despite the increase in HR. The observed activation of the RSNA during the DPNS was not expected since its activity is associated with hypertension (DiBona and Kopp, 1997; Günter et al., 2019; Osborn et al., 2021) and is known to be overactive in SHR animals (Lundin et al., 1984). We further determined that the evoked RSNA activity was not a stimulation artifact, as it was asynchronous and delayed when compared to the first electrical pulse of the DPNS. Given that DPNS also induced paw movements that might be contaminating the RSNA recordings with motion or EMG artifacts, we did a power spectral analysis to separate the 2 Hz stimulation frequency from higher frequency signals. At high frequencies (i.e., 50–100 Hz) we only observed the stimulation artifact during DPNS, with comparable power density before or after the stimulation. In contrast, the spontaneous RSNA activity in the 10–50 Hz band was increased significantly to maximal power density during DPNS. This likely reflects the induced changes in RNSA, as its spiking frequency contains several frequency bands, including 0.2–0.4, 2–6 Hz (cardiac and baroreceptors) and 10–12 Hz (Malpas, 1998). The high-frequency RSNA does not correlate with other functions, appears after baroreceptor denervation, and seems to have a central origin (Malpas and Ninomiya, 1992). Thus, these signals seem related to the functional regulation of the tubules, blood vessels, and the juxtaglomerular granular cells in the kidney, which are normally supplied by different post-ganglionic neurons with bimodal axon diameter distribution (1.2 and 1.6 μm) (Dibona, 2001).

The modulation of MAP during the DPNS is likely to be a complex interplay between the direct stimulation of small myelinated Aδ fibers and unmyelinated c-fibers likely mediating the immediate increase in RNSA (Murphy et al., 2011), and central command signals that regulate the sympathetic outflow are evoked by mechanical and metabolic changes in the muscle (Malpas, 1998), such as the activation of baroreceptors known for phasic inhibitory input to the sympathetic ganglia (Kumada et al., 1990). This interpretation is supported by reports of electrical stimulation of the central afferent axons in the renal nerve, shown to induce an immediate reduction in sympathetic

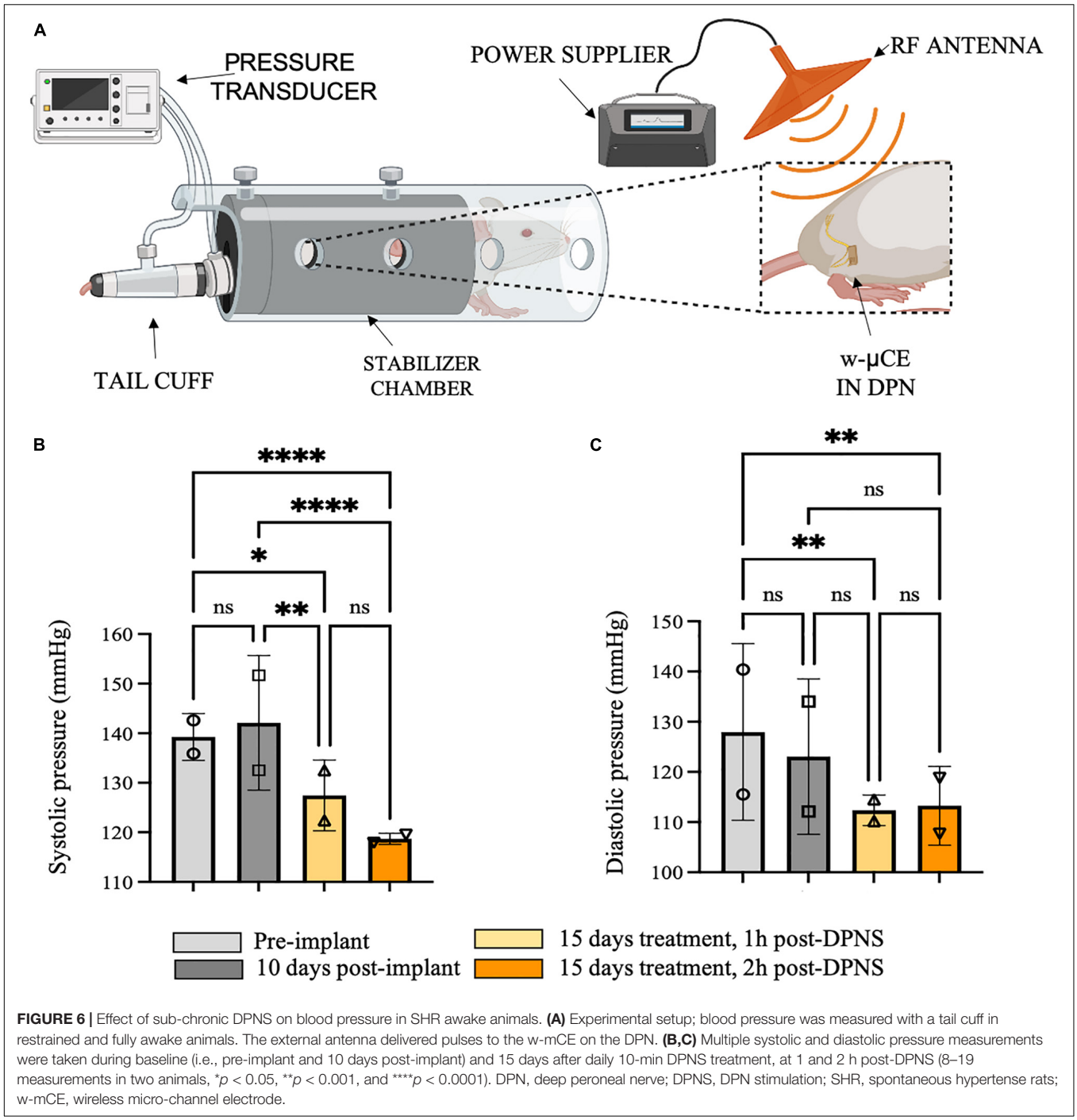

FIGURE 6 | Effect of sub-chronic DPNS on blood pressure in SHR awake animals. **(A)** Experimental setup; blood pressure was measured with a tail cuff in restrained and fully awake animals. The external antenna delivered pulses to the w-mCE on the DPN. **(B,C)** Multiple systolic and diastolic pressure measurements were taken during baseline (i.e., pre-implant and 10 days post-implant) and 15 days after daily 10-min DPNS treatment, at 1 and 2 h post-DPNS (8–19 measurements in two animals, $^{*}p < 0.05$, $^{**}p < 0.001$, and $^{****}p < 0.0001$). DPN, deep peroneal nerve; DPNS, DPN stimulation; SHR, spontaneous hypertense rats; w-mCE, wireless micro-channel electrode.

nerve activity and MAP (Aars and Akre, 1970). Therefore, a plausible mechanistic explanation of the relation between RSNA modulation and the reduction in MAP by DPNS might involve the initial pressor response activating the baroreceptors, which in turn reduced the sympathetic tone and mediated the subsequent reduction in MAP (Moffitt et al., 2005). However, the precise role of RSNA in MAP during DPNS, and the role of baroreceptor reflexes and RSNA activity, in response to DPNS reduction in MAP warrants further investigation.

This study also reported that DPNS can be elicited using fully implantable w-μCE electrodes anchored to the nerve through a Z-shaped microchannel. Stretching the nerve during device implantation did not cause apparent nerve injury, likely due to the unique elastic properties of peripheral nerves. Transient 5–10% strain to the nerve can cause minor alterations in nerve conduction that can be recovered immediately with no functional deficits (Rickett et al., 2011), and they can stretch up to 40% briefly without causing damage (Rydevik et al., 1990;

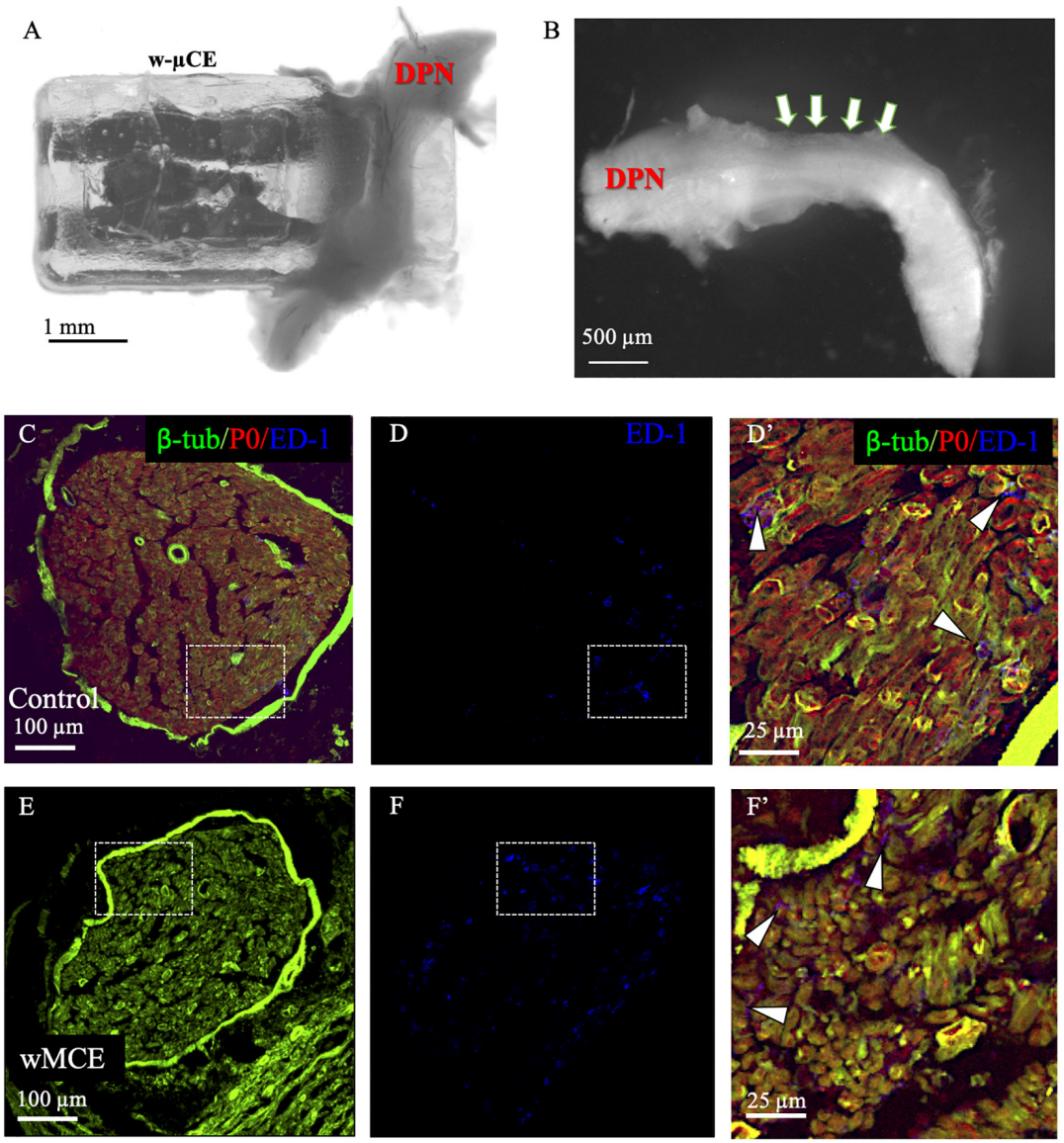

FIGURE 7 | Nerve histology after sub-chronic wMCE implantation. **(a)** Picture of DPN in the device 30 days after implantation. **(b)** Nerve segment after device removal, arrows point out the area where the electrode was implanted. Cross-section histology of control **(c–d')**, and wMCE implanted DPN **(e–f')**, **d'** and **f'** are magnifications of the dotted line squares in panel **c,d** and **e,f**, respectively. Fluorescent labels: b-tubulin (axons), P0 (myelin), ED-1 (activated macrophages).

Wall et al., 1992; Yeoh et al., 2021). In humans, extensive studies of stress and strain on peripheral nerves have indicated that 20–32% of elongation does not result in structural and functional damage (Sunderland and Bradley, 1961). This explains the fact that the w-μCE electrode implanted in the DPN for up to 30 days did not cause discomfort to the animals, and no signs of nerve injury or inflammation were observed in histological preparations.

The wireless w-μCE stimulators allowed the simultaneous evaluation of DPN neuromodulation therapy and telemetric acute BP measurements in animals 3 weeks after implantation. These animals were anesthetized so that the distance to the antenna and the stimulation could be controlled. Wireless stimulation of the DPN induced a reduction in MAP only in hypertensive animals implanted with active stimulators, but not in sham animals with inactive devices, confirming that DPNS induced an acute depressor response in animals with sub-chronic implants and that the application of RF field by the external antenna alone, did not affect the BP. We also confirmed that the DPNS induced a depressor response in restrained fully awake animals, despite the small variabilities in placing the external antenna. In these animals, systolic BP and diastolic BP were reduced for up to 2 h after DPNS, demonstrating the feasibility of this neuromodulation modality. Importantly, none of these animals showed signs of pain or discomfort during the stimulation and evoked paw movements. This is in agreement

with the low content of nociceptor fibers in this nerve and the low stimulation intensity used in this study.

LIMITATIONS

This study is limited to the evaluation of the acute and sub-chronic effects of DPNS. Further research is necessary to investigate whether BP regulation can be achieved chronically and whether continuous activation of the DPN is needed to maintain the beneficial effects of this bioelectronic treatment. It is important to note that SHR animals are not representative of all forms of human hypertension but rather are a model of essential hypertension only. Whether neural stimulation of the DPN can be effective in other types of hypertension remains to be determined.

In summary, this study reports the feasibility and effectiveness of peripheral nerve stimulation for successfully reducing the BP in SHR animals, offering support to the notion that this neuromodulation modality may be beneficial in alleviating RH.

DATA AVAILABILITY STATEMENT

The original contributions presented in the study are included in the article/supplementary material, further inquiries can be directed to the corresponding author.

ETHICS STATEMENT

The animal study was reviewed and approved by the IACUC at The University of Texas at Dallas.

AUTHOR CONTRIBUTIONS

MR-O, SS, and WV designed the research and acquired funding for the project. MR-O and CB contribute to device fabrication. MR-O, MG-G, KR, DVL, DL, JB, H-KK, and AK: *in vivo* studies. AH-R did device characterization. MR-O and MG-G did data analysis. MR-O, MG-G, SS, and WV contributed with data interpretation. MR-O and MG-G wrote the manuscript. All authors discussed the results and revised the manuscript.

FUNDING

This project was supported by the American Heart Association, Collaborative Sciences Award 18CSA33990385.

ACKNOWLEDGMENTS

We would like to thank Martha A. Romero, Marimar Becerra-Gonzalez, Nusayba El-Ali, Ken Nguyen, and Mason Garza for technical support.

REFERENCES

Aars, H., and Akre, S. (1970). Reflex changes in sympathetic activity and arterial blood pressure evoked by afferent stimulation of the renal nerve. *Acta Physiol. Scand.* 78, 184–188. doi: 10.1111/j.1748-1716.1970.tb04654.x

Bakris, G. L., Nadim, M. K., Haller, H., Lovett, E. G., Schafer, J. E., and Bisognano, J. D. (2012). Baroreflex activation therapy provides durable benefit in patients with resistant hypertension: results of long-term follow-up in the Rheos Pivotal Trial. *J. Am. Soc. Hypertens.* 6, 152–158. doi: 10.1016/j.jash.2012.01.003

Bassen, H., Schaefer, D. J., Zaremba, L., Bushberg, J., Ziskin, M., and Foster, K. R. (2005). IEEE Committee on Man and Radiation (COMAR) Technical Information Statement "exposure of medical personnel to electromagnetic fields from open magnetic resonance imaging systems". *Health Phys.* 89, 684–689. doi: 10.1097/01.hp.0000172545.71238.15

Baum, T., Rosenthale, M. E., Shropshire, A. T., and Datko, L. (1966). Cardiovascular and somatic reflexes in experimental allergic encephalomyelitis. *Circ. Res.* 18, 118–125. doi: 10.1161/01.res.18.2.118

Carey, R. M., Calhoun, D. A., Bakris, G. L., Brook, R. D., Daugherty, S. L., Dennison-Himmelfarb, C. R., et al. (2018). Resistant hypertension: detection, evaluation, and management: a scientific statement from the American heart association. *Hypertension* 72, e53–e90. doi: 10.1161/HYP.0000000000000084

Chia, R., Pandey, A., and Vongpatanasin, W. (2020). Resistant hypertension-defining the scope of the problem. *Prog. Cardiovasc. Dis.* 63, 46–50. doi: 10.1016/j.pcad.2019.12.006

Dibona, G. (2001). Functionally specific renal sympathetic nerve fibers: role in cardiovascular regulation. *Am. J. Hypertens.* 14, S163–S170. doi: 10.1016/s0895-7061(01)02084-2

Dibona, G. F., and Jones, S. Y. (2001). Dynamic analysis of renal nerve activity responses to baroreceptor denervation in hypertensive rats. *Hypertension* 37, 1153–1163. doi: 10.1161/01.hyp.37.4.1153

DiBona, G. F., and Kopp, U. C. (1997). Neural control of renal function. *Physiol. Rev.* 77, 75–197. doi: 10.4199/C00034ED1V01Y201106ISP022

DiBona, G. F., Sawin, L. L., and Jones, S. Y. (1996). Differentiated sympathetic neural control of the kidney. *Am. J. Physiol.* 271(1 Pt. 2), R84–R90. doi: 10.1152/ajpregu.1996.271.1.R84

Ewen, S., Böhm, M., and Mahfoud, F. (2017). Long-term follow-up of baroreflex activation therapy in resistant hypertension. *Hypertension* 69, 782–784. doi: 10.1161/hypertensionaha.117.09163

Flachskampf, F. A., Gallasch, J., Gefeller, O., Gan, J., Mao, J., Pfahlberg, A. B., et al. (2007). Randomized trial of acupuncture to lower blood pressure. *Circulation* 115, 3121–3129. doi: 10.1161/circulationaha.106.661140

Flack, J. M., Calhoun, D., and Schiffrin, E. L. (2018). The new ACC/AHA hypertension guidelines for the prevention, detection, evaluation, and management of high blood pressure in adults. *Am. J. Hypertens.* 31, 133–135. doi: 10.1093/ajh/hpx207

Freeman, D. K., O'Brien, J. M., Kumar, P., Daniels, B., Irion, R. A., Shraytah, L., et al. (2017). A sub-millimeter, inductively powered neural stimulator. *Front. Neurosci.* 11:659. doi: 10.3389/fnins.2017.00659

Gonzalez-Gonzalez, M. A., Kanneganti, A., Joshi-Imre, A., Hernandez-Reynoso, A. G., Bendale, G., Modi, R., et al. (2018). Thin film multi-electrode softening cuffs for selective neuromodulation. *Sci. Rep.* 8:16390. doi: 10.1038/s41598-018-34566-6

Groenland, E. H., and Spiering, W. (2020). Baroreflex amplification and carotid body modulation for the treatment of resistant hypertension. *Curr. Hypertens. Rep.* 22:27. doi: 10.1007/s11906-020-1024-x

Gu, F., Randall, E. B., Whitesall, S., Converso-Baran, K., Carlson, B. E., Fink, G. D., et al. (2020). Potential role of intermittent functioning of Baroreflexes in the etiology of hypertension in spontaneously hypertensive rats. *JCI Insight* 5:e139789. doi: 10.1172/jci.insight.139789

Günter, C., Delbeke, J., and Ortiz-Catalan, M. (2019). Safety of long-term electrical peripheral nerve stimulation: review of the state of the art. *J. Neuroeng. Rehabil.* 16:13.

Hernandez-Reynoso, A. G., Nandam, S., O'Brien, J. M., Kanneganti, A., Cogan, S. F., Freeman, D. K., et al. (2019). Miniature electroparticle-cuff for wireless

peripheral neuromodulation. *J. Neural Eng.* 16, 046002. doi: 10.1088/1741-2552/ab1c36

Janssen, B. J., van Essen, H., Vervoort-Peters, L. H., Struyker-Boudier, H. A., and Smits, J. F. (1989). Role of afferent renal nerves in spontaneous hypertension in rats. *Hypertension* 13, 327–333. doi: 10.1161/01.hyp.13.4.327

Kim, Y. T., Kanneganti, A., Fatemi, S., Nothnagle, C., Wijesundara, M., and Romero-Ortega, M. I. (2014). "A novel Microchannel Electrode Array: towards bioelectronic medical interfacing of small peripheral nerves," in *Proceedings of the 2014 36th Annual International Conference of the IEEE Engineering in Medicine and Biology Society* (Piscataway, NJ: IEEE). doi: 10.1109/EMBC.2014.6944002

Kim, Y., and Romero-Ortega, M. (2012). Material considerations for peripheral nerve interfacing. *MRS Bull.* 37, 573–580. doi: 10.1557/mrs.2012.99

Kumada, M., Terui, N., and Kuwaki, T. (1990). Arterial baroreceptor reflex: its central and peripheral neural mechanisms. *Prog. Neurobiol.* 35, 331–361. doi: 10.1016/0301-0082(90)90036-g

Lauder, L., Azizi, M., Kirtane, A. J., Böhm, M., and Mahfoud, F. (2020). Device-based therapies for arterial hypertension. *Nat. Rev. Cardiol.* 17, 614–628. doi: 10.1038/s41569-020-0364-1

Leal, A. K., Murphy, M. N., Iwamoto, G. A., Mitchell, J. H., and Smith, S. A. (2012). A role for nitric oxide within the nucleus *Tractus solitarii* in the development of muscle mechanoreflex dysfunction in hypertension. *Exp. Physiol.* 97, 1292–1304. doi: 10.1113/expphysiol.2012.065433

Li, P., Tjen-A-Looi, S. C., Cheng, L., Liu, D., Painovich, J., Vinjamury, S., et al. (2015). CME article: long-lasting reduction of blood pressure by electroacupuncture in patients with hypertension: randomized controlled trial. *Med. Acupunct.* 27, 253–266. doi: 10.1089/acu.2015.1106

Lundin, S., Ricksten, S. E., and Thoren, P. (1984). Renal sympathetic activity in spontaneously hypertensive rats and normotensive controls, as studied by three different methods. *Acta Physiol. Scand.* 120, 265–272. doi: 10.1111/j.1748-1716.1984.tb00133.x

Mahfoud, F., Schlaich, M. P., and Lobo, M. D. (2021). Device therapy of hypertension. *Circ. Res.* 128, 1080–1099. doi: 10.1161/circresaha.121.318091

Malpas, S. (1998). The rhythmicity of sympathetic nerve activity. *Prog. Neurobiol.* 56, 65–96. doi: 10.1016/s0301-0082(98)00030-6

Malpas, S. C., and Ninomiya, I. (1992). Fundamental rhythm of renal sympathetic nerve activity in anesthetized cats. *J. Auton. Nerv. Syst.* 37, 11–18. doi: 10.1016/0165-1838(92)90140-c

Mendoza, M. F., Kachur, S. M., and Lavie, C. J. (2021). Tailoring the management of hypertension to comorbidities. *Curr. Opin. Cardiol.* 36, 405–412. doi: 10.1097/HCO.0000000000000860

Mizuno, M., Iwamoto, G. A., Vongpatanasin, W., Mitchell, J. H., and Smith, S. (2014). Exercise training improves functional sympatholysis in spontaneously hypertensive rats through a nitric oxide-dependent mechanism. *Am. J. Physiol. Heart Circ. Physiol.* 307, H242–H251. doi: 10.1152/ajpheart.00103.2014

Moffitt, J. A., Grippo, A. J., and Johnson, A. K. (2005). Baroreceptor reflex control of heart rate in rats studied by induced and autogenic changes in arterial pressure. *Am. J. Physiol. Heart Circ. Physiol.* 288, H2422–H2430. doi: 10.1152/ajpheart.00057.2004

Muntner, P., Hardy, S. T., Fine, L. J., Jaeger, B. C., Wozniak, G., Levitan, E. B., et al. (2020). Trends in blood pressure control among US adults with hypertension, 1999-2000 to 2017-2018. *JAMA* 324, 1190. doi: 10.1001/jama.2020.14545

Murphy, M. N., Mizuno, M., Mitchell, J. H., and Smith, S. A. (2011). Cardiovascular regulation by skeletal muscle reflexes in health and disease. *Am. J. Physiol. Heart Circ. Physiol.* 301, H1191–H1204. doi: 10.1152/ajpheart.00208.2011

Narkiewicz, K., Ratcliffe, L. E., Hart, E. C., Briant, L. J., Chrostowska, M., Wolf, J., et al. (2016). Unilateral carotid body resection in resistant hypertension: a safety and feasibility trial. *JACC Basic Transl. Sci.* 1, 313–324. doi: 10.1016/j.jacbts.2016.06.004

Osborn, J. W., Tyshynsky, R., and Vulchanova, L. (2021). Function of renal nerves in kidney physiology and pathophysiology. *Annu. Rev. Physiol.* 83, 429–450. doi: 10.1146/annurev-physiol-031620-091656

Pettigrew, R. I., Heetderks, W. J., Kelley, C. A., Peng, G. C., Krosnick, S. H., Jakeman, L. B., et al. (2017). Epidural spinal stimulation to improve bladder, bowel, and sexual function in individuals with spinal cord injuries: a framework for clinical research. *IEEE Trans. Biomed. Eng.* 64, 253–262. doi: 10.1109/TBME.2016.2637301

Rickett, T., Connell, S., Bastijanic, J., Hegde, S., and Shi, R. (2011). Functional and mechanical evaluation of nerve stretch injury. *J. Med. Syst.* 35, 787–793. doi: 10.1007/s10916-010-9468-1

Ricksten, S. E., Noresson, E., and Thoren, P. (1979). Inhibition of renal sympathetic nerve traffic from cardiac receptors in normotensive and spontaneously hypertensive rats. *Acta Physiol. Scand.* 106, 17–22. doi: 10.1111/j.1748-1716.1979.tb06364.x

Rydevik, B. L., Kwan, M. K., Myers, R. R., Brown, R. A., Triggs, K. J., Woo, S. L., et al. (1990). An *in vitro* mechanical and histological study of acute stretching on rabbit Tibial nerve. *J. Orthop. Res.* 8, 694–701. doi: 10.1002/jor.1100080511

Shanks, J., Manou-Stathopoulou, S., Lu, C. J., Li, D., Paterson, D. J., and Herring, N. (2013). Cardiac sympathetic dysfunction in the prehypertensive spontaneously hypertensive rat. *Am. J. Physiol. Heart Circ. Physiol.* 305, H980–H986. doi: 10.1152/ajpheart.00255.2013

Sunderland, S., and Bradley, K. C. (1961). Stress-strain phenomena in human peripheral nerve trunks. *Brain* 84, 102–119. doi: 10.1093/brain/84.1.102

Touw, K. B., Haywood, J. R., Shaffer, R. A., and Brody, M. J. (1980). Contribution of the sympathetic nervous system to vascular resistance in conscious young and adult spontaneously hypertensive rats. *Hypertension* 2, 408–418. doi: 10.1161/01.hyp.2.4.408

Veiga, A. C., Milanez, M. I. O., Campos, R. R., Bergamaschi, C. T., and Nishi, E. E. (2021). The involvement of renal afferents in the maintenance of cardiorenal diseases. *Am. J. Physiol. Regul. Integr. Comp. Physiol.* 320, R88–R93. doi: 10.1152/ajpregu.00225.2020

Wall, E. J., Massie, J. B., Kwan, M. K., Rydevik, B. L., Myers, R. R., and Garfin, S. R. (1992). Experimental stretch neuropathy. Changes in nerve conduction under tension. *J. Bone Joint Surg. Br.* 74, 126–129. doi: 10.1302/0301-620X.74B1.1732240

Yeoh, S., Warner, W. S., Eli, I., and Mahan, M. A. (2021). Rapid-stretch injury to peripheral nerves: comparison of injury models. *J. Neurosurg.* 135, 893–903. doi: 10.3171/2020.5.JNS193448

Conflict of Interest: MR-O owns shares in RBI Medical, a medical device company. RBI Medical did not have any role in data collection, analysis, or the manuscript.

The remaining authors declare that the research was conducted in the absence of any commercial or financial relationships that could be construed as a potential conflict of interest.

Publisher's Note: All claims expressed in this article are solely those of the authors and do not necessarily represent those of their affiliated organizations, or those of the publisher, the editors and the reviewers. Any product that may be evaluated in this article, or claim that may be made by its manufacturer, is not guaranteed or endorsed by the publisher.

Advantages of publishing in Frontiers

OPEN ACCESS
Articles are free to read for greatest visibility and readership

FAST PUBLICATION
Around 90 days from submission to decision

HIGH QUALITY PEER-REVIEW
Rigorous, collaborative, and constructive peer-review

TRANSPARENT PEER-REVIEW
Editors and reviewers acknowledged by name on published articles

Frontiers
Avenue du Tribunal-Fédéral 34
1005 Lausanne | Switzerland

Visit us: www.frontiersin.org
Contact us: frontiersin.org/about/contact

REPRODUCIBILITY OF RESEARCH
Support open data and methods to enhance research reproducibility

DIGITAL PUBLISHING
Articles designed for optimal readership across devices

FOLLOW US
@frontiersin

IMPACT METRICS
Advanced article metrics track visibility across digital media

EXTENSIVE PROMOTION
Marketing and promotion of impactful research

LOOP RESEARCH NETWORK
Our network increases your article's readership